Numerical Simulations of Neutron Star - Black Hole Mergers

by Frank Löffler

Max–Planck–Institut für Gravitationsphysik
Albert–Einstein–Institut

Universität Potsdam

thesis supervisor: Professor Bernard F. Schutz

October 2005

To my parents.

Contents

Acknowledgments

First of all I want to thank Ed Seidel for giving me the opportunity to start my studies at the Albert-Einstein-Institute and being available for discussions despite his very busy schedule. I would like to thank Bernard Schutz and the Max-Planck-Society for general support.

Most of the numerical and hydrodynamical things and tricks I have learned from Ian Hawke, who is a great tutor in many ways. I also thank him for the massive and excellent proof-reading of this thesis. Denis Pollney receives my thanks for, among other things, his support as head of our research group, for help with any problems and little issues and also for proof-reading.

I would like to thank all the people I have worked with and whose programs I was allowed to use. Enumerating them would generate a far too long list. Nevertheless some people stand out for various smaller and bigger reasons. They are, in alphabetical order, Marcus Ansorg for very useful discussions and permission to use and modify parts of his work, Luca Baiotti and Christian Ott for their amazingly extensive proof-reading of this thesis, Thomas Radke for his assistance in `Cactus`, compiler and `OpenDX` issues, Luciano Rezzolla for his help with any upcoming physics-question, for his invitations to SISSA, his support with a fellowship of EGO and for carefully proof-reading this thesis, Erik Schnetter for all his advice concerning `Carpet` in special and `Cactus` in general, Jonathan Thornburg for all the time he has spent in answering my numerous big and little questions and also for proof-reading my thesis and Steve White for hacking our terrifying `cvs`-scripts, help and insight into `CSS` and nice discussions in between.

The results of this thesis have been obtained by using computer time allocations at the Albert Einstein Institute (AEI, Germany), the National Center for Supercomputing Applications (NCSA, USA), the University of Parma (Italy), the Leibniz-Rechenzentrum München (LRZ, Germany), the Pittsburgh Supercomputing Center (PSC, USA) and the Rechenzentrum Garching (RZG, Germany). This work was supported in part by DFG grant "SFB Transregio 7: Gravitationswellenastronomie", by NSF grants PHY-02-18750, PHY-02-44788 and PHY-03054842, by the MIUR and EU Programme

"Improving the Human Research Potential and the Socio-Economic Knowledge Base" (Research Training Network Contract HPRN-CT-2000-00137), by NASA grant NNG04GL37G and by DGAPA-UNAM grants IN112401 and IN122002.

Last, but surely not least, I want to thank my wife Katja for so many things, that it could fill pages. I would not have written this thesis without her.

Chapter 1

Overview

1.1 The black hole / neutron star problem

The behaviour of matter is not well known in very high density regimes or in very strong gravitational fields. Some reasons for this are first the technical problems to create such or similar environments on Earth or in nearby space, and second that regions where such conditions prevail are so far away that they are hard to observe with current astrophysical instruments. Prime examples of objects with very strong gravitational fields are neutron stars and black holes.

Neutron stars are the collapsed remains of formerly massive, "usual" (nuclear burning) stars with cores reaching nuclear densities (very approximately $10^{14}\mathrm{g/cm}^3$; for a more detailed discussion of the birth of neutron stars, see *e.g.* [1]). As a first approximation a neutron star may be thought of a very big (ca. 10km in radius) atomic nucleus. This, however, is only the simplest possible approximation. It neglects its constituents, because a neutron star does not only consist of neutrons, but also electrons, protons and possibly more exotic matter. This mix, which can be modeled as fluid, might also be a superfluid due to the high pressure. The above picture also neglects the neutron star crust (see *e.g.* [2–4]). This crust is a very thin lattice of neutrons at the surface of the star. However, it is, *e.g.*, an important component for modelling pulsar glitches (see *e.g.* [5–7]). It also neglects any magnetic fields, which are potentially very strong and may have a crucial influence on the structure and dynamics of neutron stars. Obviously, this is not a good way to think about a neutron star in general. However, as a first approximation and in certain situations it is possible to model a neutron star in such a way (see section 2.3).

There are many definitions as to what a black hole is. It may be thought

of as the end state of a stellar collapse in which no internal forces, such as a pressure force, is able to halt the collapse and prevent the formation of a singularity in spacetime [8, 9]. However, at least in the classical theory, no observer that could "see" such singularity would be able to communicate this information to another observer outside the black hole. This is called the "cosmic censorship hypothesis" [10].

The boundary of a black hole is the event horizon. Nothing can escape from within this horizon, not even light. This is also the definition of this horizon: a closed surface from which not even light can escape outwards (a more precise definition follows in section 2.2.2). In classical General Relativity, it is impossible for an observer to find out what is inside and come back out. In this context, anything happening inside of a black hole is irrelevant to the exterior and therefore physically not interesting. However the interior may have mathematically interesting features and may also be relevant in other theories of gravity.

Another way to look at black holes is as being collaps*ing* stars (in the case of black holes formed by collapsing stars; there are also discussions about so called primordial black holes, which formed in the very early universe, see *e.g.* [11, 12]). The reason is that once a star starts to collapse to a black hole, what one sees from outside is a larger and larger redshift and a fading of the light coming from the star. One will never see the horizon forming since (for the observer outside) it will take infinitely long for the matter of the star to collapse.

There is strong evidence that objects like neutron stars or black holes do exist [13, 14] and even collide [15–18] in our universe. Such a collision is believed to radiate a lot of energy in form the of gravitational waves (ripples in spacetime) which might be detectable by the newly built gravitational wave detectors [19] such as LIGO, Virgo and GEO and by the planned space detector LISA. Amongst the astrophysical phenomena that are the best candidates for producing detectable wave signals for the Earth-based detectors, those including highly relativistic matter near black holes stand out. Black hole / neutron star binaries are believed to be as likely to be observed as binary neutron star mergers (*e.g.* [17, 20]), with expected event rates of one per year in a sphere of about 70Mpc radius [17] and an expected detection rate of more than one event per year [14] (for LIGO II). Signals from binary neutron star and mixed binary systems in close orbit are expected to give information about the neutron star structure and equation of state (EOS) [14, 21]. However calculating these waves is far too difficult to be done analytically, therefore numerical investigations are needed. By looking at these waves it might be possible to obtain more information about the matter involved and the nearby spacetime.

Mixed binaries are also interesting for a number of other reasons, *e.g.* they could be a source of short gamma ray bursts [22–25], that last typically for about ~ 0.3s [26]. Newtonian results (*e.g.* [27]) suggest a stable or repeated, but in any case long-lasting, mass transfer from the neutron star to the black hole. However that might be different in General Relativity [28], which is required in the presence of black holes.

1.2 Previous results

Considerable effort has gone into modelling systems of binaries containing either two black holes (*e.g.* [29–43]) or two neutron stars [44–46]; see also the review article [47].

Current research into *mixed* binary systems has often been performed using Newtonian gravity. Analytical work was done, *e.g.* on stable mass transfer from a neutron star to a black hole [27]. Numerical simulations have been carried out, *e.g.* using smooth particle hydrodynamics with soft [48] and stiff [49] equations of state. Those results suggest that, depending on the mass ratio, at least part of the neutron star is tidally disrupted before the merger. They also use linearized theory (see *e.g.* [50]) to compute gravitational waves [48, 49].

Recently these systems have received more attention and there are some results in Newtonian gravity with relativistic modifications to the gravitational potential (*e.g.* see [51, 52]). There are also results using full General Relativity, *e.g.* Baumgarte et al. [53] used the conformal thin-sandwich formalism [47, 54] to create initial data for a mixed, orbiting system. They solve the constraint equations together with the Euler equations for the neutron star matter in a corotating frame, in which the system is assumed to be stationary. Using this scheme, a sequence can be generated by varying the separation of the objects. These so called "quasi-stationary sequences", assume that a stationary spacetime is a good approximation at fixed times during the inspiral. This is only an approximation, because they must lose energy and angular momentum through gravitational radiation. Therefore these orbits are called "quasi-stationary". This is a good approximation if the timescale of the infall is long compared to the orbital timescale and possible instability timescales. This is usually fulfilled if the objects are still very far away from each other. However, it becomes more and more inaccurate as they get closer and the approximation breaks down [55–57]. A dynamical evolution will be required at least from this point on. In [53], the black hole is only included as background metric around the neutron star and is not included in the computational domain. This limits these results to very large

black hole-to-neutron star mass ratios. The work presented in [58] extends this scheme to irrotational configurations. It predicts that the effect of the spin of the neutron star has only a minor effect on the location of the tidal break-up. This location is clearly important for the form of the gravitational waves produced in such an event.

In contrast to the Newtonian results, analytical, relativistic investigations suggest a merger of a mixed system to be prompt in most cases [28], *i.e.*, for the case of comparable masses. This is due to the angular momentum loss due to gravitational radiation, which causes a direct merger rather than an extended mass transfer. According to this analysis, even an accretion disc is very unlikely.

Recent work from Bishop et al. [59] computes initial data for a mixed, orbiting system for the characteristic formulation of Einstein's equations [60–63]. They can show that initial, spurious gravitational waves (due to approximations of the initial data creation scheme) quickly radiate away, so that the system relaxes to a quasi-equilibrium state with an approximate orbital motion of the star. In contrast to the other relativistic results mentioned before, these simulations also include a dynamical evolution, however only short-term (a small fraction of an orbit).

1.3 Outline

In this work I will present results of my studies aiming at numerical simulations of a black hole / neutron star binary system. I will discuss all the physical models and approximations used in chapter 2. Chapter 3 explains how this can be done using computers.

Part of the new results presented in this thesis are hydrodynamical excision techniques. They are described in detail in chapter 4. This work has been published in Phys. Rev. D **71**, 104006 in 2005 [64].

These methods have been used to perform numerical simulations of collapse of rotating neutron stars to black holes. Firstly this was a good test for the excision techniques and secondly gave new physical results, which I present in chapter 5 and which have been published in Phys. Rev. D **71**, 024035 in 2005 [65].

Different possibilities for the creation of initial data for mixed binaries are shown in chapter 6, which are different from previously published data. The problems which have been preventing long enough stable evolutions of mixed binary initial data in the past, as well as the solutions we used, are described in chapters 5 and 6. In the latter chapter, first results of simulations of these initial data for a mixed binary system are presented.

Finally I give an outline for the future work on the subject of this thesis.

1.4 Conventions and units

Throughout this work Greek indices run from 0 to 3 indicating the four dimensions of spacetime and 0 usually referring to the direction of time. Unless otherwise stated, Latin indices run from 1 to 3.

In all formulæ indices occurring twice are to be summed over the possible range for that index.

Unless stated otherwise, I adopt the convention of units in which $c = G = M_\odot = 1$. In these units, we say we *e.g.* measure time or distances by M:

$$1 \text{ M (time)} \sim 0.5 \times 10^{-2} \text{ ms} \tag{1.1}$$

$$1 \text{ ms} \sim 203 \text{ M (time)} \tag{1.2}$$

$$1 \text{ M (distance)} \sim 1.5 \text{ km} \tag{1.3}$$

$$1 \text{ km} \sim 0.67 \text{ M (distance)} \tag{1.4}$$

Chapter 2

Physical foundations

The topic of this work can be seen as consisting of two main parts: handling the spacetime and handling the dynamics of a neutron star. Both parts have their difficulties in general, as well as when simulating them on computers and both have to be combined to simulate a collision of a neutron star and a black hole in the general relativistic setting. Both also introduce a number of approximations in order to deal with the complexity of the physical problem. These approximations are explained in the following.

2.1 General Relativity

Up to the beginning of the 20th century physics treated space and time like Newton did: Space itself is a fixed, three-dimensional space in which all physical processes run without reacting back on this object. Time is measured uniformly by different observers and is independent of the position or properties in space. This is what everyone in his or her normal life usually observes. However since the beginning of the 20th century we have been able to measure the deviations from this theory and a new (or improved) theory was introduced to explain those deviations: Einstein's theory of General Relativity. The differences between the two theories are for most purposes too small in every day life to be relevant. However this is progressively changing. Examples are provided by the GPS (Global Positioning System) or the planned Galileo system. Both would fail because of time differences between the atomic clocks in the satellites and on earth, which are due to the small effect of the gravitational field of the earth [66].

This does not mean that Newton's theory is completely wrong and should not be used anymore. As already said, the differences are not important in most daily cases. Both theories (like all theories) are *lies to children* (as

defined in chapter 4 of [67] and explained more in chapter 26 of the follow-up [68]). They simplify the world to a model which a human can understand and they do it at a different level. However, one important motivation for this work are gravitational waves from mixed binary systems and the simplest model including those waves and the compact bodies of the binary system is General Relativity.

It is possible to linearise General Relativity, but this cannot be used for a system containing a neutron star and a black hole. It is also possible to "extend" Newton's theory by "Post-Newtonian" extensions[1] and include gravitational waves in those. However, these also have problems like the question of convergence to General Relativity and the question of how "accurate" a truncation at a certain order really is [69, 70]. This approximation also cannot be used near the mixed binary system. The strong gravitational fields near the binary system make the use of full General Relativity inevitably.

Not going too much into the details and examples that are usually explained in nearly every textbook, We start with one of the prominent equations related to General Relativity:

$$G_{\mu\nu} \equiv R_{\mu\nu} - \frac{1}{2} R g_{\mu\nu} = 8\pi c G T_{\mu\nu}. \tag{2.1}$$

$G_{\mu\nu}$ is the Einstein tensor and is just a combination of the Ricci tensor $R_{\mu\nu}$, the Ricci Scalar R and $g_{\mu\nu}$ which is the metric of the spacetime. The Ricci Scalar R is defined as $R \equiv R^{\mu}_{\mu}$. $R_{\mu\nu}$ is defined as a contraction of the Riemann curvature tensor (or short Riemann tensor) $R_{\mu\nu} = R^{\nu}{}_{\mu\nu\rho}$. The Riemann tensor itself is a complicated expression involving the metric and its first and (also mixed) second derivatives:

$$R^{\pi}{}_{\mu\nu\rho} = \Gamma^{\pi}_{\mu\rho,\nu} - \Gamma^{\pi}_{\mu\nu,\rho} + \Gamma^{\pi}_{n\nu}\Gamma^{n}_{\mu\rho} - \Gamma^{\pi}_{n\rho}\Gamma^{n}_{\mu\nu} \tag{2.2}$$

with

$$\Gamma^{\pi}_{\mu\rho} = \frac{1}{2} g^{\pi\nu} \left(g_{\mu\nu,\rho} + g_{\rho\nu,\mu} - g_{\mu\rho,\nu} \right). \tag{2.3}$$

It is important to keep some of its properties in mind:

$$R_{\mu\nu\rho}{}^{\pi} = -R_{\nu\mu\rho}{}^{\pi} \tag{2.4a}$$

$$R_{[\mu\nu\rho]}{}^{\pi} = 0 \tag{2.4b}$$

$$R_{\mu\nu\rho\pi} = -R_{\mu\nu\pi\rho} \tag{2.4c}$$

[1] Post-Newtonian theory expands General Relativity in terms of $\left(\frac{v}{c}\right)^2$. It is an approximation which is not good, *e.g.* for velocities near the speed of light or strong gravitational fields.

and the so called Bianchi Identity:

$$R_{\mu\nu\rho\pi;\sigma} + R_{\mu\nu\sigma\rho;\pi} + R_{\mu\nu\pi\sigma;\rho} = 0. \tag{2.5}$$

Note the use of two different derivatives, the partial derivative

$$T^{\alpha}_{,\nu} \equiv \partial_\nu T^\alpha \equiv \frac{\partial T^\alpha}{\partial x^\nu} \tag{2.6}$$

and the covariant derivative

$$T^{\alpha}_{;\nu} \equiv \nabla_\nu T^\alpha \equiv T^{\alpha}_{,\nu} + \Gamma^{\alpha}_{\mu\nu} T^\mu \tag{2.7}$$

$$T_{\alpha;\nu} \equiv T_{\alpha,\nu} - \Gamma^{\mu}_{\alpha\nu} T_\mu. \tag{2.8}$$

Looking at the right hand side of equation (2.1), there is c which is the speed of light, G which is called gravitational constant and $T_{\mu\nu}$ which is the stress-energy tensor. In the units used in this thesis (see subsection 1.4) equation (2.1) becomes:

$$G_{\mu\nu} \equiv R_{\mu\nu} - \frac{1}{2} R g_{\mu\nu} = 8\pi T_{\mu\nu}. \tag{2.9}$$

By taking the Bianchi Identity (2.5), multiplying it with $g^{\mu\rho} g^{\nu\sigma}$ and using equation (2.4a) one obtains

$$\left(R_{\mu\nu} - \frac{1}{2} R g_{\mu\nu} \right)_{;\nu} = 0. \tag{2.10}$$

Compared to equation (2.1), this yields

$$T^{\mu\nu}{}_{;\nu} = 0. \tag{2.11}$$

This is the relativistic form of energy and momentum conservation, which is already included in the field equations.

2.2 Analytic solutions

Although the general formulæ look very simple, the difficulties are hidden in the form in which they are written down. General Relativity is now known for nearly one century, but only a few analytic solutions with astrophysical relevance are known. Even those are very simple compared to reality. In the following, we will look shortly into some of them.

2.2.1 Minkowski

The Minkowski solution is a trivial solution, neglecting any energy or curvature. Special Relativity is assuming that the spacetime is the Minkowski spacetime and is not influenced by anything happening inside. The line element for the Minkowski metric in Cartesian coordinates is just

$$\mathrm{d}s^2 = -\,\mathrm{d}t^2 + \mathrm{d}x^2 + \mathrm{d}y^2 + \mathrm{d}z^2. \tag{2.12}$$

Note that this definition uses the signature $(-1, 1, 1, 1)$. However, the choice $(1, -1, -1, -1)$ is also valid and used by various authors.

2.2.2 Schwarzschild

The Schwarzschild solution was the first nontrivial solution of Einstein's equations found. Einstein himself first believed that the equations are so complicated that an exact, nontrivial solution would never be found. But a short time after he published his theory, Schwarzschild found his solution for a spherically symmetric and static spacetime containing a black hole [71] or a sphere of incompressible fluid [72].

As we know today, it is also the solution for the exterior spacetime of any spherically symmetric mass/energy distribution. It can be shown that the assumption of a spherically symmetric spacetime in vacuum automatically implies a static spacetime and that the only solution for this is the Schwarzschild metric. This is known as Birkhoff's Theorem (for a proof, see, *e.g*, [73]). The Schwarzschild metric written in Schwarzschild coordinates is given by

$$\mathrm{d}s^2 = -\left(1 - \frac{2M}{r}\right) c^2\,\mathrm{d}t^2 + \frac{1}{1 - \frac{2M}{r}}\,\mathrm{d}r^2 + r^2\left(\mathrm{d}\theta^2 + \sin\theta\,\mathrm{d}\phi^2\right). \tag{2.13}$$

Here, r denotes the coordinate distance to the singularity, θ and ϕ are the usual angles of polar coordinates and t is the time coordinate. In this coordinates, the spacetime has a coordinate singularity at $r = 2M$ while the physical singularity is at $r = 0$.

Later, Reissner and Nordstrøm extended this to charged black holes [74]. However, unlike the gravitational force, the electromagnetic force can have both signs. This is important since this way electromagnetic charges of opposite sign would attract each other and would annihilate. This is not possible with gravitational charges - masses. Therefore it is not expected that black holes do have large charges and this extension is not so important astrophysically.

Two definitions are also to be introduced here. The first is the event horizon. This is the boundary of the interior of a black hole. From inside a black hole no signal (*e.g.* light) can leave the black hole and reach spatial infinity, from outside it can. The geometric definition of an event horizon is the boundary of the past of future null infinity (assuming an asymptotically flat spacetime) [75].

The second definition is the apparent horizon. It is defined as being a outermost, closed, marginally trapped surface. This marks a surface from which signals (*e.g.* photons again) cannot move outwards at a given point in time (thus are "trapped"). This is not the same as the event horizon in general, because some photons, which can move outwards from the surface may find themselves trapped later because the surface location changed. In stationary spacetimes however, they coincide (if the apparent horizon exists, which does not have to be the case, even if an event horizon is present; for details see [76]). In contrast to the event horizon, the apparent horizon can grow faster than the speed of light and in particular it can grow discontinuously. It is also never outside the event horizon (assuming non-negativeness of local energy, see [77]).

2.2.3 Kerr

In 1963 Kerr found a solution describing a rotating black hole [78], which was also extended later to charged rotating black holes [79]. It is a generalisation of the Schwarzschild / Reissner and Nordstrøm solution. The metric for the general case

$$\begin{aligned} \mathrm{d}s^2 = &- \left(\frac{\Delta - a^2 \sin^2\theta}{\Sigma}\right) \mathrm{d}t^2 - \frac{2a \sin^2\theta (r^2 + a^2 - \Delta)}{\Sigma} \,\mathrm{d}t\,\mathrm{d}\phi \\ &+ \left[\frac{(r^2 + a^2)^2 - \Delta a^2 \sin^2\theta}{\Sigma}\right] \sin^2\theta \,\mathrm{d}\phi^2 + \frac{\Sigma}{\Delta}\,\mathrm{d}r^2 + \Sigma\,\mathrm{d}\theta^2 \end{aligned} \tag{2.14}$$

with

$$\Sigma = r^2 + a^2 \cos^2\theta \tag{2.15}$$

$$\Delta = r^2 + a^2 + e^2 - 2Mr \tag{2.16}$$

reduces to the non-charged case if $e = 0$ and to the non-rotating case if $a = 0$. Unfortunately there is no known exact, analytical solution which contains a star embedded in a Kerr metric (with rotation).

Because every star is generally expected to rotate at least a little bit [80] and in case such a star collapses to a black hole, this rotation is expected

to speed up due to angular momentum conservation, black holes are also usually expected to rotate. However non-rotating black holes are easier to handle and are still a valid configuration for simulations. Therefore they are usually chosen as test objects first, as we do in this thesis.

2.3 Neutron stars

Each class of stars has one primary force to counteract the gravitation of the star itself to prevent it from collapsing. In stars such as our sun, this is the pressure gradient coming from the heating due to fusion from lighter to heavier elements. Iron is the last element in this series, it is not possible to fuse it further without actually pumping energy into the process. Thus, the star loses its main restoring force and collapses (see [1] for a detailed description of collapse scenarios).

However it is possible that another force is able to hold that collapse: the degeneracy pressure of the electrons. In this case a white dwarf can be formed. If the white dwarf is accreting sufficient material afterwards or if the original star had too much mass already, the electron degeneracy pressure is also not strong enough to support the star and it collapses further.

During the collapse the electrons are captured by protons an heavy nuclei to form neutrons, so a small star made nearly entirely out of neutrons is formed. Those particles also have a degeneracy pressure, much higher than the one of the electrons (but on a smaller length scale). This can stop the collapse and a neutron star is formed. Because the neutrons are packed at nuclear densities, one can view neutron stars as being very big atomic nuclei. Neutron stars have been proposed first by Baade and Zwicky in 1934 [81, 82].

However, if much more mass is accreting onto the neutron star (*e.g.* from non yet collapsed outer shells of the former star) not even this pressure can prevent a further collapse. Up to now no other, stronger force is known for sure, which could again stall the collapse, to prevent the formation of a black hole. However, another class of stars, strange / quark stars, are under discussion (*e.g.* [83–85]).

The typical mass of a neutron star is about $1.4M_\odot$ and its typical radius about 12km [86]. The minimal and maximal values are not known exactly and vary depending on the model of the equation of state between 1.4 and roughly 2.5 solar masses [86, 87]. These values are expected to depend also on the physical properties like the presence of rotation, the rotation profile and the presence, form and strength of magnetic fields.

In this work we neglect the effect of magnetic fields completely, although they could potentially have crucial impact on the results. This will and

has to be extended in the future. In this work we consider only initially uniformly rotating neutron stars. Uniform rotation is expected because we assume old neutron stars. Differential rotation, which is expected after the birth of the neutron star either by a collapsing star [88] or as the end-result of a binary merger of two neutron stars [89], should have been transformed into a uniform rotation [90–92] by *e.g.* dissipative viscous effects or the coupling with non-turbulent magnetic fields.

In parts of this thesis non-rotating stars are used as a first approximation, which is, while not as likely as rotating stars, not an unphysical model, but rather just a special and simpler case. Many approximations go into the description of the matter. For example we assume the matter to be described by a single component fluid (i.e., we ignore the presence of different particles such as neutrons, electrons and protons, using only a single "particle" type with no charge). We also neglect any structure of the neutron star, *e.g.* the crust (for details see [93]). This is also connected to the approximations in the equation of state, which are discussed in the following.

It is possible to use the Newtonian gravitational potential (with corrections) to model neutron stars (see *e.g.* [51, 94–98]). However, the aim of this work is a simulation of a merger of a neutron star and a black hole, which requires the use of full General Relativity.

2.3.1 Equations of state for neutron stars

The equation of state (EOS) describes the connection between various properties of matter such as the temperature T, the mass density ρ, the internal energy ϵ, the composition and the pressure P.

The EOS of neutron stars is not well known, because the expected densities and temperatures are well above anything which could be achieved in any experimental setup today and because of the intrinsic difficulties in determining the radius of neutron stars. However, it is possible to make estimates from known equations of state in nuclear physics, experimental astronomical data or using relativistic Dirac-Brueckner-Hartree-Fock Nuclear Theory or compressible liquid drop models [93, 99, 100]. This way it is possible to obtain quite detailed equations of state. Usually these equations are given in a tabular form. However, there are also analytical representations, *e.g.* [101].

However we did not use these sophisticated equations for the studies here so far, because they are usually not freely available, quite slow to use in a simulation and there are reasonable and fast approximations, which are explained below. However this is something that can and has to be improved in later work.

A general EOS for a one-component fluid has the form

$$P = P(\rho, \epsilon), \tag{2.17}$$

where ρ is the rest-mass density, ϵ the specific energy density and P the pressure.

2.3.2 Non-perfect fluids

The stress-energy tensor of a non-perfect fluid is

$$T^{\mu\nu} = \rho(1+\epsilon)u^\mu u^\nu + (P - \zeta\phi)h^{\mu\nu} - 2\eta\sigma^{\mu\nu} + q^\mu u^\nu + q^\nu u^\mu, \tag{2.18}$$

where u^μ is the four-velocity of the fluid, ζ and η are the bulk and shear viscosities (viscosities normal and parallel to the boundary of a fluid/fluid-cell), ϕ the expansion defined as $\phi \equiv \nabla_\mu u^\mu$, $h^{\mu\nu}$ the spatial projection tensor $h^{\mu\nu} = u^\mu u^\nu + g^{\mu\nu}$ and q^μ the energy flux vector. Finally, $\sigma^{\mu\nu}$ is the symmetric, tracefree, spatial shear tensor, defined by $\sigma^{\mu\nu} = \frac{1}{2}(\nabla_\alpha u^\mu h^{\alpha\nu} + \nabla_\alpha u^\nu h^{\alpha\mu}) - \frac{1}{3}\phi h^{\mu\nu}$.

2.3.3 Perfect Fluid

A perfect fluid is an approximate description that neglects non-adiabatic effects, such as viscosity or heat transfer. We want to study cold neutron stars which are are not only cold, but also superfluid [102], hence have vanishing viscosity. Therefore the use of this approximation is justified.

The stress energy tensor of a perfect fluid is given by

$$T_{\mu\nu} = \rho h u_\mu u_\nu + P g_{\mu\nu}. \tag{2.19}$$

$h = 1 + \epsilon + \frac{P}{\rho}$ is the relativistic specific enthalpy, u^μ is the fluid four-velocity, P the pressure, ρ the rest-mass density and ϵ is the specific internal energy.

However, in this work, while speaking of a "perfect" or "ideal fluid", we always restrict ourselves to a special equation of state, the so called "Γ-law EOS":

$$P = (\Gamma_{\text{ad}} - 1)\,\rho\epsilon, \tag{2.20}$$

where Γ_{ad} is the adiabatic index of the fluid.

The Γ-law EOS with a $\Gamma \sim 2$ can be used as rough, but fast approximation to the real EOS of cold neutron stars. There are certainly more realistic EOSs, but they are usually computationally very expensive and in most cases not freely available. Therefore the EOS above is used in some cases contained in this thesis.

We will later use the equation for the energy density[2] ρ_{ADM} for a perfect fluid, hence we define it here:

$$\rho_{\mathrm{ADM}} = n^\mu n^\nu T_{\mu\nu} = W^2 \left(\rho(1+\epsilon) + P\right) - P, \tag{2.21}$$

which in the case of $W = 1$ (W is the Lorentz factor as defined later in equation (2.31)) simplifies to

$$\rho_{\mathrm{ADM}} = \rho(1+\epsilon). \tag{2.22}$$

2.3.4 Polytropic equation of state

The polytropic EOS is a special variant of the ideal fluid EOS, in which the pressure depends solely on the density. This is a restriction to a constant temperature, which amounts to a restriction to cases without big changes of internal energy which are caused by something other than density changes. This is violated near shocks. Nevertheless, this EOS is believed to be good and simple enough to be used as first approximation for matter in a neutron star near to equilibrium [103].

As already mentioned, the pressure P in this EOS is solely a function of the density ρ, instead of also involving the specific internal energy ϵ:

$$P = K\rho^\Gamma. \tag{2.23}$$

The two constants here are the polytropic constant K and the polytropic index Γ. The specific internal energy is in this case given by

$$\epsilon = \frac{K\rho^{\Gamma-1}}{\Gamma - 1}. \tag{2.24}$$

2.4 The 3+1 Formalism

One way to do numerical simulations using full General Relativity is to split the four components of the spacetime into three "space" and one "time" coordinate. Therefore it is called the "3+1" formalism. It foliates the four-dimensional spacetime (or only parts of it) into three-dimensional space-like hypersurfaces. The parameter distinguishing these hypersurfaces is then called "time". A vector is said to be timelike if its norm is negative. If it

[2]The use of ADM in the subscript of ρ_{ADM} has the historic reason that, in contrast to the rest-mass density ρ, the energy density ρ_{ADM} is occurring in the ADM equations (see section 2.6.1).

is exactly zero it is said to be null, and if it is positive it is called spacelike. Surfaces are spacelike if all tangent vectors are spacelike.

Physical laws such as General Relativity have a form such that from the knowledge of the initial state of a system all future states can be determined (that is why this is called "deterministic"). In Newtonian mechanics, for example, the trajectory of a point particle is fixed by its initial position, initial velocity and the forces acting on it. In order to "translate" this into General Relativity we need to specify the "initial state", because in General Relativity there is no notion of absolute simultaneity. An observer can define a notion of simultaneity, but this depends upon his state of motion. Thus, choosing an initial state requires choosing an initial hypersurface. With this idea in mind we first want to discuss the properties of special three-dimensional surfaces embedded in the spacetime. This is also known as "foliation of the spacetime". A foliation $\{\Sigma\}$ is a family of three-dimensional surfaces Σ that fills the four-dimensional spacetime V (or parts of it) such that locally the surfaces arise as the level surfaces of a scalar function. This is the fourth coordinate, usually called "time".

Given a spacetime, there are many possible foliations. Some of them are particularly useful for use in numerical calculations. Choosing a good slicing is an important aspect of any numerical calculation. But first we will explain the details of a general splitting. The metric tensor γ_{ab} of the hypersurfaces Σ

$$\overset{(3)}{\mathrm{d}}s^2 = \gamma_{ab}\,\mathrm{d}x^a\,\mathrm{d}x^b, \tag{2.25}$$

and the metric tensor $g_{\alpha\beta}$ of the full spacetime are related by

$$\overset{(4)}{\mathrm{d}}s^2 = -\left(\alpha\,\mathrm{d}x^0\right)^2 + g_{\alpha\beta}\,\mathrm{d}x^\alpha\,\mathrm{d}x^\beta = \gamma_{ab}\left(\mathrm{d}x^a + \beta^a\,\mathrm{d}x^0\right)\left(\mathrm{d}x^b + \beta^b\,\mathrm{d}x^0\right). \tag{2.26}$$

The three-dimensional metric tensor γ_{ab} is the spatial part of the four-dimensional metric $g_{\alpha\beta}$. Therefore it is called the spatial metric. It is the projection of $g_{\alpha\beta}$ onto Σ along $\mathbf{n}$, which is defined as a vector normal Σ. It must not be null and is normalised.

$$n_\alpha n^\alpha = 1. \tag{2.27}$$

$$\gamma_{ab} \equiv g_{ab} + n_a n_b \tag{2.28}$$

If we now take the hypersurfaces as the coordinate surfaces $x^0 =$ constant of a coordinate system with the other coordinates taken out of the three-surfaces, we can denote the components of the normal vectors by

$$n_\alpha = (\alpha, 0, 0, 0) \quad , \quad n^\alpha = \left(\tfrac{1}{\alpha}, -\tfrac{\beta^a}{\alpha}\right). \tag{2.29}$$

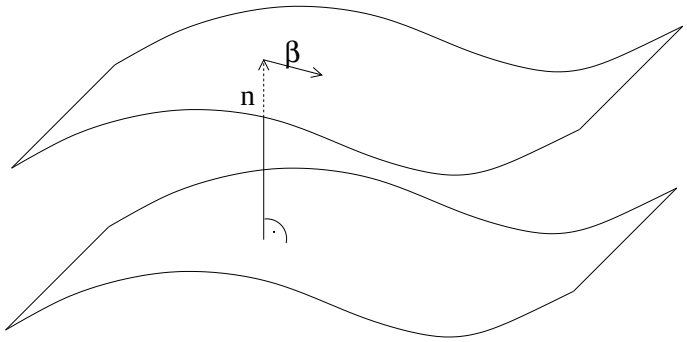

Figure 2.1: Foliation

α is usually called the lapse (not to be confused with the index α) and β^a is called the shift vector. The lapse specifies how Σ changes with changing time and the shift specifies how the coordinates move in this surface with changing time. This can be visualised as in picture 2.1. Both lapse and shift can be specified freely with different choices leading to different gauge conditions. Different gauge choices naturally do not change the physical content, but might change the numerical behaviour drastically (see also section 2.7).

Eulerian observers with a four-velocity $\mathbf{u}$ parallel to $\mathbf{n}$, which means they are at rest on slice Σ, measure the following three-velocity of matter, obtained by projecting the four-velocity $\mathbf{u}$ into Σ:

$$v^i = \frac{\gamma \mathbf{u}}{-\mathbf{n}\mathbf{u}} = \frac{\gamma^i_\nu u^\nu}{\alpha u^0} = \frac{g^i_\nu u^\nu + n^i n_\nu u^\nu}{\alpha u^0} = \frac{u^i}{\alpha u^0} - n^i = \frac{u^i}{W} + \frac{\beta^i}{\alpha}, \tag{2.30}$$

where equation (2.29) and

$$W \equiv -\mathbf{n}\mathbf{u} = \alpha u^0 \tag{2.31}$$

are used and W is called the Lorentz factor.

Using the foliation, Einstein's equations can be cast into a first-order-in-time, second-order-in-space quasi-linear system of twelve equations. which are called "evolution equations", and a set of four elliptic equations, which are usually referred to as "constraint equations". The twelve evolution equations are called like that, because they contain derivatives of γ_{ij} and a newly introduced quantity K_{ij}, the extrinsic curvature, in time.

$$K_{ij} \equiv -\gamma^k_i \gamma^l_j n_{l;k}. \tag{2.32}$$

The constraint equations do not contain such derivatives, thus their name. If these constraints are satisfied at some time in an evolution, *e.g.*, at the beginning, the evolution equations ensure that they are satisfied always in

the domain of dependence of the initial slice[3]. However while this is true analytically, this does not hold exactly in numerical simulations, which makes monitoring constraints an important tool for estimating the errors of a numerical scheme.

Using the definition for K_{ij}, its evolution equation (coming from Einstein's equations) is given by

$$\begin{aligned}\partial_t K_{ij} =& \alpha \left[\bar{R}_{ij} - 2K_{il}K^l_j + KK_{ij} - 8\pi S_{ij} + 4\pi\gamma_{ij}\left(S-\rho\right)\right] \\ &- \bar{\nabla}_i\bar{\nabla}_j\alpha + \beta^l\bar{\nabla}_l K_{ij} + K_{il}\bar{\nabla}_j\beta^l + K_{jl}\bar{\nabla}_i\beta^l\end{aligned} \tag{2.33}$$

with the bar over $\bar{R}$ and $\bar{\nabla}$ denoting the correspondence to the spatial metric γ_{ij}, not $g_{\mu\nu}$. S_{ij} is the projection of the stress-energy tensor onto the spacelike hypersurfaces and $S \equiv \gamma^{ij}S_{ij}$. The evolution equation for γ_{ij} is (coming from the definition of K_{ij}) given by

$$\partial_t\gamma_{ij} = -2\alpha K_{ij} + \bar{\nabla}_i\beta_j + \bar{\nabla}_j\beta_i. \tag{2.34}$$

The constraint equations (Hamiltonian and momentum, respectively) are

$$\bar{R} + K^2 - K_{ij}K^{ij} = 16\pi\rho_{\text{ADM}} \tag{2.35}$$

$$\bar{\nabla}_j\left(K^{ij} - \gamma^{ij}K\right) = 8\pi j^i. \tag{2.36}$$

ρ_{ADM} is the energy density of the matter and j^i is its momentum current. Suitable initial data for this formulation would be *e.g.* the quantities

$$\left\{\gamma_{ij}, K_{ij}, \text{matter variables}\right\}. \tag{2.37}$$

By defining $t \equiv x^0/\alpha$, equation (2.26) turns into the often used form

$$\overset{(4)}{\mathrm{d}}s^2 = -(\alpha^2 - \beta_i\beta^i)\,\mathrm{d}t^2 + 2\beta_i\,\mathrm{d}x^i\,\mathrm{d}t + \gamma_{ij}\,\mathrm{d}x^i\,\mathrm{d}x^j. \tag{2.38}$$

2.5 Initial Data

Creating initial data are not as simple as just setting the variables at the initial time to some values. The initial data have to fulfil the constraint equations, which in general are a system of four coupled, elliptic equations. Even though only this system has to be solved, this is a very challenging problem and has been reviewed extensively in [47]. While solving this system, the coordinates also have to be fixed.

[3]The boundary conditions are also important because they can introduce constraint violations in an evolution too.

Some systems are sufficiently simple to be known analytically. Some known solutions are not interesting for astrophysics, because they are very unlikely to occur or are too simple. In more complicated cases, however, solutions cannot be described by algebraic equations. One example is the solution for TOV stars.

2.5.1 TOV stars

TOV stands for "Tolman-Oppenheimer-Volkoff" ([104, 105]). It is a solution of General Relativity and Euler's equations for hydrostatic equilibrium, describing an asymptotically flat spacetime containing a spherically symmetric and static star. The equation of state (EOS) of its matter has to guarantee that all variables are parametrised solely by the pressure. One often-used example is the polytropic EOS, which is discussed in section 2.3.4. Since the star is spherically symmetric, the exterior of the star is described by the Schwarzschild solution (see section 2.2.2).

The equations of motion and the continuity equation must hold:

$$\nabla_\mu T^{\mu\nu} = 0 \tag{2.39}$$

$$\nabla_\mu j^\mu = 0 \tag{2.40}$$

with $j^\mu = \rho u^\mu$. An additional relation has to be given by an EOS, *e.g.*, the polytropic EOS to close this system. From this, the solution for a spacetime containing a TOV star can be obtained, which is given as an ordinary differential equation (ODE).

$$\frac{\mathrm{d}P}{\mathrm{d}r} = -\left(\rho(1+\epsilon)+P\right)\frac{m(r)+4\pi r^3 P}{r\left[r-rm(r)\right]} \tag{2.41}$$

Here $m(r)$ is the gravitational mass inside a sphere of radius r. This is given in isotropic coordinates with the radius labelled r. Schwarzschild-like coordinates are more convenient for numerical simulations. This requires a coordinate transformation using the Schwarzschild radius on which the Cartesian x, y, z coordinates live. This is labelled $\bar{r}$ here. This requirement together with a condition for the lapse coming from the assumption of a static and spherically symmetric spacetime results in the following system of

differential equations:

$$\frac{\mathrm{d}P}{\mathrm{d}r} = -(\rho(1+\epsilon)+P)\frac{m+4\pi r^3 P}{r(r-2m)}, \tag{2.42}$$

$$\frac{\mathrm{d}m}{\mathrm{d}r} = 4\pi r^2 \rho(1+\epsilon), \tag{2.43}$$

$$\frac{\mathrm{d}(\log(\alpha))}{\mathrm{d}r} = \frac{m+4\pi r^3 P}{r(r-2m)}, \tag{2.44}$$

$$\frac{\mathrm{d}(\log(\bar{r}/r))}{\mathrm{d}r} = \frac{r^{1/2}-(r-2m)^{1/2}}{r(r-2m)^{1/2}}. \tag{2.45}$$

The initial data at $r = 0$ are (for the numerical integration) $P_0 = K\rho_c^\Gamma$, $m_0 = 0$, $\phi_0 = 0$, $\bar{r}_0 = \epsilon$, $r_0 = \epsilon$, where ϵ is a very small number, which is not 0 to avoid division by zero.

Once the integration is done for the interior of the star we match to the exterior, which is the Schwarzschild solution:

$$P = 0, \tag{2.46}$$

$$\bar{r} = \frac{1}{2}\left(\sqrt{r(r-2M)}+r-M\right), \tag{2.47}$$

$$m = M, \tag{2.48}$$

$$\phi = \frac{1}{2}\log(1-2M/r). \tag{2.49}$$

The solution is now known to high numerical accuracy and can be interpolated onto other grids, *e.g.* a three-dimensional grid as initial data.

2.5.2 Michel solution

The Michel solution [106–108] describes steady state, spherical accretion of a test fluid falling from infinity onto a Schwarzschild black hole. It is usually computed in ingoing Eddington-Finkelstein coordinates which penetrate the horizon. While this is not very interesting on astrophysical grounds, it can be used as test-case for numerical codes.

Again, the polytropic EOS is used. The solution can be derived from the basic equations of mass and energy conservation for the fluid by (following Michel [106]) assuming spherical symmetry and staticity to obtain

$$\frac{d}{dr}\left(j^r\sqrt{-g}\right) = 0 \tag{2.50}$$

$$\frac{d}{dr}\left(T_0^r\sqrt{-g}\right) = 0, \tag{2.51}$$

where

$$j^{\alpha} = \rho u^{\alpha} \tag{2.52}$$

and

$$T_{\alpha\beta} = (P + \rho(1+\epsilon))\, u_{\alpha} u_{\beta} + P g_{\mu\nu} \tag{2.53}$$

are the density current and the stress energy tensor.

The background metric written in ingoing Eddington-Finkelstein coordinates is:

$$ds^2 = -\left(1 - \frac{2M}{r}\right) dt^2 + \frac{4M}{r} dt dr + \left(1 + \frac{2M}{r}\right) dr^2 + r^2 \left(d\theta^2 + \sin^2\theta d\phi^2\right). \tag{2.54}$$

The components of the covariant and contravariant metric are:

$$g_{\mu\nu} = \begin{pmatrix} -\frac{r-2M}{r} & \frac{2M}{r} & 0 & 0 \\ \frac{2M}{r} & \frac{r+2M}{r} & 0 & 0 \\ 0 & 0 & r^2 & 0 \\ 0 & 0 & 0 & r^2 \sin^2\theta \end{pmatrix} \tag{2.55}$$

and

$$g^{\mu\nu} = \begin{pmatrix} -\frac{r+2M}{r} & \frac{2M}{r} & 0 & 0 \\ \frac{2M}{r} & \frac{r-2M}{r} & 0 & 0 \\ 0 & 0 & \frac{1}{r^2} & 0 \\ 0 & 0 & 0 & \frac{1}{r^2 \sin^2\theta} \end{pmatrix}. \tag{2.56}$$

Equations (2.50) and (2.51) can be easily integrated and, using the expressions (2.52) and (2.53), one obtains:

$$\rho u^r \sqrt{-g} = C_1 \tag{2.57}$$

$$(P + \rho(1+\epsilon))\, u_t u^r \sqrt{-g} = C_2 \tag{2.58}$$

This can be simplified by dividing (2.58) by (2.57) and taking the square, which leads to

$$h^2 u_t^2 = \left(\frac{C_2}{C_1}\right)^2 = C_3, \tag{2.59}$$

where $h = 1 + \epsilon + \frac{P}{\rho}$ is the specific enthalpy. Given C_3 and a certain ρ_s at one particular u_{ts}, equation (2.59) gives the complete solution by the following

relations to other quantities:

$$C_1 = \rho_s u_s^r \sqrt{-g} \tag{2.60}$$

$$\rho = \frac{C_1}{\sqrt{-g} u^r} \tag{2.61}$$

$$P = K\rho^\Gamma \tag{2.62}$$

$$\epsilon = \frac{P}{(\Gamma - 1)\rho}. \tag{2.63}$$

To obtain the missing value u_{ts} at any point ρ_s one uses first that u_t can be expressed in terms of u^r in Eddington-Finkelstein coordinates (see the metric (2.55) and (2.56)):

$$(u_t)^2 = (u^r)^2 - g_{tt}. \tag{2.64}$$

In addition, at the sonic point the following relation holds independent of equations (2.50) and (2.51):

$$u_s^r = \sqrt{\frac{M}{2r_s}} \tag{2.65}$$

with M being the mass of the black hole. Starting from the sonic point the solution in the entire spacetime can be obtained by a Newton-Raphson iteration scheme.

2.5.3 The York-Lichnerowicz conformal decomposition

While analytically known initial data are nice to have, there are only few interesting cases for which it is available. Most interesting systems are too complicated to be handled in that way. We also cannot just give the initial data in some arbitrary way, because we have to satisfy the constraint equations (equations (2.35) and (2.36)). What we need is a way to specify some of the variables and then compute the remaining ones. This has to be done in such a way that the constraint equations are satisfied and the contained physical information is not lost. One procedure for this is the York-Lichnerowicz conformal decomposition [109–111]. It is widely used for general initial data configurations. Its main feature is the so called conformal decomposition of the metric and certain components of the extrinsic curvature plus a transverse-traceless decomposition of the latter.

First, the three-metric γ_{ij} is decomposed into a conformal factor ψ and an auxiliary metric $\tilde{\gamma}_{ij}$,

$$\gamma_{ij} = \psi^4 \tilde{\gamma}_{ij}. \tag{2.66}$$

Using this equation, the Hamiltonian constraint (2.35) becomes

$$\tilde{\nabla}^2\psi - \frac{1}{8}\psi\tilde{R} - \frac{1}{8}\psi^5 K^2 + \frac{1}{8}\psi^5 K_{ij}K^{ij} = -2\pi\psi^5\rho_{\mathrm{ADM}}. \tag{2.67}$$

Variables that have a tilde on top are associated with $\tilde{\gamma}_{ij}$. All other variables have to be seen in the context of γ_{ij}. We drop the bar over those, which was introduced in equations (2.33) to (2.36), for convenience.

The second ingredient is the splitting of the extrinsic curvature. First K is split into its trace and tracefree parts,

$$K_{ij} \equiv A_{ij} + \frac{1}{3}\gamma_{ij}K. \tag{2.68}$$

Any symmetric tracefree tensor can be split as follows:

$$S^{ij} \equiv (\mathbb{L}X)^{ij} + B^{ij} \tag{2.69}$$

with B^{ij} being a symmetric ($B^{ij} = B^{ji}$), transverse ($\nabla_j B^{ij} = 0$) and traceless ($B^i_i = 0$) tensor and

$$(\mathbb{L}X)^{ij} \equiv \nabla^i X^j + \nabla^j X^i - \frac{2}{3}\gamma^{ij}\nabla_l X^l. \tag{2.70}$$

This split can now be applied to A_{ij}. However it can also be applied to

$$\tilde{A}_{ij} \equiv \psi^2 A_{ij}. \tag{2.71}$$

These two possibilities are the difference between the conformal transverse-traceless decomposition and the physical transverse-traceless decomposition. There is no known advantage of one over the other. For a study on this see, *e.g.*, [112]. In both cases it is possible to specify the same data freely ($\tilde{\gamma}_{ij}$, $\tilde{M}^{ij}$ and K). However, the set of equations is different and also the solutions for the same specified data will in general be different, while still valid for both.

In the following we will only outline the conformal transverse-traceless decomposition, because the basic steps are quite similar in both cases and we have used this choice in our code. For a detailed discussion of both, see [47].

As the name suggests, the decomposition (2.69) is in this case applied to the conformal tracefree extrinsic curvature $\tilde{A}^{ij}$ defined by (2.71):

$$\tilde{A}^{ij} \equiv (\tilde{\mathbb{L}}X)^{ij} + \tilde{Q}^{ij}. \tag{2.72}$$

After applying equations (2.66), (2.68), (2.70), (2.71) and (2.72) to the momentum constraints (2.36), plus using

$$\tilde{\nabla}_j B^{ij} = \psi^{-10}\tilde{\nabla}_j(\psi^{10}B^{ij}) \tag{2.73}$$

and the fact that $\tilde{Q}^{ij}$ is transverse (*i.e.* $\tilde{\nabla}_j\tilde{Q}^{ij} = 0$), they read:

$$\tilde{\nabla}_j(\tilde{\mathbb{L}}X)^{ij} = \tilde{\nabla}^2 X^i + \frac{1}{3}\tilde{\nabla}^i(\tilde{\nabla}_j X^i) + \tilde{R}^i_j X^j = \frac{2}{3}\psi^6\tilde{\nabla}^i K + 8\pi\psi^{10}j^i. \tag{2.74}$$

For a general symmetric tracefree tensor, say $\tilde{M}^{ij}$, we do not know if it is transverse, but we can get its transverse-tracefree part $\tilde{Q}^{ij}$

$$\tilde{Q}^{ij} \equiv \tilde{M}^{ij} - (\tilde{\mathbb{L}}Y)^{ij} \tag{2.75}$$

by using (2.69). Since $\tilde{Q}^{ij}$ is transverse, we also find that

$$\tilde{\nabla}_j\tilde{Q}^{ij} \equiv 0 = \tilde{\nabla}_j\tilde{M}^{ij} - \tilde{\nabla}_j(\tilde{\mathbb{L}}Y^i). \tag{2.76}$$

Using equations (2.75) and (2.76), we can find the required symmetric, transverse-traceless tensor from a general symmetric traceless tensor $\tilde{M}^{ij}$. Thus we can write (2.72) as

$$\tilde{A}^{ij} \equiv (\tilde{\mathbb{L}}V)^{ij} + \tilde{M}^{ij} \tag{2.77}$$

with $V^i \equiv X^i - Y^i$ and, similarly, equation (2.74) can be written as

$$\tilde{\nabla}_j(\tilde{\mathbb{L}}V)^{ij} = \frac{2}{3}\psi^6\tilde{\nabla}^i K - \tilde{\nabla}_j\tilde{M}^{ij} + 8\pi\psi^{10}j^i. \tag{2.78}$$

Using these two equations it is possible to solve directly for V^i. Finally, the full set of equations to solve is:

$$\gamma_{ij} = \psi^4\tilde{\gamma}_{ij} \tag{2.79}$$

$$K^{ij} = \psi^{-10}\tilde{A}^{ij} + \frac{1}{3}\psi^{-4}\tilde{\gamma}^{ij}K \tag{2.80}$$

$$\tilde{A}^{ij} = (\tilde{\mathbb{L}}V)^{ij} + \tilde{M}^{ij} \tag{2.81}$$

$$\tilde{\nabla}_j(\tilde{\mathbb{L}}V)^{ij} - \frac{2}{3}\psi^6\tilde{\nabla}^i K = -\tilde{\nabla}_j\tilde{M}^{ij} + 8\pi\psi^{10}j^i \tag{2.82}$$

$$\tilde{\nabla}^2\psi - \frac{1}{8}\psi\tilde{R} - \frac{1}{12}\psi^5 K^2 + \frac{1}{8}\psi^{-7}\tilde{A}_{ij}\tilde{A}^{ij} = -2\pi\psi^5\rho_{\text{ADM}}. \tag{2.83}$$

For simplicity, in the following we will frequently choose time-symmetric initial data, which means $K_{ij} = 0$ and $j^i = 0$. The momentum constraint is in this case trivially solved and the Hamiltonian constraint simplifies to

$$\tilde{\nabla}^2\psi = -2\pi\psi^5\rho_{\text{ADM}}. \tag{2.84}$$

$\tilde{R}$ vanishes too, because we have chosen conformally flat initial data, which means that the three-metric can be expressed as

$$\tilde{\gamma}_{ij} = \eta_{ij}, \tag{2.85}$$

where η_{ij} is the metric of the Minkowski space.

As has been reported in [113, 114], it is possible to decouple the momentum and Hamiltonian constraint not only in the case of $K_{ij} = 0$, but also in the more general case of $K = 0$ (maximal slicing). In this case, the Hamiltonian constraint (2.83) depends on the solution of the momentum constraint (2.82), but not vice versa. The momentum constraint allows to specify $\tilde{M}^{ij}$ freely. Under the assumption $\tilde{M}^{ij} = 0$, this constraint becomes

$$\tilde{\nabla}^2 V^i + \frac{1}{3}\tilde{\nabla}^i \left(\tilde{\nabla}_j V^j\right) = 0. \tag{2.86}$$

Bowen and York [113] found a solution for this equation. It is given by

$$V^i = -\frac{1}{4r}\left[4P^i + n^i n_j P^j\right] + \frac{1}{r^2}\epsilon^{ijk} n_j S_k. \tag{2.87}$$

r is the distance from some special point (the location of a black hole) and P^i and S^i are two vector fields which can be interpreted as the linear and angular momentum of the black hole.

Using this solution, K_{ij} can be computed via

$$\begin{aligned} K_{ij} = &\frac{3\psi^{-2}}{2r^2}\left[P_i n_j + P_j n_i - (\Delta_{ij} - n_i n_j) P^k n_k\right] + \\ &\frac{3\psi^{-2}}{r^3}\left[\epsilon_{kil} S^l n^k n_j + \epsilon_{kjl} S^l n^k n_i\right] \end{aligned} \tag{2.88}$$

and can be inserted into the Hamiltonian constraint (2.83).

2.6 Evolution

Computing the initial data amounts to calculating the solution on one of the slices of spacetime, which is then called initial slice. The computation of future (or past) slices and the appropriate choice of boundary conditions is what is usually called "evolution" and is the topic of the following chapter.

2.6.1 The evolution system: BSSN

The ability to perform long-term numerical simulations of self-gravitating systems in general relativity strongly depends on the formulation adopted

for the Einstein equations. The covariant nature of these equations (the "many-fingered time" of relativity, see [50]) leads to difficulties in constructing an appropriate coordinate representation which would allow for stable and accurate simulations. Over the years, the standard approach has been mainly based upon the unconstrained solution of the $3+1$ ADM formulation [115] (see subsection 2.4) of the field equations, which, despite large-scale and dedicated collaborations [116–118], has been shown to lack the stability properties necessary for long-term numerical simulations.

In recent years, however, a considerable effort has been invested in extending and changing the set of equations solved by, in some way, including the solution of the constraint equations on each spatial hypersurface [119, 120], or by reformulating the ADM approach in order to achieve long-term stability (see *e.g.* [121] and references therein).

Building on the experience developed with lower-dimensional formulations, Nakamura, Oohara and Kojima [122] presented in 1987 a conformal traceless reformulation of the ADM system which subsequent authors (see *e.g.* [123–131]) demonstrated to be robust enough to accomplish such a goal for different classes of spacetimes, including black holes and neutron stars (both isolated and in coalescing binary systems) [29, 65, 127, 132–135]. The most widespread version developed from this formalism was introduced by [123, 124] and is commonly referred to as the BSSN (Baumgarte-Shapiro-Shibata-Nakamura) or NOK (Nakamura-Oohara-Kojima) formulation.

We will outline this formulation below. More details and how this is actually implemented in our code `Cactus` can be found in [127, 134].

The original ADM formulation casts the Einstein equations into a first-order in time, quasi-linear [136] system of equations. The dependent variables are the three-metric γ_{ij} and the extrinsic curvature K_{ij}. The twelve evolution equations (2.33), (2.34) and the four constraint equations (2.35), (2.36) have already been introduced in section 2.4.

Details of our particular implementation of the conformal traceless reformulation of the ADM system as proposed by [122–124] are extensively described in [127, 134] and we will only describe the basic steps towards it here.

Starting from the evolution equations for K_{ij} (2.33) and γ_{ij} (2.34) the BSSN formulation makes use of a conformal decomposition of the three-metric, defining the conformal factor ψ:

$$\gamma_{ij} = \psi^4 \tilde{\gamma}_{ij} = e^{4\phi} \tilde{\gamma}_{ij} \tag{2.89}$$

This conformal factor can be chosen such that

$$\tilde{\gamma} = \det \tilde{\gamma}_{ij} = 1. \tag{2.90}$$

The tracefree part A_{ij} of K_{ij} (see equation 2.68)

$$A_{ij} \equiv K_{ij} - \frac{1}{3}\gamma_{ij}K. \tag{2.91}$$

can also be conformally decomposed:

$$\tilde{A}_{ij} = e^{-4\phi}A_{ij}. \tag{2.92}$$

Assuming zero shift for simplicity here, the evolution equations for $\tilde{\gamma}_{ij}$ and ϕ then read:

$$\partial_t\tilde{\gamma}_{ij} = -2\alpha\tilde{A}_{ij} \tag{2.93}$$

$$\partial_t\phi = -\frac{1}{6}\alpha K. \tag{2.94}$$

From (2.33) one can find the evolutions equation for K and $\tilde{A}_{ij}$

$$\partial_t K = -\gamma^{ij}\nabla_i\nabla_j\alpha + \alpha\left[\tilde{A}_{ij}\tilde{A}^{ij} + \frac{1}{3}K^2 + \frac{1}{2}(\rho_{\text{ADM}} + S)\right] \tag{2.95}$$

$$\partial_t\tilde{A}_{ij} = e^{-4\phi}\left[-\nabla_i\nabla_j\alpha + \alpha(R_{ij} - S_{ij})\right]^{\text{TF}} + \alpha\left(K\tilde{A}_{ij} - 2\tilde{A}_{il}\tilde{A}^l_j\right). \tag{2.96}$$

However as has been shown [123, 124], there are many ways to write these equations using the constraint equations.

Furthermore, so called "conformal connection functions" $\tilde{\Gamma}^i$ are introduced:

$$\tilde{\Gamma}^i = \tilde{\gamma}^{jk}\tilde{\Gamma}^i{}_{jk} = -\partial_j\tilde{\gamma}^{ij}, \tag{2.97}$$

where $\tilde{\Gamma}^i_{jk}$ is the Christoffel symbol of the conformal metric. Note that the second equality only holds if (2.90) is satisfied, which might be violated numerically. These $\tilde{\Gamma}^i$ are used to simplify the following separation of the Ricci tensor into two parts:

$$R_{ij} = \tilde{R}_{ij} + R^{\phi}_{ij}, \tag{2.98}$$

where $\tilde{R}_{ij}$ is the Ricci tensor of the conformal metric

$$\tilde{R}_{ij} = -\frac{1}{2}\tilde{\gamma}^{lm}\tilde{\gamma}_{ij,lm} + \tilde{\gamma}_{k(i}\partial_{j)}\tilde{\Gamma}^k + \tilde{\Gamma}^k\tilde{\Gamma}_{(ij)k} + \tilde{\gamma}^{lm}\left(2\tilde{\Gamma}^k_{l(i}\tilde{\Gamma}_{j)km} + \tilde{\Gamma}^k_{im}\tilde{\Gamma}_{klj}\right) \tag{2.99}$$

and R^{ϕ}_{ij} are additional terms depending on ϕ:

$$R^{\phi}_{ij} = -2\tilde{\nabla}_i\tilde{\nabla}_j\phi - 2\tilde{\gamma}_{ij}\tilde{\nabla}^l\tilde{\nabla}_l\phi + 4\tilde{\nabla}_i\phi\tilde{\nabla}_j\phi - 4\tilde{\gamma}_{ij}\tilde{\nabla}^l\phi\tilde{\nabla}_l\phi. \tag{2.100}$$

The round brackets enclosing indices denote symmetrisation ($T_{(ij)} = \frac{1}{2}(T_{ij} + T_{ji})$). The terms $\tilde{\Gamma}^i$ in equation (2.99) could be computed using the Christoffel symbols, but this approach would lead derivatives of the three-metric which are not particularly useful. Evolving the $\tilde{\Gamma}^i$'s as independent variables with their own evolution equations is computationally expensive. However, as shown in [127, 137], it is worth the effort.

The evolution equations for the $\tilde{\Gamma}^i$ are given by

$$\partial_t \tilde{\Gamma}^i = -\partial_j \left(2\alpha \tilde{A}^{ij} - 2\tilde{\gamma}^{m(j}\beta^{i)}_{,m} + \frac{2}{3}\tilde{\gamma}^{ij}\beta^l_{,l} + \beta^l \tilde{\gamma}^{ij}_{,l} \right). \tag{2.101}$$

As with the terms in equation (2.96) there are again several choices to write this equation and as pointed out by [124] the above choice leads to an unstable system. Better behaviour can be obtained by eliminating the divergence of $\tilde{A}^{ij}$ with the help of the momentum constraint:

$$\begin{aligned} \partial_t \tilde{\Gamma}^i = &- 2\alpha \tilde{A}^{ij} + 2\alpha \left(\tilde{\Gamma}^i_{jk}\tilde{A}^{kj} - \frac{2}{3}\tilde{\gamma}^{ij}K_{,j} - \tilde{\gamma}^{ij}S_j + 6\tilde{A}^{ij}\phi_{,j} \right) \\ &- \partial_j \left(\beta^l \tilde{\gamma}^{ij}_{,l} - 2\tilde{\gamma}^{m(j}\beta^{i)}_{,m} + \frac{2}{3}\tilde{\gamma}^{ij}\beta^l_{,l} \right). \end{aligned} \tag{2.102}$$

Equations (2.93), (2.94), (2.95), (2.96) and (2.102) form the set of evolution equations. Note that the ADM formulation did not involve evolution equations for the conformal factor, the trace of the extrinsic curvature K and the "conformal connection functions" $\tilde{\Gamma}^i$, but only for the three-metric γ_{ij} and the extrinsic curvature K_{ij}.

We note that although the final mixed, first and second-order, evolution system for $\left\{\phi, K, \tilde{\gamma}_{ij}, \tilde{A}_{ij}, \tilde{\Gamma}^i\right\}$ is not in any immediate sense hyperbolic, the principle part of the formulation, when reduced to first order form, is equivalent to a hyperbolic system [138–140]. In the formulation of [123], the auxiliary variables $\tilde{F}_i = -\sum_j \tilde{\gamma}_{ij,j}$ were used instead of the $\tilde{\Gamma}^i$.

In [127, 137], the improved properties of this conformal traceless formulation of the Einstein equations were compared to the ADM system. In particular, in [127] a number of strongly gravitating systems were analysed numerically with *convergent* HRSC methods with *total-variation-diminishing* (TVD) schemes using the equations described in [141]. These included weak and strong gravitational waves, black holes, boson stars and relativistic stars. The results showed that this treatment leads to numerical evolutions of the various strongly gravitating systems which did not show signs of numerical instabilities for sufficiently long times. However, it was also found that the conformal traceless formulation requires grid resolutions higher than the ones

needed in the ADM formulation to achieve the same accuracy, when the foliation is made using the "K-driver" approach discussed in [142]. Because in long-term evolutions error-growth rate is acceptable if it comes with stability, we have adopted the conformal traceless formulation as our standard form for the evolution of the field equations.

2.6.2 Boundary conditions

With the exception in which a compactified domain is used, spatial infinity is not included in the computational domain. Thus, the domain has to be cut at some finite distance from the interesting region and boundary conditions have to be imposed. Doing so for Einstein's equations is not easy in general. The mixed first/second order form of the BSSN evolution equations and the fact that some of the quantities involved are not tensors, but have their own transformation laws, complicate the problem even further. The constraints should also be satisfied at the boundary.

One example of trivial boundary conditions is the static boundary condition, which is a special case of a Dirichlet boundary condition [143]. Here the evolved variables are simply not updated at the boundary. They stay at their initial values. This condition is adequate in stationary cases. However, in cases in which waves are present, it is very bad since it reflects the waves back into the domain.

Another trivial example is the von-Neumann boundary condition (specifying the derivatives at the boundary [143]) with zero spatial derivative. In this case the values at the boundary are copied from points inside the domain (normal to the surface of the boundary). This condition is in dynamical situations better than the static boundary condition, because part of the waves can leave the domain, but a part is still reflected.

In our code the most used boundary conditions are the outgoing radiation boundary conditions by Alcubierre et al. [134]:

$$f = f_0 + u\frac{r - vt}{r} + \frac{h(t)}{r^n}, \tag{2.103}$$

where f is the quantity in question, f_0 is the asymptotic value of f and v is the wave speed (the speed of light in our case). Condition (2.103) is adequate if the boundary is in an approximately flat region of the spacetime. The term containing $h(t)$ is introduced to account for possible infall of the coordinates. The power of r^n is unknown and has to be assumed. Empirically, a value of $n = 3$ has shown to have a good effect for this boundary condition, but this might also depend on the quantity in question.

Another type of frequently applied boundary conditions are the so called Robin boundary conditions. This is a physically motivated boundary condition. It assumes a certain fall-off of the variables at large radii:

$$f = f_0 + \frac{k}{r^n}, \tag{2.104}$$

with a constant k. It is related to the radiation boundary condition, but without information about the time evolution.

All these boundary conditions do not satisfy the constraint equations, thus pollute the interior of the simulation with constraint violation. However, this can be reduced by putting the boundary further out. Also the constraint violations coming from the central regions are often much worse.

2.6.3 The Riemann Problem

The Riemann problem is a special initial value problem (IVP) consisting of a partial differential equation (PDE), here the linear advection equation,

$$u_t + a u_x = 0, \tag{2.105}$$

with a being a constant, and initial data, which are given by

$$u(x,0) = u_0(x) = \begin{cases} u_{\mathrm{L}} & \text{if } x < 0 \\ u_{\mathrm{R}} & \text{if } x > 0 \end{cases} . \tag{2.106}$$

u_{L} and u_{R} are the left and the right, constant initial values. This initial data have a discontinuity at $x = 0$ if $u_{\mathrm{L}} \neq u_{\mathrm{R}}$.

The solution for the linear advection equation is simple. Any point of the initial profile is expected to propagate a distance $d = at$ in time t, so does the discontinuity at $x = 0$. This characteristic curve $x = at$ will separate the characteristic curves to the left, on which the solution has a value of u_{L}, from the curves to the right, on which the solution has a value of u_{R}. So the solution is

$$u(x,t) = u_0(x - at) = \begin{cases} u_{\mathrm{L}} & \text{if } x - at < 0 \\ u_{\mathrm{R}} & \text{if } x - at > 0 \end{cases} . \tag{2.107}$$

The Riemann problem is important for the numerical solution of the Euler equations. An exact, closed-form solution to the Riemann problem does not exist in this case[144]. However, it is possible to use iterative schemes to obtain the solution to any desired accuracy. Those schemes are called "Riemann solvers" (see also section 3.4.2).

2.6.4 The Valencia formulation for relativistic hydrodynamics

Many physical systems can be described by conservation laws. Such laws are also called "conservative laws". This means that some quantities are not changed by physical processes happening inside the system, which is why these quantities are called "conserved quantities". In our simulations, one example of such a conserved quantity is the rest-mass. The conservation of rest-mass is particularly important in shocks, because only conserved rest-mass and momentum can guarantee for correct shock speeds [145]. The conservation is ensured by the Euler equations. Numerical simulations, however, always make errors. These errors can accumulate and destroy the conservation. In this section we describe a method to avoid the accumulation of those errors on the conserved quantities.

A conservative scheme can be implemented for any system in balance law form

$$\partial_t \mathbf{u} + \partial_i \mathbf{f}^{(i)}(\mathbf{u}) = \mathbf{s}(\mathbf{u}), \tag{2.108}$$

where $\mathbf{f}^{(i)}(\mathbf{u})$ and $\mathbf{s}(\mathbf{u})$ are the flux vectors and the source terms, respectively [146]. By doing this in the case of the general relativistic hydrodynamic system conservation of rest-mass, momentum and energy can be achieved [147–149].

Here the conservation equations for the stress-energy tensor $T^{\mu\nu}$ and for the matter current density j^μ

$$\nabla_\mu T^{\mu\nu} = 0 \,, \qquad \nabla_\mu j^\mu = 0 \tag{2.109}$$

are written in flux-conservative form (2.108). Note that the right-hand side (the source terms) depends only on the metric, and its first derivatives, and on the stress-energy tensor. Furthermore, while the system in equation (2.108) is not strictly hyperbolic, strong hyperbolicity is recovered in a flat spacetime, where $\mathbf{s}(\mathbf{u}) = 0$ (see equation (2.113) below). Note also that the system is not strictly a conserved one because of the source terms $\mathbf{s}$, but again in flat space the sources $\mathbf{s}$ vanish.

As shown by [148], in order to write system (2.109) in the form of system (2.108), the *primitive* hydrodynamical variables $\mathbf{u} \equiv (\rho, v_i, \epsilon)$ have to be mapped to the so called *conserved* variables $\mathbf{q} \equiv (D, S_i, \tau)$ via the relations

$$\begin{aligned} D &\equiv W\rho \,, \\ S_i &\equiv \rho h W^2 v^i \,, \\ \tau &\equiv \rho h W^2 - P - D \,, \end{aligned} \tag{2.110}$$

where $h \equiv 1 + \epsilon + P/\rho$ is the specific enthalpy and $W \equiv (1 - \gamma_{ij} v^i v^j)^{-1/2}$ is the Lorentz factor. Note that only five of the seven primitive variables are independent. This is usually called the Valencia form [147, 148] which has also been used by [65, 128, 141].
Using

$$v^i = \frac{u^i}{\alpha u^0} + \frac{\beta^i}{\alpha} \tag{2.111}$$

the flux vector becomes

$$\mathbf{f}^i(\mathbf{u}) = \left(D\left(v^i - \frac{\beta^i}{\alpha}\right), S_j\left(v^i - \frac{\beta^i}{\alpha}\right) + P\delta^i_j, \tau\left(v^i - \frac{\beta^i}{\alpha}\right) + Pv^i \right) \tag{2.112}$$

and the sources are given by

$$\mathbf{s}(\mathbf{u}) = \left(0, T^{\mu\nu}\left(\frac{\partial g_{\nu j}}{\partial x^\mu} - \Gamma^\delta_{\nu\mu} g_{\delta j}\right), \alpha\left(T^{\mu 0}\frac{\partial \ln\alpha}{\partial x^\mu} - T^{\mu\nu}\Gamma^0_{\nu\mu}\right)\right). \tag{2.113}$$

Relations (2.112) and (2.113) are then to be inserted into

$$\frac{1}{\sqrt{-g}}\left[\partial_t\left(\sqrt{\gamma}\mathbf{q}^T\right) + \partial_i\left(\sqrt{\gamma}\mathbf{f}^i(\mathbf{u})\right)\right] = \mathbf{s}(\mathbf{u}). \tag{2.114}$$

In order to close the system of hydrodynamics equations, an EOS which relates the rest-mass density and the energy density to the pressure must be specified. In this thesis this has been done using either the polytropic EOS or the "ideal fluid" EOS, as described in section 2.3.

Additional details of the formulation we use for the hydrodynamics equations can be found in [146]. We stress that an important feature of this formulation is that it extends to a general relativistic context the powerful numerical methods developed in classical hydrodynamics, in particular HRSC schemes based on linearised Riemann solvers (see [146]). Such schemes are essential for a correct representation of shocks, whose presence is expected in several astrophysical scenarios. Two important results corroborate this view. The first one, by Lax and Wendroff [150], states that a stable scheme converges to a weak solution of the hydrodynamical equations. The second one, by Hou and LeFloch [145], states that, in general, a non-conservative scheme will converge to the wrong weak solution in the presence of a shock, hence underlining the importance of flux-conservative formulations. For a full introduction to HRSC methods the reader is referred to [144, 151, 152].

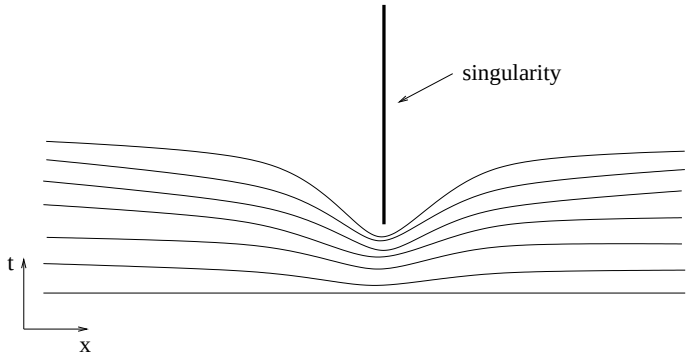

Figure 2.2: Singularity avoiding lapse

2.7 Gauge conditions

As mentioned in section 2.4, the lapse function α and the shift vector β^a can be chosen freely. The most trivial setting is

$$\alpha = 1, \quad \beta^a = 0, \tag{2.115}$$

which simplifies the equations a lot. However, numerically, such a gauge is not the best choice for many cases. One reason can be that one wants to avoid a (forming) singularity. One can do that by lowering the lapse near the singularity. This is visualised in figure 2.2. However, this has the problem of grid-stretching near the singularity, also visible in the figure. Because of this, high gradients develop, which cannot be resolved anymore at some point and the numerical scheme fails. Another reason for nontrivial gauge choices is usually to prevent coordinate points from falling into black holes. This can be achieved by a non zero shift vector in the radial direction. Yet another case of nontrivial gauge choice is a co-rotating shift for rotating binary configurations.

Various possibilities of gauges have been implemented and tested and are in use. More details about the gauges implemented in our codes can be found in [127, 153]. Here we limit ourselves to the specific gauge choices used in this thesis.

In particular, we have used the following slicing condition (Bona-Massó slicing [154]):

$$(\partial_t - \beta^a \partial_a)\, \alpha = -f(\alpha)\alpha^2\, (K - K_0) \tag{2.116}$$

with $f(\alpha) > 0$ and $K_0 \equiv K(t = 0)$. This is the general form of many well known slicing conditions. For example, setting $f = 1$ is the so called "harmonic" slicing condition, while $f = \frac{q}{\alpha}$, with q being an integer, is the generalised "1+log" slicing condition [33, 154], which is singularity-avoiding [155].

It bends the slices as shown in figure 2.2. All simulations with a nontrivial gauge choice used this latter condition, with $q = 2$.

The 1+log slicing condition mimics [33] the action of the maximal slicing condition [109], which is determined from the condition that the mean extrinsic curvature of the slices vanishes at all times ($K = 0$, $\partial_t K = 0$). Two of the nice properties of maximal slicing are that it is also singularity-avoiding [156] and it produces a lapse profile, which is often smoother than the one produced by the 1+log slicing condition [33]. However, it involves solving the elliptic equation

$$\bar{\Delta}\alpha = \beta^i \partial_i K + \alpha K_{ij} K^{ij}. \tag{2.117}$$

The solution of this equation is computationally very demanding, which is why we often prefer the 1+log condition. However, we are aware that "gauge pathologies" could develop with this slicing [157–159].

For the shift we used the "Gamma-driver" shift condition (see [134, 153]) that is driving the shift in a way such that the $\tilde{\Gamma}^i$ of the BSSN system (see equation (2.97)) are constant. Restricting the evolution of the $\tilde{\Gamma}^i$ to 0 is called the "Gamma-freezing" condition, which is closely related to the minimal distortion shift condition[4] [160]. Note that the minimal distortion condition is covariant, while the "Gamma-freezing" (so also the "Gamma-driver") is not.

In all the cases involving a non-trivial shift condition, we have used the following Gamma-driver condition:

$$\partial_t^2 \beta^i = F \partial_t \tilde{\Gamma}^i - \nu \partial_t \beta^i, \tag{2.118}$$

where F and ν are positive functions of space and time. These parameters can be tuned to obtain stable evolutions. ν controls the dissipation term, which is needed to avoid strong oscillations in the shift. Typical values for both parameters are $F = 3/4$ and $\nu = 3$, which are not varied in space or time.

2.8 Summary

In this chapter, most of the continuum physics which is needed later has been described. This started with a short introduction into Einstein's equations of General Relativity in section 2.1. There are some astrophysically relevant

[4] The minimal distortion shift condition tries to minimise the changes in the three-metric components. Because it involves elliptic equations, it is computationally very demanding and it was not successful in numerical simulations [155].

solutions to these equations, of which some have been described in section 2.2. The structure and used models for cold neutron stars are summarised in section 2.3.

For numerical purposes, the four-dimensional spacetime is often split into three-dimensional slices, using the $3+1$ formalism, which is described in section 2.4. Numerical simulations require initial data on one of these slices. In section 2.5, some analytical solutions are mentioned and a procedure to obtain more general initial data is explained. Schemes for the evolution of Einstein's and Euler's equations are, as well as boundary conditions, described in section 2.6. Finally, in section 2.7, some common gauge conditions are listed.

Chapter 3

Discretisation

For evolving a spacetime numerically in a computer, there is need for a discretisation of the variables representing the spacetime. The idea is to solve the discretised problem and show that this solution converges to the solution of the continuous problem in the limit of infinite resolution.

Discretisation then poses two main problems:

- resolution
- boundaries

Because the computer is limited in memory, one cannot have infinite resolution. The "shape" of the spacetime has to be stored in some way in a finite-size memory. There are a number of methods to achieve this.

The continuum problem has to be discretised in space and time. Different ways to do the space discretisation are introduced below and the following sections. We treat the time integration separated by using the method of lines, which is outlined in section 3.3.

The next section is about finite difference and finite volume methods. We use finite difference methods for solving Einstein's equations while finite volume techniques are used to solve Euler's equations. The way how both methods are discretising the continuum is quite similar: while in finite difference methods the value of a variable at a certain point represents the value of the continuum variable at that point, in finite volume methods, it represents the average of the continuum variable over the cell around that point.

In spectral and finite element methods on the other hand, the continuum problem is discretised using a set of basis functions. While this is done individually in a potentially large number of domains in finite element methods, in spectral methods the continuum is divided, if at all, only in a small number of domains. Spectral methods are explained in section 3.2.

The boundaries are a problem present in both methods. It is possible to compactify the domain, such that it covers the whole space up to spatial infinity and there is no need for complicated outer boundaries. However there are other problems which have to be solved in this case, *e.g.* reflection of waves from the stretched grid once the waves cannot be resolved anymore. If one, on the other hand, does not compactify, one has to place some artificial boundary on the computational domain. Boundary conditions have already been discussed in section 2.6.2.

3.1 Finite difference and finite volume methods

One of the differences between finite difference methods and spectral methods is the way derivatives are computed. Finite difference methods express continuous differential operators with their Taylor-expanded expressions which are suitably truncated at the desired order. In practice, differential operators acting on a given function are then replaced by algebraic expressions of the values of the function at specific points. These points are called "grid points". For convenience, they are often uniformly separated. One very simple example is calculating the slope of u at a cell i by

$$\partial_x u_i = \frac{1}{\Delta x}\left(u_{i+1} - u_i\right) + O(\Delta x) \tag{3.1}$$

with $\Delta x = x_{i+1} - x_i$ being the grid spacing. This introduces an error of the order of Δx, which depends on the resolution. Using a higher resolution (a smaller Δx) helps to keep this error small. This can be used as a test (see also section 3.6).

The amount of grid points a computer can store is limited as well as the speed at which the equations can be solved using these points, so they have to be carefully distributed. For simplicity a lot of codes use a distribution of uniformly spaced grid points which is also fixed in time. Usually they also do not compactify the computational domain. This, however, has two disadvantages. The first is that one can only simulate a part of the slice of spacetime because one cannot have a slice containing infinity. This then means one has to set boundary conditions and finding good ones turns out to be very difficult. The second problem is arising out of the first one. Because one does not have ideal boundary conditions[1] one wants to have the errors

[1] That is because they would have to simulate all the physics going on outside the computational domain.

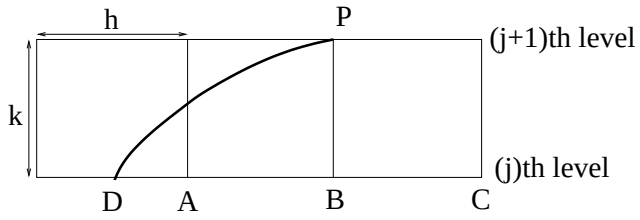

Figure 3.1: sketch of a discretised spacetime

caused by them not influence the computation too much, so one aims to put the boundaries as far away from the interesting region as possible. Doing that using a single, uniformly spaced grid while keeping the resolution high in interesting parts of the computational domain exceeds usually very quickly the available computational resources. As has been shown [161], simulations using a uniform grid for calculating gravitational wave results which could be used as template to look for real signals using one of the current detectors would require much bigger and faster computers than available in the foreseeable future.

To save computational resources, modern finite differencing codes often do something called "mesh refinement". Regions of the computational domain with large errors, typically due to large gradients, can get better resolved than others by introducing multiple uniform grids with different spacings, covering the slice. This does not remove the need for a special boundary treatment, since it is not possible to go to infinity by just using mesh refinement. But the boundaries can be put much further away from the interesting regions. Further details about this can be found in section 3.1.3.

3.1.1 The CFL condition

Within the von-Neumann stability analysis [136], the Courant-Friedrichs-Lewy (CFL) condition is a necessary and sufficient condition for the stability of a first-order hyperbolic differential equation.

Assume such an equation has been approximated by a difference equation of the form

$$u_{i,j+1} = c_1 u_{i-1,j} + c_2 u_{i,j} + c_3 u_{i+1,j} \tag{3.2}$$

with i denoting the cell index and j the time level as indicated in figure 3.1. Then u_P (the solution of the finite-difference equation at P) depends on the values of u at the mesh points A, B and C. The thick line in figure 3.1 denotes the characteristic curve of the hyperbolic equation through D and P. If the initial values at A, B or C are altered, u_P will be changed, but these alterations will not affect the solution of the original, *continuous* differential

equation at P which depends on the initial value at D. In this case, u_P cannot converge to the solution of the differential equation.

For stability, D must lie between A and C. This is called the "CFL condition". If, for example, the characteristic of the differential equation is approximated by a linear function and its slope is given by $\mathrm{d}x/\,\mathrm{d}t = a$, this means that

$$C \equiv k/h \leq a \tag{3.3}$$

must hold with C being called the "Courant factor". For our simulations the speed of the characteristics cannot exceed 1, the speed of light. Because of numerical errors, more complicated equations, higher dimensions and the connected stability problems, we use a Courant factor smaller than 1, usually 0.25.

3.1.2 `Cactus / CactusEinstein`

`Cactus`, or the `Cactus` Computational Toolkit, is a code framework to help constructing numerical simulations (see [162] for details). It is developed at the Albert Einstein Institute (Golm), at the Louisiana State University (Baton Rouge) at by numerous people around the world. This public domain code provides low-level facilities such as parallelisation, input/output, portability on different platforms and several time integration schemes to solve general systems of partial differential equations. It was originally designed for numerical relativity, but today it is used in various fields of numerical research, including climate modeling.

`Cactus` contains routines for input and output as well as checkpointing[2], the use of parameter files and a build system for modular extensions, which are called thorns. Using these thorns it is easy to implement any specific detail while the modular structure helps to develop such a suite by a large group of people.

3.1.3 Mesh refinement - `Carpet`

In simulations with three-dimensional, uniformly spaced grids, so called unigrid simulations, doubling the resolution means increasing the memory requirement by a factor of eight and increasing the computing power requirement by a factor of sixteen (because of smaller timesteps required by the CFL condition, see section 3.1.1). Even with today's supercomputers these limits are too high for desired resolutions [161].

[2]Checkpointing: stopping a simulation after writing all data to disk and restarting at the same point using these data.

One possible remedy is to use the fact that in most cases high resolution is only required at some part of the grid. In these regions the grid is "refined" and this can happen multiple times. Because of simplicity this is usually done by doubling the resolution, which means dividing the grid step by two. The time step has to be divided by two as well, which means that a fine grid is doing two (small) time steps to reach the same time as a coarse grid by doing one (large) step. Because the regions which are refined are typically much smaller than the whole computational domain, this saves a lot of memory and computing time. The caveat is that is it much more complicated to program and parallelise.

`Carpet` is a `Cactus` thorn which implements Berger-Oliger, fixed, box-in-box mesh refinement [163–168] in `Cactus`. Most other tools, which were available at the time of its introduction and were written for uniform grids, still work without or with only minor changes. The thorn providing the unigrid setup is called `PUGH`.

3.2 Spectral Methods

An alternative to finite difference or finite volume methods, described in the previous section, is spectral methods. As already mentioned, one of the differences between spectral and finite difference methods is the way derivatives are calculated. Spectral methods use spectral transformations (*e.g.* Fourier or Chebyshev transformations) to obtain derivatives. Certain distributions of the so called "colocation points" are best to represent a function by its spectral approximation. However, one can think of spectral methods as finite difference methods which use the whole grid for the stencil. One of the key advantages is that given a differentiable spacetime this needs much less memory and is often more accurate than finite difference methods. The reason is their usually exponentially convergence in contrast to finite difference methods, which typically only have polynomial (*e.g.* 2nd or 4th order) convergence.

Spectral methods also have disadvantages, one of which has already been mentioned: they only work well with differentiable functions. The number of coefficients needed to resolve a function appropriately rapidly grows with the steepness of the function and discontinuities cannot be represented even with an infinite number of coefficients. This is called the "Gibbs' effect" [144, 169, 170]. A Fourier transformation in general involves infinitely many coefficients. Since one cannot store that many coefficients, one has to truncate this series at some point. While there is no boundary in the space itself (if compactified), this truncation causes an error like the error coming

from finite grid spacings and calculating derivatives on it in finite difference methods. However, the convergence behaviour is often better in spectral methods.

The choice for one of the two possibilities to differentiate spacetimes on a computer should depend on the problem that is being solved. Neither one or the other can be called *best* for all or nearly all current problems.

3.3 The method of lines

The method of lines (MoL) is a way of separating the time integration from the other steps involved in an evolution [144, 151, 171]. The idea is to convert a system of partial differential equations (PDEs) into a system of ordinary differential equations (ODEs) by leaving the problem continuous in time first, but discretise in space.

Well known stable ODE integrators such as Runge-Kutta [172, 173] can be used in the time integration, so that instabilities can only arise from the spatial discretisation or the equations themselves. It can also be implemented in a modular way into an evolution code, which allows for easier debugging and is more flexible for future extensions.

MoL itself does not have a precise truncation error but, rather, it acquires the truncation order of the time-integrator employed. Several integrators are available in our implementation of MoL, including the second-order Iterative-Crank-Nicolson (ICN) solver and Runge-Kutta (RK) solvers of first to fourth-order accuracy. The second and third-order RK solvers are known to be TVD whilst the fourth-order is known to not be TVD [174, 175]. A more detailed description can be found *e.g.* in work of Thornburg [176, 177].

3.4 Hydrodynamical discretisation

The numerical methods that we use for the evolutions of the hydrodynamic variables are all High–Resolution Shock–Capturing (HRSC) methods. They are based on an idea by Godunov [178]. In other methods discontinuities are often a major problem because these schemes usually do not conserve the mass, leading to wrong shock speeds (see section 2.6.4). Even if there are no discontinuities present in the initial data, this is a problem for two reasons. Firstly, physically continuous data are (in finite difference methods) discretised as discontinuous and piecewise constant data. Secondly, non-linear properties of the hydrodynamical equations can generally produce non-linear waves with discontinuities forming in finite time even from smooth

initial data [144, 179] (see *e.g.* Burger's equation [180]).

Godunov methods consist of setting and solving at every cell interface of the numerical grid a local Riemann problem (see section 2.6.3). We take the semi-discrete or method of lines reconstruction-evolution viewpoint where the continuum equations are considered to be discretised in space only [144, 151]. The resulting system of ordinary differential equations (ODEs) can then be solved numerically with any stable solver. In what follows we shall specialise to the case of a uniform Cartesian grid. In this subsection Latin indices denote the cell index.

The calculation of the terms required for the hydrodynamic part of the ODE splits into the following steps:

1. Calculation of the source terms $\mathbf{s}(\mathbf{u}(x^{(1)}_{j_1}, x^{(2)}_{j_2}, x^{(3)}_{j_3}))$ at all grid points.

2. For each direction $x^{(i)}$:

   - Reconstruction of the data $\mathbf{u}$ to both sides of a cell boundary. In this way, two values $\mathbf{u}_{_L}$ and $\mathbf{u}_{_R}$ of $\mathbf{u}_{j_i+1/2}$ are determined at the cell boundary; $\mathbf{u}_{_L}$ is obtained from cell j_i (left cell) and $\mathbf{u}_{_R}$ from cell $j_i + 1$ (right cell).
   - Solution at the cell boundary of the approximate Riemann problem having the values $\mathbf{u}_{_{L,R}}$ as initial data.
   - Calculation of the inter-cell flux $\mathbf{f}^{(x^{(i)})}(\mathbf{u}_{j_i+1/2})$, that is, of the flux across the boundary between a cell (*e.g.*, the j_i-th) and its closest neighbour (*e.g.*, the $(j_i + 1)$-th).

3. Recovery of the primitive variables (see equation (2.110)) and computation of the stress-energy tensor for use in the Einstein equations.

During a timestep of an evolution, the primitive variables are used to obtain the connection with the spacetime evolution code. The conserved variables are computed from these and are then evolved in the hydrodynamics evolution code. From these then the new primitive variables are computed. Doing this conversion between the primitive and conserved variables once or multiple times each timestep is expensive, but gives a high accuracy.

The computation of the source terms is purely local, as is the recovery of the primitive variables. Therefore there is no issue to address when part of the grid is excised. The computation of the stress-energy tensor is not purely local, as some derivatives of spacetime quantities are required. However, when using excision boundary conditions as described later in section 3.5 there are sufficient data at the excision boundary to compute these derivatives.

The modifications required for hydrodynamical excision must be performed in the reconstruction and flux calculation steps. These modifications are explained in the following sections.

3.4.1 Reconstruction methods

In finite difference methods the data are given as piecewise constant and discontinuous data. In our case the integral average of the variables of the numerical cell is stored. However, Godunov methods need the values of these variables at the cell boundaries. Reconstruction methods give these data, "reconstructing" the (often, but not always) continuous solution.

Three separate reconstruction methods are considered here. Each one is applied in a dimensionally split fashion (for simplicity); the reconstructions are performed along each coordinate axis in turn. Although some of the reconstruction methods considered here have formal convergence orders that are better than two, the formal, global convergence order of the code is at best two. This is due to the extension to multiple dimensions[3] and the coupling to the spacetime, which we usually evolve using second-order methods. The flux through the cell boundary is approximated by the flux through the point in the middle of the cell boundary, using the reconstructed fluid variables and a second order approximation of the metric terms. Note that the use of reconstruction methods with orders of accuracy larger than second do not necessarily yield a global truncation error that is larger than second order. This is the case, for instance, in a multi-dimension simulation in which the directional splitting reduces the global truncation error to second order.

The method with the lowest formal order of accuracy is a slope limited total variation diminishing (TVD) method [181]. The essentially non-oscillatory (ENO) methods [182] may have extremely high orders of accuracy and are more accurate in absolute terms than TVD. However, it is often more efficient to use the Piecewise Parabolic Method (PPM) [183] even though it only has at most third–order accuracy.

Here we use the same conventions concerning subscripts and superscripts to denote cells, cell boundaries and left or right sided cell boundary values as introduced by figure 3.2.

[3]We only reconstruct the functions at the centers of the cell faces. To obtain better convergence orders than two in multiple dimensions they would have to be reconstructed on more than one point on such a face. See *e.g.* [144] for details on directional splitting.

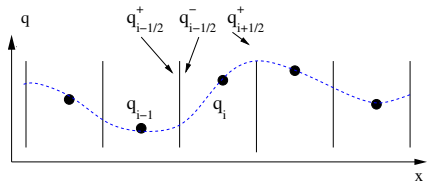

Figure 3.2: A schematic view of the subscripts and superscripts to denote cells

Slope–limited TVD

TVD stands for total variation diminishing [181]. Given a function $u = u(x)$, the total variation is defined as

$$TV(u) = \lim_{\delta \to 0} \sup \frac{1}{\delta} \int_{-\infty}^{\infty} |u(x+\delta) - u(x)| dx. \tag{3.4}$$

If $u(x)$ is smooth, equation (3.4) becomes

$$TV(u) = \int_{-\infty}^{\infty} |u'(x)| dx. \tag{3.5}$$

For $u = u_i$ being a discrete function, the total variation is defined as

$$TV(u) = \sum_{i=-\infty}^{\infty} |u_{i+1} - u_i|. \tag{3.6}$$

The total variation is important, because it can be proven that methods with total variation diminishing (TVD) converge (for details, see [144, 184–186]).

One subclass of TVD methods follows the slope-limiter (or flux-limiter) approach (see [187] and [144] for details). In this case, the reconstruction is given by an average of a first–order and a second–order reconstruction. To reconstruct the variable q in the cell centred at x_i two local "slopes" are defined,

$$\begin{aligned} \Delta_i^- &\equiv q_i - q_{i-1}, \\ \Delta_i^+ &\equiv q_{i+1} - q_i, \end{aligned} \tag{3.7}$$

which are then averaged to get the slope in the cell $\bar{\Delta}_i = (\Delta_i^- + \Delta_i^+)/2$. This slope is then multiplied by a *limiter* which is a function ϕ of the local slopes $\phi = \phi(\Delta_i^-, \Delta_i^+)$. This *limited slope* $\bar{\Delta}_i$ then gives the cell boundary data by

$$q_{i\pm 1/2} = q_i \pm \frac{1}{2} \bar{\Delta}_i. \tag{3.8}$$

If the slopes are not limited (i.e., the limiter $\phi = 1$) then the method is second order accurate. However, in the presence of steep gradients or discontinuities such a reconstruction will be oscillatory due to Gibbs' effects [144]. In these regions the limiter reduces the slopes to avoid overshoots, retaining monotonicity of the reconstruction.

We typically use the Van Leer monotised centred method

$$\phi = \begin{cases} 0 & \text{if } \Delta_i^- \Delta_i^+ < 0, \\ \text{sign}(\Delta_i^- + \Delta_i^+)\min(2|\Delta_i^-|, 2|\Delta_i^+|, 1/2(|\Delta_i^-| + |\Delta_i^+|)) & \text{otherwise} \end{cases} \tag{3.9}$$

although a variety of others (minmod, Superbee, see [144]) have also been implemented. This method is simple and computationally the least expensive to implement, but is at most second-order accurate, dropping to first-order at local extrema and discontinuities.

ENO

The essentially non-oscillatory (ENO) methods of Harten et al. [182] are a very general class of methods. Here we only consider the simple ENO reconstruction of the variables as given by Shu in [188]. This provides arbitrary order of accuracy in space.

As in the TVD case, ENO reconstructions are cell based. The p^{th} order reconstruction compares all possible polynomial stencils of size p containing the cell to be reconstructed. The "least oscillatory" stencil is chosen by minimising the absolute values of the divided differences that make up the stencil.

Let p be the order of the reconstruction. Suppose we are reconstructing the scalar function q in cell i. We start with cell i. We then add cell j to the stencil, where $j = i \pm 1$, where we choose j to minimise the Newton undivided differences:

$$q\left[i-1, i\right] \equiv q_i - q_{i-1}, \tag{3.10a}$$

$$q\left[i, i+1\right] \equiv q_{i+1} - q_i. \tag{3.10b}$$

We then recursively add more cells, minimising the higher order Newton divided differences $q\left[i-1, \ldots, i+j\right]$ defined by

$$\begin{aligned} q\left[i-1, \ldots, i+j\right] \;=\; & q\left[i, \ldots, i+j\right] - \\ & q\left[i-1, \ldots, i+j-1\right]. \end{aligned} \tag{3.11}$$

The reconstruction at the cell boundary is given by a standard p^{th} order polynomial interpolation on the chosen stencil.

Shu [188] has outlined an elegant way of calculating the cell boundary values solely in terms of the stencil and the known data. If the stencil is given by

$$S(i) = \{i - r, \ldots, i + p - r - 1\}, \tag{3.12}$$

for some integer r, then there exist constants c_{rj} depending only on the grid x_i such that the boundary values for cell I_i are given by

$$\begin{array}{rcl} q_{i+1/2} & = & \sum_{j=0}^{p-1} c_{r,j} q_{i-r+j}, \\ q_{i-1/2} & = & \sum_{j=0}^{p-1} c_{r-1,j} q_{i-r+j}. \end{array} \tag{3.13}$$

The constants $c_{r,j}$ are given by the rather complicated formula

$$c_{r,j} = \left\{ \sum_{m=j+1}^{p} \frac{\sum_{l=0,l\neq m}^{p} \prod_{q=0,q\neq m,l}^{p} \left(x_{i+1/2} - x_{i-r+q-1/2} \right)}{\prod_{l=0,l\neq m}^{p} \left(x_{i-r+m-1/2} - x_{i-r+L-1/2} \right)} \right\} \Delta x_{i-r+j}. \tag{3.14}$$

This calculation simplifies considerably if the grid is evenly spaced. For this case the coefficients up to seventh–order are given by Shu [188].

PPM

The PPM scheme of Colella and Woodward [183], generalised to relativistic flows by Martí and Müller [189], is third–order accurate in space and includes special cases to ensure monotonicity at shocks, sharpening of contact discontinuities, and shock detection.

The outline of the general PPM method is as follows. The first step is to interpolate a quartic polynomial to the cell boundary,

$$q_{i+1/2} = \frac{1}{2}\left(q_{i+1} + q_i\right) + \frac{1}{6}\left(\delta_m q_i - \delta_m q_{i+1}\right), \tag{3.15}$$

where

$$\delta_m q_i = \begin{cases} \min \begin{pmatrix} |q_{i+1} - q_{i-1}|, \\ 2|q_{i+1} - q_i|, \\ 2|q_i - q_{i-1}| \end{pmatrix} \operatorname{sign}(q_{i+1} - q_{i-1}) & \text{if } (q_{i+1} - q_i)(q_i - q_{i-1}) > 0 \\ 0 & \text{otherwise.} \end{cases} \tag{3.16}$$

At this point we set both left and right states at the interface to be equal to the interpolated value,

$$q^+_{i+1/2} = q^-_{i+1/2} = q_{i+1/2}. \tag{3.17}$$

This reconstruction will be oscillatory near shocks. Before the monotonicity-preserving step, two other steps may be applied.

Firstly we may "steepen" discontinuities. This is to produce sharper profiles and is only applied to discontinuities that are mostly a contact (see [183] for details). This procedure replaces the cell boundary reconstructions of the density with

$$\rho^+_{i-1/2} \equiv \rho^+_{i-1/2}(1-\eta) + \left(\rho_{i-1} + \frac{1}{2}\delta_m\rho_{i-1}\right)\eta, \tag{3.18a}$$

$$\rho^-_{i+1/2} \equiv \rho^-_{i+1/2}(1-\eta) + \left(\rho_{i+1} - \frac{1}{2}\delta_m\rho_{i+1}\right)\eta, \tag{3.18b}$$

where η is defined as

$$\eta \equiv \max\left[0, \min\left(1, \eta_1(\tilde{\eta} - \eta_2)\right)\right], \tag{3.19}$$

where η_1, η_2 are constants and

$$\tilde{\eta} \equiv \begin{cases} \dfrac{\rho_{i+2} - 2\rho_{i+1} + 2\rho_{i-1} - \rho_{i-2}}{-6(\rho_{i+1} - \rho_{i-1})} & \text{if } \begin{array}{l} -\delta^2\rho_{i+1}\delta^2\rho_{i-1} > 0 \quad \text{and} \\ |\rho_{i+1} - \rho_{i-1}| - \epsilon_{\mathrm{s}}\min(|\rho_{i+1}|, |\rho_{i-1}|) > 0 \end{array} \\ 0 & \text{otherwise} \end{cases} \tag{3.20}$$

with ϵ_{s} another constant and

$$\delta^2\rho_i \equiv \rho_{i+1} - 2\rho_i + \rho_{i-1}. \tag{3.21}$$

Suggested values for the constants η_1, η_2 and ϵ_{s} can be found in [183].

Another step that may be performed before monotonicity enforcement is the "flattening" of the zone structure near shocks. This adds simple dissipation, altering the reconstructions to

$$q^+_{i-1/2} \equiv \nu_i q^+_{i-1/2} + (1-\nu_i)q_i, \tag{3.22}$$

$$q^-_{i+1/2} \equiv \nu_i q^-_{i+1/2} + (1-\nu_i)q_i, \tag{3.23}$$

where

$$\nu_i \equiv \begin{cases} \max\left[0, 1 - \max\left(0, \omega_2\left(\dfrac{p_{i+1} - p_{i-1}}{p_{i+2} - p_{i-2}} - \omega_1\right)\right)\right] & \text{if } \begin{array}{c} \epsilon\min(p_{i-1}, p_{i+1}) \\ < p_{i+1} - p_{i-1} \\ \text{and} \\ v^x_{i-1} - v^x_{i+1} > 0 \end{array} \\ 1 & \text{otherwise} \end{cases} \tag{3.24}$$

and ω_1, ω_2 and ϵ are again constants with suggested values given in [183]. Note that this step is a simplification of the one in [183, 189], which reduces

the communication overhead in parallel runs. No problems were encountered using this modification.

The final step is applied to preserve monotonicity, which prevents oscillatory reconstruction near shocks. The following replacements are made:

$$q^+_{i-1/2} \equiv q^-_{i+1/2} = q_i \text{ if } (q^-_{i+1/2} - q_i)(q_i - q^-_{i+1/2}) \leq 0, \tag{3.25a}$$

$$q^+_{i-1/2} \equiv 3q_i - 2q^-_{i+1/2} \text{ if } \begin{array}{r}(q^-_{i+1/2} - q^+_{i-1/2})\left(q_i - \frac{1}{2}(q^+_{i-1/2} + q^-_{i+1/2})\right) \\ > \frac{1}{6}(q^-_{i+1/2} - q^+_{i-1/2})^2,\end{array} \tag{3.25b}$$

$$q^-_{i+1/2} \equiv 3q_i - 2q^+_{i-1/2} \text{ if } \begin{array}{r}(q^-_{i+1/2} - q^+_{i-1/2})\left(q_i - \frac{1}{2}(q^+_{i-1/2} + q^-_{i+1/2})\right) \\ < -\frac{1}{6}(q^-_{i+1/2} - q^+_{i-1/2})^2.\end{array} \tag{3.25c}$$

3.4.2 Riemann solvers

Once a reconstruction procedure has provided data on either side of each cell boundary, this is then used to specify the initial states of a Riemann problem for the Euler equations. Since the exact solution [190] is still too costly to use, even when recast in an efficient form [191, 192], we have implemented here three different approximate Riemann solvers.

The first and simplest method implemented is the HLLE (Harten-Lax-van-Leer-Einfeldt) method [184]. This approximates the solution using only two waves with the intermediate state given by the conservation of the mass-flux. This method is very efficient but diffusive. The second method is the Roe solver [193]. This solves a linearised problem at each boundary, approximating every wave by either a shock or a contact discontinuity. This method is less efficient but very accurate. However, it may have problems near sonic points. The third method is the Marquina solver [194, 195]. This is similar to the Roe solver, except that at possible sonic points a Lax-Friedrichs flux (analogous to the HLLE method) is used, ensuring that the solution does not contain rarefaction shocks. Note that we use the modified method of Aloy et al. [196] instead of the original method.

Both the Roe and Marquina solvers require the computation of the eigenvalues and eigenvectors (from both the right and left cell) of the linearised Jacobian matrices $\mathbf{A}_L$ and $\mathbf{A}_R$ given by $\mathbf{f}_L = \mathbf{A}_L\mathbf{q}_L$ and $\mathbf{f}_R = \mathbf{A}_R\mathbf{q}_R$. We use an implementation of the analytic expression for the left eigenvectors [149], thus avoiding the computationally expensive inversion of the three 5×5 matrices of the right eigenvectors, associated to each spatial direction. We also use a compact version of the flux formula (a variant on the methods described in [197]) to increase speed and accuracy. These improvements bring

a $\sim 40\%$ reduction of the computational time spent in the solution of the hydrodynamics equations and a $\sim 5-10\%$ reduction in evolutions involving also the time integration of the Einstein equations. The small overall gain in efficiency is due to the fact that less than half of the computational time is spent computing the update of the hydrodynamic variables, while the other half spent in the update of the spacetime field variables. Of the time spent computing the hydrodynamic update terms around one third is spent solving the Riemann problem. These improvements were made by Joachim Frieben while working at the Universidad de Valencia.

Although an integral part of the full HRSC method, the Riemann solvers are irrelevant for the problem of excision, as we will explain below. The solver employed in most simulations performed is the modified Marquina solver described in [196, 197].

3.4.3 Treatment of the atmosphere

At least mathematically, the region outside our initial stellar models is assumed to be perfect vacuum. Independently of whether this represents a physically realistic description of a compact star, the vacuum represents a singular limit of the equations (2.108) and must be treated artificially. Here, we have followed a standard approach in computational fluid dynamics, also implemented in [89, 128], and added a tenuous "atmosphere" filling the computational domain outside the star. Duez et al. suggested new strategies in form of correction terms instead of an atmosphere and presented simulations in [198]. Unfortunately, it is not possible to apply these corrections to our scheme because we use the conservation form of our hydrodynamical equations (2.108), which we are using to guarantee the correct evolution of shocks.

We have treated the atmosphere as a perfect fluid governed by the same polytropic EOS used for the bulk matter, but having a zero coordinate velocity. Furthermore, its rest-mass density is several (usually seven) orders of magnitude smaller than the initial central density. Note that the atmosphere used for the calculation of the initial data and the one evolved during the simulations need not be the same. Indeed, for the initial stellar models used for the collapse calculations we have typically set the atmosphere to be two orders of magnitude smaller than the evolved one to minimise spurious matter accretion onto the black hole. In the pulsation tests presented in section 3.7, on the other hand, the initial and evolved atmospheres are the same.

The evolution of the hydrodynamics equations in grid-zones where the atmosphere is present is the same as the one used in the bulk of the flow. Fur-

thermore, when the rest-mass density in a grid-zone falls below the threshold set for the atmosphere, that grid-zone is simply not updated in time.

As mentioned in Section 5.4.2, for simulations of, *e.g.*, collapsing stars, the use of a tenuous atmosphere has no dynamical impact and does, *e.g.*, not produce any increase of the masses of black holes. With the rest-mass densities we typically use for the atmosphere, and using the mass accretion rates measured after an apparent surface is first found (in section 5.4.2), we have estimated that a net increase of $\sim 1\%$ in the black-hole mass would require an integration time of $\sim 10^4 M$, but all of those simulations are much shorter. These systematic errors are well below our truncation errors, even at the highest resolutions we can afford.

3.4.4 Shock tube tests

One often used test for hydrodynamical codes is the "shock tube test". It is done on a flat background without spacetime evolution and forms a global Riemann problem. The initial data involve a discontinuity of the density and the pressure, usually in a plane in three-dimensional space. Parameters are the form and orientation of the initial discontinuity and the left and right densities and pressures. The results for the simple case of a plane shock are known analytically [199] and can be used for comparisons to the numerical results.

Using our code `Whisky`, we can show excellent agreement with the analytic solution. This can be seen in figure 3.3 which used the following initial state:

$$\begin{aligned} \rho_R &= 1; \;\; p_R = 1.666 \times 10^{-6}; \;\; v_R = 0 \; , \\ \rho_L &= 10; \;\; p_L = 13.333; \qquad\;\; v_L = 0 \; . \end{aligned}$$

That shocks also pose no problems for the new hydrodynamical excision boundaries can be seen in section 4.5.1.

3.4.5 `Whisky`

`Whisky` is the name of a new three-dimensional fully general relativistic hydrodynamics code using HRSC techniques and a conformal traceless formulation of the Einstein equations. The Einstein and hydrodynamics equations are finite-differenced on a Cartesian grid and solved using state-of-the-art numerical schemes. It is fully integrated into the `Cactus` framework (see 3.1.2) as suite of thorns and provides the stress-energy tensor for the spacetime evolution scheme.

While the `Whisky` code is entirely new, its initial development has benefited in part from the release of a public version of the general relativistic

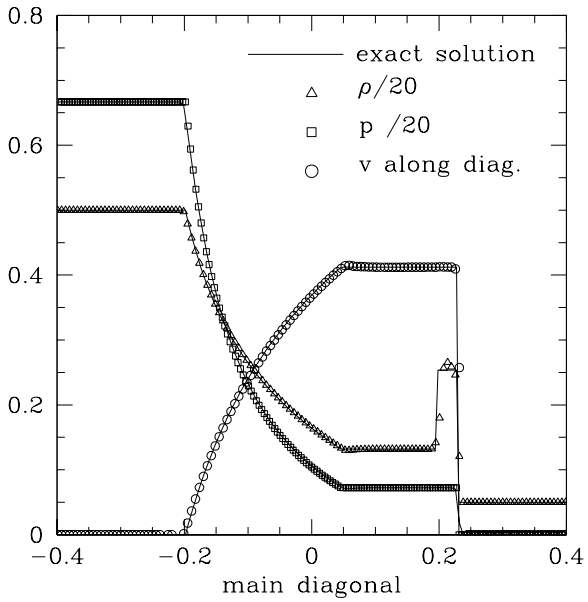

Figure 3.3: Solution of a Riemann problem set on the main diagonal of the cubic grid. The figure shows the comparison of the hydrodynamic variables evolved with `Whisky` (indicated by symbols) with the exact solution. The numerical simulation was obtained with the van Leer TVD reconstruction method and the Roe Riemann solver on a grid with 140^3 points.

hydrodynamics code described in [128, 141], which was developed in great part by the group at the Washington University at St. Louis.

The code incorporates the expertise developed over the past years in the numerical solution of the Einstein equations and of the hydrodynamics equations in a curved spacetime (see [127, 128], but also [146] and references therein) and is the result of a collaboration among several European Institutes [200], the "EU-network". It also contains important recent developments regarding in particular new numerical methods for the solution of the hydrodynamics equations that have been described in detail in [201] and have been briefly reviewed already in this section. These include: *(i)* the Piecewise Parabolic Method (PPM) [183] and the Essentially Non-Oscillatory (ENO) methods [182] for the cell reconstruction procedure; *(ii)* the Harten-Lax-van-Leer-Einfeldt (HLLE) [184] approximate Riemann solver, the Marquina flux formula [196]; *(iii)* the analytic expression for the left eigenvectors [149] and the compact flux formulae [197] for a Roe-type Riemann solver and a Marquina flux formula; *(iv)* the use of a "method of lines" (MoL) approach for the implementation of high-order time evolution schemes [144, 151]; *(v)* the possibility to couple the general relativistic hydrodynamics equations with a conformally decomposed three-metric. The incorporation of these new numerical techniques in the code has led to a much improved ability to simulate relativistic stars, as will be shown in section 3.7.

While other thorns provide at each time step a solution [127] of the spacetime parts of the Einstein equations (2.9), the `Whisky` code provides the time evolution of the hydrodynamics equations, expressed through conservation equations for the stress-energy tensor $T^{\mu\nu}$ (equation (2.39)) and for the matter current density j^{μ} (equation (2.40)).

3.5 Excision applied to spacetime variables

Simulations including black holes usually involve singularities present inside the numerical domain. This is problematic for numerical codes, because this is often connected to large gradients or even infinities in some of the variables near the singularity and they cannot be represented or resolved.

One way to bypass this is sometimes to stagger the grid such that the singularity is between two grid-points. However often the gradients are still too large [202, 203]. This is also not always possible due to restrictions of the grid setup, *e.g.* with vertex-centred mesh refinement, such as `Carpet` combined with symmetry boundaries.

Another way is to extract the singular behaviour into some not evolved quantity, *e.g.* using a static conformal factor [204]. However this can only

be applied in special cases and certainly only if the singularity is already present in the initial data and is not moving in the coordinates used by the simulation.

Another way to handle the singularity is to exclude it from the computational domain [35, 133, 153, 205–220]. This is called excision and should theoretically be trivial, if just a part inside a black hole apparent horizon is excised, which is what is always done. The reason is that no signal can travel from inside the black hole to the outer regions, thus there should be no requirement for a boundary condition as long as the boundary is spacelike and the light cones are pointing entirely inwards.

However, gauge waves[4] can have speeds much larger than the speed of light and can leave the black hole, causing instabilities in the code. In addition, if one does not use variable stencils depending on the causal structure (causal differencing [217, 221]), some data have to be given for the discrete variables at each boundary. Therefore a discrete excision boundary condition is still necessary.

There is a large freedom in how to set this condition. We use the so called simple excision technique [133], which extrapolates the information normal to the boundary from points further outside the excision region. Given a point p at the boundary at which values have to be given for a variable f, and a point q, which is outside the excision region and is normal to its boundary as seen from p, the new value at p is obtained by assuming the same time derivative of f at q and p:

$$f_p^{i+1} = f_p^i + f_q^{i+1} - f_q^i, \tag{3.26}$$

where the superscript denotes the timestep and the subscript denotes the point at which the value of f is taken. This extrapolation is applied to the following quantities during evolution (if these quantities are evolved): $\tilde{\gamma}_{ij}, \psi, K, A_{ij}, \tilde{\Gamma}^i, \alpha, \beta^i$. Despite being so simple, this has been proven to be remarkably stable in a number of simulations (*e.g.* [222]), but as will be seen as one result of this work, has to be improved in the future.

We usually use the location of the apparent horizon as an indication of where to place the excision boundary and always excise only a part of its interior. Because the apparent horizon is always inside the event horizon, no physical signal from this boundary should be able to reach the outside. However, this does not imply that the light cones are always pointing entirely inside the excised region, as for a cubical excision region it was shown for the case of Schwarzschild black hole that the length of the cube has to be smaller

[4]The gauge conditions are often also evolved and their evolution equations may have characteristic speeds larger than the speed of light without violating Einstein's equations.

than $4\sqrt{3}/9M \approx 0.77M$ for this requirement to hold [213]. Because the problem are caused by the corners of the cube, we usually use another type of excision boundary, called a Lego[5] sphere, which is a sphere approximated by the Cartesian grid [133]. This does not remove the problem with the corners entirely; the sphere consists of a lot of corners on the discrete level, but it often works better than a cube in practice [222].

3.6 Convergence tests

The errors which arise due to the discretisation of the physical problem, *e.g.* by approximating derivatives by finite differences, depends on the resolution chosen. This gives the possibility to check for errors in a simulation by comparing the data to simulations of the same problem, but different resolution.

Typically methods are said to be of first, second or even higher order. This means for the example of second order that increasing the resolution by a factor of two decreases the error by an order of four (2^n with n being the convergence order).

One might think that because of this using very high order methods would give the best results and therefore the aim should be to use orders as high as possible. While this is partly true, it does not take the problems of higher order methods into account. Firstly it is not easy to implement them (correctly) in a code. But more importantly, higher order methods also require a wider stencil: for a derivative at a given point labelled i they need more points away from i: $i-1, i-2, ...$ This is problematic in two ways. The not so severe is that decomposing the computational domain into multiple chunks (which is usually done for parallelised simulations) requires more overhead. The more problematic one is connected to boundary conditions. They then have to provide consistent data on more than one or two points away from the boundary. Because of the problems of higher order methods, most of the recent simulations use second or fourth-order methods.

It is important to compare the order of the obtained convergence to the expected order of the methods used. This is easy in the case of a known, analytical solution, because then it is easy to check if the error made by discretising the problem converges to the known solution by the expected order.

However, for most problems an analytical solution is not known. In this case it is possible to check for the convergence order to *some* solution by comparing simulations with three different resolutions. The obtained order

[5] "Lego" is a registered trademark of the LEGO corporation (`http://www.lego.com/eng/Default.aspx`)

of convergence o can be calculated by the following expression, using one of the involved quantities q (*e.g.* the density) taken from simulations with low, middle and high resolution, differing in a factor of two:

$$2^o = \frac{q_{\rm low} - q_{\rm middle}}{q_{\rm middle} - q_{\rm high}}. \tag{3.27}$$

3.7 Numerical tests with stars

We consider the evolution of a stable relativistic polytropic spherical (TOV) star. As this is a static solution, no evolution is expected. Yet as shown in figure 3.4, both a small periodic oscillation and a small secular increase of the central density of the star are detected during the numerical evolution of the equations. Both effects have a single explanation. The initial data contain a small truncation error. This error is responsible for triggering radial oscillations which appear as periodic variations in the central density. With increasing resolution, the truncation error is reduced and so is the amplitude of the oscillation. The secular growth of the central density is probably related to the violation of the constraint equations. It converges to zero with increasing resolution. Note that the convergence rate is not exactly second-order but slightly smaller, because the reconstruction schemes are only first-order accurate at local extrema (*i.e.* the centre and the surface of the star) thus increasing the overall truncation error [29].

To further investigate the accuracy of our implementation of the hydrodynamics equations, we have suppressed the spacetime evolution and solved just the hydrodynamics equations in the fixed spacetime of the initial TOV solution. This approximation is referred to as the "Cowling approximation" and is widely used in perturbative studies of oscillating stars. In this case, in addition to the confirmation of the convergence rate already checked in fully evolved runs, we have also compared the frequency spectrum of the numerically induced oscillation with the results obtained by an independent axisymmetric code [223] and with perturbative analyses.

In figure 3.5 we show a comparison between the two codes reporting the power spectrum of the central density oscillations computed with the `Whisky` code and the corresponding frequencies as obtained with perturbative techniques and with the 2D code. Clearly the agreement is very good with an error below 1% in the fundamental frequency. The fact that the frequencies computed numerically coincide with the physical eigenfrequencies calculated through perturbative analysis allows us to use our code to study the physical properties of linear normal-modes of oscillation even if such oscillations are generated numerically.

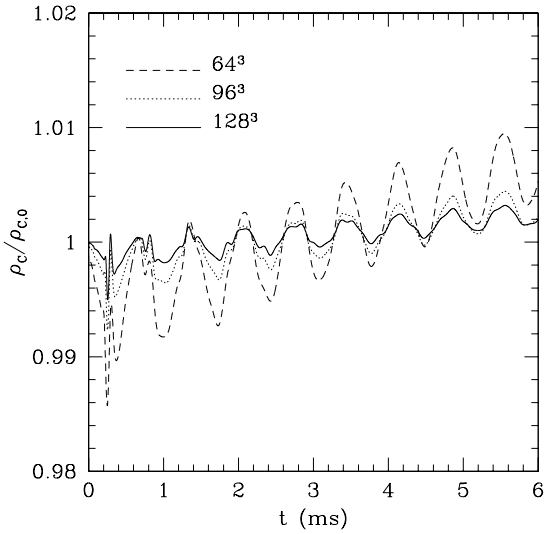

Figure 3.4: Central mass-density, normalised to the initial value, in a stable TOV star ($M = 1.4\,M_\odot$ and polytropic exponent $\Gamma = 2$) evolution at different resolutions. PPM and Marquina were used for all runs.

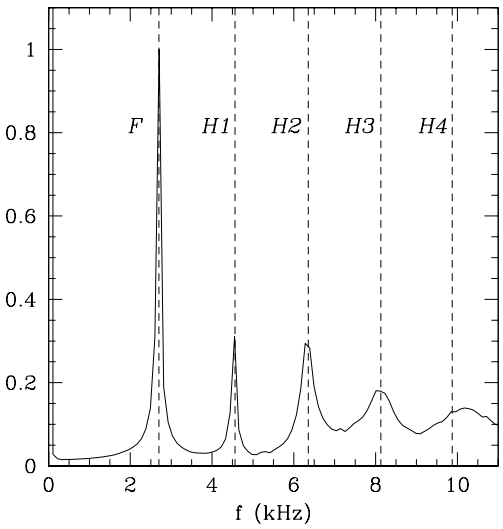

Figure 3.5: Fourier transform of the central mass-density evolution of an $M = 1.4\,M_\odot$, $\Gamma = 2$ stable TOV star performed with 128^3 grid points. The units on the vertical axis are arbitrary. F is the fundamental mode and Hx are higher modes of the star.

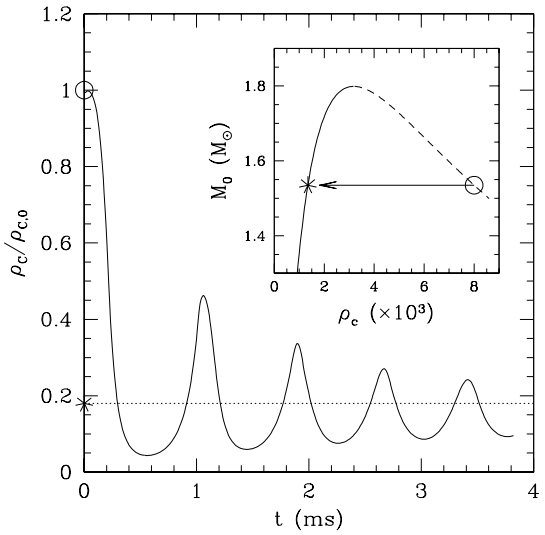

Figure 3.6: Normalised central mass-density evolution of an $M = 1.4\,M_\odot$, $\Gamma = 2$ unstable TOV star performed with 96^3 grid points.

The last test performed in the linear regime consists of the evolution of stationary solutions of rapidly rotating stars, with angular velocity up to 95% of the allowed mass-shedding limit for uniformly rotating stars. In this case, a number of small improvements on the boundary and gauge conditions have allowed us to extend considerably the timescale of our evolutions of stable rapidly rotating stars, which can now be evolved for about $60ms$, a timescale which is 3 times larger than the one previously reported in [128]. In analogy with the non-rotating case, the truncation error triggers quasi-radial oscillations in the star. Such pulsations converge to zero with increasing resolution. Determining the frequency spectrum of fully relativistic and rapidly rotating stars is an important achievement, allowing the investigation of a parameter space which is astrophysically relevant but too difficult to treat with current perturbative techniques.

Finally, we have considered tests of the non-linear dynamics of isolated spherical relativistic stars. To this purpose we have constructed TOV solutions that are placed on the unstable branch of the equilibrium configurations (see inset of figure 3.6). The truncation error in the initial data for a TOV solution is sufficient to move the model to a different configuration and in `Whisky` this leads to a rapid migration toward a stable configuration of equal rest-mass but smaller central density. Such a violent expansion produces large amplitude radial oscillations in the star that are either at constant amplitude, if the polytropic EOS (2.23) is used, or are damped through shock

heating, if the ideal fluid EOS (2.20) is used and the equation for τ is evolved in time. A summary of this dynamics is presented in figure 3.6, which shows the time series of the normalised central density for a TOV solution. Note that the asymptotic central density tends to a value corresponding to a rest-mass slightly smaller than the initial one (straight dotted line). This is the energy loss due to the internal dissipation.

3.8 Summary

While chapter 2 described the continuum physics, the topic of this chapter was the discretisation of the continuum physics in order to be able to do computer simulations. Two different methods for discretisation have been introduced (finite difference and finite volume methods in section 3.1 and spectral methods in section 3.2). Time integration of the evolution equations is done by the method of lines, which is outlined in section 3.3.

A scheme for excision of spacetime variables is explained in section 3.5 followed by descriptions of two kinds of tests which are often useful: convergence tests in section 3.6 and oscillation tests with stars in section 3.7.

Chapter 4

Excision methods for HRSC schemes

The results of this chapter have been published as [64]. The original idea, due to Ian Hawke, which worked for TVD and ENO, did not work straightforward for PPM. It was my work to solve those problems for PPM. On that way, I found further problems with this reconstruction method and introduced a modification to it - MPPM, which solves a those severe problems. Except the simulations involving the Michel solution, which are due to Andrea Nerozzi, I did all simulations and most of the analysis.

The methods and codes described here have been used in [65], but this work [64] was published later. This is the reason why [65] is referenced here, but described later in this thesis in chapter 5.

4.1 Motivation

The crucial problem for numerical simulations involving 3D general relativity which must be overcome to simulate such physical systems is stability. With current formulations of the vacuum Einstein equations it is possible to produce long term simulations of black holes in certain situations [133, 153, 207]. These simulations typically require some part of the computational domain inside the black hole to be *excised*, with an inner boundary condition placed on a spacelike surface inside the apparent horizon (see also section 3.5).

In contrast most simulations including hydrodynamics have either been performed on a fixed spacetime background, or have only been run until a short time after the formation of the black hole [224]. There have been fully dynamical simulations of matter with black holes in axisymmetry such as [225], but few in 3D [65, 226, 227].

In this chapter we will present a simple method for excision boundaries applied to hydrodynamics. The boundary condition is based on high-resolution shock-capturing (HRSC) methods which may be used in a hydrodynamics code, and theoretically could be applied to any system using such HRSC methods. We show how it can be applied to three different, standard reconstruction schemes: total variation diminishing (TVD), essentially non-oscillatory (ENO) and the piecewise-parabolic method (PPM). Because of some problems found using this boundary condition with the PPM scheme we introduce a modified version of PPM (MPPM), which solves these problems. This excision method, combined with a suitable excision method for the spacetime, allows long term simulations of matter in black hole spacetimes. This has been shown *e.g.* using our hydrodynamics code called `Whisky` in [65].

The outline of this chapter is as follows. In section 4.2 and 4.3 respectively we outline the equations and HRSC methods that will be used. The modifications required at excision boundaries are given in section 4.4. Section 4.5 contains the tests used to validate the boundary conditions.

4.2 Model and equations

We are interested in simulating hydrodynamical flows near black holes, so we use the equations of general relativistic hydrodynamics coupled to a dynamical spacetime, described by full general relativity. We use the flux-conservative Valencia 3+1 formulation of the hydrodynamical equations, see section 2.6.4, and we will consider the standard perfect fluid gamma-law EOS (2.20) and often we will restrict to the polytropic EOS (2.23). This is a good approximation to neutron star matter in a cold neutron star and in the absence of shocks and this is fulfilled in the cases discussed in this chapter.

4.3 Numerical methods

Our code implements three independent approximate Riemann solvers (Roe, HLLE, modified Marquina). Although an integral part of the full HRSC method they are irrelevant for the problem of excision, as explained below. The Riemann solver employed in all tests shown below is the modified Marquina solver described in [196, 197].

We implemented the excision scheme in four reconstruction methods, namely TVD, ENO, PPM (for these see 3.4.1) and MPPM. The latter is a variant of PPM, and it is introduced for the first time here. It solves some

problems found using PPM near the excision region. Therefore we call it MPPM for "modified PPM".

4.3.1 MPPM

As we shall see below there are situations where the PPM scheme does not give good results. This is due to the use of a fixed stencil in the first part of the PPM algorithm where the interpolated value is computed. This can cause problems with supersonic flows and when, as in our excision method, we try to match to a non-PPM method. To avoid this problem the modified PPM scheme changes the interpolated value in (3.15). The modified method uses the same steps as the PPM scheme after the interface values are set in equation (3.17) (discontinuity steepening, zone flattening and monotonicity preservation).

PPM uses the points at $i-2$, $i-1$, i, $i+1$, $i+2$ for the fourth order interpolation function to obtain a value at $i+\frac{1}{2}$. In the case of supersonic flow this centred stencil takes too much information from one side and too little from the other. Because of this, the method may produce small amplitude oscillations that are stable (due to the other steps in the PPM method) but which do not converge away. To cure this we need to use a stencil that depends on the data in some way.

In particular, we calculate the minimum and maximum characteristic velocities from the minimum and maximum eigenvalues λ_- and λ_+ of the Jacobian matrix $\partial\mathbf{f}/\partial\mathbf{q}$. Depending on these values, we define

$$\alpha = \frac{\lambda_- + \lambda_+}{|\lambda_-| + |\lambda_+|}, \tag{4.1}$$

which is a continuous function of the characteristic speeds that has value ± 1 whenever the flow is supersonic. Please note that because of this definition α can only be in the range $[-1, 1]$.

Using α we calculate the initial boundary states

$$q^+_{i+1/2} = \begin{cases} |\alpha|\, q_L + (1-|\alpha|)\, q_{i+1/2}, & \text{if} \quad \alpha < 0, \\ |\alpha|\, q_R + (1-|\alpha|)\, q_{i+1/2}, & \text{if} \quad \alpha > 0 \end{cases} \tag{4.2}$$

with

$$q_L = \frac{1}{12}\left(13q_{i+1} - 5q_{i+2} + q_{i+3} + 3q_i\right), \tag{4.3}$$

$$q_R = \frac{1}{12}\left(13q_i - 5q_{i-1} + q_{i-2} + 3q_{i+1}\right). \tag{4.4}$$

In this way we shift the stencil at most one cell to the side depending smoothly on the data. Note that this choice is arbitrary and could be chosen in a different way, but was sufficient for the tests used here. Because the value of the interpolating function at the boundary can be outside the range given by the values at the neighbouring cells q_i and q_{i+1}, we set the boundary values $q^+_{i+1/2}$ and $q^-_{i+1/2}$ in that case to be equal to the closest nearby cell value. Once the interpolated value is set we proceed as in the PPM case with the steps required to, *e.g.*, preserve monotonicity, as given in equations (3.18–3.25).

This procedure takes the characteristic speeds of the data into account and should therefore be more suitable to extreme cases where both minimal and maximal speeds have the same sign and are not close to zero. However, in cases with minimal and maximal characteristic speeds of the same size, but different sign, it should be as good as PPM.

4.4 Excision boundaries

Excision boundaries are based on the principle that a closed region of spacetime that is causally disconnected from the rest of the simulated spacetime can be ignored without affecting the results in the exterior spacetime (see section 3.5). A black hole event horizon is given indeed by the boundary of such a causally disconnected region of spacetime. As generically a curvature singularity will form within the horizon it will be necessary to remove it, and the associated steep gradients, from the numerical domain.

Excision boundaries are usually placed within a trapped surface such as an apparent horizon, as it is not possible to find the event horizon locally in time. We note that for a cubical region that is excised on a Cartesian grid to be a true trapped surface it may have to be placed well within the horizon, as pointed out by [213]. However, inflow boundary conditions applied to surfaces within the apparent horizon have been shown to work well for the evolution of vacuum spacetimes [222].

The same considerations apply to the hydrodynamical variables as to the spacetime field variables. Again there will be a region of spacetime in which the fluid is causally disconnected from the exterior. In practise due to the coupling with the spacetime field this will coincide with the event horizon as for the spacetime field. However, if the spacetime field variables have been excised then in principle there is no need to excise the hydrodynamical field variables at all, as these are not expected to blow up and form singularities independently of the spacetime field variables.

In practise unacceptable numerical errors are found if the hydrodynamical variables are not excised. In particular at typical resolutions it is possible

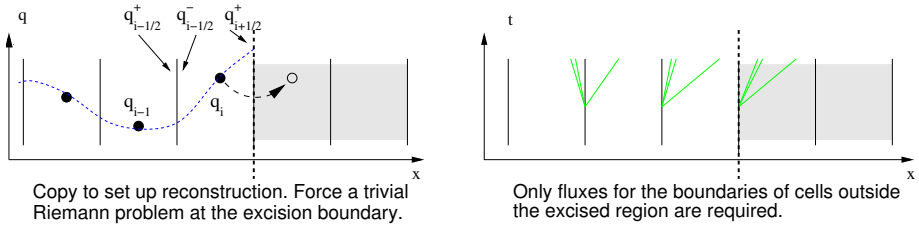

Figure 4.1: A schematic view of the excision algorithm. The excised region is indicated by the shaded grey cells and the excision boundary by the vertical dotted line. In the left panel we indicate how the reconstruction method is modified near the excision boundary. The values required to compute the fluxes for the cell next to the boundary are indicated, along with the method used (simple copying) to "extend" the data across the excision boundary. Using this we can compute the fluxes through the cell boundaries for all cells outside the excised region. As shown in the right panel, these are the only fluxes required (the green lines indicating the characteristics).

for numerical effects in the interior of the black hole horizon to propagate out of the horizon through the hydrodynamical variables. Although we will exploit the independence *in principle* of the use of excision boundaries for the different field variables later, in practise both should be used simultaneously.

Note that, in non-vacuum spacetimes, the excision boundaries for the hydrodynamical and the metric fields need not be the same. For the fluid quantities, in fact, all characteristics emanating from an event in spacetime will propagate within the sound-cone at that event, and, for physically realistic EOSs, this sound-cone will always be contained within the light-cone at that event. As a result, if a region of spacetime contains trapped surfaces, both the hydrodynamical and the metric fields are causally disconnected and both can be excised there. On the other hand, there may be situations, *e.g.*, when the bulk flow is locally supersonic but no trapped surfaces are present, in which it is possible (at least in principle) to excise the hydrodynamical fields without having to do the same for the metric fields. We have not used this option here and the hydrodynamical excision implemented in our simulations has always been made within regions of the spacetime contained inside trapped surfaces.

Excision boundary methods can be viewed in a number of different ways. Viewed at the level of the differential equations, all characteristics of physical quantities are going into the excision region. At the level of the Riemann problem, all possible waves from the solution of the Riemann problem must be contained within the excision region.

This immediately suggests a method that could be used at the excision boundary. As a HRSC method naturally changes the stencil locally depending on the data, we just need to guarantee that the data used to construct the flux at the excision boundary are the physically relevant data outside the excision region. This also suggests that the natural choice to put the excision boundary is not a cell centre, but a cell boundary.

While very simple, this method is not stable in general. It is equivalent to filling the first cell inside the excision region by linear extrapolation from the exterior (for a second–order HRSC method such as slope limited TVD reconstruction). This is not guaranteed to reduce the total variation of the solution, and so even simple examples do fail with this boundary condition.

On the other hand the simplest outflow boundary condition at the excision boundary does not have this problem. In particular, we may apply zero–order extrapolation (a simple copy) to all variables at the boundary to create data at the first cell inside the excision region (note that setting the hydrodynamical fields inside the excised region to zero would still yield an outflow boundary condition, but leads to incorrect outflow speeds). This is done for each of the four reconstruction methods. If one method requires more cells for the stencil in the interior of the excision region, we can then force the stencil to only consider the data in the first cell and the exterior as above. Although the actual implementation of this excision technique may depend on the reconstruction method used, the working principle is always the same.

A summary of our method is as follows:

1. Any point for which all possible reconstruction stencils are contained within the exterior spacetime (i.e., do not contain an excised point) is evolved in the normal fashion.

2. Any point which is contained within the excised region is not evolved at all.

3. All other points have at least one stencil that contains an excised point. To update these other points we must reconstruct the data to both sides of each cell boundary. Once this is done the Riemann problem can be solved, the boundary flux found and the update computed. In order to reconstruct the data we do the following:

   (a) The values for all variables in the cell next to the excision boundary are copied to the first cell within the excision boundary.

   (b) A reconstruction of all cells is produced using only the data outside the excision region and the first cell within. The precise

method depends on the global reconstruction method used and is explained below. In outline, the idea is to retain the order of accuracy by retaining the same size of the stencil if possible.

(c) This method produces reconstructed data on both sides of every cell boundary *except* for the excision boundary, where only the reconstruction from the exterior can be produced. At this boundary we assume on physical grounds that the solution of the Riemann problem must be given by the exterior state (as this is assumed to be an outflow boundary). Therefore at these points we do not solve the Riemann problem, but calculate the flux from the exterior reconstruction (see Fig. 4.1).

As an aside, we note that this means the method is independent of the choice of Riemann solver. However, the choice of a *trivial* Riemann problem at points that are not excised but where the reconstructed states are identical (*e.g.*, in the atmosphere) can lead to gains in computational efficiency.

To completely describe our method in practice we just need to describe how the stencil is altered with the specific reconstruction methods we use. In what follows we consider a set of cells in one dimension. The coordinate is labelled x, the cell centres x_i, and the cell boundaries $x_{i\pm1/2}$ in an obvious notation. The excision boundary will be denoted $x_{B+1/2}$, with the cell x_{B+1} being excised. We want to calculate the update term for the cell centred at x_B by calculating the fluxes at $x_{B\pm1/2}$.

Excision of the spacetime variables is applied using the *simple Lego* excision method described in section 3.5.

4.4.1 Slope-limited TVD

In this case it is clear that only the reconstructions at $x_{B\pm1/2}$ are affected by the excision region. It is also clear that setting

$$\bar{\Delta}_B = \frac{1}{2}\left(\Delta_B^- + \Delta_B^+\right) = 0, \tag{4.5}$$

ensures that only data outside the excision region are used and is consistent with the TVD reconstruction.

4.4.2 ENO

As described in section 3.4.1 the ENO method uses a stencil width depending on the desired order of accuracy p. Hence the reconstruction in the cells centred between x_B and x_{B-p+2} are affected by the excision region.

It is clear how to ensure that the stencil chosen by the ENO reconstruction does not include any points from inside the excision region. The first divided differences that include points within the excision region are set to extremely large values with oscillating and growing amplitude such as $(-i)^i \times 10^{10}$ where i is the index of the cell ($i > 0$). The higher order divided differences are calculated from these, ensuring that the least oscillatory stencil does not include points from the excision region, but more points away from it. This is a simple application of the principle outlined by Shu [188] for dealing with outflow boundaries with ENO methods.

4.4.3 PPM

PPM uses a point stencil of five points, but reconstructs around a cell boundary instead of in a cell. Hence the reconstructions affected by the excision region are the reconstruction at left edge of $x_{B+1/2}$ and both reconstructions at $x_{B-1/2}$.

We have not attempted to find a consistent third–order reconstruction for these points. Instead we use the identical reconstruction as in the TVD case of section 3.4.1. As this provides a second–order stable reconstruction at an outflow boundary it does not affect the order of accuracy in the rest of the domain.

4.4.4 MPPM

Since excision should only be applied on a boundary with only outgoing characteristics, α should only be -1 or 1 depending on the direction of the boundary. Because of the symmetry of the cases, without loss of generality we assume $\alpha = 1$ from here on, that is assuming the excision boundary to be to the right of the computational domain.

In the case $\alpha = 1$ we effectively use a stencil with one point to the right and three points to the left instead of the usual symmetric four point stencil of the interpolation step of PPM. Because of this, we can use the usual MPPM procedure in the whole domain except for only one point next to the excision boundary. There we set the left and right boundary values to be the cell value as in the TVD case.

4.5 Numerical tests

In this Section we present some simple numerical tests to validate our approach. The results were calculated using the `Whisky` code [65]. Where the

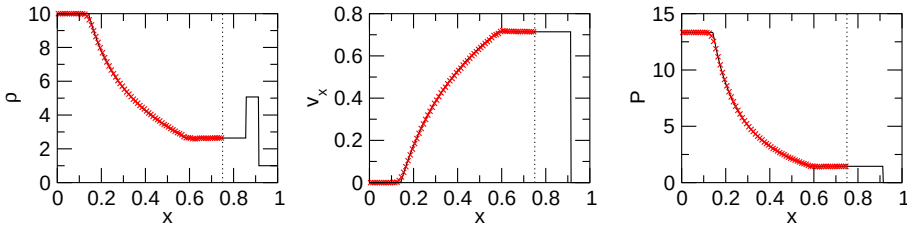

Figure 4.2: A simple shock propagating parallel to the x axis hits an excision boundary normal to the x axis (dotted line). As expected, the shock is completely absorbed. The solid line is the exact solution, the crosses are the numerical solution for the PPM scheme. Plots of the other reconstruction methods show qualitatively the same behaviour. The time shown is $t = 0.5$.

spacetime was evolved an implementation [127, 137] of the BSSN formulation of [123, 124] was used, with the excision method given in [133]. Apparent horizons were found using the code described in [228] and event horizons using the code described in [229]. All codes use the `Cactus` framework [162].

4.5.1 Shock wave tests

Special relativistic shock tubes are the simplest possible test. For this test the spacetime background is fixed to be Minkowski spacetime in standard coordinates. It is simple to choose initial data such that the chosen excision boundary is an outflow boundary for all time. In particular, we are using initial data in which $\rho_L = 10$, $\rho_R = 1$, $v_L = v_R = 0$, $P_L = 40/3$ and $P_R = 2/3 \times 10^{-6}$ and the velocity is normal to the interface. The ideal fluid equation of state, Eq. (2.20), is used, with $\Gamma = 5/3$.

We have considered three different cases. The first and simplest was a shock aligned with a coordinate axis with the excision boundary normal to the shock. The second and numerically more complex was a shock along the diagonal of the 3D box with the excision boundary normal to the shock. The final test consisted of a shock not aligned with the grid and with the excision boundary given by a Lego sphere. The test requires more care in setting the domain evolved as the excision boundary is no longer an outflow boundary over the entire spacetime, but only within a localised region. Here we set the domain such that the intersection of the excision boundary with the domain forms a hemisphere.

The results of the first test for PPM are shown as an example in Fig. 4.2. All methods give nearly the same results, are stable and for all methods the shock passes cleanly through the excision boundary, with the results matching the analytic solution well. All other tests showed similar results,

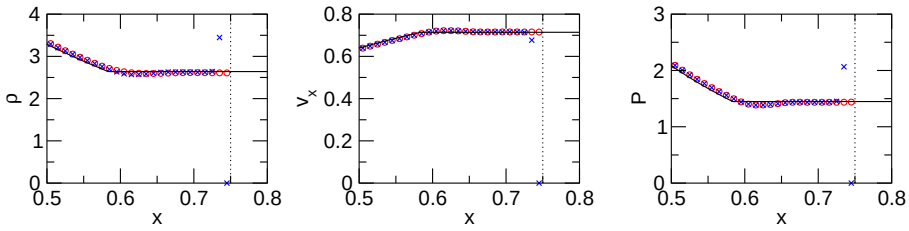

Figure 4.3: As in Fig. 4.2, a shock is propagated parallel to the x axis through an excision boundary. In this case a non-conservative excision boundary condition is used. This excision boundary condition, which is based on setting all variables in the first excised cell to very small ("atmosphere") values gives inaccurate but stable results. The circles represent the stable and accurate numerical result found using the excision boundary method described in this chapter.

with stable and accurate results independent of the relative geometry of the shock and excision boundary.

An example of what may go wrong with an incorrect excision boundary condition is shown in Fig. 4.3. Here the standard excision boundary condition presented in section 4.4 is compared to an alternative method where the first point inside the excision region is set to very small values. The result is a stable evolution which is correct except for a few points near the boundary. Here the density overshoots except for the point nearest the boundary which itself drops to atmosphere values. Although in this simple test the boundary condition is inaccurate, but stable, this seems unlikely to remain the case in more complex situations. Other boundary conditions, such as first–order extrapolation to the first point within the excision region, fare even worse, as they actually fail to produce a stable evolution even on this simple test.

4.5.2 Michel solution

The Michel solution [106] is a stationary solution of spherical accretion onto a Schwarzschild black hole in the test fluid approximation, for more details see section 2.5.2.

The solution is derived from the basic equations of mass and energy conservation for the fluid and is obtained numerically using a Newton–Raphson iteration scheme.

The first three plots in Fig. 4.4 show a part of the results of a series of runs made to test the Michel solution. In these plots the ENO reconstruction method is used, but the graphs look very similar for TVD, PPM and MPPM. We set the Michel solution to be our initial data, then we evolve it and verify

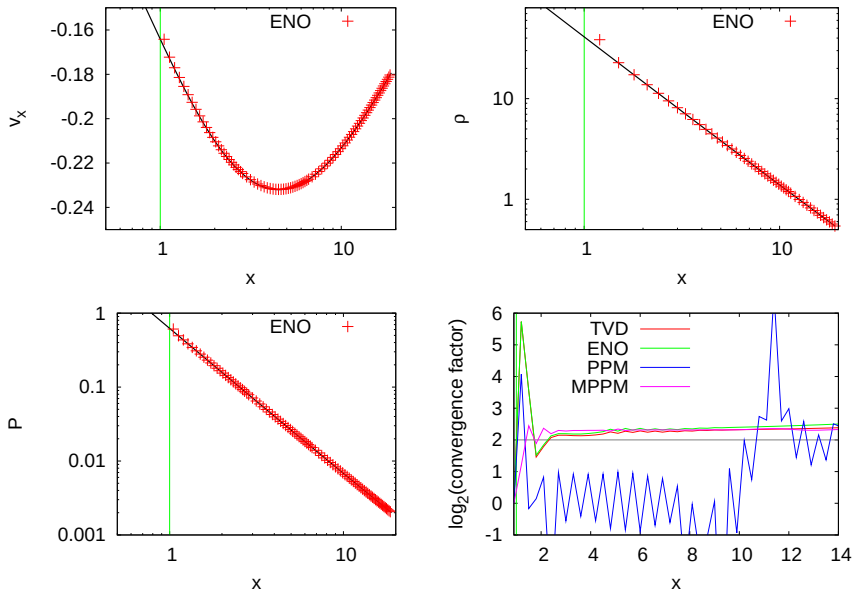

Figure 4.4: Michel solution compared with the numerical evolution for the ENO method. All other methods look very similar in the physical quantities. The graphs show the values for the x component of the velocity v_x, the density ρ, and the pressure p of the fluid. Each quantity is evolved until time $t = 40$ (in units of the background black hole mass), and the numerical values are compared with the exact solution (the solid line in the graphs). The x axis is the radial distance expressed in black hole units. The excision region is delimited by the vertical, dotted line. The last graph shows the convergence factor of all reconstruction methods, where the expected second–order convergence is seen for all methods except for PPM.

its accuracy. In the plot, the exact solution is compared with the computed solution at time $t = 40$ (in units of the background black hole mass). Using a logarithmic plot we show the results for the density, x-velocity and pressure. The two sets of data are in very good agreement, as expected from the staticity of the solution. It is possible to notice a slight discrepancy in the first grid point next to the excision region (dotted line). This discrepancy is related to the lower accuracy which we have there, visually amplified on the plot by the choice of logarithmic scale. This is the case for all reconstruction methods.

The fourth plot in Fig. 4.4 shows instead the convergence factor obtained for all the reconstruction methods on the same set of simulations. As evident in the figure, PPM does not show convergence, while the other reconstruction methods show the expected convergence factor of approximately two. We will

discuss the possible reason for that later (see section 4.3.1).

4.5.3 Neutron Star collapse

As the next test we consider the collapse of a neutron star, in a simulation in which both the spacetime and the matter are evolved. This test is considerably more difficult than previous tests, requiring both hydrodynamic fields and spacetime to be consistently excised, and requiring a dynamic excision region.

As in [128] a spherically symmetric polytrope with $K = 100$, $\Gamma = 2$ and a central density of $\rho_c = 8 \times 10^{-3} \approx 4.95 \times 10^{15}\,\mathrm{g\,cm^{-3}}$ is used. The collapse was induced by lowering K by 2% and rescaling the matter variables to enforce the solution of the constraints. Note that because this satisfies the constraints and the spacetime is not changed, the ADM (Arnowitt-Deser-Misner) mass of the system is also not changed by this.

Due to the symmetry of the problem we only evolve one octant of the grid. The spacetime is evolved using the BSSN formulation and the excision methods described in [133, 153]. The apparent horizon, if it can be found, is located using the horizon finder described in [228]. The gauge conditions used are "1+log" slicing for the lapse and the gamma-driver condition given in equation (45) of [134]. The event horizon is located using the code described in [229]. The TVD scheme is used.

In Fig. 4.5 we show the mass of the event and apparent horizons of the black hole found by measuring their surface areas and using $M = (A/16\pi)^{1/2}$ and the ADM mass computed by the initial data solver for comparison[1]. At early times the expected results are seen: the mass of the apparent horizon is less than the mass of the event horizon which is less than the total ADM mass of the spacetime. At late times large violations of the Hamiltonian constraint develop, errors in the determination of the horizon become large and lead eventually to the crash of the code at around $t = 0.455$ms. Without excision the code crashes shortly after formation of the apparent horizon.

We believe that the origin of these instabilities lies in the spacetime exci-

[1]The ADM mass can be defined [230] as a surface integral over a sphere with infinite radius:

$$M_{\mathrm{ADM}} = \frac{1}{16\pi} \oint_{\infty} \sqrt{\gamma}\gamma^{ij}\gamma^{kl}(\gamma_{ik,j} - \gamma_{ij,k})\,\mathrm{d}S_l \tag{4.6}$$

. This is, assuming $\alpha = 1$ at infinity, equivalent to

$$M_{\mathrm{ADM}} = \frac{1}{16\pi} \int \left(\alpha\sqrt{\gamma}\gamma^{ij}\gamma^{kl}(\gamma_{ik,j} - \gamma_{ij,k})\right)_{,l} \mathrm{d}^3x \tag{4.7}$$

.

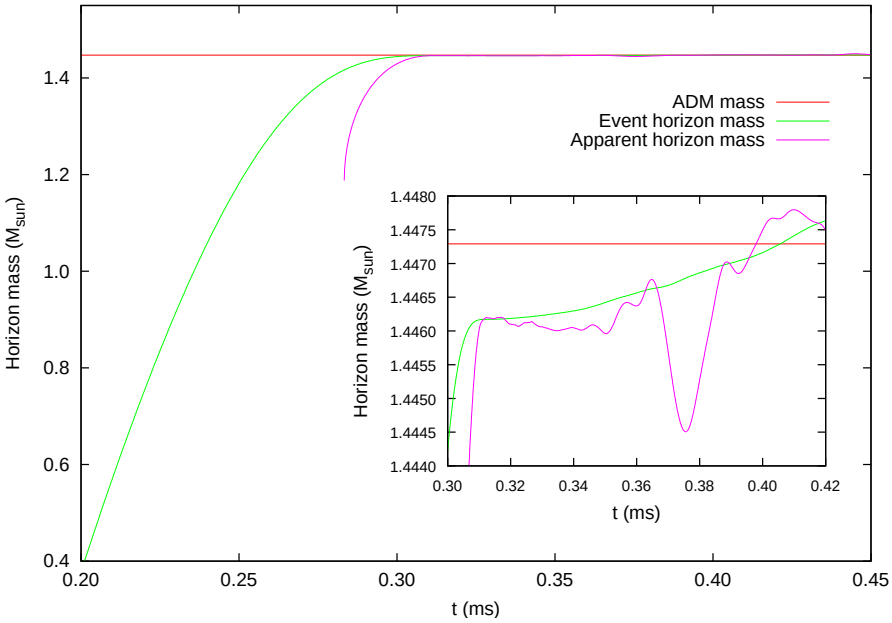

Figure 4.5: Horizon masses for the collapse of a spherically symmetric neutron star. At early times the evolution is stable and accurate. The neutron star collapses smoothly into the horizon and the matter is excised. The horizon masses as measured by apparent and event horizon finders are very close to the total ADM mass of the initial spacetime, as expected. At late times instabilities lead to inaccuracies, as seen in the inset, before the simulation fails.

sion technique, and not the hydrodynamic excision described here. This can be seen much more clearly in another test, where we used a slowly rotating neutron star (model D1 of [65]) and excise the spacetime variables and the matter variables at different times and compare the evolution of the 2-norm of the Hamiltonian constraint in the two cases. Note that it is not possible to first excise the spacetime variables and later the hydrodynamics because the hydrodynamics code is very sensitive to errors in the spacetime. Therefore we always first excise the hydrodynamical variables and then switch on the excision of the spacetime at a later time. We excise the hydrodynamic variables shortly after an apparent horizon is found (which in this case is at a *coordinate* time of 0.546ms) and vary the coordinate time, $t_{\rm ex}$, when the spacetime is first excised.

In this test we used the PPM method. In contrast to the test using the Michel solution (Sec. 2.5.2) this was found to work well. We believe that the short timescale on which matter collapse into the excised region combined with the resolution available in a realistic 3D simulation and the strong dynamics involved mean that the problems encountered in Sec. 2.5.2 are not apparent in this test.

Figure 4.6 shows the Hamiltonian constraint violation for simulations where the excision time $t_{\rm ex}$ is varied. For comparison, a simulation where neither the hydrodynamical variables nor the spacetime variables were excised, and a simulation where only the hydrodynamical variables are excised, are also shown.

Where the hydrodynamical or spacetime variables are excised the Hamiltonian constraint violation inside the excised region is not taken into account. At the point where either set of variables is excised the constraints are clearly meaningless within the excision region. We expect this to have no effect on the exterior spacetime as demonstrated numerically in, *e.g.*, [222]. The constraint violations in the exterior spacetime clearly are meaningful, and we will be most interested in the behaviour shortly after either set of variables is excised

It is clear that shortly after the time when the spacetime variables are excised there is a sudden exponential increase in the violation of the constraints. This does not happen at the time when the excision of the hydrodynamical variables first takes place. We believe this indicates that the cause of the instabilities encountered is the method used to excise the spacetime variables. Whilst we cannot rule out instabilities from the hydrodynamical excision, the simulation where only the hydrodynamical variables are excised seems to lose accuracy due to classical slice stretching effects and not due to the high frequency oscillations which are instead observed when excising the spacetime variables.

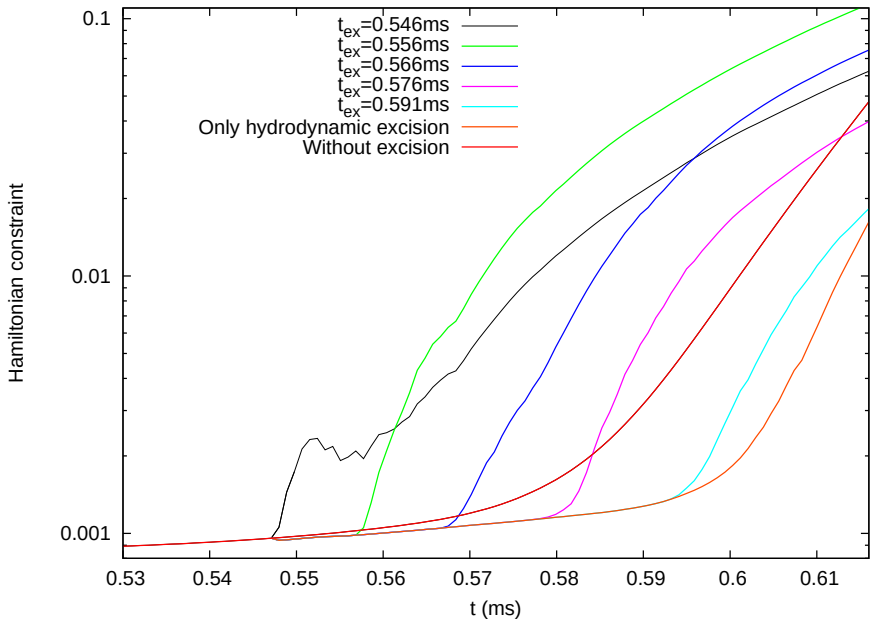

Figure 4.6: The Hamiltonian constraint violation over time, plotted for different starting times $t_{\rm ex}$ of the spacetime excision. In every case (except the reference case where no excision is used) the hydrodynamical variables are excised as soon as the apparent horizon is found at $t = 0.547$ms. Instabilities at the excision boundary are believed to be the cause of the eventual failure of the simulation. Here it is clear that when the excision boundary condition is applied to the spacetime variables there is an immediate exponential growth in the constraint violation. In contrast, no growth is seen at the time when the hydrodynamical variables are excised. The instabilities which are indicated by the exponential growth of the constraint violations are clearly triggered by the spacetime excision.

4.6 Summary

In this chapter we have shown a simple method of providing a consistent excision boundary condition for systems of equations in conservation law form evolved with HRSC schemes. Although we have only applied this technique to the Valencia formulation of relativistic hydrodynamics [147–149] we expect the results to apply to any system where the conservation law form can be applied. The method is simple and works on a broad range of HRSC schemes.

The tests of section 4.5 show that the method works for shocks, steady state cases, and dynamical evolutions. The shock tests are particularly simple and enlightening, showing that an incorrect boundary condition may lead to inconsistency or numerical instabilities. The Michel solution test shows that our boundary conditions are also suited to long term steady state evolutions with strong gradients.

The dynamical collapse of a spherically symmetric Tolman-Oppenheimer-Volkoff (TOV) star shows the advantages and current limitations of our methods. The collapse to a black hole is accurately followed long past the formation of the horizon, the mass of which is computed to high accuracy. However, the simulation does not continue indefinitely, eventually failing due to a numerical instability. Simulations including rotation show the same features and, by varying the initial time at which excision is applied, there is evidence that the cause of the instabilities is the excision method applied to the spacetime variables, not the hydrodynamical method. However we want to emphasise that although we believe that the simple Lego excision boundary condition is the cause of the instabilities, the excision of the spacetime variables is nevertheless improving the length of the simulations in the cases described here.

In the context of the topic of this work these new excision boundary conditions are crucial for mixed binary simulations. Currently we see no problems arising from using the new hydrodynamic excision scheme for those simulations, in contrast to the spacetime excision scheme, which might be the reason for stability problems.

It has been suggested that HRSC methods may improve spacetime evolutions for certain hyperbolic formulations of Einstein's equations (*e.g.* [154, 231, 232]). If such a method were used, excision boundary conditions such as those presented in this chapter should be easy to adapt. There are also other approaches to applying excision boundary conditions that show great promise (*e.g.* [214, 233, 234]). It is, however, not clear if these methods will work in situations where fundamental variables may become discontinuous. In such cases the methods presented here could then be used for a matter field, and any alternative method could be used for the spacetime.

Chapter 5

3D simulations of rotating NS collapse

The results of this chapter have been published as [65]. I wrote parts of the code (*e.g.* see chapter 4), performed some of the simulations presented and participated in the analysis, which was done collaboratively among all authors of [65].

5.1 Motivation

The simulation of a mixed binary involves the dynamics of a black hole, coupled to matter sources. It also involves initial data, created by a new code, which itself should also be tested. Besides, the new excision schemes for the hydrodynamics needed testing in dynamical spacetimes. It also needs mesh refinement, which has only recently been successfully implemented in 3D numerical Relativity and little used in 3D relativistic hydrodynamics(*e.g.* [135]). Ideally these issues are tested independently. Therefore we looked for a simpler problem which could initially be looked at with simulations on uniform grids but which also required the use of hydrodynamic excision in full General Relativity. Ideally this would also be of physical interest. We found this with the numerical investigation of gravitational collapse of rotating stellar configurations leading to black-hole formation.

This was a long standing problem in numerical relativity. Numerical simulations of stellar gravitational collapse to black holes provide a unique mean of computing the gravitational waveforms emitted in such events, believed to be among the most important sources of detectable gravitational radiation.

However, the modelling of black hole spacetimes with collapsing matter sources in multi-dimensions is one of the most formidable efforts of numerical

relativity. This is due, on one hand, to the inherent difficulties and complexities of the system of equations which is to be integrated, the Einstein field equations coupled to the general-relativistic hydrodynamics equations, and, on the other hand, to the immense computational resources needed to integrate the equations in the case of three-dimensional (3D) evolutions. In addition to the practical difficulties encountered in the accurate treatment of the hydrodynamics involved in the gravitational collapse of a rotating neutron star to a black hole, the precise numerical computation of the gravitational radiation emitted in the process is particularly challenging as the energy released in gravitational waves is much smaller than the total rest-mass energy of the system.

In addition to the improvements achieved in the formulation of the field equations (see section 2.6.1), successful long-term 3D evolutions of black holes in vacuum have been obtained in the last few years using excision techniques (see 3.5). The simulations presented here show the applicability of excision techniques *also* in non-vacuum spacetimes, namely during the collapse of rotating neutron stars to Kerr black holes. The excision technique, which is applied once the black-hole apparent horizon is found, may extend considerably the lifetime of the simulations, at least with the resolutions used here. This, in turn, allows for an accurate investigation of the dynamics of the trapped surfaces formed during the collapse, from which important information on the mass and spin of the black hole, as well as on the amount of energy which is lost to gravitational radiation, can be extracted. While our study was nearing completion, we have learnt that a similar approach has also been implemented with success [226].

The presence of rotation in the collapsing stellar models requires multidimensional investigations, either in axisymmetry or in full 3D. The numerical investigations of black-hole formation (beyond spherical symmetry) started in the early 1980's with the pioneering work of Nakamura [235]. He adopted the (2+1)+1 formulation of the Einstein equations in cylindrical coordinates and introduced regularity conditions to avoid divergences at coordinate singularities. Nakamura used a "hypergeometric" slicing condition which prevents the grid points from reaching the singularity when a black hole forms. The simulations could track the evolution of the collapse of a $10M_\odot$ "core" of a massive star with different amounts of rotational energy, up to the formation of a rotating black hole. However, the numerical scheme employed was not accurate enough to compute the emitted gravitational radiation. In subsequent works, Nakamura [236] (see also [122]) considered a configuration consisting of a neutron star with an accreting envelope, which was thought to mimic mass fall-back in a supernova explosion. Rotation and infall velocity were added to such a configuration, simulating an evolution dependent on

the prescribed rotation rates and rotation laws.

Later on, in a series of papers [215, 237–239], Bardeen, Stark and Piran studied the collapse of rotating relativistic polytropes to black holes, succeeding in computing the associated gravitational radiation. The gravitational field and hydrodynamics equations were formulated using the $3+1$ formalism in two spatial dimensions, using the radial gauge and a mixture of singularity-avoiding polar and maximal slicings. The initial model was a spherically symmetric relativistic polytrope of mass M in equilibrium. The gravitational collapse was induced by lowering the pressure in the initial model by a prescribed (and often very large) fraction and by simultaneously adding an angular momentum distribution approximating rigid-body rotation. Their simulations showed that Kerr black-hole formation occurs only for angular momenta less than a critical value. Furthermore, the energy ΔE carried away through gravitational waves from the collapse to a Kerr black hole was found to be $\Delta E/Mc^2 < 7 \times 10^{-4}$, the shape of the waveforms being nearly independent of the details of the collapse.

The axisymmetric codes employed in the aforementioned works adopted curvilinear coordinate systems which may lead to long-term numerical instabilities at coordinate singularities. These coordinate problems have deterred researchers from building 3D codes in spherical coordinates[1]. Recently, a general-purpose method (called "cartoon"), has been proposed to enforce axisymmetry in numerical codes based on Cartesian coordinates and which does not suffer from stability problems at coordinate singularities [240]. It should be noted, however, that the stability properties of the cartoon method are not fully understood yet, as discussed by [241]. Using this method, Shibata [242] investigated the effects of rotation on the criterion for prompt adiabatic collapse of rigidly and differentially rotating polytropes to a black hole, finding that the criterion for black-hole formation depends strongly on the amount of angular momentum, but only weakly on its (initial) distribution. The effects of shock heating when using a non-isentropic equation of state (EOS hereafter) are important in preventing prompt collapse to black holes in the case of large rotation rates.

More recently, Shibata [126, 224, 243] has performed axisymmetric simulations of the collapse of rotating supramassive neutron stars to black holes for a wide range of polytropic and other EOSs and with an improved implementation of the hydrodynamics solver (based on approximate Riemann solvers) with respect to the original implementation used in [242]. Parametrising the "stiffness" of the EOS through the polytropic index N, the final state of the collapse is a Kerr black hole without any noticeable disc formation, when

[1] A discussion of how equations in axisymmetry can be regularised can be found in [215].

the polytropic index N is in the range $2/3 \leq N \leq 2$. Based on the specific angular momentum distribution in the initial star, Shibata has estimated an upper limit to the mass of a possible disc as being less than 10^{-3} of the initial stellar mass [224]. Similar limits have been found in semi-analytic work done by Shapiro [244].

Three-dimensional, fully-relativistic simulations of the collapse of supramassive uniformly rotating neutron stars to rotating black holes were presented in [125]. The simulations focused on $N = 1$ polytropes and showed no evidence of massive disc formation or outflows. These results are in agreement with those obtained in axisymmetry [126, 224] and with the new simulations reported by [226] (both in axisymmetry and in 3D) which show that for a rapidly rotating polytrope with $J/M^2 < 0.9$ (J being the angular momentum) all the mass falls promptly into the black hole, with no disc being formed. Hence, all existing simulations agree that massive disc formation from the collapse of neutron stars requires differential rotation, at least for a polytropic EOS with $1 \leq N \leq 2$.

Here, we present the results of new, fully 3D simulations of gravitational collapse of uniformly rotating neutron stars, both secularly and dynamically unstable, which we model as relativistic polytropes. The angular velocities of our sample of initial models range from slow rotation to the mass-shedding limit. For the first time in such 3D simulations, we have detected the *event* horizon of the forming black hole and showed that it can be used to achieve a more accurate determination of the black-hole mass and spin than it would be otherwise possible using the area of the *apparent* horizon. We have also considered several other approaches to measure the properties of the newly formed Kerr black hole, including the recently proposed *isolated* and *dynamical horizon* frameworks. A comparison among the different methods has indicated that the dynamical horizon approach is simple to implement and yields estimates which are accurate and more robust than those of the equivalent methods.

The simulations are performed with a new general relativistic hydrodynamics code, the `Whisky` code (see 3.4.5). As mentioned before, we have implemented in the `Whisky` code a robust excision algorithm which allows extending the lifetime of the simulations far beyond the evolution times when the black holes first form. Our calculations start from initially axisymmetric stellar models but are performed in full 3D to allow for departures from the initial axial symmetry. Overall, our results show that the dynamics of the collapsing matter is strongly influenced by the initial amount of angular momentum in the progenitor neutron star, which, when sufficiently high, leads to the formation of an unstable flattened object. All of the simulations performed for realistic initial data and a polytropic equation of state show

no evidence of shock formation preventing a prompt collapse to a black hole, nor the presence of matter on stable orbits outside the black hole. It should be noted, however, that both of these conclusions may change if the initial stellar models are rotating differentially.

The use of numerical grids with uniform spacing and the present computational resources have placed the outer boundary of our computational box in regions of the spacetime where the gravitational waves have not yet reached their asymptotic form. As a result, the information on the gravitational waveforms that we extract through perturbative techniques [245, 246] does not provide interesting information besides the obvious change in the stellar quadrupole moment. Work is now in progress to use mesh refinement techniques [247] to move the outer boundary sufficiently far from the source so that important information can be extracted on the gravitational wave emission produced during the collapse. The results of these investigations have be presented in a companion paper [65] and are presented in chapter 4.

This chapter is organised as follows: Section 5.2 describes the formulation we adopt for the Einstein and hydrodynamics equations, the way they are implemented in the code and a brief discussion of how the excision techniques can be employed within a hydrodynamical treatment making use of high-resolution shock-capturing (HRSC) schemes. The technical details concerning the numerical implementation of the hydrodynamical equations has already been discussed in section 3.4. Section 5.3 is devoted to describing the various properties of the initial stellar models. The following two Sections, 5.4 and 5.5, present our results regarding the dynamics of the collapsing stars and of the trapped surfaces, respectively. In both cases we will be considering and comparing the dynamics of slowly and of rapidly rotating stellar models. The chapter ends with Section 5.6, which contains a summary of the results obtained and the perspectives for further investigations.

5.2 Basic equations and their implementation

We used the BSSN formulation (see section 2.6.1) for evolving the field equations together with the $1 + \log$ lapse and "gamma2" shift conditions (see section 2.7). The hydrodynamics was evolved using the `Whisky` code, which makes use of HRSC methods (see section 2.6.4).

Excision of the hydrodynamics was done by the methods described in chapter 4 or [64]. The regions of spacetime and hydrodynamics excision always coincide and, if they are used, are used both at the same time.

The location of the excision boundary itself is based on the determination of the apparent horizon which, within the `Cactus` code, is obtained using

the fast finder of Thornburg [228]. The excision boundary is placed a few grid-points (typically 4), within a surface which is 0.6 times the size of the apparent horizon. This may not be a suitable outflow boundary on a Cartesian grid or even in the continuum limit, as pointed out by [213, 248]. However, similar or larger excision regions show no problems in vacuum evolutions and since the sound-cones are always contained within the light-cones, we expect no additional problems to arise from the hydrodynamics.

5.3 Initial stellar models

As mentioned earlier, this chapter is specially dedicated to study the gravitational collapse of slowly and rapidly rotating supramassive relativistic stars, in uniform rotation, that have become unstable to axisymmetric perturbations. Given equilibrium models of gravitational mass M and central energy density e_c along a sequence of fixed angular momentum or fixed rest mass, the Friedman, Ipser & Sorkin criterion $\partial M/\partial e_c = 0$ [249] can be used to locate the exact onset of the *secular* instability to axisymmetric collapse. The onset of the *dynamical* instability to collapse is located near that of the secular instability but at somewhat larger central energy densities. Unfortunately, no simple criterion exists to determine this location, but the expectation mentioned above has been confirmed by the simulations performed here and by those discussed in [125]. Note that in the absence of viscosity or strong magnetic fields, the star is not constrained to rotate uniformly after the onset of the secular instability and could develop differential rotation. In a realistic neutron star, however, viscosity or intense magnetic fields are likely to enforce a uniform rotation and cause the star to collapse soon after it passes the secular instability limit.

The initial data for our simulations are constructed using a 2D numerical code, that computes accurate stationary equilibrium solutions for axisymmetric and rapidly rotating relativistic stars in polar coordinates [250]. The data are then transformed to Cartesian coordinates using standard coordinate transformations. The same initial data routines have been used in previous 3D simulations [127, 128, 251] and details on the accuracy of the code can be found in [252].

For simplicity, we have focused on initial models constructed with the polytropic EOS (2.23), choosing $\Gamma = 2$ and polytropic constant $K_{\rm ID} = 100$ to produce stellar models that are, at least qualitatively, representative of what is expected from observations of neutron stars. More specifically, we have selected four models located on the line defining the onset of the secular instability and having polar-to-equatorial axes ratio of roughly 0.95, 0.85,

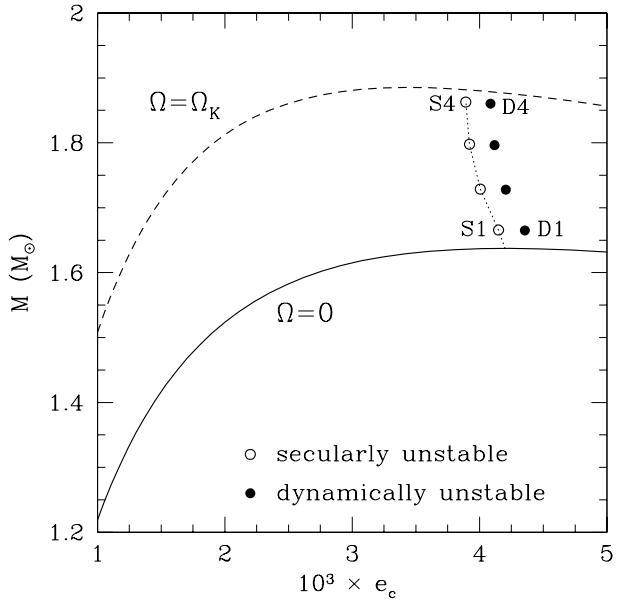

Figure 5.1: Gravitational mass shown as a function of the central energy density for equilibrium models constructed with the polytropic EOS, for $\Gamma = 2$ and polytropic constant $K_{\rm ID} = 100$. The solid, dashed and dotted lines correspond to the sequence of non-rotating models, the sequence of models rotating at the mass-shedding limit and the sequence of models that are at the onset of the secular instability to axisymmetric perturbations. Also shown are the secularly (open circles) and dynamically unstable (filled circles) initial models used in the collapse simulations.

0.75 and 0.65 (these models are indicated as S1–S4 in Fig. 5.1), respectively. Four additional models were defined by increasing the central energy density of the secularly unstable models by 5%, keeping the same axis ratio. These models (indicated as D1–D4 in Fig. 5.1) were expected and have been found to be dynamically unstable.

Fig. 5.1 shows the gravitational mass as a function of the central energy density for equilibrium models constructed with the chosen polytropic EOS. The solid, dashed and dotted lines correspond respectively to: the sequence of non-rotating models, the sequence of models rotating at the mass-shedding limit and the sequence of models that are at the onset of the secular instability to axisymmetric perturbations. Furthermore, the secularly and dynamically unstable initial models used in the collapse simulations are shown as open and filled circles, respectively.

Table 5.1 summarises the main equilibrium properties of the initial mod-

Table 5.1: Equilibrium properties of the initial stellar models. The different columns refer respectively to: the central rest-mass density ρ_c, the ratio of the polar to equatorial coordinate radii r_p/r_e, the gravitational mass M, the circumferential equatorial radius R_e, the angular velocity Ω, the ratio J/M^2 where J is the angular momentum, the ratio of rotational kinetic energy to gravitational binding energy $T/|W|$, and the "height" of the corotating ISCO $h_+ = R_+ - R_e$. All models have been computed with a polytropic EOS with $K_{\rm ID} = 100$ and $\Gamma = 2$.

Model	$\rho_c \times 10^{-3}$	r_p/r_e	M	R_e	$\Omega \times 10^{-2}$	J/M^2	$T/\|W\| \times 10^{-2}$	h_+
S1	3.154	0.95	1.666	7.82	1.69	0.207	1.16	1.18
S2	3.066	0.85	1.729	8.30	2.83	0.363	3.53	0.51
S3	3.013	0.75	1.798	8.90	3.49	0.470	5.82	0.04
S4	2.995	0.65	1.863	9.76	3.88	0.545	7.72	–
D1	3.280	0.95	1.665	7.74	1.73	0.206	1.16	1.26
D2	3.189	0.85	1.728	8.21	2.88	0.362	3.52	0.58
D3	3.134	0.75	1.797	8.80	3.55	0.468	5.79	0.10
D4	3.116	0.65	1.861	9.65	3.95	0.543	7.67	–

els. The circumferential equatorial radius is denoted as R_e, while Ω is the angular velocity with respect to an inertial observer at infinity, and r_p/r_e is the ratio of the polar to equatorial coordinate radii. The height of the corotating innermost stable circular orbit (ISCO) is defined as $h_+ = R_+ - R_e$, where R_+ is the circumferential radius for a corotating ISCO observer. Note that in those models for which a value of h_+ is not reported, all circular geodesic orbits outside the stellar surface are stable. Other quantities shown are the central rest-mass density ρ_c, the angular momentum J, and the ratio of rotational kinetic energy to gravitational binding energy $T/|W|$.

5.4 Dynamics of the matter

This Section discusses the dynamics of the matter during the collapse of the initial stellar models described in the preceding section. All of the simulations reported here have been computed using a uniformly spaced computational grid for which symmetry conditions are imposed across the equatorial plane. Different spatial resolutions have been used to check convergence and improve the accuracy of the results, with the finest resolution having been obtained using $288^2 \times 144$ cells. While the precise numbers depend on the resolution used and on the model simulated, as a general rule we have used $\sim 50\%$ of the cells in the x-direction to cover the star in the case D1 and $\sim 66\%$ of

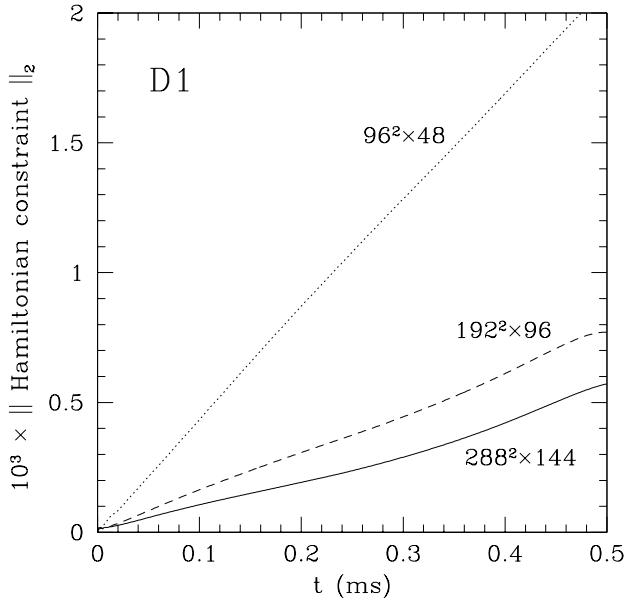

Figure 5.2: L_2 norm of the Hamiltonian constraint violation for the initial model D1 shown as a function of time. The different lines refer to different grid resolutions, but in all cases the IVP was solved after the pressure was uniformly decreased to trigger the collapse.

the cells in the x-direction to cover the star in D4. As a result, the outer boundary is set at ~ 2.0 times the stellar equatorial radius for D1 and at ~ 1.4 times the stellar equatorial radius for D4.

The hydrodynamics equations have been solved employing the Marquina flux formula and a third-order PPM reconstruction, which was shown in [223] to be superior to other methods in maintaining a highly-accurate angular-velocity profile (see also [251, 253] for recent 3D evolutions of rotating relativistic stars with a third-order order PPM reconstruction). The Einstein field equations, on the other hand, have been evolved using the ICN evolution scheme, the "1+log" slicing condition and the "Gamma-driver" shift conditions [153]. Finally, both polytropic and ideal-fluid EOSs have been used, although no significant difference has been found in the dynamics between the two cases. This is most probably related to the small J/M^2 of the uniformly rotating initial models considered here. This implies a relatively rapid collapse and as a result we do not see any shock formation (see below for a more complete discussion). Hereafter we will restrict our attention to a polytropic EOS only.

Given an initial stellar model which is dynamically unstable, round-off

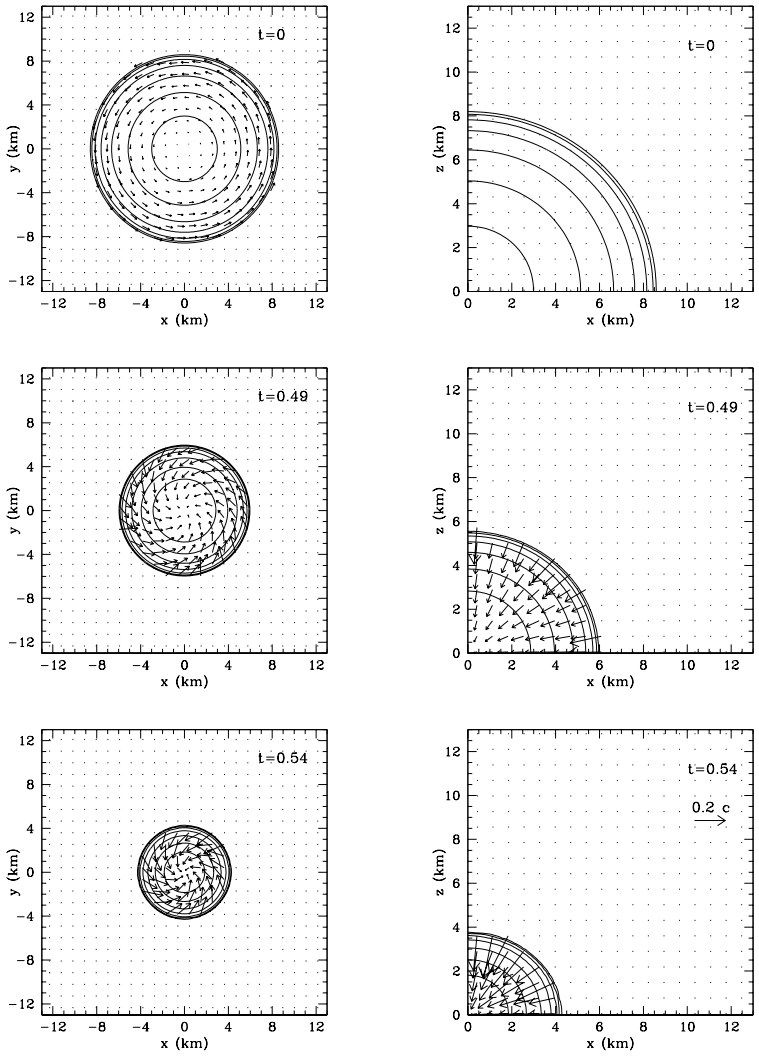

Figure 5.3: Collapse sequence for the slowly rotating model D1. Different panels refer to different snapshots during the collapse and show the isocontours of the rest-mass density and velocity field in the (x, y) plane (left column) and in the (x, z) plane (right column), respectively. The isobaric surfaces are logarithmically spaced and a reference length for the vector field is shown in the lower right panel for a velocity of 0.2 c. The time of the different snapshots appears in the top right corner of each panel and it is given in ms, while the units on both axes are expressed in km. See main text for a discussion and Fig. 5.5 for a comparison with the collapse of a rapidly rotating model.

errors would be sufficient to produce an evolution leading either to the gravitational collapse to a black hole or to the migration to the stable branch of the equilibrium configurations [128] (we recall that both evolutions are equally probable mathematically, although it is easier to imagine that it would collapse to a black hole). In general, however, leaving the onset of the dynamical instability to the cumulative effect of the numerical truncation error is not a good idea, since this gives an initial instability amplitude (and thus a time for the instability to grow to any fixed larger amplitude) which depends on the grid resolution used.

For this reason, we induce the collapse by slightly reducing the pressure in the initial configuration. This is done uniformly throughout the star by using a polytropic constant for the evolution K that is smaller than the one used to calculate the initial data $K_{\rm ID}$. The accuracy of the code is such that only very small perturbations are sufficient to produce the collapse and we have usually adopted $(K_{\rm ID} - K)/K_{\rm ID} \lesssim 2\%$.

After imposing the pressure reduction, the Hamiltonian and momentum constraints are solved to enforce that the constraint violation is at the truncation-error level. We refer to this procedure as to solving the initial value problem (IVP), which ensures that second order convergence holds from the start of the simulations, as shown in Fig. 5.2 for the L_2 norm of the Hamiltonian constraint. Strict second-order convergence is lost when the excision is introduced, although the code remains convergent at a lower rate while the norms of the Hamiltonian constraint start to grow exponentially (this is not shown in Fig. 5.2). We are presently investigating the origin of the deterioration of the convergence rate at the time of excision, although this is somewhat unavoidable when excising a spherical region in a Cartesian rectangular grid in the course of the evolution.

Details on how we solve the IVP implementing the York-Lichnerowicz conformal transverse-traceless decomposition can be found in [47]. If, on the other hand, the IVP is not solved after the pressure change, the constraints violation increases twice as fast and converges to second order only after an initial period of about 20 $M \sim 0.17$ ms. To assess the validity of our procedure to trigger the collapse, we also perform the pressure change after the evolution has started and without solving the IVP. In this case, after the system has recovered from the perturbation, the violation of the constraints is only a few percent different from the case in which the IVP is solved. Furthermore, other dynamical features of the collapse, such as the instant at which the apparent horizon is first formed (see Section 5.5 for a detailed discussion), do not vary by more than 1%.

The dynamics resulting from the collapse of models S1–S4 and D1–D4 are extremely similar and no qualitative differences have been detected. How-

ever, as one would expect, models D1–D4 collapse more rapidly to a black hole (the formation of the apparent horizon appears about 5% earlier in coordinate time), are computationally less expensive and therefore better suited for a detailed investigation. As a result, in what follows we will restrict our discussion to the collapse of the dynamically unstable models and distinguish the dynamics of case D1, in Section 5.4.1, from that of model D4, in Section 5.4.2.

5.4.1 Slowly rotating stellar models

We start by discussing the dynamics of the matter by looking at the evolution of the initial stellar model D1 which is slowly rotating (thus almost spherical, with $r_p/r_e = 0.95$) and has the largest central density (*cf.* Fig. 5.1 and Table 5.1).

We show in Figs. 5.3–5.4 some representative snapshots of the evolution of this initial model. The different panels of Fig. 5.3, in particular, refer to the initial and intermediate stages of the collapse and show the isocontours of the rest-mass density and velocity field in the (x, y) plane (left column) and in the (x, z) plane (right column), respectively. The isobaric surfaces are logarithmically spaced starting from $\rho = 2.0 \times 10^{-5}$ and going up to $\rho = 2.0 \times 10^{-3}$ at the stellar interior. The velocity vector field is expressed in units of c and the length for a velocity of $0.2\,c$ is shown in the lower-right panel. Panels on the same row refer to the same instant in time and this is indicated in ms in the top-right corner of each panel. The units on both axes are expressed in km and refer to coordinate lengths. This sequence has been obtained with a grid of $288^2 \times 144$ zones but the data for the velocity field have been down-sampled to produce clearer figures. The data have also been restricted to a single octant in the (x, z) plane to provide a magnified view. In all cases, however, the whole extent of the numerical grid is reported in the figures.

Overall, the sequence shown in Fig. 5.3 is simple to illustrate. During the collapse of model D1 spherical symmetry is almost preserved; as the star increases its compactness and the matter is compressed to larger pressures, the velocity field acquires a radial component (which was zero initially) that grows to relativistic values. This is clearly shown in the panels at $t = 0.49$ ms and $t = 0.54$ ms, which indicate that the star roughly preserves the ratio of its polar r_p and equatorial r_e radii (see also Fig. 5.7), while radial velocities in excess of $\sim 0.28\ c$ can be easily reached. The behaviour of the angular velocity during this collapse will be analysed in more detail in Section 5.4.3, but we can here anticipate that it does not show appreciable departures from a profile which is uniform inside the star.

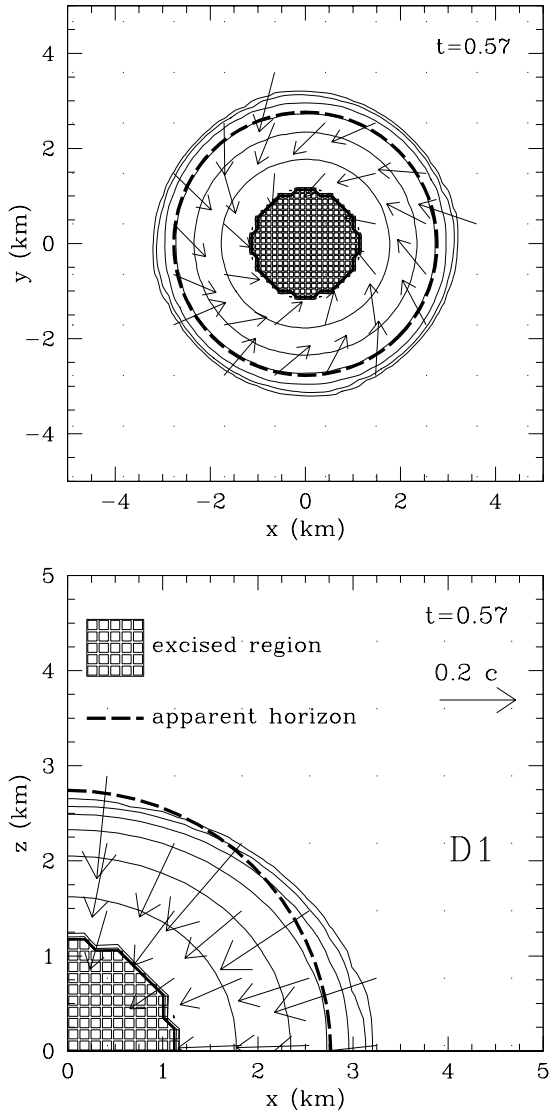

Figure 5.4: Magnified view of the final stages of the collapse of models D1. A region around the singularity that has formed is excised from the computational domain and is shown as an area filled with squares. Also shown with a thick dashed line is the coordinate location of the apparent horizon. Note that because of rotation this surface is not a two-sphere, although the departures are not significant and cannot be appreciated from the Figure (*cf.* Fig. 5.16 for a clearer view).

Soon after $t = 0.54$ ms, (*i.e.* at $t = 0.546$ ms $= 66.7\ M$ in the high-resolution run), an apparent horizon is found and when this has grown to a sufficiently large area, the portion of the computational domain containing the singularity is excised. A discussion of how the trapped surfaces are studied in practice will be presented in Section 5.5, while details on the hydrodynamical excision have been given in chapter 4. Here, we just remark that the use of an excised region and the removal of the singularity from the computational domain is essential for extending the calculations significantly past this point in time. Figure 5.4 shows a magnified view of the final stages of the collapse of model D1. Indicated as an area filled with squares is the excised region of the computational domain, which is an approximation of a sphere on the uniform Cartesian grid, *i.e.* a "Lego-sphere". Also shown with a thick dashed line is the coordinate location of the apparent horizon and it should be remarked that, because of rotation, this surface is not a coordinate two-sphere, although the departures are not significant and cannot be appreciated in Fig. 5.4 (see Section 5.5 and Table 5.2 for details). At $t = 0.57$ ms, the time which Fig. 5.4 refers to, most of the matter has already fallen within the apparent horizon and has assumed an oblate shape.

The numerical calculations were carried out up to $t \simeq 0.73$ ms $\sim 89.2\ M$, thus using an excised region in a dynamical spacetime for more than 26% of the total computing time. By this point, all of the stellar matter has collapsed well within the event horizon and the Hamiltonian constraint violation has become very large.

Overall, confirming what was already discussed by several authors in the past, the gravitational collapse of the slowly rotating stellar model D1 takes place in an almost spherical manner and we have found no evidence of shock formation which could prevent the prompt collapse to a black hole, nor appreciable deviations from axisymmetry (*cf.* left panel of Fig. 5.4). It is possible, although not likely, that these qualitative features may be altered when a realistic EOS is used, since in this case shocks may appear, whose heating could stall or prevent the prompt collapse to a black hole. However, as mentioned in section 5.1, more dramatic changes are expected to appear if the initial configurations are chosen to have larger initial angular momenta and in particular when $J/M^2 \gtrsim 1$ [126, 226]. A first anticipation of the important corrections that centrifugal effects could produce is presented in the following Section, where we examine the dynamics of a rapidly rotating stellar model.

5.4.2 Rapidly rotating stellar models

We next consider the dynamics of the matter during the collapse of model D4 which, being rapidly rotating, is already rather flattened initially (*i.e.*

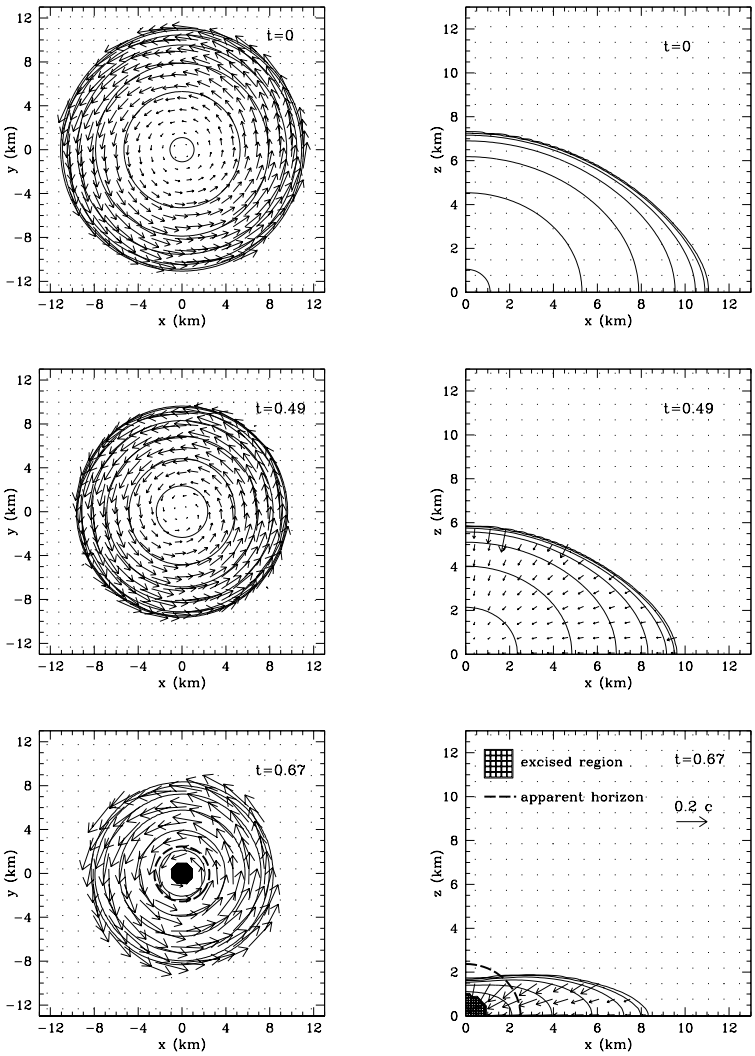

Figure 5.5: Collapse sequence for the rapidly rotating model D4. The conventions used in these panels are the same as in Fig. 5.3, which can be used for a comparison with the collapse of a slowly rotating model. Note that a region around the singularity that has formed is excised from the computational domain and is indicated as an area filled with squares. Also shown with a thick dashed line is the coordinate location of the apparent horizon.

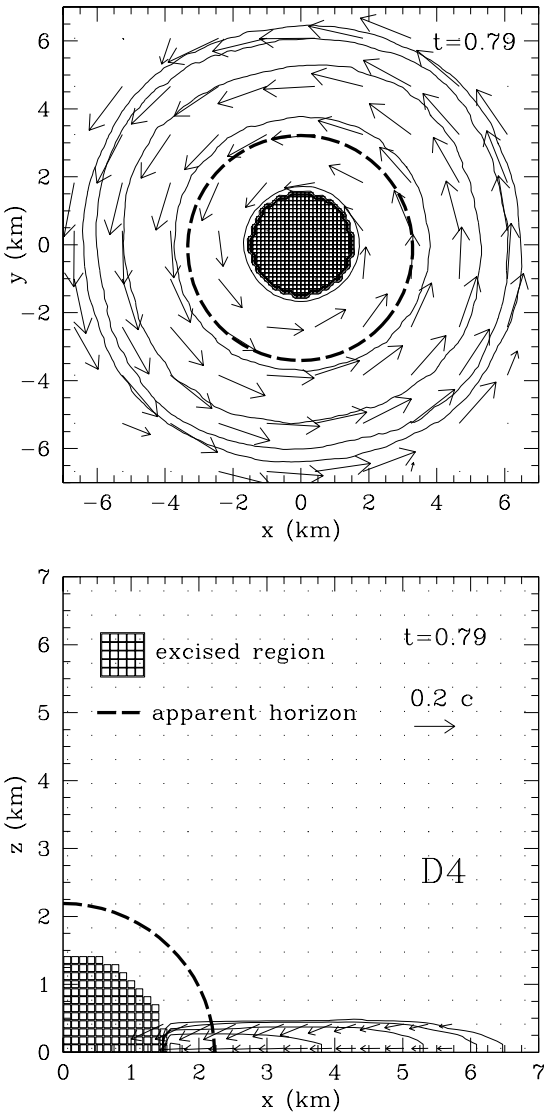

Figure 5.6: Magnified view of the final stages of the collapse of models D4. Note that a region around the singularity that has formed is excised from the computational domain and this is indicated as an area filled with squares. Also shown with a thick dashed line is the coordinate location of the apparent horizon. Note that because of the rapid rotation, this surface has significant departures from a two-sphere (*cf.* Fig. 5.16 for a clearer view).

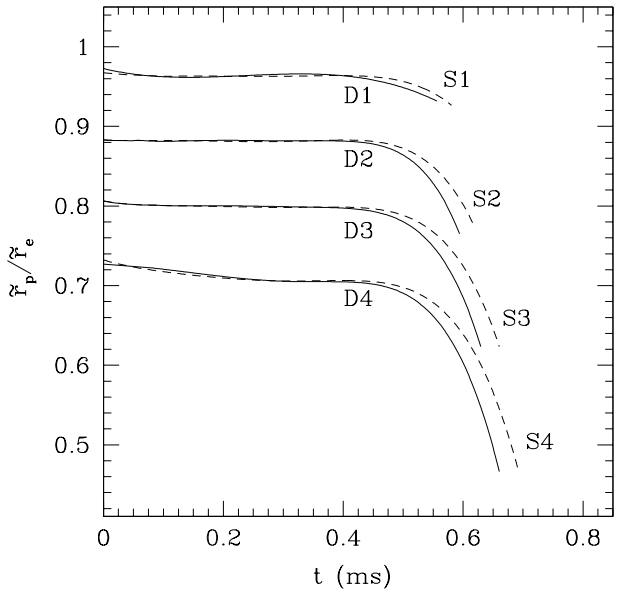

Figure 5.7: Ratio of the proper polar radius to the proper equatorial radius for all the initial models. Each curve ends at the time when, for each simulation, all the matter along the z-axis has fallen below the apparent horizon.

$r_p/r_e = 0.65$) and has the largest J/M^2 among the dynamically unstable models (*cf.* Fig. 5.1 and Table 5.1).

As for the slowly rotating star D1, we show in Figs. 5.5– 5.6 some representative snapshots of the evolution of this rapidly rotating model. The data have been computed using the same resolution of $288^2 \times 144$ zones and the isocontour levels shown for the rest-mass density are the same used in Fig. 5.3–5.4. It is apparent from the panels of Fig. 5.5 referring to $t = 0$, that model D4 is considerably more oblate than D1, as one would expect for a star rotating at almost the mass-shedding limit.

Also in this case, we believe that the sequence in Fig. 5.5 is simple to illustrate. Note, in particular, how the dynamics is very similar to the one discussed for model D1 up to a time $t \sim 0.49$ ms. However, as the collapse proceeds, significant differences between the two models start to emerge and in the case of model D4 the large angular velocity of the progenitor stellar model produces significant deviations from a spherical infall. Indeed, the parts of the star around the rotation axis that are experiencing smaller centrifugal forces collapse more promptly and, as a result, the configuration increases its oblateness.

This is illustrated in Fig. 5.7, which shows the time evolution of the ratio

of the polar and equatorial proper radii for all models in Table 5.1 (note that these ratios should not be confused with those in Table 5.1 that refer, instead, to coordinate radii). Each curve in Fig. 5.7 extends until all of the matter along the z-axis has fallen inside the apparent horizon of the newly formed black hole. Clearly, in all cases the oblateness increases as the collapse proceeds and this is much more evident for those stellar models that are rapidly rotating initially. In particular, for the most rapidly rotating models D4 and S4, the ratio between polar and equatorial proper radii becomes as small as 0.45 at the time when the matter on the rotation axis is below the apparent horizon.

At about $t = 0.64$ ms (*i.e.* at $t = 0.649$ ms $= 70.8\ M$ in the high-resolution run), the collapse of model D4 produces an apparent horizon. Soon after this, the central regions of the computational domain are excised, preventing the code from crashing and thus allowing for an extended time evolution. The dynamics of the matter at this stage is shown in the lower panels of Fig. 5.5, which refer to $t = 0.67$ ms and where both the location of the apparent horizon (thick dashed line) and of the effective excised region (area filled with squares) are shown. By this time the star has flattened considerably, all of the matter near the rotation axis has fallen inside the apparent horizon, but a disc of low-density matter remains near the equatorial plane, orbiting at very high velocities $\gtrsim 0.2\ c$. The appearance of an effective barrier preventing a purely radial infall of matter far from the rotational axis may be the consequence of the larger initial angular momentum of the this collapsing matter and of the pressure wave originating from the faster collapse along the rotational axis. Note, in fact, that the radial velocity at the equator does not increase significantly at the stellar surface between $t \simeq 0.49$ and $t \simeq 0.67$ ms, but that it actually slightly decreases (*cf.* the (x, z) planes in the mid and lower panels of Fig. 5.5). This is the opposite of what happens for the radial velocity of the fluid elements in the stellar interior on the equatorial plane: it grows also in this time interval. A more detailed discussion of this behaviour will be made in Section 5.5.4.

Note that the disc formed outside the apparent horizon is *not* dynamically stable and, in fact, it rapidly accretes onto the newly formed black hole. This is shown in Fig. 5.6, which offers a magnified view at a later time $t = 0.79$ ms. At this stage the disc is considerably flattened but also has large radial inward velocities which induce it to be accreted rapidly onto the black hole. Note that as the area of the apparent horizon increases, so does the excised region, which is allowed to grow accordingly. This can be appreciated by comparing the areas filled with squares in the lower panels of Fig. 5.5 (referring to $t = 0.67$ ms) with the corresponding ones in Fig. 5.6 (referring to $t = 0.79$ ms).

By a time $t = 0.85$ ms, essentially all (*i.e.* more than 99.9%) of the residual stellar matter has fallen within the trapped surface of the apparent horizon and the black hole thus formed approaches the Kerr solution (see Section 5.5). Note that a simple kinematic explanation can be given for the instability of the disc formed during this oblate collapse and comes from relating the position of the outer edge of the disc when this first forms, with the location of the ISCO of the newly formed Kerr black hole. Measuring accurately the mass and spin of the black hole reveals, in fact, that the ISCO is located at $x = 11.08$ km, which is always larger than the outer edge of the disc (*cf.* lower panels of Fig. 5.5). Such behaviour is not surprising since we are here dealing with initial models with a moderate J/M^2, that collapse essentially on a dynamical timescale, and for which pressure gradients cannot play an important role. As a result, simple point-like particle motion in stationary spacetimes is a sufficient approximation to the dynamics.

Also for model D4, a more detailed discussion (*e.g.* of the evolution of the distribution of angular velocity, or of the disc rest-mass) will be presented in Section 5.4.3. Here, however, we can anticipate that when analysed more closely the rest-mass in the disc and outside the apparent horizon is effectively very small and that the angular velocity shows appreciable departures from a uniform profile.

A more quantitative description of the rest-mass density evolution is presented in Fig. 5.8, where different lines show the profiles of the rest-mass density along the x-axis on the equatorial plane. The values are normalised to the initial value at the stellar centre, with different labels referring to different times and in particular to $t = 0.0$ (dashed line), 0.25, 0.40, 0.49, 0.54, 0.65, 0.67, 0.74, 0.79 and 0.89 ms, respectively. Line 5, furthermore, is shown as dotted and refers to the time when the apparent horizon is first formed. After this time, the excised region is cut from the computational domain as shown in the inset of Fig. 5.8, which illustrates the final stages of the evolution. Note that as the matter falls into the black hole, the apparent horizon increases its radius and thus the location of the excised region moves outside. This is clearly shown in the inset. Note also that the rest-mass density does not drop to zero outside the stellar matter but is levelled off to the uniform value of the atmosphere, whose rest-mass density is seven orders of magnitude smaller than the initial central density.

It should be remarked that such a tenuous atmosphere has no dynamical impact and does not produce any increase of the mass of the black hole that can be appreciated in our simulations. With such rest-mass densities, in fact, it would take a time $\sim 10^4 M$ to produce a net increase of $\sim 1\%$ in the black-hole mass. Clearly, these systematic errors are well below the truncation errors, even at the highest resolutions.

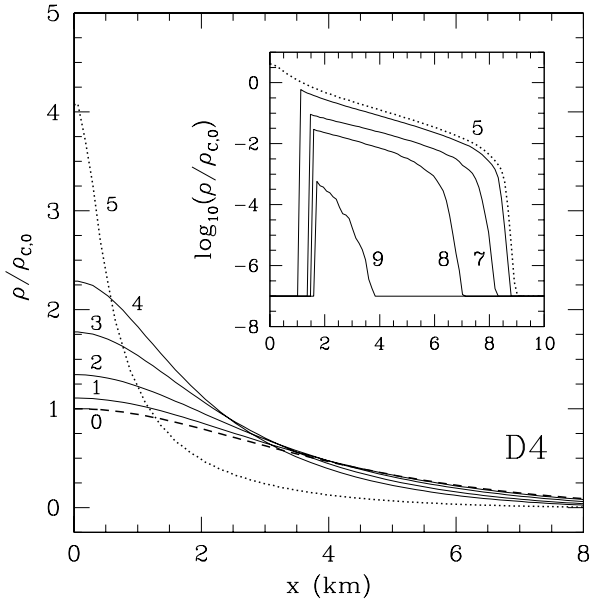

Figure 5.8: Rest-mass density of model D4 normalised to the initial value at the stellar centre. The profiles are measured along the x-axis on the equatorial plane and refer to different times (see main text for details). Line 5, shown as dotted, corresponds to the time when the apparent horizon is first found. The inset shows a magnified view of the final stages of the evolution using a logarithmic scale and also the location of the excised region as it grows in time.

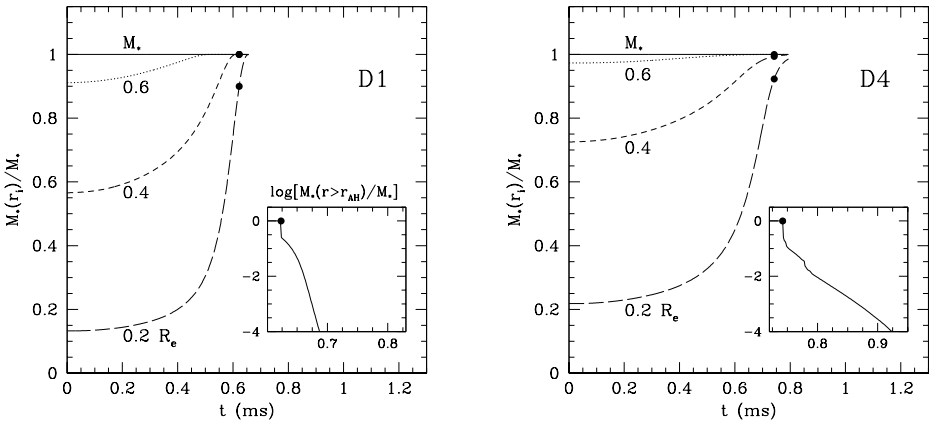

Figure 5.9: Evolution of the mass fraction versus time during the collapse of D1 (left panel) and D4 (right panel). The rest-mass is measured within two-spheres of coordinate radii $r_i = 0.2, 0.4$ and 0.6 times the initial stellar equatorial circumferential radius R_e (*cf.* Table 5.1). Marked with filled dots on the different lines are the times at which the apparent horizon is first found (the data refer to a simulation with $96^2 \times 48$ grid-zones). The insets in both panels show, on a logarithmic scale, the evolution of the normalised rest-mass outside the apparent horizon. Note that this is appreciably non-zero for a rather long time in case of model D4.

The simulation ends at $t = 0.91$ ms $\sim 93.6\,M$, when the rest-mass density is everywhere at the atmosphere level and the violations of the Hamiltonian constraint are large. By this time the evolution has been carried for more than 28% of the total time using a singularity excising region. Also in this case, we do not find evidence of shock formation nor of significant deviations from axisymmetry.

As mentioned in the Introduction, all simulations to-date agree that no massive and stable discs form for initial models of neutron stars that are uniformly rotating and when a polytropic EOS with $1 \leq N \leq 2$ is used. Our results corroborate this view and in turn imply that the collapse of a rapidly rotating old and cold neutron star cannot lead to the formation of the central engine believed to operate in a gamma-ray burst, namely a rotating black hole surrounded by a centrifugally-supported, self-gravitating torus. Relativistic simulations with more appropriate initial data, accounting in particular for the extended envelope of the massive progenitor star which is essential in the so called collapsar model of gamma-ray bursts [254], will be necessary to shed light on the mechanism responsible for such events.

Convincing evidence has recently emerged [226] that a massive disc can be produced if the stellar models are initially rotating differentially and with initial total angular momenta $J/M^2 \gtrsim 1$, as it may happen for young and hot neutron stars. In this case, the massive disc could emit intense gravitational radiation either through its oscillations [255] or as a result of the fragmentation produced by non-axisymmetric instabilities [226].

5.4.3 Disc formation and differential rotation

We now discuss in more detail two interesting properties of the matter dynamics in both slowly and rapidly rotating models: the evolution of the rest-mass outside the apparent horizon and the development of differential rotation during the collapse.

In order to monitor the changes of the rest-mass distribution during the collapse we define the rest-mass within a two-sphere of coordinate radius $r_i < R_e$ as (see, for instance, [256])

$$M_*(r_i) = \int_{r' < r_i} \rho \alpha u^0 \sqrt{\gamma}\, \mathrm{d}^3\mathbf{x}' \,, \tag{5.1}$$

where $\mathrm{d}^3\mathbf{x}'$ is the 3D coordinate volume element. Shown in Fig. 5.9 is the evolution of the rest-masses measured within several representative two-spheres for models D1 (left panel) and D4 (right panel), respectively. Different lines refer to different coordinate radii for the two-spheres (*i.e.* $r_i = 0.2, 0.4$ and

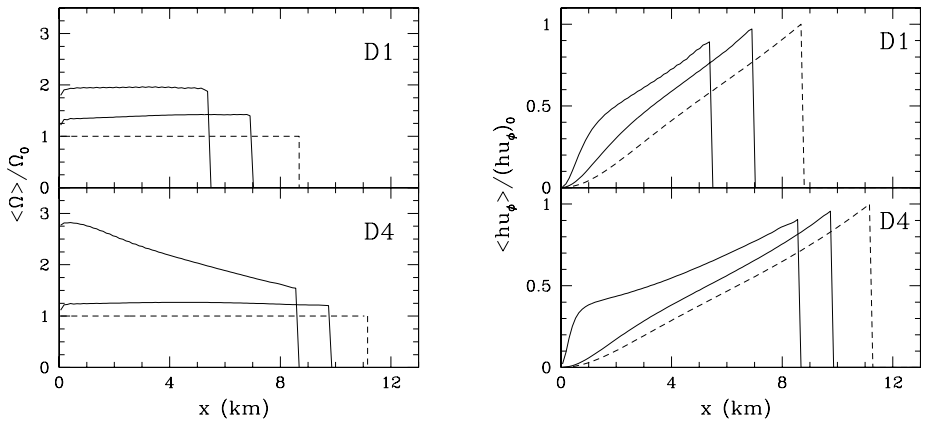

Figure 5.10: Evolution of the averaged angular velocity $\langle\Omega\rangle$ (left panel) and of the averaged angular momentum per unit mass $\langle hu_\phi\rangle$ (right panel). Both quantities are measured at the stellar equator, are normalised to the initial value at the stellar surface and refer to both models D1 (upper parts) and D4 (lower parts).

0.6 R_e, where R_e is the initial equatorial circumferential radius) and are normalised to the total rest-mass within the computational domain M_*, shown as a solid line. Marked instead with filled dots are the values of $M_*(r_i)$ at the times when the apparent horizon is first found; for simplicity, the data shown in Fig. 5.9 refer to a simulation with $96^2 \times 48$ grid-zones, but for this quantities higher resolutions have just the effect of shifting the time at which the apparent horizon is first found.

As mentioned before, the excised region is not introduced immediately after the apparent horizon has been found, but only when this has grown to a sufficiently large size. When this happens, the inner part of the computational domain is removed and the integrals (5.1) are no longer meaningful. As a result, all of the curves in Fig. 5.9 are truncated at the time when the excision region is first introduced, which occurs at $t = 0.72$ ms and $t = 0.79$ ms for models D1 and D4, respectively.

A rapid comparison between the two panels of Fig. 5.9 is sufficient to identify the differences in the rest-mass evolution in slowly and rapidly rotating models. Firstly, the rest-mass distribution is very different already initially, being more uniform in D1 and more centrally concentrated in D4, as can be appreciated by comparing M_* at $r_i = 0.4R_e$ and $0.6R_e$. Secondly, the rest-mass infall is much faster for the slowly rotating model D1, while it is more progressive for model D4, as shown by the change in the fractional

mass ratio at $r_i = 0.4R_e$. Finally, the amount of matter outside $r_i = 0.4R_e$ at the time when the apparent horizon is found, and which is very close to the amount of matter outside the apparent horizon, is different in the two cases, being essentially zero for model D1 and a few percent for model D4. A clearer view of this is presented in the two insets of Fig. 5.9 which show, on a logarithmic scale, the evolution of the normalised rest-masses outside the apparent horizons, *i.e.* $M_*(r > r_{\rm AH})/M_*$, since these first form and as they grow in time. It is interesting to note the different behaviour in this case with a rapid decrease when the rotation rate is small and a much slower one in the case of a rapidly rotating progenitor (Note that the two insets cover the same timescale although they refer to a different time interval.).

Two additional comments are worth making. The first one is that M_* effectively includes also the rest-mass in the atmosphere but this is always $\lesssim 10^{-4}$ of the total rest-mass. The second one is that M_* in Fig. 5.9 does not simply refer to the initial value of the total rest-mass but is effectively computed at each step and appears constant in time because of the ability of the code to preserve rest-mass. A closer look at the solid curve in Fig. 5.9 reveals, in fact, that M_* varies over time to less than one part in 10^4.

An interesting question to ask at this stage is whether these uniformly rotating models will develop any degree of differential rotation as the collapse proceeds. Part of the interest in this comes from the fact that neutron stars are thought to rotate differentially, at least during the initial stages of their life. This is expected to hold both when the neutron star is produced through a stellar core collapse, in which case the differential rotation may be present already in the stellar progenitor and is then amplified during collapse [88], and when the neutron star is the end-result of a binary merger of neutron stars [89]. However, as the neutron star cools and grows older, dissipative viscous effects or the coupling with non-turbulent magnetic fields are expected to bring the star into uniform rotation (see [90–92] for a detailed description of this process). It is therefore interesting to investigate whether a degree of differential rotation will be produced also during the final collapse of a uniformly rotating star to a Kerr black hole. To answer this question we have monitored both the averaged angular velocity $\langle\Omega\rangle$, defined as

$$\langle\Omega\rangle \equiv \frac{1}{2}\left(\left.\frac{u^\phi}{u^t}\right|_{x-\rm axis} + \left.\frac{u^\phi}{u^t}\right|_{y-\rm axis} \right) \,, \tag{5.2}$$

and the corresponding averaged angular momentum per unit mass $\langle hu_\phi\rangle$, which is a conserved quantity along the path lines of fluid elements in an axisymmetric (but not necessarily stationary) spacetime [257]. Note that $u^\phi/u^t = \alpha v^\phi - \beta^\phi$ and the average over the two different directions is here

used to compensate the small errors that are produced in the evaluation of these quantities near the axes.

We note that our measure of the differential rotation will depend on the specific slicing chosen. However, for the simulations reported here, the length-scale of variation of the lapse function at any given time is always larger than the stellar radius at that time, ensuring that the events on the same time slice are also close in proper time. A useful measure of the differential rotation that develops during collapse is the departure from unity of the ratio of the values of Ω at the centre and at the surface of the star on the equatorial plane and it is instructive to compare how this varies in the dynamics of the two models D1 and D4, which have been evolved using the same slicing.

The time evolution of $\langle\Omega\rangle$ and $\langle hu_\phi\rangle$ is presented in the two panels Fig. 5.10, whose lower parts refer to model D4 while the upper ones refer to model D1. Both quantities are shown normalised to their initial value at the stellar surface. Let us concentrate on the slowly rotating model first. The different lines refer to three representative times which are $t = 0.0$ (shown as dashed), $t = 0.45$ and 0.52 ms, respectively. Initially, the angular velocity is, by construction, uniform throughout the star (left panel) and the corresponding specific angular momentum grows linearly with the distance from the stellar centre (right panel). As the collapse proceeds and the stellar size decreases, the angular velocity is expected to increase while the angular momentum per unit mass remains constant. This is indeed what happens for model D1, whose specific angular momentum is conserved with an overall error at the stellar surface which is always less than 10% and which decreases with resolution. A similar behaviour is observed also much later in the simulation, when the apparent horizon has been found and the singularity has been excised. Overall, the angular velocity in the collapsing model D1 grows like $\Omega(t) \propto r_e^{-n}$, where $n \simeq 1.5$ and therefore less than it would do in the case of the collapse of a Newtonian, uniform density star (*i.e.* $n = 2$); which is a result of relativistic and rotational effects (see [258]).

A comparison of the lower parts of the two panels in Fig. 5.10 is sufficient to realize that the evolution of the angular velocity is rather different for a rapidly rotating stellar model. The different lines in this case refer to $t = 0.0, 0.48$ and 0.65 ms, respectively, and it is apparent that a non-negligible degree of differential rotation develops as the collapse proceeds, with a difference of a factor ~ 2 between the angular velocity of the inner and outer parts of the collapsing matter as the apparent horizon first appears. Clearly, this differential rotation is produced very rapidly and will persist only for a very short time before the star is enclosed in a trapped surface.

It is difficult to establish, at this stage, whether the differential rotation

generated in this way could produce a phenomenology observable in some astrophysical context and more detailed investigations, in particular of the coupling of this differential rotation with magnetic fields [259, 260], are necessary. Finally, it is worth remarking that while differential rotation develops for model D4 but not for D1, the specific angular momentum is conserved to the same accuracy in both models.

5.5 Dynamics of the horizons

In order to investigate the formation of a black hole in our simulations, we have used horizon finders, available through the `Cactus` framework, which compute both the *apparent* horizon and the *event* horizon. The apparent horizon, which is defined as the outermost closed surface on which all outgoing photons normal to the surface have zero expansion, is calculated at every time step and its location is used to set up the excised region inside the horizon. Specific technical details about the handling of the excised region for the fields are presented in [133, 153], while a brief discussion of how the hydrodynamical excision is performed in `Whisky` was presented in chapter 4.

In contrast, the event horizon, which is an expanding null surface composed of photons which will eventually find themselves trapped, is computed *a posteriori*, once the simulation is finished, by reconstructing the full spacetime from the 3D data each simulation produces. In stationary black-hole systems, where no mass-energy falls into the black hole, the apparent and event horizons coincide, but generally (in dynamical spacetimes) the apparent horizon lies inside the event horizon. We have here used the fast solver of Thornburg [228] to locate the apparent horizon at every time step, and the level-set finder of Diener [229] to locate the event horizon after the simulation has been completed and the data produced are post-processed.

In all cases considered, we have found that the event horizon rapidly grows to its asymptotic value after formation. With a temporal gap of $\sim 10M$ after the formation of the event horizon, the apparent horizon is found and then it rapidly approaches the event horizon, always remaining within it. With the exception of the initial gap, the horizon proper areas as extracted from the apparent and event horizon are very close (see *e.g.* Fig. 5.16).

5.5.1 Measuring the Event-Horizon Mass

We measure the mass of the newly formed black hole to estimate the amount of energy that is emitted as gravitational radiation during the collapse. In particular, we do a simple energy accounting, comparing the mass of the black

hole with the ADM mass of the spacetime computed by the initial data solver on a compactified grid extending to spatial infinity [250]. This value is slightly different (1% in the worst case) from the one which is instead computed on the finite domain of our computational grid at the initial time and after the constraints are solved. The difference between the two values can be used to define an "error-bar" for our measure of the black-hole mass and hence of the energy in gravitational waves (*cf.* Fig. 5.15). Two notes are worth making about this error before we go on to discuss how the black-hole mass is actually measured. Firstly, the difference between the two masses represents the truncation error produced by the finite size of the computational domain and is conceptually distinct from the truncation error introduced by the finite differencing. While the first is assumed to be constant in time, the second in general grows with time (especially after the excision is made) and is monitored through the calculation of the constraint equations. Secondly, this error-bar sets a global lower limit on the accuracy of our measure of asymptotic quantities and therefore on the energy lost to gravitational waves during the collapse. No reliable measure of this lost energy can be made below the error-bar even if the constraint equations are solved to a larger precision (this will be discussed in more detail in Section 5.5.3).

The first and simplest method of approximating the black-hole mass is to note that, for a Kerr (or Schwarzschild) black hole, the mass can be found directly in terms of the event-horizon geometry as

$$M = \frac{C_{\rm eq}}{4\pi} \,, \tag{5.3}$$

where $C_{\rm eq} \equiv \int_0^{2\pi} \sqrt{g_{\phi\phi}} d\phi$ is the proper equatorial circumference. Provided there is a natural choice of equatorial plane, it is expected that, as the black hole settles down to Kerr, $C_{\rm eq}$ will tend to the correct value. However, as numerical errors build up at late times it may be impossible to reach this asymptotic regime with sufficient accuracy.

The estimate of M coming from the use of (5.3) is presented in Fig. 5.11, which shows the time evolution of the event-horizon equatorial circumference. The two lines refer to two different resolutions ($288^2\times144$ and $192^2\times96$ zones, respectively) and should be compared with the value of the ADM mass $M_{\rm ADM}$ (indicated with a short-long dashed line), and with the error-bars as deduced from the initial data. Shown in the small inset are the results for model D1, while those for model D4 are in the main panel.

Note that if a measure of the event horizon is not available, equation (5.3) could be computed using the equatorial circumference of the apparent horizon (this is what was done, for instance, in [226]). Doing so would yield results that are similar to those shown in Fig. 5.11, although with a slightly larger

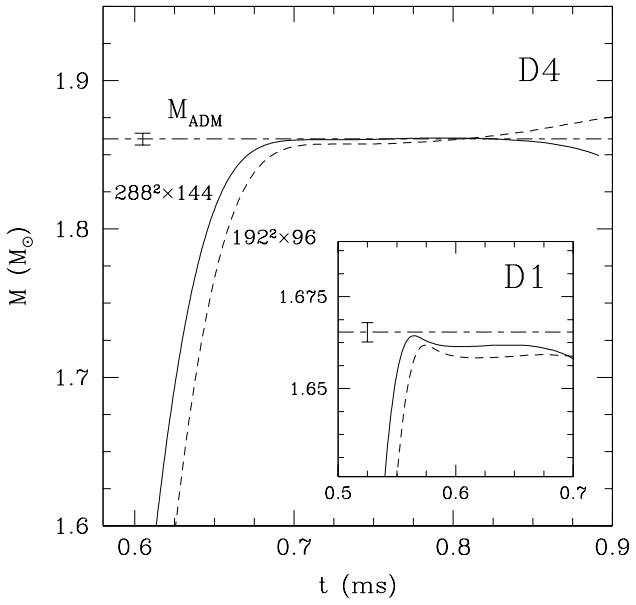

Figure 5.11: Convergence of the measure of the black-hole mass as the resolution is increased. The curves refer to estimates using the event-horizon equatorial circumference [*i.e.* equation (5.3)] and have been obtained using $288^2 \times 144$ and $192^2 \times 96$ zones, respectively. Shown in the small inset are the results for model D1, while those for model D4 are in the main panel.

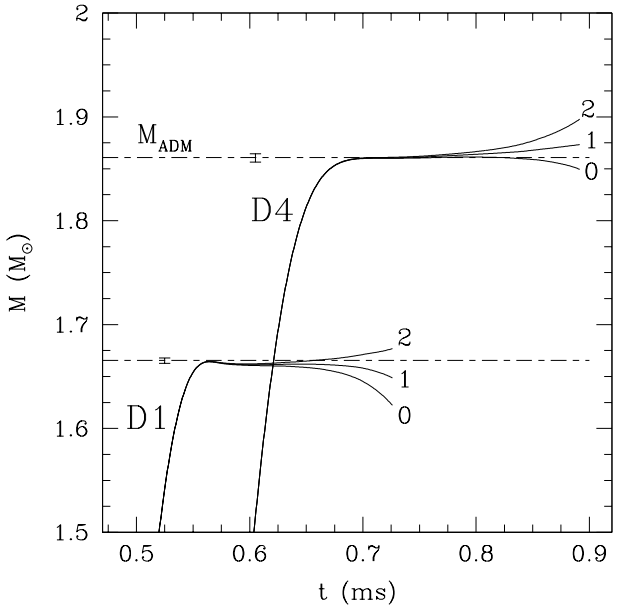

Figure 5.12: Evolution of the event-horizon mass $M = C_{eq}/4\pi$ for models D1 and D4. Different lines refer to the different initial guesses for the null surface and are numbered 0, 1 and 2. Note that they converge exponentially to the correct event-horizon surface for decreasing times.

deviation from $M_{\rm ADM}$. This is because we have found the apparent horizon to systematically underestimate the equatorial circumference. In particular, in the high-resolution run for model D4, the differences between the apparent and event-horizon equatorial circumferences are $\lesssim 2$ %.

Clearly, as the equatorial circumference grows, the agreement with the expected ADM mass improves as it does with the use of higher spatial resolution. However, equally evident is that the errors grow as the collapse proceeds and this is due, in part, to the loss of strict second-order convergence at later times, but also to the way the event horizon is found. The level-set approach of [229], in fact, needs initial guesses for the null surface, which converge exponentially to the correct event-horizon surface for decreasing times, hence introduces a systematic error in the calculation of the event horizon at late times. This is shown in Fig. 5.12, which presents the evolution of the event-horizon mass $M = C_{eq}/4\pi$ for models D1 and D4. Different lines refer to the different initial guesses and are numbered "0", "1" and "2", respectively (note that for the curves shown in Fig. 5.11 the initial guesses "0" and "1" were used for cases D4 and D1, respectively).

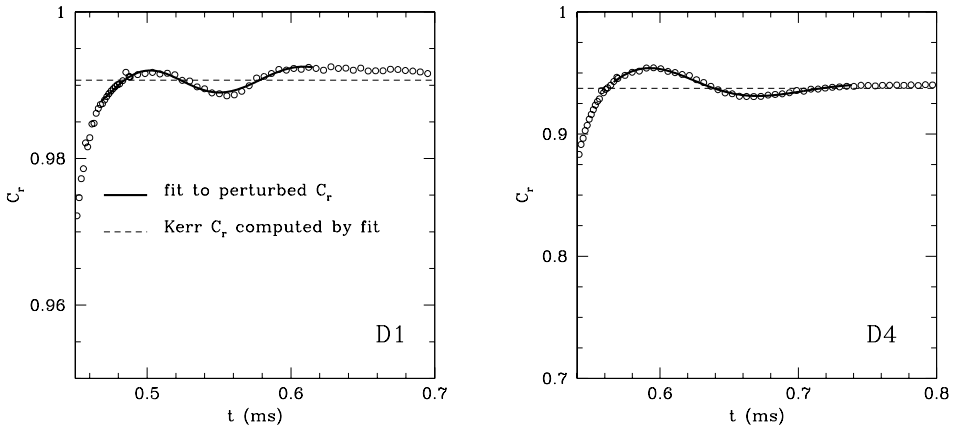

Figure 5.13: Fitting the oblateness of the event horizon to QNMs of a Kerr black hole. The fit is shown with the solid line, while the open circles represent the computed values of C_r. The estimate for C_r of a Kerr black hole having the fitted value of a/M_{hor} is shown with a dashed line.

5.5.2 Measuring the angular momentum of the black hole

A major difficulty in an accurate measurement of M lies in the calculation of its non-irreducible part, *i.e.* in the part that is proportional to the black-hole angular momentum J. We now discuss a number of different ways to calculate J from the present simulations; these measurements will then be used to obtain alternative estimates of M in Section 5.5.3.

Measuring J from the Horizon Distortion

In a series of papers studying the dynamics of distorted black-hole spacetimes, it was shown that the horizon geometry provides a useful measure of the black-hole properties both in vacuum [261–264] and when these are accreting matter axisymmetrically [225]. In particular, the idea is to look at the distortion of the horizon using the ratio of polar and equatorial proper circumferences, $C_r \equiv C_{\rm pol}/C_{\rm eq}$. For a perturbed Kerr black hole this is expected to oscillate around the asymptotic Kerr value with the form of a quasi-normal mode (QNM). By fitting to this mode we extract an estimate of the angular momentum parameter a/M_{hor} from the relation [265]

$$\frac{a}{M_{hor}} = \sqrt{1-(-1.55+2.55C_r)^2}\,, \tag{5.4}$$

where we have indicated with M_{hor} the black-hole mass as measured from expression (5.4), which coincides with M only if the spacetime has become axisymmetric and stationary. The fit through expression (5.4) is expected to be accurate to $\sim 2.5\%$ [265].

The fit itself depends on an initial guess for a/M_{hor} and we start from a Schwarzschild black hole and iterate till the desired convergence is reached. This measure is not gauge invariant, although equation (5.4) is independent of the spatial coordinates up to the definition of the circumferential planes, but works adequately with the gauges used here. The fit is best performed shortly after black-hole formation as the oscillations are rapidly damped. This minimises numerical errors but in those cases where matter continues to be accreted, it may lead to inaccurate estimates of the angular momentum.

Examples of the fitting procedure are shown in Fig. 5.13, in which the fit is shown as a solid line, while the open circles represent the computed values of C_r; these are slightly noisy as a result of the interpolation needed by the level-set approach to find points on the horizon two-surface [229]. The estimate for C_r of a Kerr black hole having the fitted value of a/M_{hor} is shown as a dashed line. Note that the values of $a/M_{hor} = 0.21$ and $a/M_{hor} = 0.54$ are very close to the total J/M^2 of the initial stellar models, *i.e.* 0.2064 and 0.5433, as shown in Table 5.2. This demonstrates that, to within numerical accuracy, the entire angular momentum of the spacetime ends up in the black hole.

Table 5.2: Estimates of the black-hole angular momentum J/M^2 through the oblateness of the event horizon. The oscillations in the oblateness of the event horizon can be fitted to the normal modes of a Kerr black hole. Note that for each model the measured angular momentum is remarkably close to that of the initial spacetime $(J/M^2)_{\rm ADM}$. Also reported are the initial ADM mass, the value of the equatorial circumference as obtained through the fit $(C_r)_{\rm EH}$, and the corresponding value obtained through the estimated spin parameter $(C_r)_{\rm Kerr}$.

Model	$M_{\rm ADM}$	$(J/M)^2_{\rm ADM}$	$(J/M^2)_{\rm EH}$	$(C_r)_{\rm EH}$	$(C_r)_{\rm Kerr}$
D1	1.6653	0.2064	0.21	0.99	0.9916
D2	1.7281	0.3625	0.36	0.97	0.9734
D3	1.7966	0.4685	0.47	0.95	0.9544
D4	1.8606	0.5433	0.54	0.94	0.9372

Using expression (5.4) to estimate the angular momentum J introduces an error, if the black hole has not yet settled to a Kerr solution. Having this

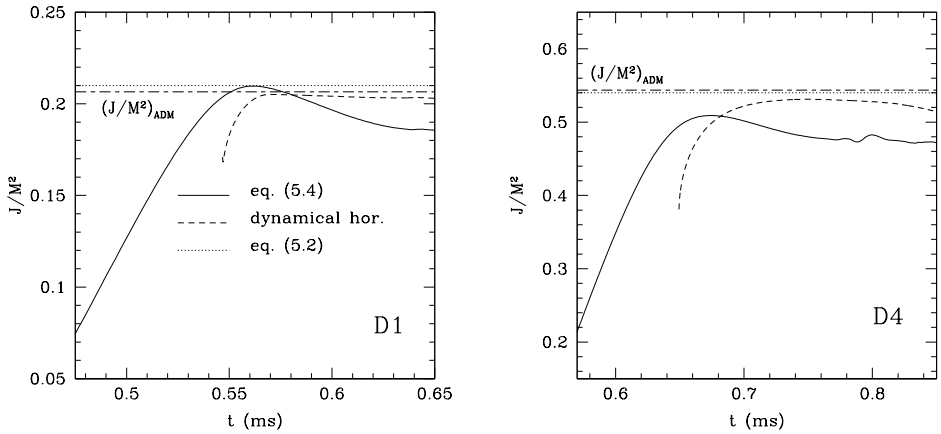

Figure 5.14: Comparison of the different measures of the angular momentum for the cases D1 (left panel) and D4 (right panel). The estimate using the fit to the circumference ratio (see left panel of Fig. 5.13) is also shown. The dynamical horizon spin measurement is considerably more accurate at late times as the event-horizon surfaces will diverge exponentially at this point. Shown with the horizontal short-long dashed lines are the values of $(J/M^2)_{\rm ADM}$ in the two cases as measured from the initial data (see main text for details).

in mind, however, it is possible to estimate the angular momentum as

$$J = \left(\frac{a}{M_{hor}}\right) M_{hor} M \simeq \left(\frac{a}{M_{hor}}\right) M^2 \ . \tag{5.5}$$

Measuring J with the dynamical-horizon framework

A second method of approximating J and hence measuring M is to use the *isolated* and *dynamical* horizon frameworks of Ashtekar and collaborators [266–270]. This assumes the existence of an axisymmetric Killing vector field intrinsic to a marginally trapped surface such as an apparent horizon. This gives an unambiguous definition of the spin of the black hole and hence of its total mass. If there is an energy flux across the horizon, the isolated horizon framework needs to be extended to the *dynamical* horizon formalism [269, 271].

In practice, our approach to the dynamical horizon framework has been through the use of a code by Schnetter which implements the algorithm of [270] to calculate the horizon quantities. The advantage of the dynamical horizon framework is that it gives a measure of mass and angular momentum which is accurately computed locally, without a global reconstruction of the spacetime. One possible disadvantage is that the horizon itself is required to be (close to) axisymmetric; so in case it deviates largely from axial symmetry, no information can be found. However, because arbitrarily large distortions are allowed as long as they are axisymmetric, we have not encountered problems in applying the dynamical horizon framework to the horizons found in our simulations.

Measuring J from the Angular Velocity of the Event Horizon

A third method for computing J only applies if an event horizon is found and if its angular velocity has been measured. In a Kerr background, in fact, the generators of the event horizon rotate with a constant angular velocity $\omega \equiv -g_{t\phi}/g_{\phi\phi} = \sqrt{g_{tt}/g_{\phi\phi}}$. In this case the generator velocity can be directly related to the angular momentum parameter as

$$\frac{a}{M} = \frac{J}{M^2} = \left[\frac{A\omega^2}{\pi}\left(1 - \frac{A\omega^2}{4\pi}\right)\right]^{1/2} \ . \tag{5.6}$$

As with the previous approximations, expression (5.6) is strictly valid only for a Kerr black hole and will therefore contain a systematic error which, however, decays rapidly as the black-hole perturbations are damped. On the other hand, the event horizon generator velocities have the considerable advantage that everything is measured instantaneously and the values of ω are

valid whether or not the background is an isolated Kerr black hole. The disadvantage, though, is that, as mentioned above, the numerical event horizon surfaces become systematically less accurate at late times (*cf.* Fig. 5.12).

Comparison of angular momentum measurements

A detailed comparison of the three different methods for measuring the angular momentum of the black hole is shown in Fig. 5.14. The measurement of angular momentum using the angular velocity of the generators is shown as solid lines. Both for slowly (left panel) and rapidly (right panel) rotating stellar models, the event horizon has zero area (and thus zero angular momentum) when it is first formed. However, as the rotating matter collapses, the event horizon area and angular momentum grow, the black hole is spun up and, to numerical accuracy, the total angular momentum of the spacetime is contained within the black hole (*cf.* Fig. 5.13). At late times, the estimate using the generator velocities of the event horizon drifts away, probably due to a combination of gauge effects and the systematic errors in the trial guesses for the null surfaces.

In the case of the slowly rotating model D1, in particular, the estimate from the dynamical horizon finder is perfectly stable (*cf.* dashed line in the left panel of Fig. 5.14), indicating that an approximately stationary Kerr black hole has been formed by the time the simulation is terminated. In the case of the rapidly rotating model D4, however, this is no longer the case as matter continues to be accreted also at later times, when the errors have also increased considerably. As a result, the measure of the spin through the dynamical horizon finder is less accurate and does not seem to have stabilised by the time the simulation ends (*cf.* dashed line in the right panel of Fig. 5.14). This may indicate that the final black hole has not settled down to a Kerr black hole on the timescales considered here.

5.5.3 Black-Hole Mass from the Christodoulou Formula

It was shown by Christodoulou that, in the axisymmetric and stationary spacetime of a Kerr black hole, the square of the black-hole mass M is given by [272]

$$M^2 = M_{\rm irr}^2 + \frac{4\pi J^2}{A} = \frac{A}{16\pi} + \frac{4\pi J^2}{A} \,, \tag{5.7}$$

where $M_{\rm irr}$ is the irreducible mass, A is the event-horizon proper area, and J is the black-hole angular momentum. As the black hole approaches a stationary state at late times, the apparent and event horizons will tend to

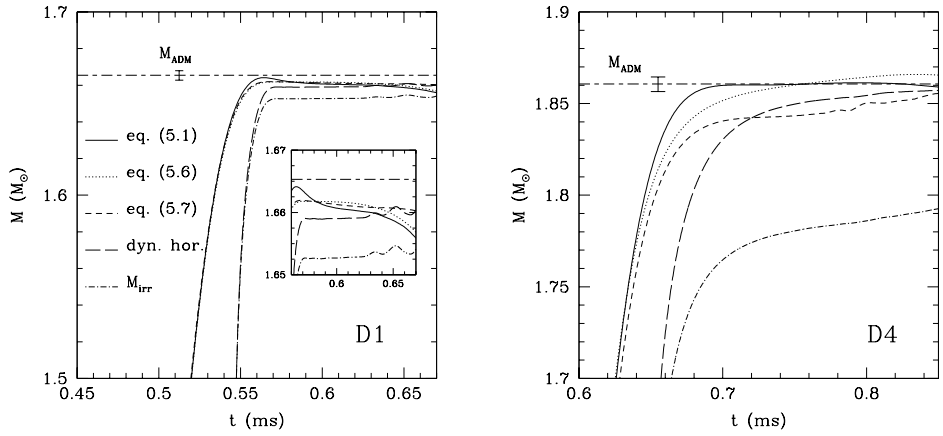

Figure 5.15: Comparison of the five different approaches used in the measure of the total black-hole mass for the collapse of models D1 and D4. Different lines refer to the different methods discussed in the main text. The left panel (model D1), shows that the different methods are overall comparable when the rotation is slow, but that differences are already present (this is as shown in the inset). The right panel (model D4) shows that the different measures can be considerably different when the rotation is large.

coincide and in that case the mass of the black hole is very well approximated by the above formula.

We have applied the above formula, using the various methods for measuring the angular momentum J. In particular, using the method for obtaining J from the distortion of the event horizon, through equation (5.5), the black-hole mass is given by

$$M^2 = \frac{A}{8\pi}\left(\frac{M_{hor}}{a}\right)^2\left[1-\sqrt{1-\left(\frac{a}{M_{hor}}\right)^2}\right] \ . \tag{5.8}$$

If, on the other hand, J is found from the angular velocity ω of the event horizon, then it is possible to use (5.6) in (5.7) and obtain

$$M^2 = \frac{A}{16\pi - 4A\omega^2} \ . \tag{5.9}$$

In the framework of dynamical horizons, expression (5.7) holds for *any* axisymmetric isolated or dynamical horizon, independently of whether it is stationary.

Figure 5.15 collects the four different ways of measuring the black-hole mass for the collapse of models D1 and D4. The different lines refer to the

different approaches we have outlined above. In addition, we display the irreducible mass $M_{\rm irr}$. The left panel of Fig. 5.15, in particular, shows the results of the different measures for the slowly rotating model D1. Because in this case all of the matter rapidly collapses into the black hole, the different estimates of the total mass agree very well. However, already in this slowly rotating case the irreducible mass of the apparent horizon is noticeably lower. The left panel also shows that while the different methods provide comparable estimates, only the one corresponding to equation (5.3) (*i.e.* the solid line) falls for some time within the error-bar provided by the initial estimate of $M_{\rm ADM}$ (this is particularly evident in the inset). Because when this happens the norms of the Hamiltonian constraint have not yet started to grow exponentially and the largest value of the constraint violation is about an order of magnitude smaller (*i.e.* the $\rm L_1$ norm of the Hamiltonian constraint is $\sim 4.9 \times 10^{-4}$ at $t = 0.56$ ms) we can use the error-bar in $M_{\rm ADM}$ to place an upper bound of 0.5% $M_{\rm ADM}$ to the energy lost through the emission of gravitational radiation in this case. Clearly, the true bound is certainly considerably lower and we expect that with accuracies comparable to the ones of 2D simulations, our estimates of the efficiency of gravitational radiation emission could converge to the values of Stark and Piran [237].

The right panel of Fig. 5.15, on the other hand, shows the results of the different mass measures for the rapidly rotating model D4. In this case, the contribution from the spin energy is considerably larger and noticeable differences appear among the different approaches. Since all seem to have systematic errors, this makes it less trivial to establish which method is to prefer. On one hand, those methods using information from the event-horizon equatorial circumference or that fit the perturbations of the event horizon [*i.e.* equations (5.3) and (5.8)] seem to provide accurate estimates at earlier times but suffer of the overall inaccuracy at later stages, when the initial guesses for the null surface are distinct. It is indeed at these early times that these measurements are within the error-bar provided by the initial estimate of $M_{\rm ADM}$. On the other hand, those methods that measure the angular velocity of the null generators [*i.e.* equation (5.9)] or that use the dynamical horizon framework, produce reasonably accurate estimates, that converge with resolution, that monotonically grow in time and that are within the error-bar of the initial estimate of $M_{\rm ADM}$. Furthermore, in the case of the dynamical horizon framework, this is not only physically expected, given that a small but non-zero fraction of the matter continues to be accreted nearly until the end of the simulation, but it is also guaranteed analytically.

Because of these differences in the measures of M and because the black hole does not have time to settle down to a constant total mass, the upper bound on the energy emission is more conservative than in the D1 case. In

particular, taking again as a reference the time when the estimate relative to equation (5.3) is within the error-bar (*i.e.* at $t = 0.70$ ms) and the largest value of the constraint violation is about an order of magnitude smaller (*i.e.* the L_1 norm of the Hamiltonian constraint is $\sim 1.2 \times 10^{-3}$) and is not yet growing exponentially, we place an upper bound of 1% $M_{\rm ADM}$ on the energy lost through gravitational radiation. Once again, we expect the true value to be considerably smaller.

One obvious and expected result is that the irreducible mass in the collapse of model D4 (the dot-dashed line in the right panel of Fig. 5.15) deviates by a large amount from the actual black hole mass, since it does not include the rotational energy of the black hole.

Finally, we will make a comment on the different methods used for measuring the mass and spin of a black hole in a numerical simulation. Although the direct comparison of many different methods employed here have provided valuable information on the dynamics of the system, we have found the dynamical horizon framework to be simple to implement, accurate and not particularly affected by the errors from which equivalent approaches seem to suffer, as shown in our Figs. 5.15 and 5.14. As a result, we recommend its use as a standard tool in numerical relativity simulations.

5.5.4 Reconstructing the global spacetime

All of the results presented and discussed in the previous Sections describe only a small portion of the spacetime which has been solved during the collapse. In addition to this, it is interesting and instructive to collect all of these pieces of information into a *global* description of the spacetime and look for those features which mark the difference between the collapse of slowly and rapidly rotating stellar models. As we discuss below, these features emerge in a very transparent way within a global view of the spacetime.

To construct this view, we use the worldlines of the most representative surfaces during the collapse, namely those of the equatorial stellar surface, of the apparent horizon and of the event horizon. For all of them we need to use properly defined quantities and, in particular, circumferential radii. The results of this spacetime reconstruction are shown in Fig. 5.16, whose left and right panels refer to the collapse of models D1 and D4, respectively. The different lines indicate the worldlines of the circumferential radius of the stellar surface (dotted line), as well as of the apparent horizon (dashed line) and of the event horizon (solid line). Note that for the horizons we show both the equatorial and the polar circumferential radii, with the latter being always smaller than the former. For the stellar surface, on the other hand, we show the equatorial circumferential radius only. This is because the calcula-

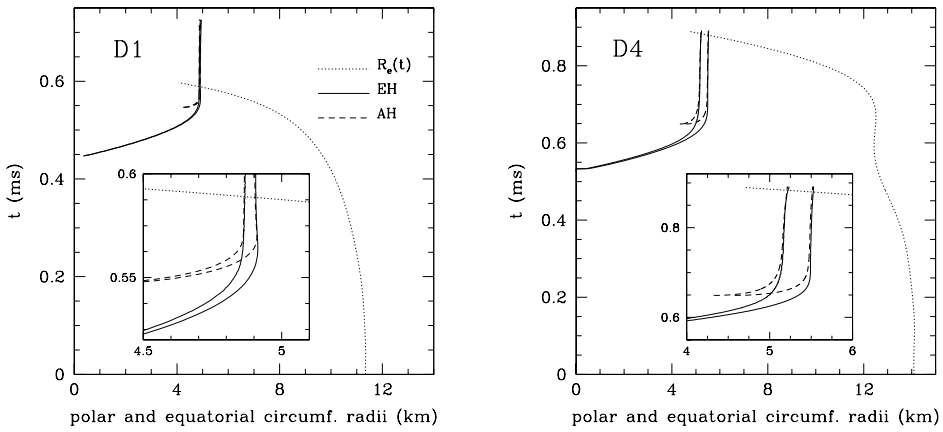

Figure 5.16: Evolution of the most relevant surfaces during the collapse for the D1 and D4 cases. Solid, dashed and dotted lines represent the worldlines of the circumferential radii of the event horizon, of the apparent horizon and of the stellar surface, respectively. Note that for the horizons we plot both the equatorial and the polar circumferential radii, while only the equatorial circumferential radius is shown for the stellar surface. Shown in the insets are the magnified views of the worldlines during the final stages of the collapse.

tion of the stellar polar circumferential radius requires a line integral along the stellar surface on a given polar slice. Along this contour one must use a line element which is suitably fitted to the stellar surface and diagonalised (see [264] for a detailed discussion). In the case of model D4, however, this is difficult to compute at late times, when the disc is formed and the line integral becomes inaccurate.

Note that in both panels of Fig. 5.16 the event horizon grows from an essentially zero size to its asymptotic value. In contrast, the apparent horizon grows from an initially non-zero size and, as it should, is always contained within the event horizon. At late times, the worldlines merge to the precision at which we can compute them. A rapid look at the two panels of Fig. 5.16 is sufficient to appreciate the different properties in the dynamics of the collapse of slowly and rapidly rotating models.

Firstly, in the case of model D1, the differences between the equatorial and polar circumferential radii of the two trapped surfaces are very small and emerge only in the inset that offers a magnified view of the worldlines during the final stages of the collapse. This is not the case for model D4, for which the differences are much more evident and can be appreciated also in the main panel. Of course, this is what one expects given that the ratio of

these two quantities depends on a/M and is ~ 1 for a slowly rotating black hole (*cf.* Table 5.2).

Secondly, the worldlines of the stellar equatorial circumferential radius are very different in the two cases. In the slowly rotating model D1, in particular, the star collapses smoothly and the worldline always has negative slope, thus reaching progressively smaller radii as the evolution proceeds (*cf.* left panel of Fig. 5.16). By time $t \simeq 0.59$ ms, the stellar equatorial circumferential radius has shrunk below the corresponding value of the event horizon. In the case of the rapidly rotating model D4, on the other hand, this is no longer true and after an initial phase which is similar to the one described for D1, the worldline does not reach smaller radii. Rather, the stellar surface slows its inward motion and, at around $t \sim 0.6$ ms, the stellar equatorial circumferential radius does not vary appreciably. Indeed, the right panel of Fig. 5.16 shows that at this stage the stellar surface moves to slightly larger radii. This behaviour marks the phase in which a flattened configuration has been produced and the material at the outer edge of the disc experiences a stall (*cf.* the middle and lower panels of Fig. 5.5). As the collapse proceeds, however, also this material will not be able to sustain its orbital motion and, after $t \sim 0.7$ ms, the worldline moves to smaller radii again. By a time $t \simeq 0.9$ ms, the stellar equatorial circumferential radius has shrunk below the corresponding value of the event horizon.

5.6 Summary

Although 3D numerical relativity has been a very active research area for several years now, there are still a number of technical issues to be addressed and physical problems to be investigated in detail. Separate progress has been made so far in obtaining long-term stable evolutions of vacuum spacetimes and of spacetimes with matter. Both of them have posed significant numerical problems because of the existence of horizons containing physical singularities, in one case, and the development of non-linear hydrodynamical phenomena such as shocks, in the other. In black-hole vacuum spacetimes, these problems have successfully been dealt with by using better suited formulations of the Einstein equations and by employing excision techniques for the regions of the spacetime containing the singularity. In spacetimes containing matter, on the other hand, sophisticated numerical techniques (such as the HRSC methods) have been employed to accurately track the dynamics of the shocks.

Here, we have combined these two different approaches by implementing excision techniques within a *forming* horizon, thus following the dynamics of

the matter as it accretes onto the developing black hole. We have shown that doing so allows the numerical evolution to proceed uninhibited from fully regular initial conditions of matter in equilibrium and devoid of trapped surfaces, up to a vacuum spacetime featuring an event horizon enclosing an excised physical singularity. This new important ability in numerical relativity evolutions will help in a more detailed investigation of complex astrophysical systems, such as the coalescence of neutron star or neutron star / black hole binaries, both considered as prime candidates for the detection of gravitational waves, and of the collapse of stellar cores, considered as the progenitors of gamma-ray bursts.

As a first astrophysical problem for our novel setup of codes, we have here focused on the collapse of rapidly rotating relativistic stars to Kerr black holes. The stars are assumed to be initially in uniform rotation and dynamically unstable to axisymmetric perturbations. While the collapse of slowly rotating initial models proceeds with the matter remaining nearly uniformly rotating, the dynamics is shown to be very different in the case of initial models rotating near the mass-shedding limit, for which strong differential rotation develops. Although the stars become highly flattened during collapse, attaining a disc-like shape, the collapse cannot be halted because the specific angular momentum is not sufficient for a stable disc to form. Instead, the matter in the disc spirals towards the black hole and angular momentum is transferred inward to produce a spinning black hole.

Several different approaches have been employed to compute the mass and angular momentum of the newly formed Kerr black hole. Besides more traditional methods involving the measure of the geometrical properties of the apparent *and* event horizons, we have fitted the oscillations of the perturbed Kerr black hole to specific quasi-normal modes obtained by linear perturbation theory. In addition, we have also considered the recently proposed *isolated* and *dynamical* horizon frameworks, finding it to be simple to implement and yielding estimates which are accurate and more robust than those of other methods. This variety of approaches has allowed for the determination of both the mass and angular momentum of the black hole with an accuracy unprecedented for a 3D simulation. These measures, in turn, have allowed us to set upper limits on the energy and angular momentum that could be lost during the collapse in the form of gravitational radiation.

Work using mesh-refinement techniques was already in progress to extract more precise information and waveforms for the gravitational radiation recorded at large distances from the collapsing stars. However, this aspect of the gravitational collapse was not yet considered in this work. It has been reported in another paper [135].

The results of this test show that the new hydrodynamical excision bound-

ary conditions work well also in dynamical spacetimes. We do not expect problems applying them to the mixed binary case. However, this does not apply to the spacetime excision scheme, which we believe is the major problem at late times of the evolution. This is expected to be an even bigger problem in the mixed binary case, because the singularity which has to be excised is already present in the initial slice.

Chapter 6

Black hole - neutron star systems

In this chapter we describe the different steps towards evolutions of a binary system of a neutron star and a black hole. First, we discuss ways to obtain initial data by solving the constraint equations. So far, we limit this to time-symmetric, axisymmetric configurations because if simplicity. Some of the methods used to solve for the constraints need a nontrivial initial guess. Therefore we first discuss the methods used to solve the constraint equations in the sections 6.3 to 6.5 and then describe how a good initial guess can be obtained in section 6.6. Most of this work is original, however we used and modified an elliptic solver, which was written by Marcus Ansorg.

Finally, in section 6.6, we describe problems and their solutions in three-dimensional evolutions of the mentioned initial data and present preliminary results of those evolutions. These results are not yet published elsewhere.

6.1 Introduction

Binary systems of compact bodies are believed to be among the major sources of gravitational waves, which could be detected with the newly built gravitational wave detectors [19]. These compact objects can be black holes or very compact stars, like neutron stars. The amplitude of the gravitational waves from such systems is believed to be largest during the merging phase, in which the strong gravitational field near the two merging objects, and thus the use of General Relativity, plays a crucial role. However, analytically this is too difficult. Therefore, numerical simulations are the best way to obtain a better understanding of this short, but very dynamical phase.

Binary systems of two black holes have been the focus of a lot of research

for many years, (*e.g.* see [29–43]). Binary neutron star systems have also been studied considerably in the past, see *e.g.* [44–46]. Current research into neutron star - black hole (mixed) systems has often been performed using Newtonian gravity or Newtonian gravity with relativistic modifications to the gravitational potential [51]. There are some results using full General Relativity (*e.g.* [28, 53, 58, 59]), but there is so far no long-term dynamical evolution of a neutron star - black hole merger using full General Relativity.

Such an evolution is part of the aim of this thesis. This consists of two parts: creating initial data for such a system and evolving these data in time. This chapter first explains different methods of constructing initial data for a binary system composed of a neutron star and a black hole. Using these data, preliminary results of evolutions are presented in section 6.6.

We will show two different ways of obtaining initial data for such a spacetime. Both methods follow the York procedure (see section 2.5.3) and they solve the same equation (2.84), using however different numerical methods (finite difference multigrid versus spectral methods) and using a different computational domain (finite versus compactified). While they should produce the same solution, one method requires a non-trivial initial guess.

Therefore we first explain how to obtain a suitable initial guess for a mixed binary system in section 6.2. Then, details about York's procedure with matter follow in section 6.3. We will mention the first of the two methods for solving this procedure only briefly in section 6.4, before we explain the details of the second method in section 6.5. Finally we will present the first preliminary results of evolutions of such data in section 6.6.

6.2 Obtaining a good initial guess

In this section we describe a way to obtain a good guess for the solution of the initial data problem, which will be discussed in more detail in the following sections. This guess should be as close as possible to the actual solution either because some numerical methods require it to reach convergence or because one expects that in this way the physical quantities will change only slightly when solving the constraint equations.

The idea of "combining" two spacetimes comes from Newtonian gravity. In this theory the gravitational potential of a combination of bodies is the linear combination of the single ones. This is due to the linearity of the Poisson equation for the gravitational potential. This ceases to be true in General Relativity, whose equations are non-linear.

What is usually needed for evolutions is initial data with some known physical properties and vanishing or at least small (and converging) con-

straint violations. Using a formalism such as York's (see subsection 2.5.3) the constraints can be solved before evolution. However at least some implementations of numerical solvers fail if the initial guess is not already close to the final result. Therefore it is important for such solvers (like the version of BAM [273] we used) to provide an initial guess as close as possible to the actual solution.

We are able to create an initial slice containing a TOV star with very high accuracy (see section 2.5.1). This TOV initial data can then be combined with any spacetime, *i.e.* Schwarzschild, and the result would be the initial guess for the initial value problem solver (IVP), solving the equations of York's procedure. We have implemented two simple ways of "combining" spacetimes. The first way is to introduce a parameter which defines for each grid point which of the two initial spacetimes should be used. Since both the TOV solution and Schwarzschild can be written in a conformally flat form, it is reasonable to take the values of that spacetime with the largest value of $\Psi^4 = \gamma_{ii}$ (both spacetimes are also spherically symmetric) at that point. Therefore we called this method the "maximum" method.

Another way is to combine the values of the different initial spacetimes on one grid-point. We found that the following method gives reasonable results. N denotes the number of spacetimes to combine and the superscript in brackets denotes the number of the spacetime.

$$\gamma_{ii} = \sum_{s=0}^{N} \left(\gamma_{ii}^{(s)} - 1 \right) + 1 \tag{6.1}$$

$$\gamma_{ij} = \sum_{s=0}^{N} \gamma_{ij}^{(s)} \quad \text{for} \quad i \neq j \tag{6.2}$$

$$K_{ij} = \sum_{s=0}^{N} K_{ij}^{(s)} \tag{6.3}$$

Since this is doing some kind of averaging (the extrinsic curvature K_{ij} is zero in most of the cases we look at and the off-diagonal metric terms are much smaller than the diagonal metric elements), we called this method the "average" method. Example plots of Ψ^4 are shown in figures 6.1 to 6.3.

Both of these methods produce data that violate the constraint equations. But they violate them in different ways. The "maximum" method violates them only in a special region, the region where neighbouring points are taken from another spacetime. The Hamiltonian constraint is violated strongly at these two-surfaces in the three-dimensional slice. In the "average" method the maximum of the violations is orders of magnitudes smaller

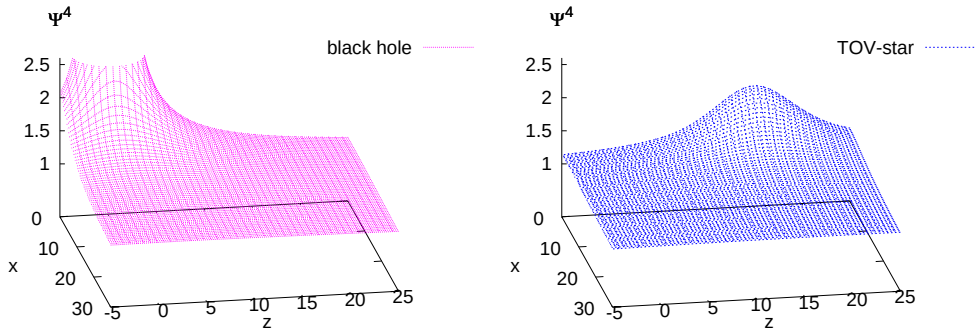

Figure 6.1: Ψ^4 for a Schwarzschild black hole and a TOV star

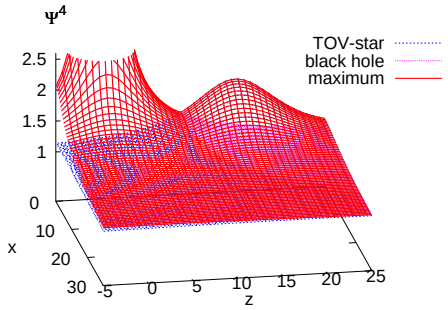

Figure 6.2: Ψ^4 for the initial and the combined spacetimes using the "maximal" method

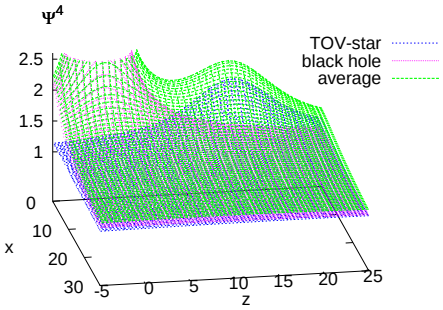

Figure 6.3: Ψ^4 for the initial and the combined spacetimes using the "average" method

than in the "maximum" method, but it is spread over the whole spacetime. Which method is the best to use depends on what the combined slice is used for. We use this combined slice as input for an elliptic solver in order to solve the Hamiltonian constraint. We found that, in this case, the average method is the better choice.

6.3 Solving the York procedure with matter

We assume time-symmetry, maximal slicing and vanishing shift and velocities, i.e. $K_{ij} = 0$, $\beta^i = 0$ and $v^i = 0$. This is approximating a head-on binary system with an initial large separation. The reason for these approximations is that equation (2.82) is fulfilled automatically and that equation (2.83) is simplified to equation (2.84). The conformal factor for a Schwarzschild black hole in isotropic coordinates with the physical singularity at r_i is

$$\psi_{\text{BH}} = 1 + \frac{m}{2|r - r_i|}. \tag{6.4}$$

We decompose ψ in the following way, which is called the "puncture" approach [204]:

$$\psi = \frac{1}{\alpha} + u \tag{6.5}$$

where α is defined as

$$\alpha = \frac{2\,|r - r_i|}{m}. \tag{6.6}$$

We will then solve for u. The advantage of solving for u instead of ψ is that ψ diverges at the puncture while u does not, since the singular behaviour is taken into α, which is fixed.

We use that equation (2.84) is fulfilled for equation (6.4). Then we can reduce the elliptic equation for ψ to an elliptic equation for u,

$$\tilde{\nabla}^2 u = -2\pi \left(\frac{1 + \alpha u}{\alpha}\right)^5 \rho_{\text{ADM}}. \tag{6.7}$$

In this equation we see that the terms with α in the denominator would tend to diverge as we get closer to the coordinate r_i where the black-hole is situated. In order to avoid this, we impose that the density ρ_{ADM} should go to zero faster than $|r - r_i|^5$. Since we only want to use initial data with a star outside of the black hole, we can enforce this by treating the density as being zero outside the star.

Using this setup, equation (6.7) is solved using an elliptic solver to obtain a spacetime fulfilling the Hamiltonian constraint. Of course, the solution

found in this way will have physical quantities, such as black hole horizon mass, different from those of the initial guess. Because of this, the physical variables need to be computed again after the solution has been found.

We cannot solve equation (2.84) (or equation (6.7)) directly using ρ_{ADM}, because it can be shown [274] that this does not produce a solution in general. What we have to fix instead of ρ_{ADM} is some $\tilde{\rho}$, which could *e.g.* be obtained from ρ_{ADM} by

$$\tilde{\rho} \equiv \rho_{\mathrm{fixed}} = \psi^n \rho_{\mathrm{ADM}}, \tag{6.8}$$

with (as is also shown in [274]) $n > 5$. This leaves the freedom to choose n. There are two choices which stand out.

Using that

$$j^j = \psi^{-10} \tilde{j}^j \tag{6.9}$$

we can guarantee that the local "dominance of energy" condition [274] on the sources

$$\rho_{\mathrm{ADM}}^2 - \gamma_{ij} j^i j^j \geq 0 \tag{6.10}$$

holds for all $\psi > 0$, if

$$\rho_{\mathrm{ADM}} = \psi^{-8} \tilde{\rho}, \tag{6.11}$$

because then

$$\rho_{\mathrm{ADM}}^2 - \gamma_{ij} j^i j^j = \psi^{-16} \left(\tilde{\rho}^2 - \tilde{\gamma}_{ij} \tilde{j}^i \tilde{j}^j \right). \tag{6.12}$$

The other outstanding choice is

$$\rho_{\mathrm{ADM}} = \psi^{-6} \tilde{\rho}, \tag{6.13}$$

because one has "mass conservation" in this case in the form

$$\int_\Sigma \rho_{\mathrm{ADM}} \sqrt{\det \gamma}\, \mathrm{d}^3x = \int_\Sigma \tilde{\rho} \sqrt{\det \tilde{\gamma}}\, \mathrm{d}^3x, \tag{6.14}$$

which follows from

$$\sqrt{\det \gamma} = \psi^6 \sqrt{\det \tilde{\gamma}}. \tag{6.15}$$

We have chosen equation (6.11), such that equation (6.7) becomes:

$$\tilde{\nabla}^2 u = -2\pi \left(\frac{1 + \alpha u}{\alpha} \right)^{-3} \tilde{\rho}. \tag{6.16}$$

This solution uses the assumption $K_{ij} = 0$. However, as was shown in section 2.5.3, time-asymmetric data is also possible in general (see equation (2.88)). Since the matter velocities j^i also have to vanish in this case, adding matter sources follows a procedure similar to the one outlined above.

6.4 Using BAM as the elliptic solver

We used two different elliptic solvers to solve the time-symmetric solution. At the beginning of this work the only available and fast elliptic solver that had been integrated into Cactus was a multigrid solver, written as standalone code by Bernd Brügman, BAM [273].

Because BAM is tightly coupled to a uniform grid, the version in Cactus is also not maintained anymore and because uniform grids are often too limiting for state of the art simulations, we had to switch to another solver. However, the version of the code using BAM included also the possibility of time-asymmetric initial data, which is not (yet) part of the new code.

6.5 Using TwoPunctures as elliptic solver

Looking for a new solver, we had a list of needed properties in mind: it had to provide the solution on a mesh refined grid, it had to be fast and it should be easy to use. All of these points could be addressed by a Cactus thorn called TwoPunctures, written by Marcus Ansorg [275], which is calculating initial data for two puncture black holes using a spectral method.

However, this method has a limitation. It only uses one domain to cover the interior and exterior of the star. This is a limitation, because spectral methods converge exponential only if the functions are infinitely differentiable. This is not the case at the surface of the star in this problem. Some metric components are only two times differentiable. We therefore cannot expect exponential convergence. Future work will go into extending this solver to at least two domains, one for the interior and one for the exterior of the star.

6.5.1 The Method

The code already solved York's procedure in vacuum. It is used to obtain initial data for a binary black hole problem. The equation for the momentum constraint equation is not changed by the inclusion of matter, provided that the matter velocities are zero (see equation (2.82)). However, the Hamiltonian constraint equation with matter has an additional term on the right hand side:

$$\tilde{\nabla}^2\psi - \frac{1}{8}\psi\tilde{R} - \frac{1}{8}\psi^5 K^2 + \frac{1}{8}\psi^5 K_{ij}K^{ij} = -2\pi\psi^5\rho_{\mathrm{ADM}}. \tag{6.17}$$

We will first outline the spectral method we used without matter (for details see [275]) before the term for the matter is introduced.

The basic form of the elliptic equation to be solved for a function u is

$$f(u) = \delta u + \varrho(u) = 0. \tag{6.18}$$

Here δ denotes the Laplace operator and ϱ is a source term which in general depends on u. To compactify the space we will introduce a coordinate transformation from a Cartesian grid (x, y, z) to (A, B, ϕ)

$$x = b\,\frac{A^2+1}{A^2-1}\,\frac{2B}{1+B^2}, \tag{6.19}$$

$$y = b\,\frac{2A}{1-A^2}\,\frac{1-B^2}{1+B^2}\cos\phi, \tag{6.20}$$

$$z = b\,\frac{2A}{1-A^2}\,\frac{1-B^2}{1+B^2}\sin\phi, \tag{6.21}$$

with b being the separation of the two singularities and

$$A \in [0,1], \quad B \in [-1,1], \quad \phi \in [0, 2\pi], \tag{6.22}$$

where ϕ is the standard azimuthal coordinate in a spherical polar coordinate system. u has to obey a physical falloff condition at spatial infinity,

$$\lim_{r\to\infty} u = 0, \tag{6.23}$$

and because the variable A is introduced such that

$$r \to \infty \Longleftrightarrow A \to 1, \tag{6.24}$$

we can ensure this falloff by defining a function U as

$$u = (A-1)U. \tag{6.25}$$

The computational domain (A, B, ϕ) will then be discretised in such a way that

$$U_{ijk} = U(A_i, B_j, \phi_k), \tag{6.26}$$

with

$$0 \le i < n_A, \quad 0 \le j < n_B, \quad 0 \le k < n_\phi. \tag{6.27}$$

A_i, B_j and ϕ_k are chosen to be

$$A_i = \sin^2\left[\frac{\pi}{2n_A}\left(i+\frac{1}{2}\right)\right], \tag{6.28a}$$

$$B_j = -\cos\left[\frac{\pi}{n_B}\left(j+\frac{1}{2}\right)\right], \tag{6.28b}$$

$$\phi_k = 2\pi\frac{k}{n_\phi}. \tag{6.28c}$$

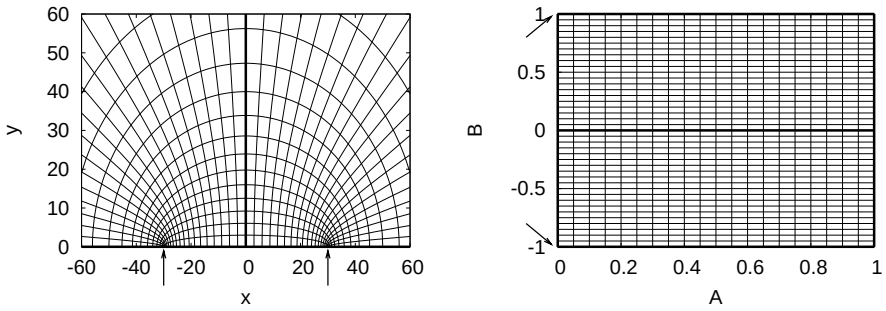

Figure 6.4: The coordinate lines of A and B, on the left hand plot on the Cartesian grid, on the right hand plot on its own grid. The arrows denote the location of the singularities ($b = 30$).

Note that we do not introduce a coordinate transformation on ϕ. The left hand side of figure 6.4 shows the coordinate lines of A and B on the Cartesian grid (ϕ suppressed). It is clearly visible that the resolution is highest near the punctures sitting at the locations indicated by the arrows. The resolution is decreased between them and further decreases as infinity is approached.

By the inverse of the coordinate transformation (6.19) this is mapped to the rectangular box shown at the right hand side of figure 6.4. The arrows again mark the location of the punctures and spatial infinity has been compactified to the surface $A = 1$. Note that this is a surface because these plots suppress the unchanged ϕ coordinate.

By this special coordinate transformation, in addition to achieving compactification, one ensures an important property for the function u, which is being solved for, namely that it is infinitely differentiable in the whole domain, even near or at the puncture locations in the case of zero momenta of the punctures. This ceases to be true if a stellar surface is present, as this introduces functions that are not infinitely differentiable. In the case of nonzero momenta, logarithmic terms appear at spatial infinity ($A = 1$), but the overall solution can still be found. We will focus only on the case of vanishing momenta. More details can be found in [275].

The nonlinear equation (6.18) is solved with a Newton-Raphson method. The solution U is written as

$$U = \lim_{N \to \infty} U_N, \tag{6.29}$$

$$U_{N+1} = U_N - V_N, \tag{6.30}$$

where V_N satisfies the linear problem

$$J_N V_N = b_N \tag{6.31}$$

with

$$J_N = \frac{\partial f}{\partial U}\left(U_N\right) \tag{6.32}$$

$$b_N = f\left(U_N\right). \tag{6.33}$$

There are a number of ways to solve a linear system arising from spectral methods. The main problem here is not of mathematical nature, but is the efficiency. Here we use a preconditioned "Biconjugate Gradient Stabilized" method [276].

This approach so far only solves for vacuum spacetimes optionally including two punctures with possible momenta. We extended this to spacetimes including matter. However, this is restricted to vanishing momenta of the involved objects so far. The reason is that in the case of two punctures in vacuum, the momentum constraint can be satisfied trivially since the needed quantities are known analytically. When matter is present however, this is no longer the case and the momentum constraint must be solved together with the Hamiltonian constraint. This can be done in a way similar to the one for the Hamiltonian constraint and will be the focus of future work.

The inclusion of the matter term is now straightforward and done as described in section 6.3, by solving equation (6.16) under the assumption that the matter density near the singularity is zero.

Figure 6.5 shows a flowchart of the procedure. The solution has to be evaluated (or interpolated) onto the finite difference, Cartesian grid. While this is a conceptionally simple operation, it often takes longer (in computer time) than to find the solution itself. In typical simulations (see section 6.5.2) it is up to ten times more computationally expensive. This depends strongly on the resolutions of the grid for the spectral method and the one of the Cartesian grid. However, this operation has the the advantage that it can be parallelised very easily, which is not the case for the elliptic solver. Thus, the number of processors used also changes the ratio between the time spent in finding the solution and in evaluating it onto the Cartesian grid.

However, we did not address one problem: spectral methods assume that the underlying functions are infinitely differentiable. In this case, they reach exponential convergence. Because of this, they often have much higher accuracy, compared to similar finite difference methods using the same resources. However, spectral methods do not work so well on functions which are not infinitely differentiable. In the case of the spectral method used here, the non-differentiability at the punctures is hidden in a coordinate transformation, thus it shows exponential convergence (see [275]). However, this is not expected anymore if a matter source in the form of a TOV star is included. The reason for this is that the metric terms are only two times differentiable

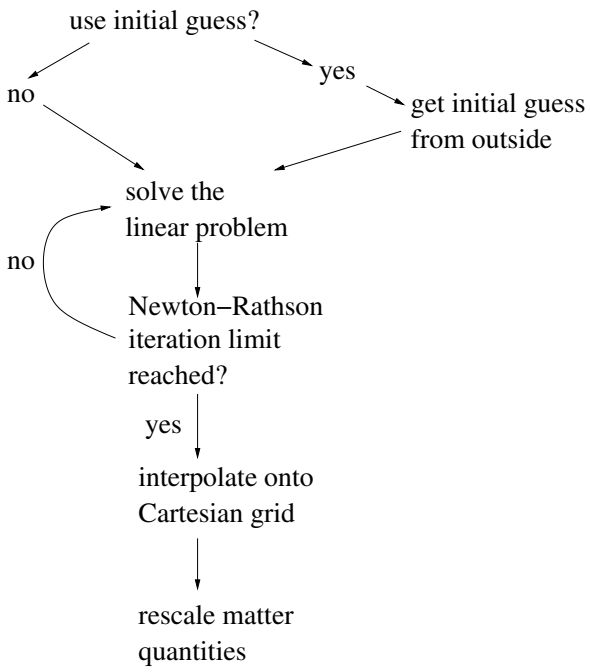

Figure 6.5: Flowchart of the procedure of solving the initial value problem using the `TwoPunctures` method including matter.

at the surface of the star. Because of this, we do not expect exponential convergence.

6.5.2 Results

In this subsection we will present tests of the `TwoPunctures` method, mainly convergence tests. Because convergence was already shown for the case of one and two black holes (see [275]), We will concentrate on solutions including source (matter) terms. The TOV solution is a natural candidate for this, because the solution is known analytically. After showing convergence in this case, the convergence for the mixed binary case will be presented.

Single TOV Star

Consider a configuration of one TOV star with a mass of $1.14 M_\odot$ (2.27×10^{33}g), which with $\Gamma = 2$ and $K = 100$ leads to a coordinate radius of about 9.25M. This star is placed on the x-axis, at the location of one of the two punctures of the spectral grid ($x = -30$), and both puncture masses are set to zero. A flat metric (Minkowski) is used as initial guess for the elliptic

solver. As the solution is known to very high accuracy, this is used to test the method and the code.

There are two different parts which have to be tested: the convergence of the spectral solver to the real solution and the convergence of the evaluation of the spectral solution onto the Cartesian grid. Note that for the first case it is not practical to plot the convergence factor as defined in equation (3.27), because the shape of the underlying variables changes with changing resolution (because the colocation points of the spectral method change) and there are many zero-crossings. However, it is possible to show the convergence of the 2-norm of the Hamiltonian constraint violation. For the case of the convergence of the evaluation of the spectral solution onto the Cartesian grid, using the convergence factor itself is possible, but only for quantities which rely on (finite difference) derivatives of the evaluated variables. The ideal candidate for this is, again, the Hamiltonian constraint violation.

Figure 6.6 shows the Hamiltonian constraint violation along the x-axis nearby the star and figure 6.7 shows the same over the whole domain, both scaled for second and third order convergence. Both figures suggest a convergence rate of third order. The violations near $x = 30$ result from errors near one of the corners of the grid of the spectral solver.

However, as can be seen from figures 6.8 and 6.9, which show the same for lines parallel to the y-axis through the centre of the neutron star and the location of the second "puncture", this is not the case in the whole domain. These figures suggest only second order. Because of limitations of computer time, the computational domain of these simulations only covers a thin "bar" (*e.g.* $7 \times 7 \times 800$ points) parallel to the axes. Two-dimensional or even three-dimensional simulations with the same resolution are not possible for memory or runtime reasons.

Figures 6.10 and 6.11 show the norm of the Hamiltonian constraint violation for different spectral resolutions in a log-log plot together with lines indicating the slope of convergence orders of 2.5 and 3. These plots suggest an order convergence of at least 2.5. However, we are aware that this is only the norm over the computed domain (which is in both cases a very narrow box in one particular direction) and this is an averaged quantity.

Because the convergence rate is only of third order in a specific region (the x-axis), and of second order otherwise, we can only state second order for the whole method. This is in agreement with our expectations, that we cannot reach exponential convergence.

For the tests of the evaluation we use the Hamiltonian constraint violation again. We expect second order convergence, because the finite difference methods for calculating these violations from the evaluated quantities are second order, but as we show in the following, this is not achieved in the

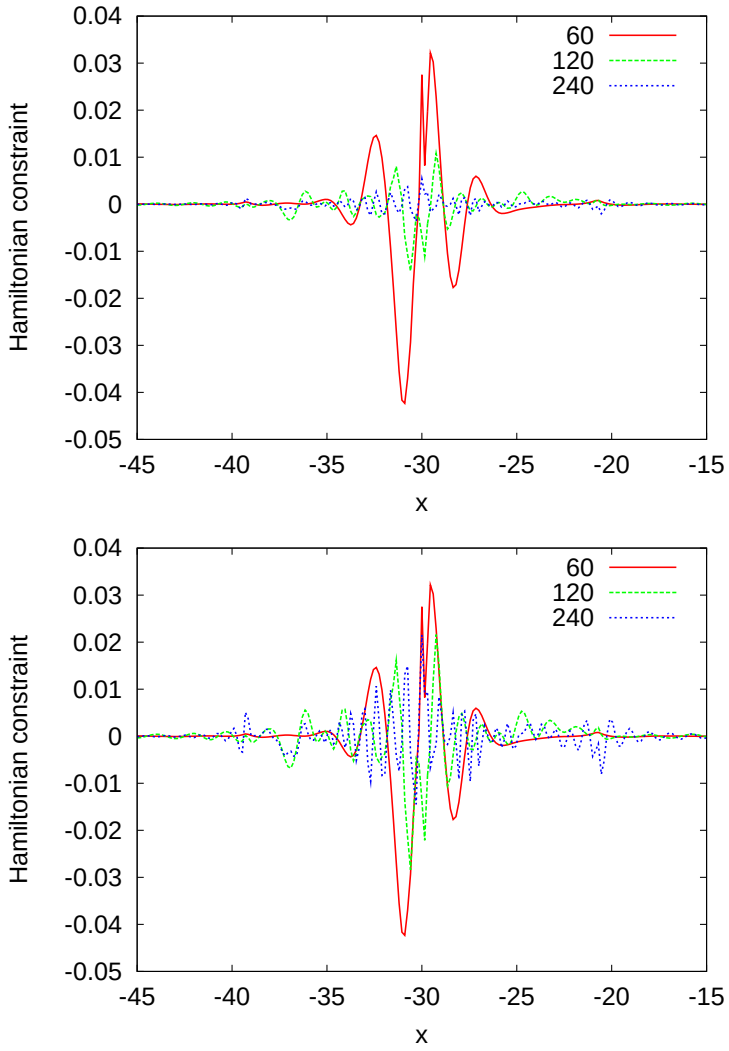

Figure 6.6: Scaled Hamiltonian constraint convergence for second order (upper plot) and third order (lower plot) along the x-axis nearby a single neutron star (TOV) with its centre at $x = -30$ and for different spectral resolutions.

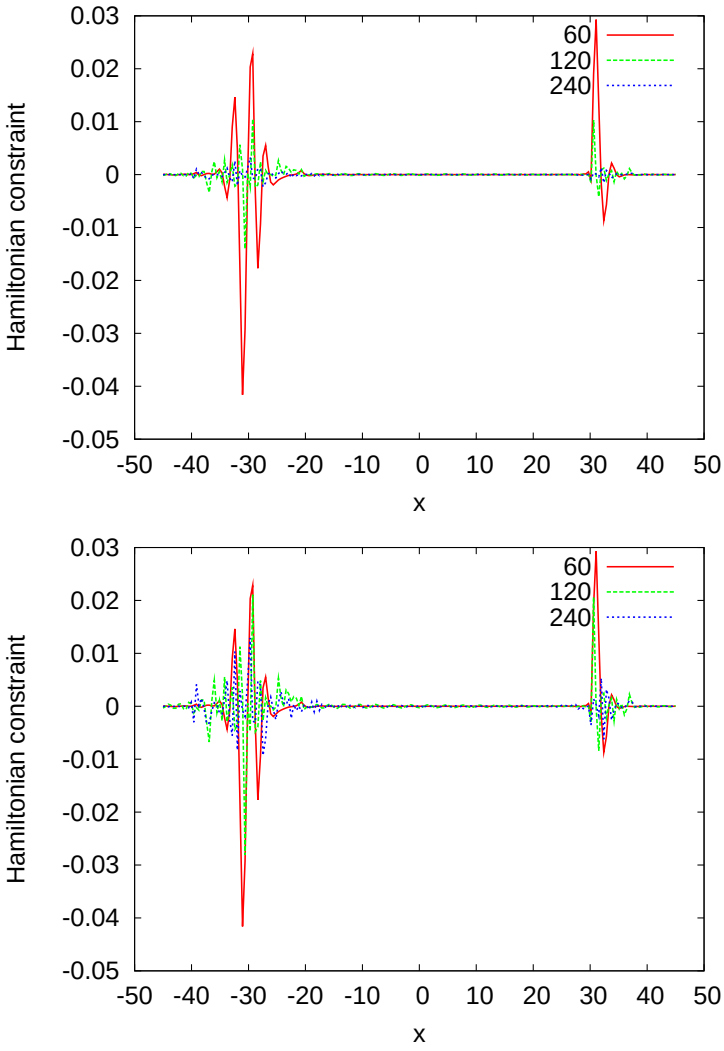

Figure 6.7: Scaled Hamiltonian constraint convergence for second order (upper plot) and third order (lower) along the x-axis of the entire computational domain including a single neutron star (TOV) with its centre at $x = -30$ and for different spectral resolutions.

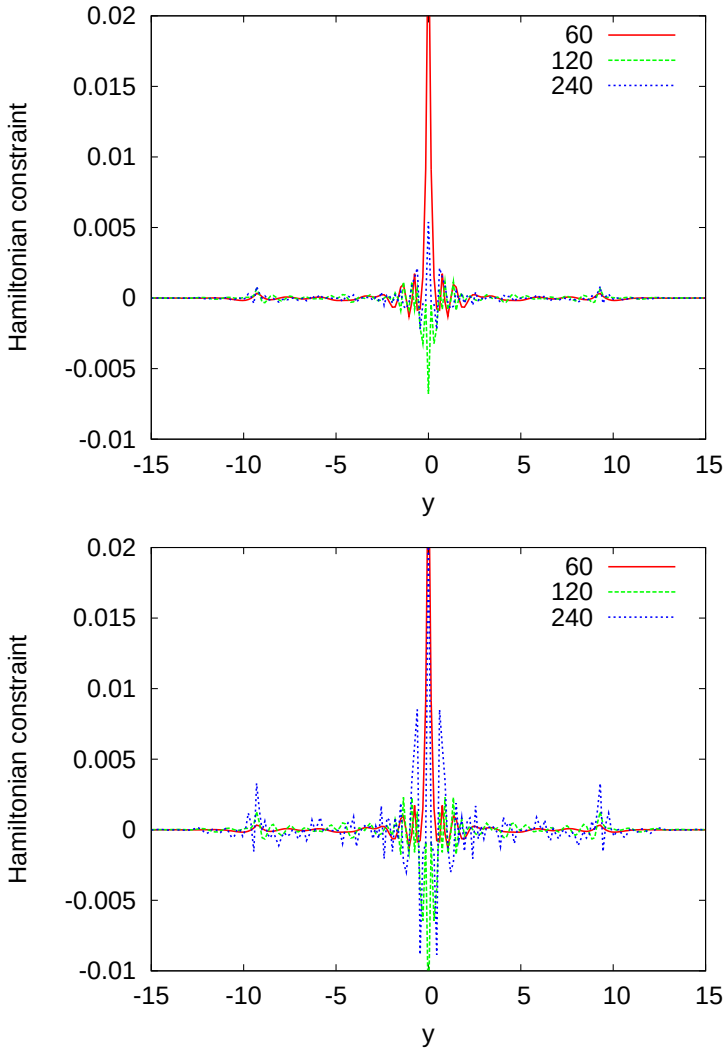

Figure 6.8: Scaled Hamiltonian constraint convergence for second order (upper plot) and third order (lower plot) parallel to the y-axis through the centre of a single neutron star (TOV), which is located at $y = 0$. Different lines denote different spectral resolutions.

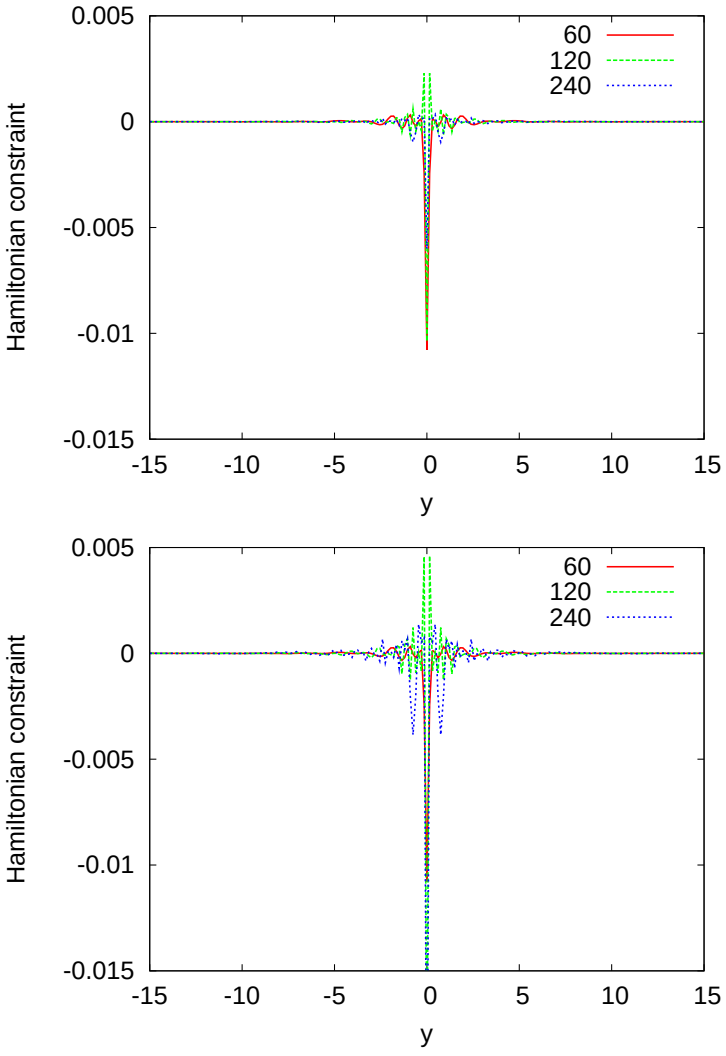

Figure 6.9: Scaled Hamiltonian constraint convergence for second order (upper plot) and third order (lower plot) parallel to the y-axis for a single neutron star (TOV), but through the location of the second "puncture". Different lines denote different spectral resolutions.

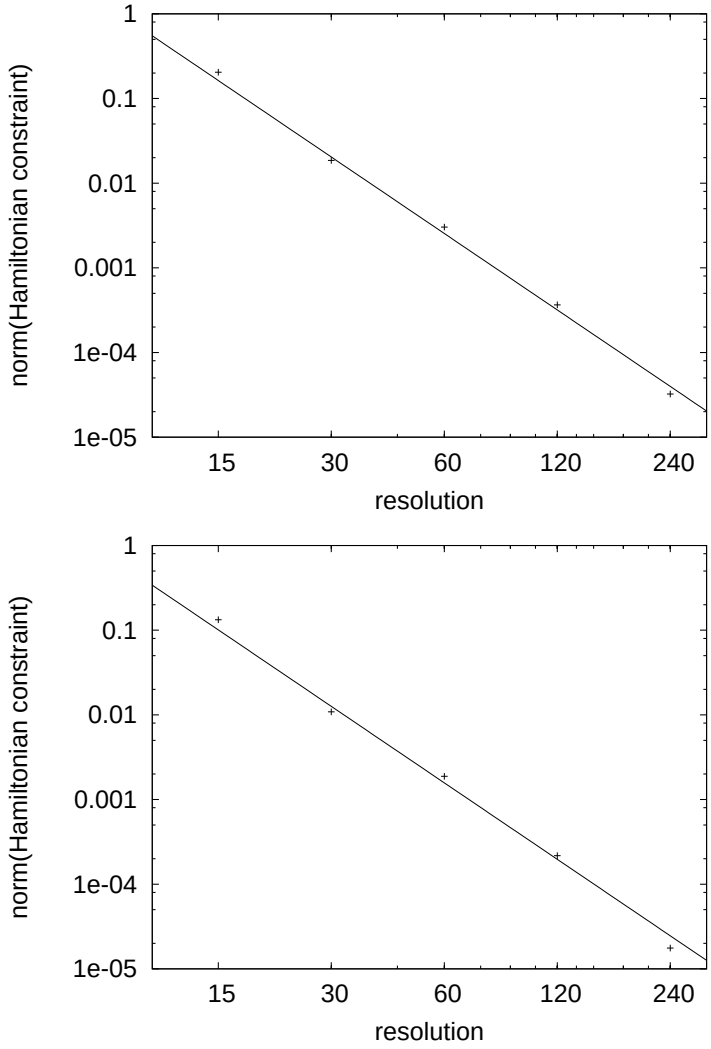

Figure 6.10: Norm of the Hamiltonian constraint along the x-axis nearby the neutron star (TOV) (upper plot) and including the whole domain (upper right) for different spectral resolutions. The solid line corresponds to a third order convergence as comparison.

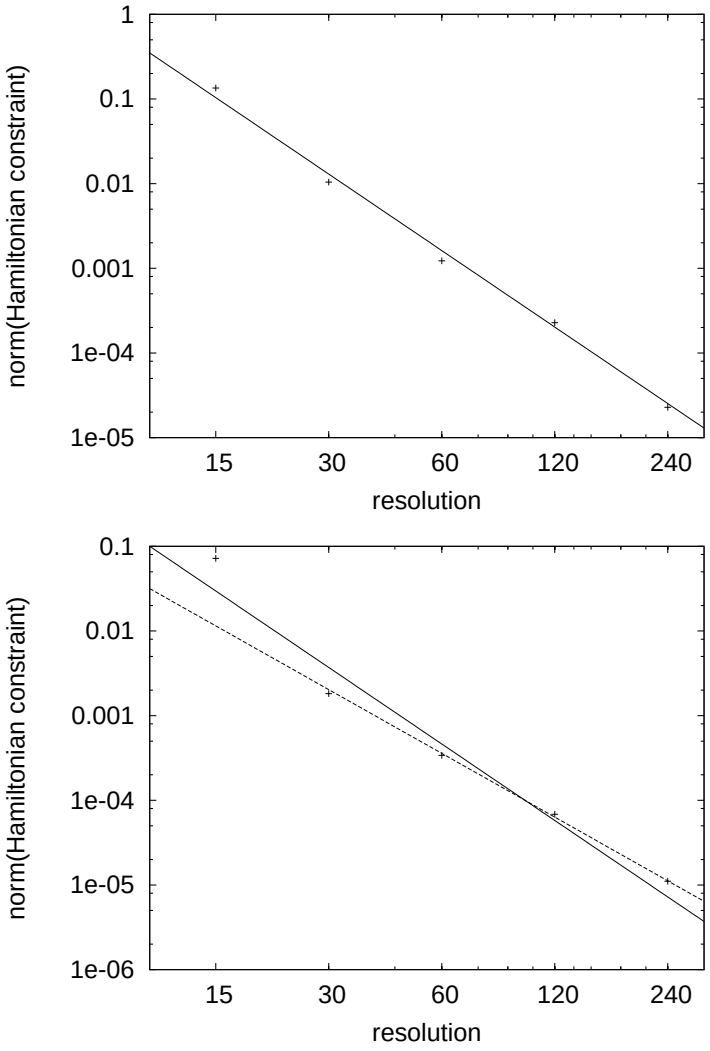

Figure 6.11: Norm of the Hamiltonian constraint parallel to the y-axis, through the centre of the neutron star (TOV) (upper plot) and into the same direction through the location of the second "puncture" (lower plot), both for different spectral resolutions. The solid line corresponds to a third order convergence and the dashed line to a convergence order of 2.5 as comparison.

whole domain.

The spike at the x-axis in figure 6.8 is due to errors near the boundary of the spectral grid at $y = 0$. This causes non-smooth first derivatives perpendicular to the x-axis in the metric. Because the Hamiltonian constraint uses first and second derivatives of those, this small error is the cause of the complete absence of convergence on the x-axis when changing the resolution of the Cartesian grid, which is shown in figure 6.12. However it converges to zero with increasing spectral resolution. We conclude that the evaluations used indeed converge at an order of two, except near the x-axis, where this is impossible because of errors in the evaluated function.

Since this is a convergence test using the TOV solution, which is known to very high precision, we cannot only compare results for different spectral resolutions with each other, but also compare with the exact result. This is done in figures 6.13 to 6.15. These show the error of the conformal factor, scaled for second and third order of convergence. Figure 6.13 shows that on one side of the star, which is at approx. $x = -39$M, the solution is only second order convergent, while near the other side the convergence rate is three.

Figures 6.14 and 6.15 show a slice through the centre of the star and the location of the second "puncture", in both cases parallel to the y-axis. This, again, does not show third order convergence, but clearly at least second order.

That the surface of the star is a difficult region for the spectral representation is visible in figures 6.6 and 6.9 (the coordinate-radius of the star is ≈ 9M). This is expected because the source terms are not infinitely differentiable there. We believe that the overall second order of the convergence is caused by this. We also have to use a quite high resolution (*e.g.* `60x60x4` as compared to `15x15x4` in the binary black hole case) to obtain reasonable results (which can be seen in figure 6.16). This dramatically increases the runtime for initial data, but it is still tolerable (several hours to a day at most on a normal workstation).

Mixed binary data

Because we already have shown convergence of the evaluation onto the Cartesian grid in section 6.5.2 and this is not changed here, we concentrate on convergence with changing spectral resolution. Note that we do not use uniform grids for these data, because for practical reasons it is not possible to use the resolution needed to resolve the black hole in the entire computational domain, which also covers the neutron star. Instead, we use box-in-box mesh refinement.

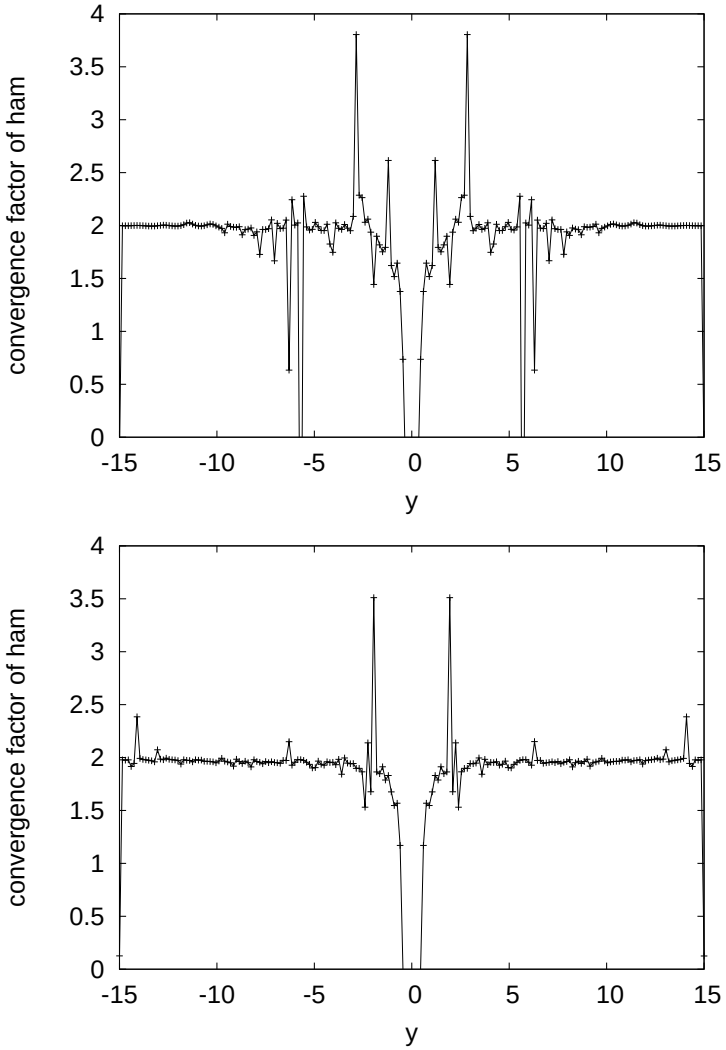

Figure 6.12: Convergence factor of the Hamiltonian constraint for increasing resolution of the Cartesian grid. The slices shown are parallel to the y-axis, through the star (upper plot) and through the location of the second "puncture" (lower plot).

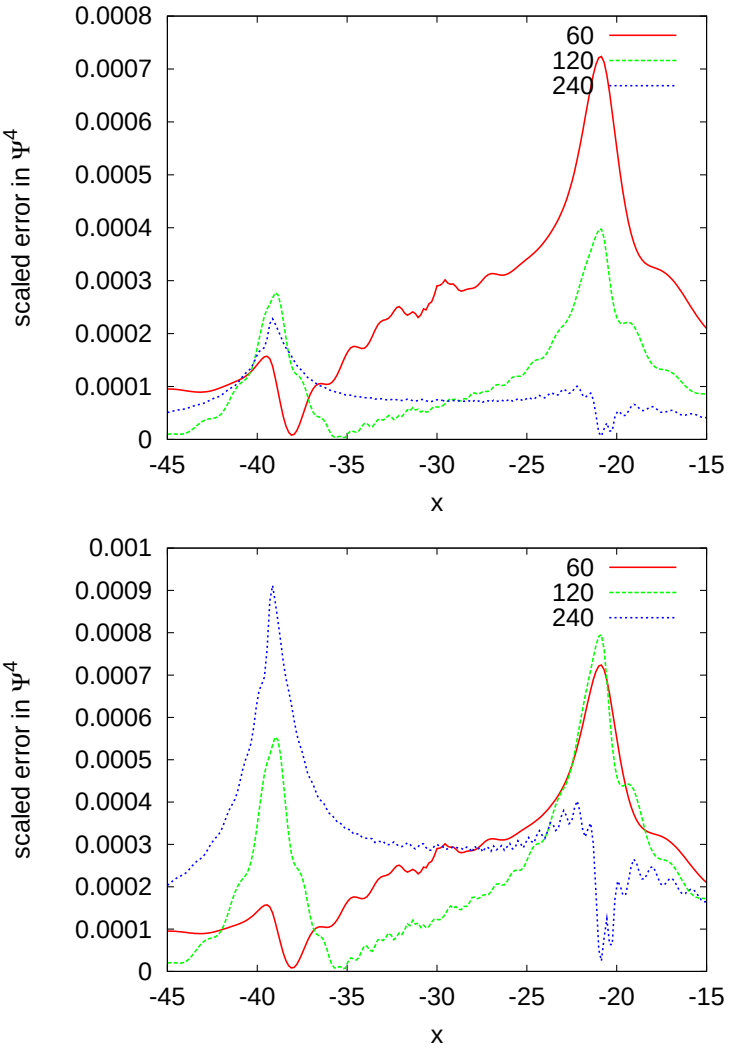

Figure 6.13: Error in the conformal factor for different spectral resolutions along the x-axis, through the star, scaled for second order (upper plot) and third order (lower plot) of convergence.

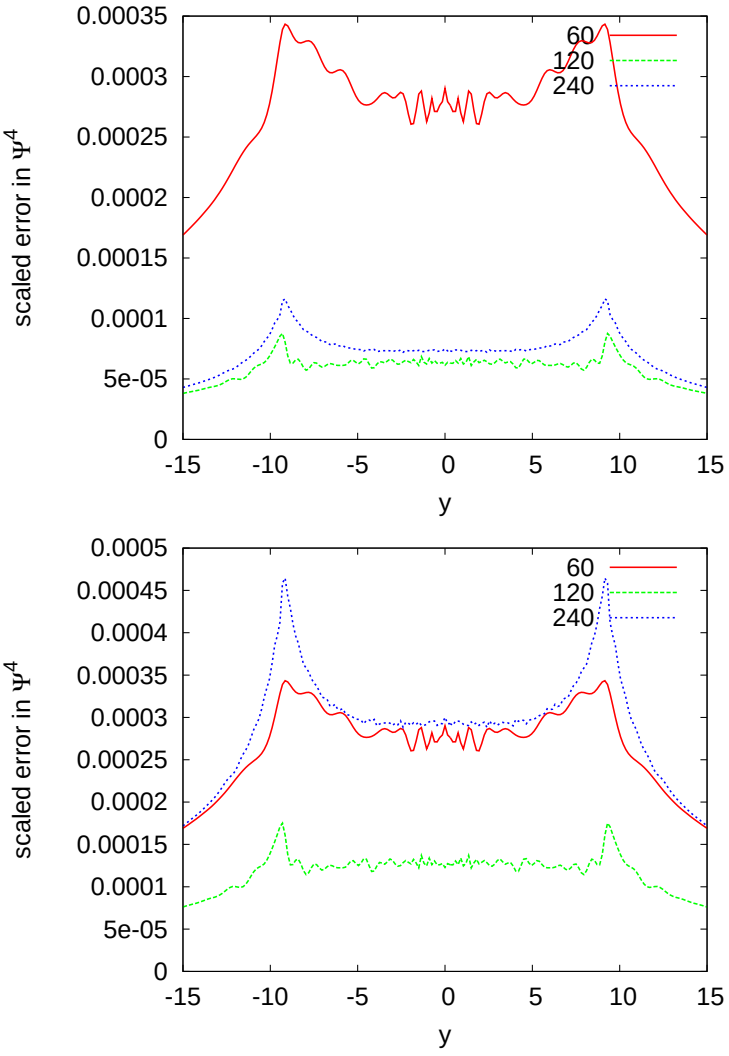

Figure 6.14: Error in the conformal factor for different spectral resolutions parallel to the y-axis, through the centre of the star, scaled for second order (upper plot) and third order (lower plot) of convergence.

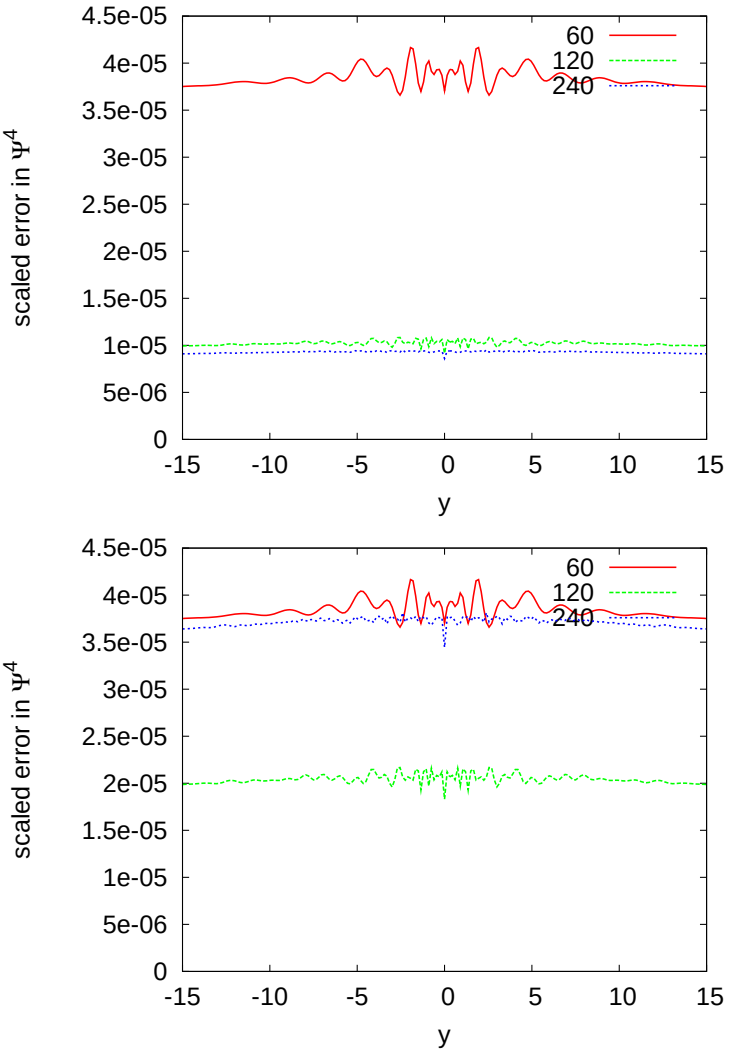

Figure 6.15: Error in the conformal factor for different spectral resolutions parallel to the y-axis, through the location of the second "puncture", scaled for second order (upper plot) and third order (lower plot) of convergence.

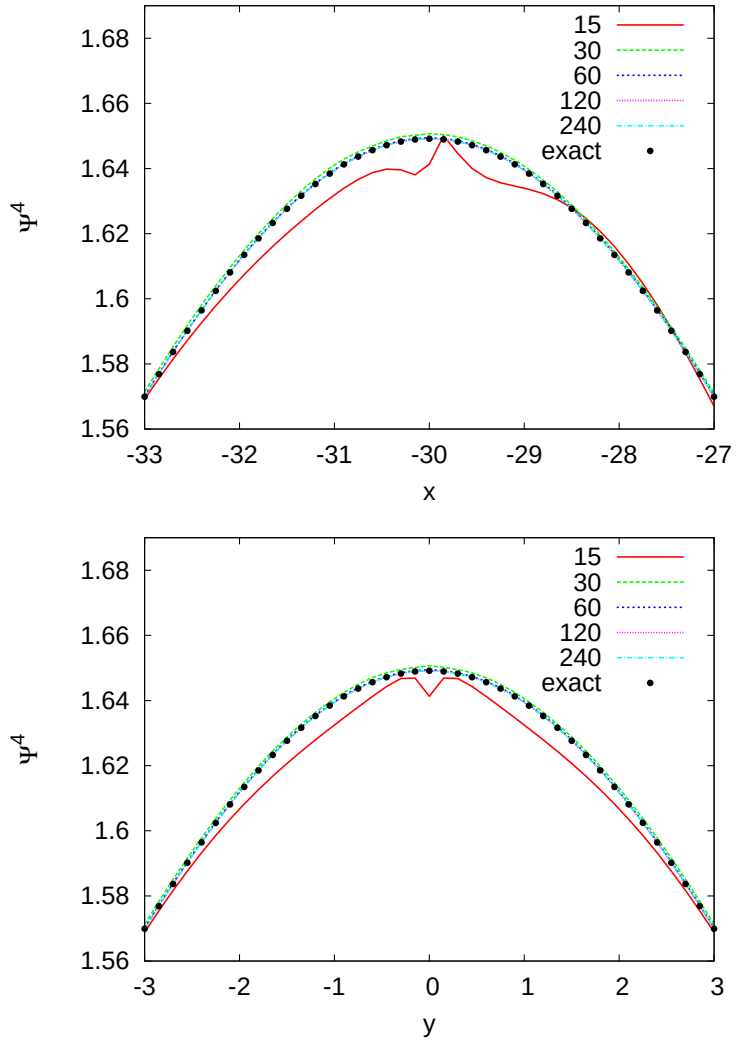

Figure 6.16: Conformal factor plotted for different spectral resolutions, along the x-axis (upper plot) and y-axis (lower plot) and zoomed to the centre of the star at ($x = -30$M,$y = 0$M). The errors at low resolution are clearly visible.

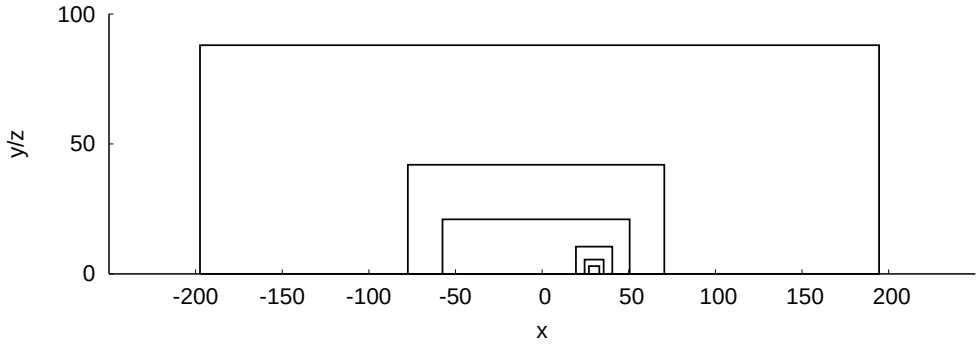

Figure 6.17: Computational setup of the mixed binary problem discussed here. Shown are the borders of the six mesh refinement levels. Due to the use of reflection symmetry at the x-y and the x-z plane, we only have to use grid points at positive y and positive z coordinates.

The physical setup for the following study is a neutron star with mass 1.14M and a black hole with mass 5M at a coordinate distance of 60M from each other ($b = 30$). The initial velocities are zero, the initial data is conformally flat and time-symmetric. We vary the resolution of the spectral solver to test the convergence of the scheme.

The setup of the computational domain is sketched in figure 6.17. We use six levels of mesh refinement, of which three are refining the region around the black hole which needs higher resolution due to its small size compared to the neutron star. Due to the use of reflection symmetry at the x-y and the x-z plane, we only have to use grid points at positive y and positive z coordinates.

The Hamiltonian constraint violation, scaled to second and third order of convergence, is plotted in figures 6.18 and 6.19, which suggests a convergence order between two and three, except near the boundary, where it does not converge at all. However, the constraint violation is very small in that part of the domain ($\approx 1 \times 10^{-9}$) and, as will be shown later, the errors in an evolution are much larger. To quantify the convergence order further, the norm of the Hamiltonian constraint violations for different resolutions is shown in figure 6.20 together with a line indicating second order convergence. Provided that the resolution on the Cartesian grid is high enough, this shows roughly second order convergence while changing the spectral resolution.

Figure 6.21 shows the ADM mass (see equation (4.6)) of the system for different spectral resolutions and evaluated on the spectral grid, which is compactified and includes spatial infinity (the ADM mass is defined at spatial infinity), in contrast to the limited Cartesian grid. As one can see, the ADM

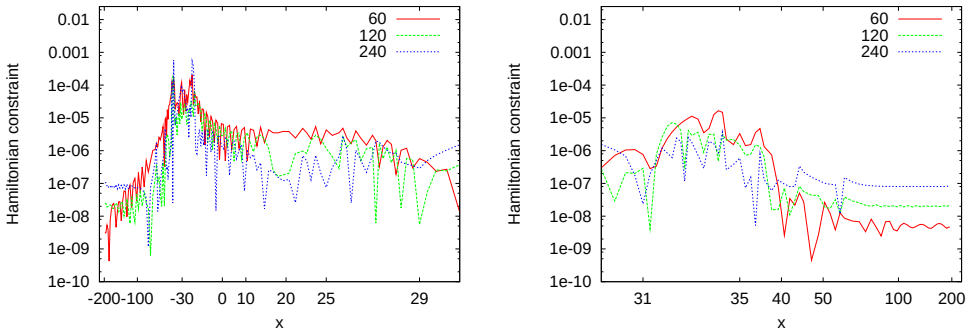

Figure 6.18: Scaled Hamiltonian constraint convergence for second order of convergence, parallel to the x-axis for a mixed binary system with the neutron star centre at $x = -30$M and the black hole at $x = 30$M. The logarithmic x-axis is used to visualise all refinement levels. The region at the center of the black hole which is not shown due to this, is not important because it will get excised in evolutions.

mass converges to a value of about 5.7808M and the order of convergence computed from the three resolutions 30, 60 and 120 is about 2.1 and from the three resolutions 60, 120 and 240 is about 3.1.

6.6 Evolutions of mixed binary data

This section contains preliminary results of evolutions of these initial data. We are able to evolve it through the merger and obtain a black hole without matter in its exterior. However, the data are not fully analysed yet and there are still problems, which will be explained in the following.

We use the same initial data as in section 6.5.2. It is expected that the two compact objects move towards the center of mass, which is located near the black hole, because it is more massive.

We found three major problems while trying to evolve this data. The first, and most serious one, is the spacetime excision scheme, which produces large errors at the excision boundaries. This has already be seen and predicted in work presented in chapter 4. These errors eventually propagate out of the apparent horizon. While no physical signal could do that, gauge and numerical effects are still able to cross that boundary. Without measures against this, it would limit the runs to about 40M in coordinate time, while the merger takes place in a coordinate time of approximately 300M. In general it is not a good practice to use only the runtime as indication for good or bad results. However, in this case the runtimes are so much below

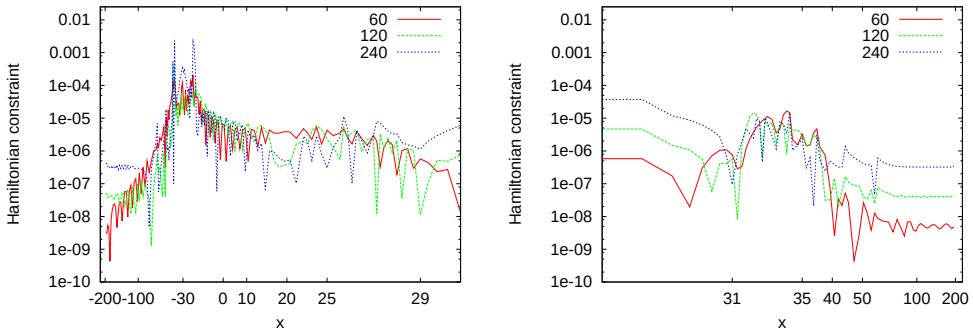

Figure 6.19: Scaled Hamiltonian constraint convergence for third order of convergence, parallel to the x-axis for a mixed binary system with the neutron star centre at $x = -30$M and the black hole at $x = 30$M. The logarithmic x-axis is used to visualise all refinement levels. The region at the center of the black hole which is not shown due to this, is not important because it will get excised in evolutions.

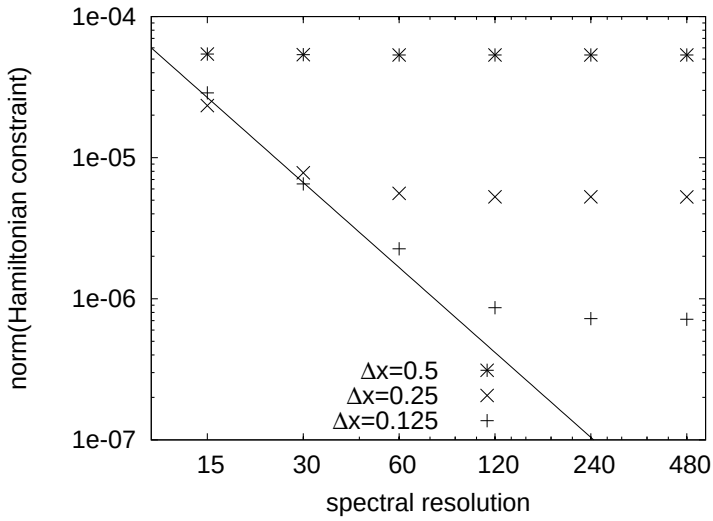

Figure 6.20: Norm of the Hamiltonian constraint along the x-axis for different spectral (x-axis) and resolutions of the Cartesian grid. The solid line corresponds to a second order convergence as comparison.

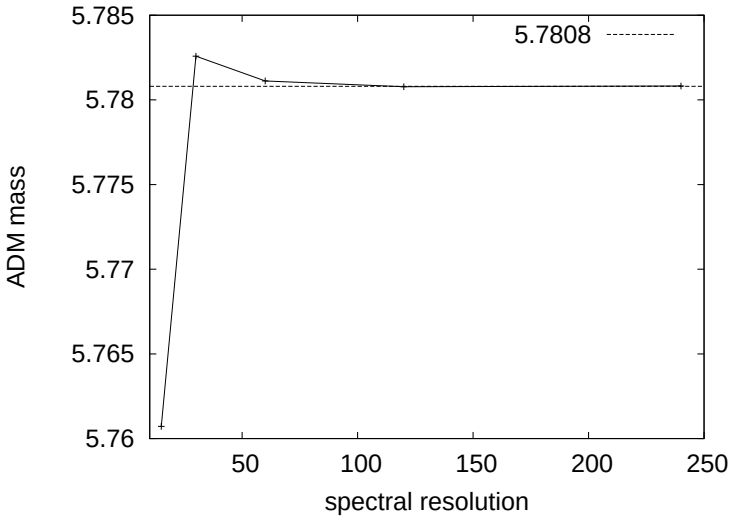

Figure 6.21: ADM mass for different spectral resolutions.

the expected time of a merger, that the use of the time of stability as measure is justified.

The errors near the excision boundary manifest themselves as oscillations in the evolved spacetime variables, *e.g.* γ_{ij} and K_{ij}. To attenuate this problem, we add a Kreiss-Oliger [277] dissipation term to the right hand sides of their evolution equations and we do the same for the gauge quantities. The dissipation term for a quantity q is of the type

$$f_{\rm diss} = -\epsilon_{\rm diss}(\Delta x)^3(\partial_x)^4 q, \tag{6.34}$$

where $\epsilon_{\rm diss}$ is the dissipation coefficient, which can be variable in space and time. Using a fourth-order finite-difference representation of the partial derivative, the dissipation term has the form

$$f_{\rm diss} = -\frac{\epsilon_{\rm diss}}{16}\frac{(q_{i-2} - 4q_{i-1} + 6q_i - 4q_{i+1} + q_{i+2})}{\Delta x}. \tag{6.35}$$

We apply this dissipation in the whole computational domain (because of the second problem, discussed below) with a small value, $\epsilon_{\rm diss}^{\rm outside}$, which rises inside the apparent horizon with a constant, steep slope to its maximal value, $\epsilon_{\rm diss}^{\rm inside}$. We found that the value of the slope is not changing the stability of the runs significantly and use a very steep one, which effectively is nearly a step-function, as can be seen in figure 6.22, where we already use the optimal values in our case of $\epsilon_{\rm diss}^{\rm outside} = 0.01$ and $\epsilon_{\rm diss}^{\rm inside} = 0.1$. We justify these values in the following.

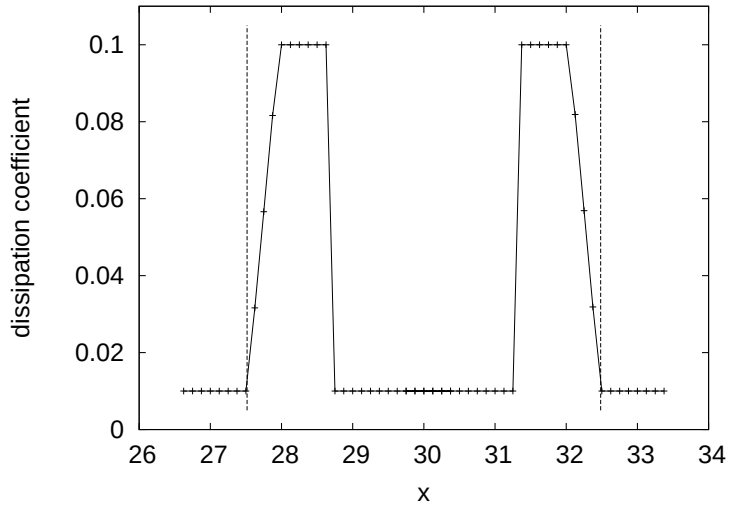

Figure 6.22: Dissipation coefficient $\epsilon_{\rm diss}^{\rm inside}$ near the black hole. The location of the apparent horizon is indicated with the dashed line. The value around $x = 30$ is lower because this is inside the excision region, where the value does not matter.

The dependence of $\epsilon_{\rm diss}^{\rm inside}$ on the stability of the simulations is shown in figure 6.23, using $\epsilon_{\rm diss}^{\rm outside} = 0$. The optimum value is approximately $\epsilon_{\rm diss}^{\rm inside} = 0.1$, which we use in the following.

The second problem while evolving these data is connected to the use of mesh refinement. The problem with the introduction of refined grids is the natural introduction of refinement boundaries. Small errors are introduced at these boundaries, which can easily lead to instabilities of the code (*e.g.* see [247]). One commonly used possibility to cure those small oscillations, which eventually trigger instabilities, is again dissipation. But in contrast to the dissipation applied inside the apparent horizon, a value of $\epsilon_{\rm diss}^{\rm outside} = 0.01$ is usually enough. The effect of this dissipation outside the apparent horizon on the life-time of the simulations is shown in figure 6.24. There we show the dependency of the life-time on the size of the excision region with and without dissipation outside the apparent horizon. The excision region is in all cases a sphere with a fixed radius. Note that without the small dissipation outside, the lifetime does not seem to have a precise dependence on the size of the excision region. We believe that this is caused by the small errors at the refinement boundaries interacting with the errors from the excision region (which are strongly depending on the shape of the excised region). However if we apply a small dissipation in the whole computational domain, these errors are damped and the simulations have a longer life-time, which

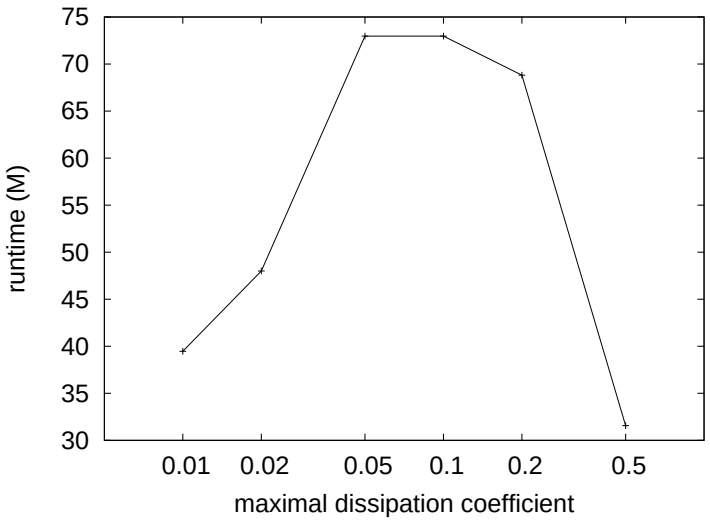

Figure 6.23: Runtime (in coordinate time) depending on the value of the dissipation coefficient $\epsilon_{\text{diss}}^{\text{inside}}$ near the black hole, with $\epsilon_{\text{diss}}^{\text{outside}} = 0$.

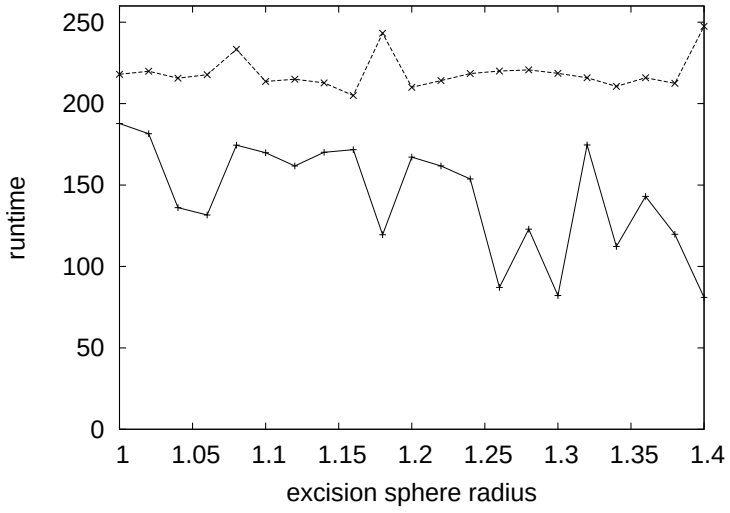

Figure 6.24: Shown is the runtime (in coordinate time) of the evolutions. The solid line represents simulations with $\epsilon_{\text{diss}}^{\text{outside}} = 0$, the dashed line represents simulations with $\epsilon_{\text{diss}}^{\text{outside}} = 0.01$. As can be seen, a small amount of dissipation does not only increase the runtime, it also reduces the undesired dependence of the runtime on the size of the excision sphere.

shows only a weak dependence on the size of the excision region.

The third of the problems encountered is related to the motion of the black hole and it is the cause of the crashes of the simulations shown in figure 6.24. This is the obvious consequence of the fact that the excised region is held fixed.

If nothing is done to prevent the black hole from moving, a very steep gradient of the metric develops near the excision boundary of the black hole towards the neutron star (grid stretching). Eventually, this peak cannot be resolved anymore, and a code crash inevitably follows.

An obvious solution to this problem is to allow for the motion of the excised region, which, in turn, requires a proper handling of the regions of the grid that need no longer to be excised, but rather to be populated with relevant data (see *e.g.* [216, 233, 278]). This is technically possible, but not yet implemented in our code. Another possibility would be to let the excision region grow while making sure that all points inside this region stay inside. While this could indeed potentially increase the life-time, it is limited by the size of the apparent horizon (which can also shrink during the simulation, and actually does so during the merger, as will be shown later in figure 6.30) and the distance (in coordinate length) the black hole is moving. The third possibility, which has proven to be successful in our implementation, is to try to minimise the black hole movement by steering the shift vector according to the position of the apparent horizon. This idea is not new; it was already mentioned in [142, 279].

We used the latter possibility in the following. In addition to the Gamma-driver shift condition, mentioned in section 2.7, we use a constant shift correction depending on the position of the apparent horizon. The shift is then adjusted, using a damped, harmonic oscillator approach, such that the position is driven back to a desired place. This is similar to the approach used in [37].

Assume the desired position to be x_d, the actual measured position to be x_m and define $x_h \equiv x_m - x_d$. Then the contribution to the shift evolution which is coming from this correction can be calculated using a damped, harmonic oscillator

$$T^2 \ddot{x_h} + 2Td\dot{x_h} + x_h = 0 \tag{6.36}$$

with T defining the timescale and d the damping factor of the oscillator. This leads to

$$\ddot{x_h} = -\frac{1}{T^2}(2Td\dot{x_h} + x_h), \tag{6.37}$$

which is added to the right hand side of the evolution equation for the shift vector (2.118), for each coordinate direction.

The constants T and d have to be adjusted according to the specific problem, where excessively small values for T or excessively large values for d can lead to instabilities. A too large value for T reduces the effect of this correction and is not helpful. A too small value for d can lead to undesired oscillations in the shift. We found that values of $T = 10$ and $d = 1$ work best in our particular case. Using this correction, the position of the black hole can be held fixed allowing for the evolution to proceed and it increases the life-time of the simulations from ≈ 230M to ≈ 1700M.

As expected, both objects start to move towards the center of mass. However, because we use the shift to keep the black hole at a fixed position on the grid, only the neutron star appears to be moving in these coordinates. This can be seen in figures 6.25 to 6.28, which shows snapshots of the rest mass density together with the apparent horizon of the black hole, plotted over the x-y-plane. This shows a direct merger, no matter is left outside the apparent horizon.

In the early phase of the simulation, the neutron star starts to oscillate for a little less than one period of the fundamental frequency, before the influence of the black hole starts to show as an increasing frequency of the oscillation and finally the star is captured. The maximum density of the star is shown in figure 6.29 together with a trigonometric function with the frequency of the fundamental mode of the unperturbed star (at ≈ 1.28kHz), measured in a separate simulation. Despite the fact that the procedure of obtaining the initial data in general changes the physical quantities of the initial guess, the two frequencies are, at least at the beginning of the merger, remarkably similar.

The black hole is not oscillating before the merger, but is expected to start damped oscillations afterwards. The frequency of the quasi normal mode for a black hole [280, 281] with $l = 2$ and $n = 0$ is approximately

$$f \approx 0.37367 \times 2\pi(5142\text{Hz}) \times (M_\odot/M). \tag{6.38}$$

Figure 6.31 shows the ratio of the circumferences of the black hole in the yz/xy-planes for two different resolutions and a fit with a frequency of $f = 2.06$kHz as comparison. Using equation (6.38), this corresponds to a black hole mass of ≈ 5.86M. The agreement with the measured mass of the apparent horizon in the simulation using the higher resolution is remarkable (see figure 6.32). However, this ceases to be the case for lower resolution. This shows that high resolution near the black hole apparent horizon is crucial.

The mass of the apparent horizon is plotted over time in figure 6.32. Before merger, the mass should be approximately constant, but shows a

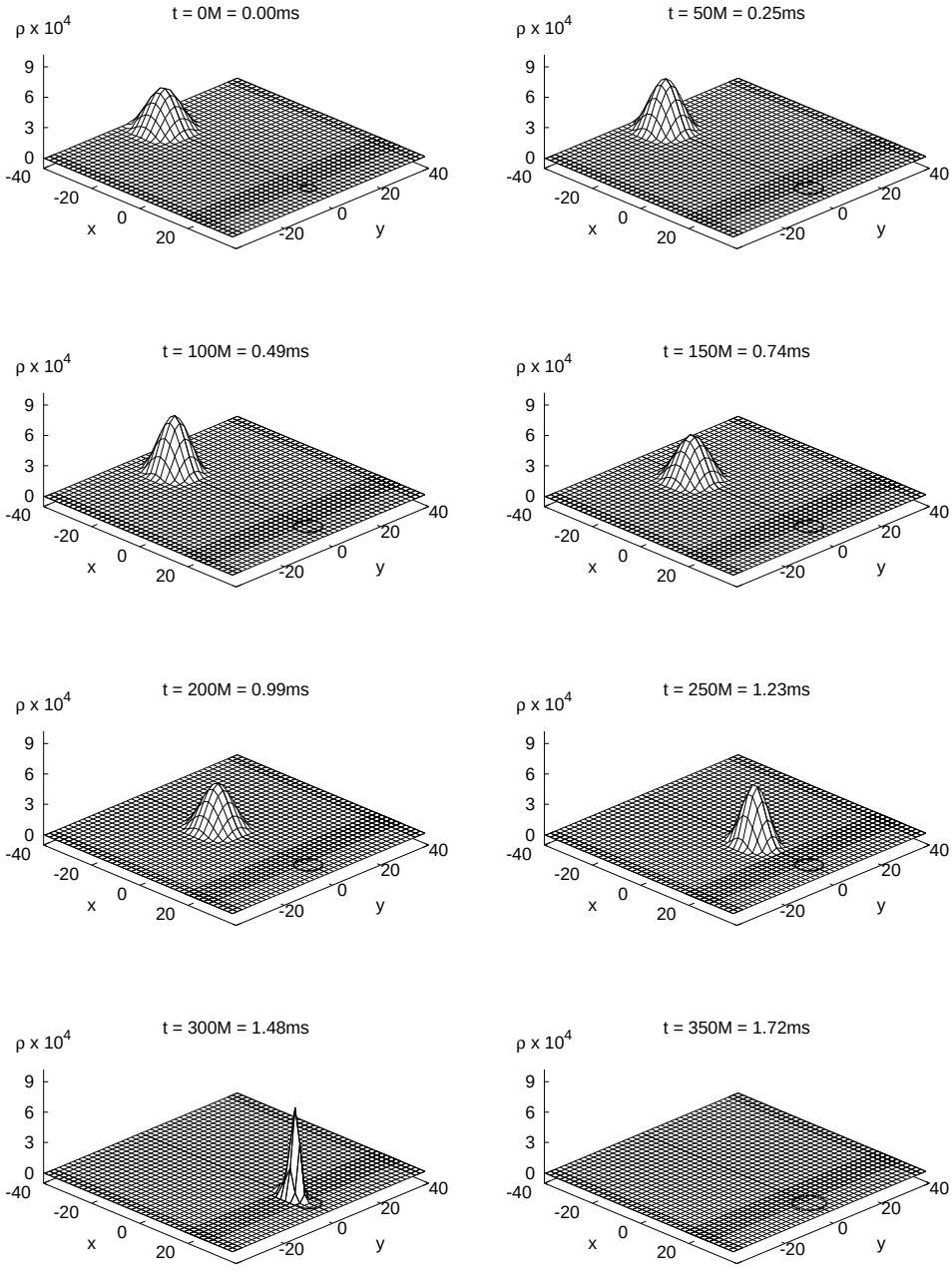

Figure 6.25: Rest mass density and apparent horizon shape in the x-y-plane. Shown are times from 0M to 350M in steps of 50M (from top left to bottom right).

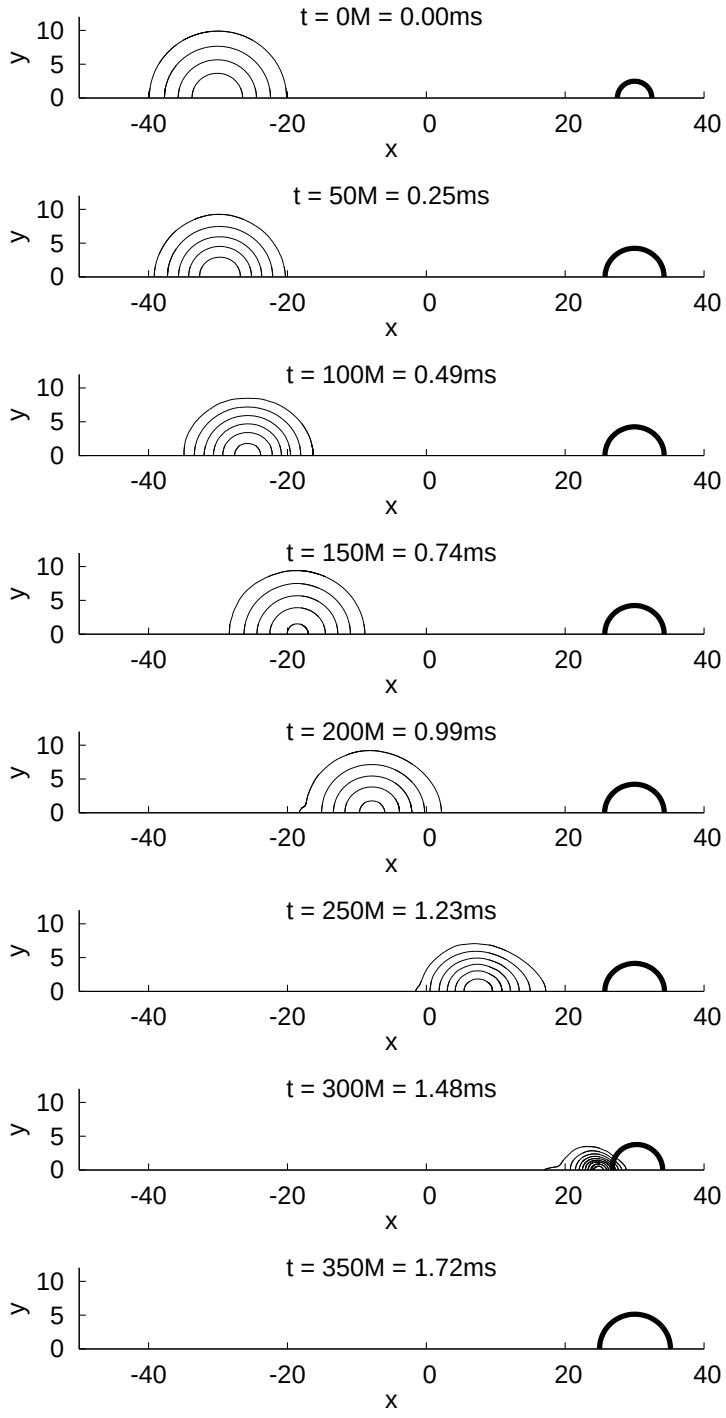

Figure 6.26: Isocontours of the rest mass density and apparent horizon shape in the x-y-plane. Shown are times from 0M to 350M in steps of 50M.

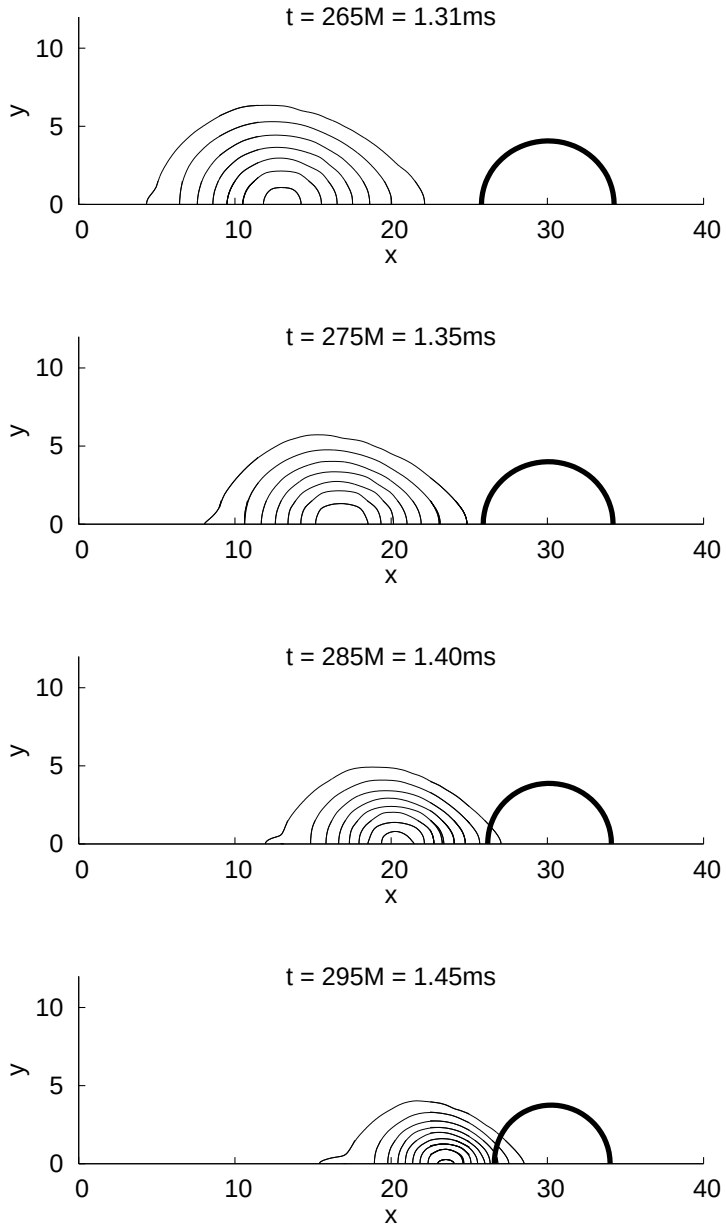

Figure 6.27: Isocontours of the rest mass density and apparent horizon shape in the x-y-plane. Shown are times from 265M to 295M in steps of 10M.

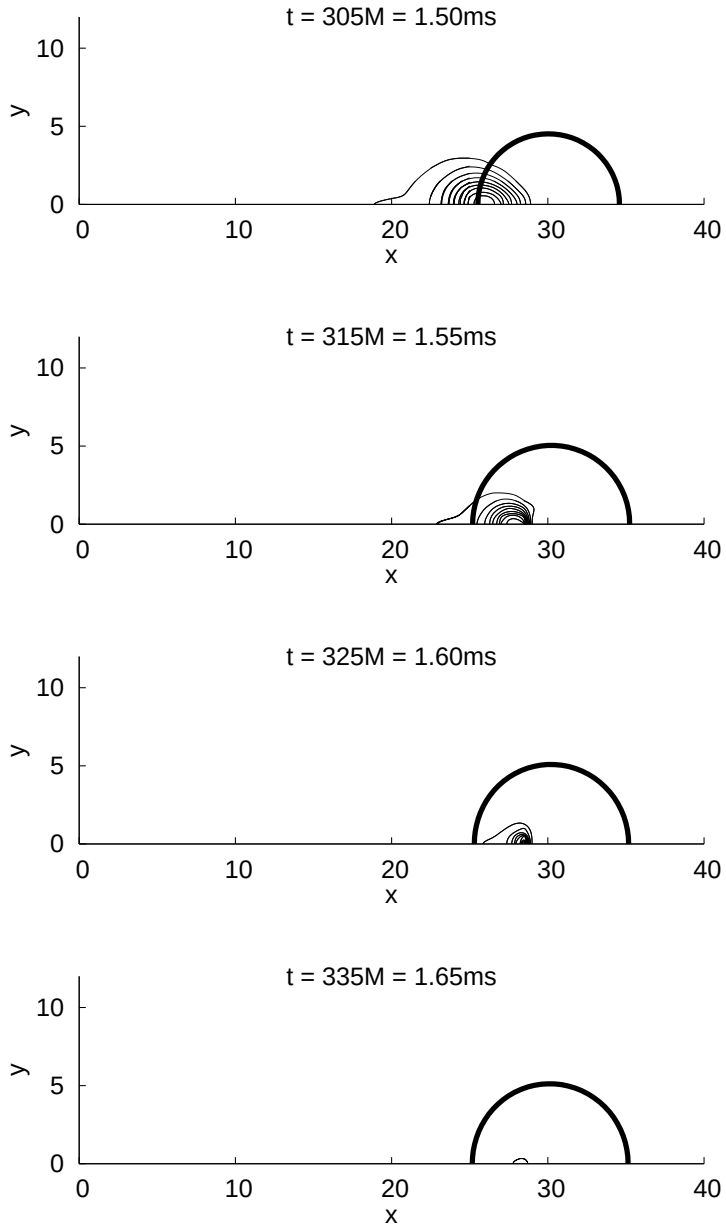

Figure 6.28: Isocontours of the rest mass density and apparent horizon shape in the x-y-plane. Shown are times from 305M to 335M in steps of 10M.

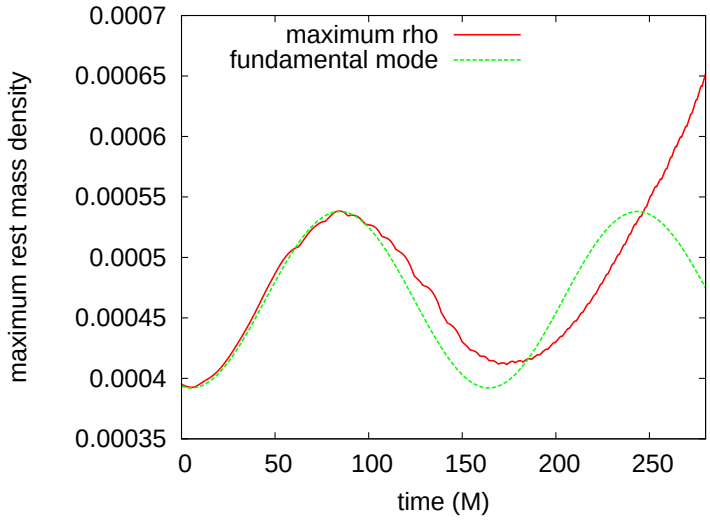

Figure 6.29: Shown is the maximal rest mass density ρ over time (solid line) and as comparison a trigonometric function with the frequency of the fundamental mode of the unperturbed star of $f \approx 1.28$kHz.

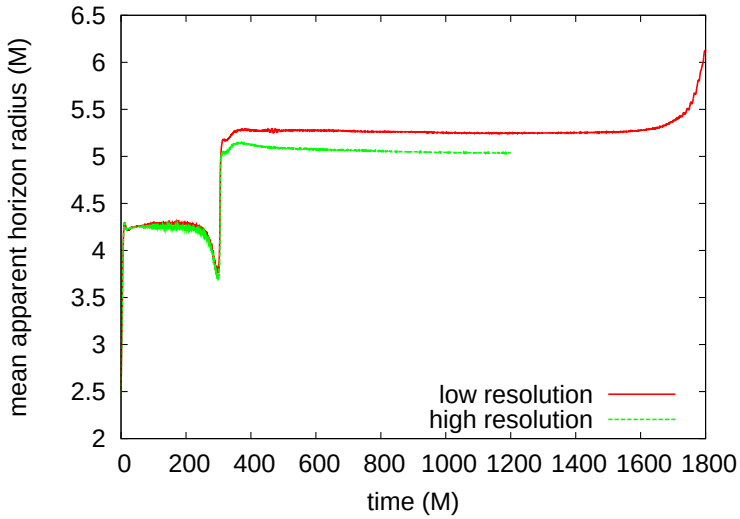

Figure 6.30: Shown is the coordinate radius of the black hole for two different resolutions, depending on time. For a short time after the start of the simulation, the radius increases from 2.5M to more than 4M, because the shift is not yet large enough the prevent the grow. At the time of merger, the radius shortly and rapidly decreases, in order to increase to reach a more or less stable value. In this high-resolution case, however, this value is slowly decreasing.

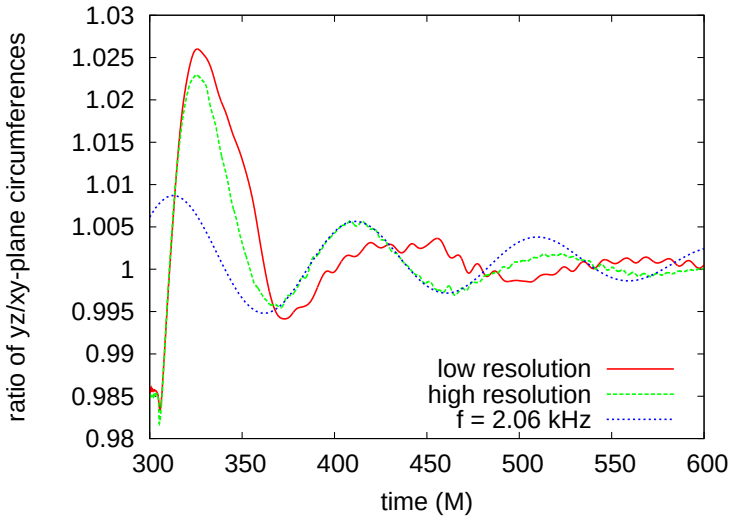

Figure 6.31: Shown is the ratio of the circumferences of the black hole in the yz/xy-planes for two different resolutions and a fit with a frequency of $f \approx 2.06$kHz as comparison.

small, constant drift to higher masses. There is some spurious radiation content in the spacetime initially, which could cause such a drift. However, this drift decreases strongly with increasing resolution, as can be seen in the zoomed figure 6.33. This indicates that the drift is not due to spurious radiation, but is a numerical effect. At $t \approx 300$, the neutron star merges with the black hole, thus the mass of the apparent horizon increases. After the neutron star is captured and no more matter is falling into the black hole, its mass is again nearly constant in the low-resolution case, and starts to decrease slightly in the high-resolution case. This decrease is due to numerical errors, which we believe are due to the slightly decreasing apparent horizon radius. This could be cured by an adapted shift condition in future simulations.

The mass of the final black hole should not be greater than the initially measured ADM mass. In fact, it should be a bit smaller, because part of the energy of the system should have been radiated out of the computational domain in form of gravitational waves. However, in our simulations the mass of the final black hole is larger than the ADM mass. Part of this error is coming from the drift of the measurement of the apparent horizon mass. In figure 6.34, the effect of the drift has been removed by subtracting the mass increase produced by it until the merger. This shows, that the difference of the mass of the final black hole and the ADM mass is not only caused by the drift, but is also a result of the truncation error. This suggests that the resolution is still not adequate to resolve the merger correctly. The zoomed

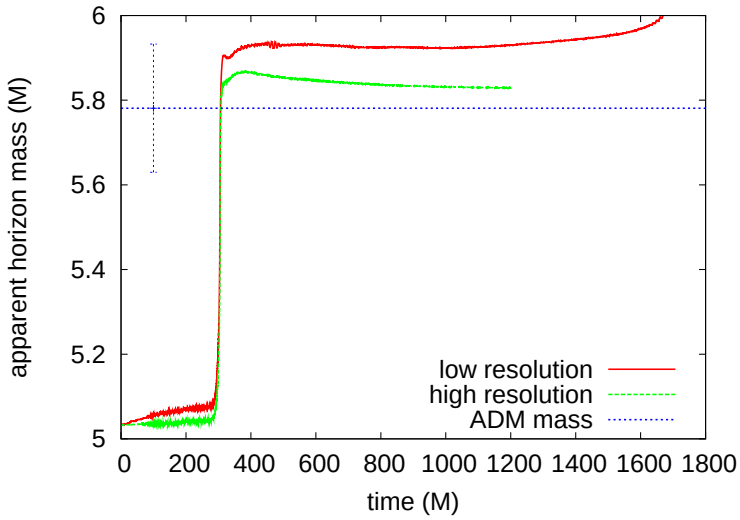

Figure 6.32: Mass of the apparent horizon over time for two different resolutions and compared to the ADM mass, which is measured on the initial data and which is different on the finite computational domain, as is indicated by the error bars.

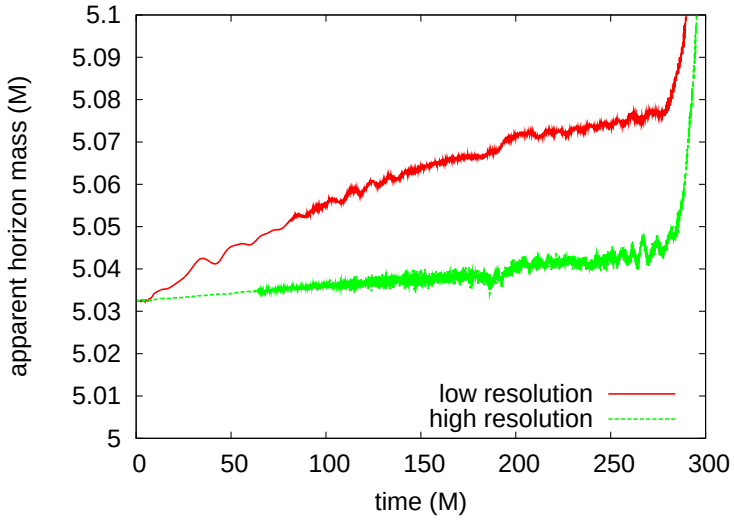

Figure 6.33: Mass of the apparent horizon over time for two different resolutions and zoomed to visualise the resolution-depending drift.

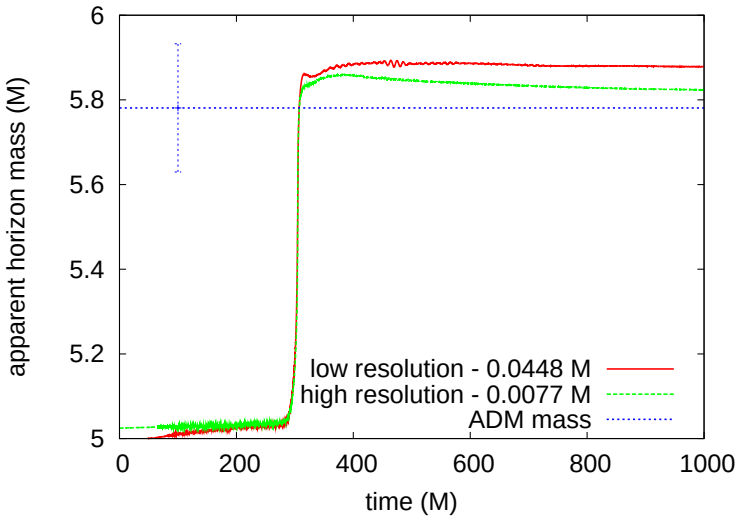

Figure 6.34: Mass of the apparent horizon over time with the effect of the mass drift removed for shortly before merger ($t = 280$M) for two different resolutions and compared to the ADM mass, which is measured on the initial data and which is different on the finite computational domain, as is indicated by the error bars.

figure 6.35 shows that the steep mass increase is not resolved correctly at low resolution and is potentially also not well resolved at the high resolution used here. However, simulations with even higher resolution are computationally so demanding, that they have to be the topic of future work.

Another possible source for this difference, or part of it, could be errors coming from the excision boundary. The problem is that during the merger, the coordinate radius of the apparent horizon shortly decreases below its nearly constant value before the merger, as can be seen in figure 6.30. Hence, also the distance between the apparent horizon and the excision boundary decreases, and the errors coming from this boundary might influence the exterior of the black hole. This undesired effect of a shrinking apparent horizon radius is due to the shift condition we use. We plan to investigate in modifications to this condition to attenuate or eliminate this effect.

However, it is not expected that the mass of apparent horizon after the merger converges to the ADM mass measured initially. The reason is that the ADM mass has to be measured at infinity. Using finite grids, as we do here, results in an error, which depends on the location of the boundary. The larger the computational domain is, the smaller this error is. We used a variant of equation (4.6) to calculate an approximation to the ADM mass

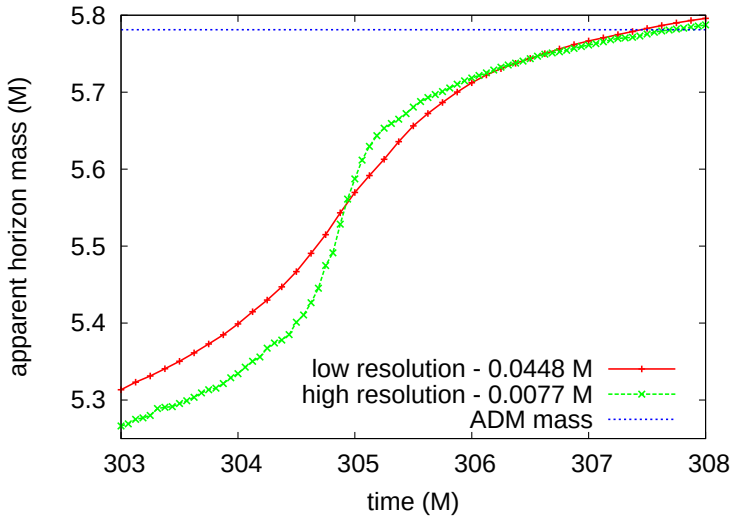

Figure 6.35: Mass of the apparent horizon over time with the effect of the mass drift removed for shortly before merger ($t = 280$M) for two different resolutions and compared to the ADM mass, which is measured on the initial data. Shown is a zoom at the merger time to show the steep increase of the mass of the black hole.

on the finite grid:

$$M_{\mathrm{ADM}} = \frac{1}{16\pi} \oint_{\infty} \alpha \sqrt{\gamma} \gamma^{ij} \gamma^{kl} (\gamma_{ik,j} - \gamma_{ij,k}) \, \mathrm{d}S_l. \tag{6.39}$$

This differs from equation (4.6) by the factor α inside the integral. For evaluations of those equations at infinity, $\alpha = 1$ is assumed, and they are equal. For evaluations at a finite distance, however, this is usually not the case and the approximation of the ADM mass is gauge-dependent [230].

This approximation of the ADM mass can be used to obtain a lower limit on the error of the ADM mass in the system. For our case, the value given by the approximation, using equation (6.39) because $\alpha \neq 1$, and measured using a surface of finite size (the largest possible cuboid, due to the shape of the computational domain), is ≈ 5.93M, which is indicated as error bar in figure 6.34. That this error is indeed decreasing with increasing size of the computational domain, and is approaching the value measured at infinity, is shown in figures 6.36 and 6.37. This shows, that much larger computational domains are needed to reduce the error on the mass of the final black hole.

One important quantity to monitor the quality of a simulation is the violation of the constraints. Figure 6.38 shows the 2-norm of the Hamiltonian constraint violations plotted over time. Soon after starting the simulation,

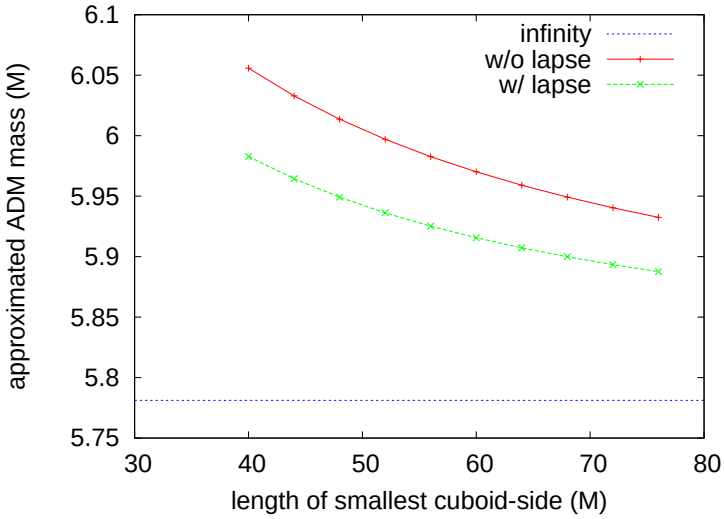

Figure 6.36: Shown is the dependence of the values of two different approximations of the ADM mass, both using a surface integral over a cuboid, on the size of that cuboid. The value evaluated at infinity is shown as comparison.

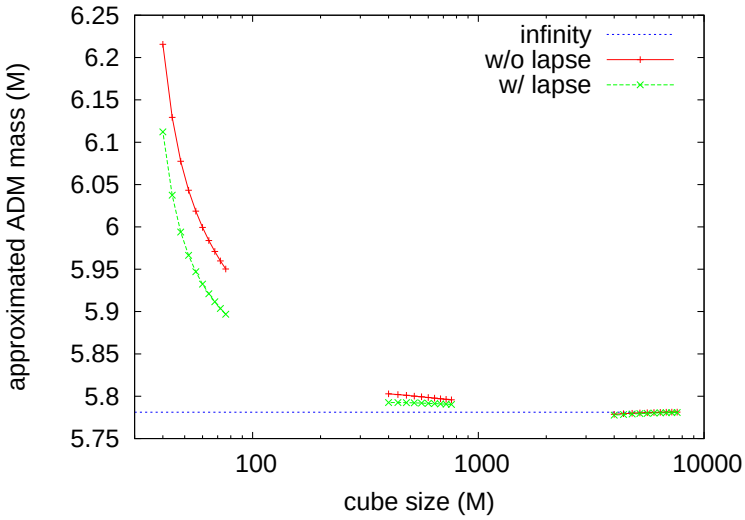

Figure 6.37: Shown is the dependence of the values of two different approximations of the ADM mass, both using a surface integral over a cube, on the size of that cube, for a wide range of sizes. Because of this wide range, the three disconnected parts of each curve belong to different resolutions of the finite difference grid. The value evaluated at infinity is shown as comparison.

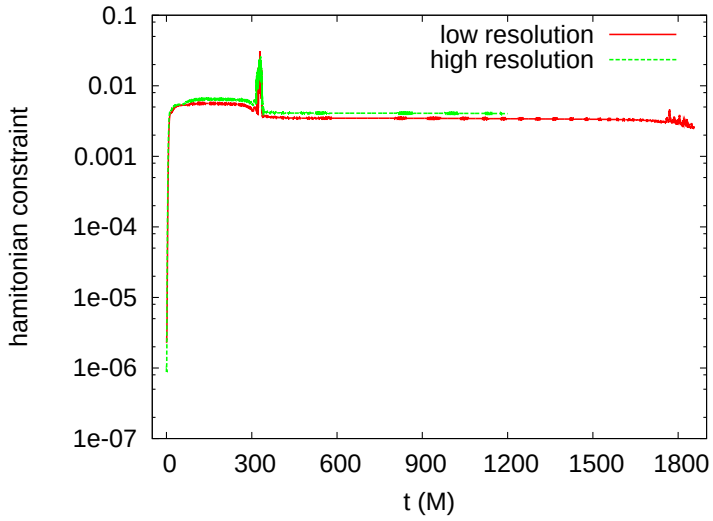

Figure 6.38: 2-norm of the Hamiltonian constraint violation over time. The time of merger is $\approx$ 300M. The value of the 2-norm of the Hamiltonian constraint is larger for higher resolution because the errors near the excision boundary are bigger in this case and they dominate the 2-norm, and because convergence is lost after $\approx$ 100M

the norm increases from the value of the initial data ($\approx 2.5 \times 10^{-6}$) by roughly three orders of magnitude. This indicates that the errors of the initial data are much smaller than the errors introduced by evolving these data. At the time of merger ($t \approx$ 300M), the violation increases rapidly by an order of magnitude, but after the merger, it settles to a smaller value than post-merger. The rise is due to the matter crossing many mesh refinement boundaries and finally the excision boundary. The fall to lower constraint violations after the merger is due to the fact that after the merger no matter is left[1].

From shortly after the merger up to $t \approx$ 1700M the violation is roughly constant, but then a rapid instability appears. The value of the 2-norm of the Hamiltonian constraint is larger for higher resolution because the errors near the excision boundary are bigger in this case and they dominate the 2-norm.

It is very important to test convergence of a numerical code not only of the initial data, but also during the simulation. Evolutions with lower resolution

[1]The term on the right-hand-side of the Hamiltonian constraint equation (2.35) has to cancel with the other terms in the presence of matter, which does not hold for the truncation error of those parts. However, in the absence of matter, the truncation error coming from the matter terms is zero, leading to an overall smaller truncation error.

than $\Delta x = 0.125$M in figure 6.20 can not be used because they resolve the problem too poorly. This is partly due to the fact that the excision region has to have a minimum size of about ≈ 8 points in the radial direction, while on the other hand, it should be as small as possible compared to the apparent horizon radius to minimise the impact the excision boundary conditions have on the region near and outside the apparent horizon.

If the finest grid has $\Delta x = 0.125$M, an excision sphere with at least 8 points in radial direction has a radius of 1M while the initial apparent horizon radius of the black hole is 2.5M. In the following, we will use an excision region of radius 1.14M.

Higher resolutions than $\Delta x = 0.125$M are possible, but the computational requirements increase by a factor of sixteen every time the resolution is doubled. Using double resolution we show convergence (or the lack of it) up to a time of 400M in figure 6.39. Except at a very low value of the Hamiltonian constraint violation ($\approx 5 \times 10^{-9}$), the initial data shows second-order convergence. The lack of convergence at this low level is not problematic, because the errors introduced by the boundary and the evolution are much bigger. At $t = 100$M the simulation is still second-order convergent in most parts of the domain. The exceptions are the region a few points away from the excision boundary, which is to be expected because the excision boundary condition is not fulfilling Einstein's equations, and the region near the outer boundary. The boundary condition of the outer boundary also does not fulfill Einstein's equations. These errors are polluting the interior of the evolution with the speed of light. The shortest distance from the center of the domain to the outer boundary is 100M. At $t = 400$M, these errors had time to cross the domain already up to two times and the convergence is destroyed.

There are two possibilities to overcome this problem. The first and elegant way would be to improve the outer boundary conditions. A lot of effort has already gone in that direction (*e.g.* [117, 246, 282–287]). However, we are not aware of better boundary conditions available for our situation at the moment. The other possibility is to put the outer boundary as far away from the interesting region as possible by using a large, coarse grid. This is computationally very expensive, but it is the most practical solution at the moment.

6.7 Future Work

While we are now able to simulate the merger of a black hole and a neutron star using time-symmetric and axisymmetric initial data, there are still problems to be solved. The first is that we have to be able to show convergence

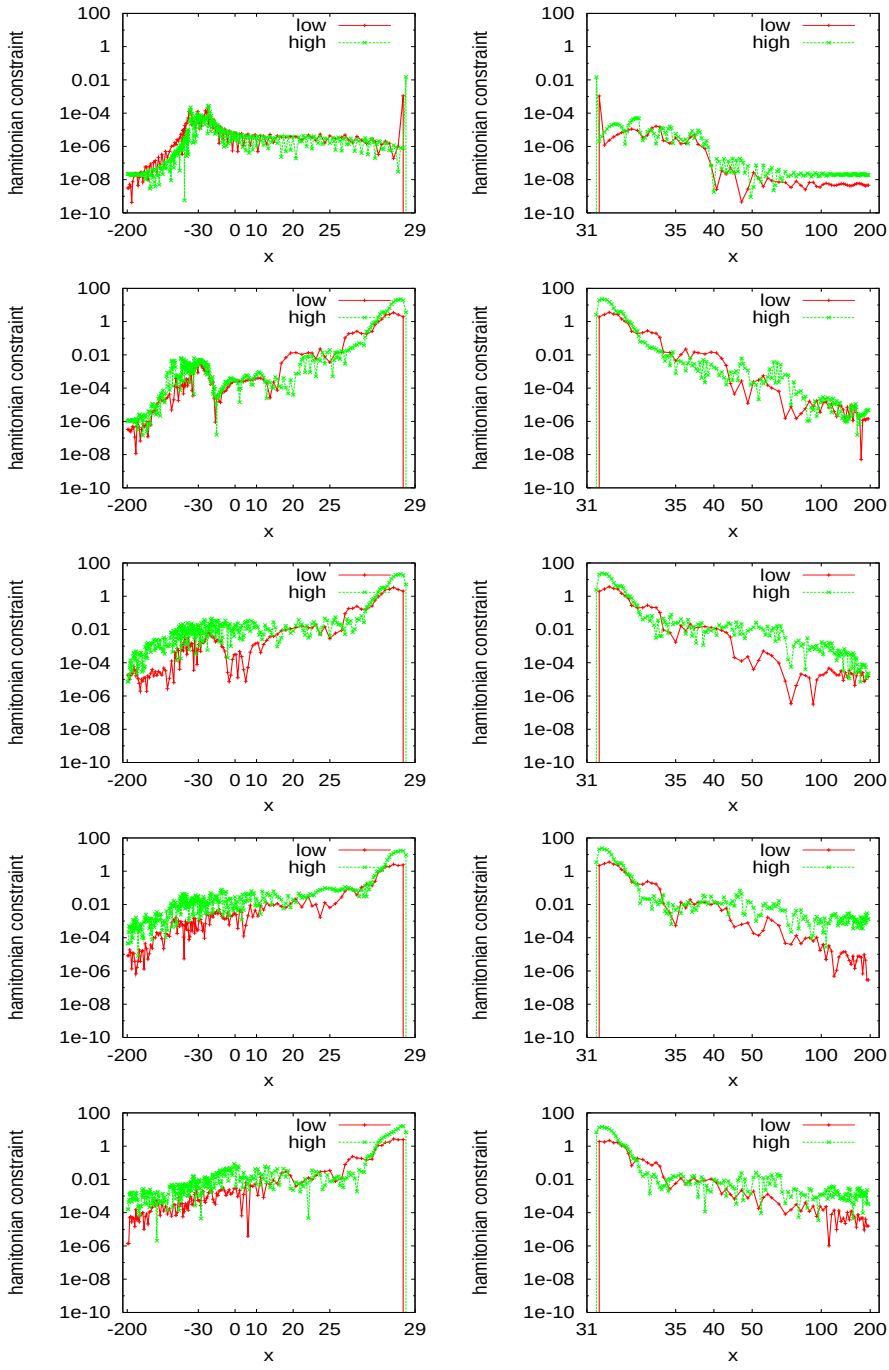

Figure 6.39: Hamiltonian constraint violation along the x-direction for two resolutions, scaled for second order of convergence. Shown are times from 0M to 400M in steps of 100M (from top down).

of the simulations even after the merger. This is related to the quality of the outer boundary conditions. To reduce the effect of the errors from these conditions, the position of the outer boundaries will have to be set much further away from the binary system. This requires further, computationally more expensive simulations because of the bigger computational domain.

Another problem is the error coming from the excision boundary conditions on the spacetime variables. Dissipation is able to attenuate, but not solve this problem. Excision boundary conditions for the spacetime variables are a long-standing problem (*e.g.* [133, 217–220]), but they still have to be investigated in future work. There is hope, that this problem can be solved in the near future. One reason for this belief is the presence of analytical studies of such boundaries, *e.g.* based on summation by parts techniques as in [213, 214, 233], which show much better behaviour near the excision boundary. Another reason are upcoming codes using multipatch techniques in which it is natural to align excision boundaries to grid boundaries and which show extraordinary stability near the excision region [234].

The techniques described in this thesis can in principle also be applied to the creation of initial data for a binary system of two neutron stars and its evolution. Comparing the differences of mergers of binary black hole, mixed binary and binary neutron star systems, in particular differences in the produced gravitational waves, would also be very interesting.

Future work is not only necessary on the evolutions, also the initial data will have to be extended. The current initial data solver is limited to time-symmetric initial data, because the momentum constraints of Einstein's field equations are not solved. We do not expect major problems in removing this limitation, because this already had been done once (see section 6.4) for an old code.

Once this is resolved, a wide and detailed study of mixed binary systems can be started. The main goals are, firstly, to understand the dynamics of such systems better, *e.g.* the occurrence and form of disruption of the neutron star before merger, and secondly, to extract the gravitational wave signals from those merger simulations.

However, it is likely that some of the many simplifications of the currently used model also have to be lifted to gain physically meaningful data. Some of the possible improvements are more realistic EOSs and the treatment of magnetic fields, on which work is already going on (see *e.g.* [288, 289]).

The methods and simulations presented in this thesis are only a starting point for detailed studies of binaries of a neutron star and a black hole. Both, improved methods and models, and simulations using higher resolutions and/or better adapted coordinates (*e.g.* multi-grid-models), will have to be the focus of future work.

Such detailed studies of mixed binary systems are expected to give information about the radiated gravitational waves and may also help to clarify the processes involved in short gamma ray bursts [25].

6.8 Summary

In this chapter, different approaches for obtaining initial data for a mixed binary system have been discussed. These methods have in common that they solve the elliptic equation for the Hamiltonian constraint in the York-Lichnerowicz conformal decomposition. The currently used solver uses spectral methods with adapted coordinates on one domain.

In the second part of the chapter, preliminary results of evolutions using the previously discussed initial data are shown. A number of problems encountered, and how they can be solved or at least attenuated, is mentioned.

One of these problems is the error, which is introduced by the excision boundary conditions on the spacetime variables. We show, that the use of dissipation in the region between this boundary and the apparent horizon can attenuate this problem. However, better excision boundary conditions for the spacetime variables will have to be the focus of future work.

The second problem is that small errors coming from the mesh refinement boundaries possibly lead to instabilities. We show, that the use of a very small amount of dissipation, also outside the apparent horizon, can stabilise the simulations.

The third, big problem is connected with the motion of the black hole. As expected, the black hole starts to move towards the center of mass. However, the excision region covering parts of the interior of the black hole is fixed on the grid of the simulation. We show, that an additional correction term to the shift can be used to minimise the movement of the black hole on the grid. This gauge choice allows evolutions which are stable even for a long time after merger.

The simulations are stable at least for a time of ≈ 1700M after the merger, which happens at $t \approx 300$M. This is important for future work on extraction of gravitational waves because of the time the waves need to travel to the far-field, where the extraction has to be done.

A last problem which is most probably the result of the previously mentioned ones is the lack of convergence after some evolution time. We believe, that this is connected to errors coming from the outer boundary. A bigger computational domain decreases and delays this error growth near the binary, but such simulations are computationally very expensive and will be the focus of future work.

Summary

We described in this thesis, how one of the main obstacles in the way towards a simulation of a merger of a neutron star and a black hole, the treatment of the hydrodynamics at excision boundaries, can be removed. It has been shown that these methods are tested and work reliably (see chapter 4). This work has been published in Phys. Rev. D **71**, 104006 in 2005 [64].

We have underlined, that modifications to parts of the already existing numerical schemes for the treatment of the hydrodynamics equations are necessary in strong gravitational fields, *e.g* near a black hole. We have implemented and tested these modifications (MPPM) and have shown that they yield to accurate and convergent solutions.

The new excision methods for the hydrodynamics have been applied to the study of the gravitational collapse of uniformly rotating neutron stars to Kerr black holes (see chapter 5), which has been published in Phys. Rev. D **71**, 024035 in 2005 [65]. The ability to successfully perform these simulations for sufficiently long times relies on the already mentioned excision techniques and suggests, that these methods also work well in the case of a merger of a neutron star with a black hole.

Different approaches for obtaining initial data for such a system have been discussed in the first part of chapter 6. These methods have in common that they solve the elliptic equation for the Hamiltonian constraint in the York-Lichnerowicz conformal decomposition. The currently used solver uses spectral methods with adapted coordinates on one domain.

The second part of chapter 6 shows preliminary results of evolutions using the previously discussed initial data. A number of problems encountered, and how they can be solved or at least attenuated, is mentioned.

One of the problems is the error, which is introduced by the excision boundary conditions on the spacetime variables. We show, that the use of dissipation in the region between this boundary and the apparent horizon can attenuate this problem. However, better excision boundary conditions for the spacetime variables will have to be the focus of future work.

The second problem is that small errors coming from the mesh refinement

boundaries possibly lead to instabilities. We show, that the use of a very small amount of dissipation, also outside the apparent horizon, can stabilise the simulations.

The third, big problem is connected with the motion of the black hole. As expected, the black hole starts to move towards the center of mass. However, the excision region covering parts of the interior of the black hole is fixed on the grid of the simulation. We show, that an additional correction term to the shift can be used to minimise the movement of the black hole on the grid. This gauge choice allows evolutions which are stable even for a long time after merger.

The results obtained with these corrections are still preliminary. The simulations are stable at least for a time of ≈ 1700M after the merger, which happens at $t \approx 300$M. This is important for future work on extraction of gravitational waves because of the time the waves need to travel to the far-field, where the extraction has to be done.

A last problem which is most probably the result of the previously mentioned ones is the lack of convergence after some evolution time. We believe, that this is connected to errors coming from the outer boundary. A bigger computational domain decreases and delays this error growth near the binary, but such simulations are computationally very expensive and will be the focus of future work.

Zusammenfassung

In dieser Dissertation wurde beschrieben, wie eine der größeren Schwierigkeiten auf dem Weg zu Simulationen eines Zusammenstoßes eines Neutronensterns und eines schwarzen Lochs, nämlich die Behandlung der Hydrodynamik an Ausschneiderändern, beseitigt werden kann. Es wurde dargelegt, dass diese Methoden gut getestet sind und verlässlich arbeiten (siehe Kapitel 4). Diese Arbeit wurde in Phys. Rev. D **71**, 104006 (2005) [64] veröffentlicht.

Es hat sich gezeigt, dass in starken Gravitationsfeldern Änderungen an Teilen der schon existierenden numerischen Techniken für die Behandlung der Hydrodynamikgleichungen notwendig sind. Wir haben diese Änderungen (MPPM) implementiert und getestet und haben gezeigt, dass sie zu richtigen und konvergierenden Lösungen führen.

Die neuen Ausschneidemethoden für die Hydrodynamik wurden in einer Studie zu gravitativem Kollaps gleichförmig rotierender Neutronensterne zu schwarzen Löchern (Kerr) angewandt (siehe Kapitel 5), die in Phys. Rev. D **71**, 024035 (2005) [65] veröffentlicht wurde. Die Fähigkeit, diese Simulationen erfolgreich mit einer ausreichenden Simulationszeit durchzuführen, hängt von den genannten Ausschneidetechiken ab und deutet an, dass diese Methoden auch im Fall einer Simulation eines Zusammenstoßes eines Neutronensterns mit einem schwarzen Loch funktionieren.

Im ersten Teil des Kapitel 6 werden verschiedene Ansätze für die Gewinnung von Anfangsdaten für solch ein System diskutiert. Diese Methoden haben gemein, dass sie die elliptische Gleichung für die Hamiltonbedingung im Formalismus der York-Lichnerowicz-konformen-Zerlegung lösen. Der im Moment verwendete Lösungsalgorithmus benutzt spektrale Methoden mit an das Problem angepassten Koordinaten für den gesamten Lösungsbereich.

Im zweiten Teil von Kapitel 6 werden vorläufige Ergebnisse von Evolutionen der zuvor diskutierten Anfangsdaten gezeigt. Die Probleme beim Aufbau solcher Simulationen und deren Lösung beziehungsweise Abschwächung sind außerdem erwähnt.

Eines dieser Probleme ist der Fehler, der durch die ungenügend gute Ausschneidebedingung der Raumzeitvariablen entsteht. Wir konnten zeigen, dass

Dissipation im Bereich zwischen dem inneren Rand und dem scheinbaren Horizont des schwarzen Lochs das Problem abschwächen kann. Natürlich wären bessere Ausschneiderandbedingungen der Raumzeitvariablen vorzuziehen, müssen aber Gegenstand zukünftiger Arbeit bleiben.

Ein zweites Problem sind die kleinen Fehler, die von den Gitterverfeinerungsgrenzen herrühren und unter Umständen zu Instabilitäten führen. Wir haben gezeigt, dass eine schwache Dissipation, auch außerhalb des scheinbaren Horizonts, die Simulationen stabilisieren kann.

Das dritte der größeren Probleme hängt mit der Bewegung des schwarzen Lochs zusammen. Erwartungsgemäß beginnt das schwarze Loch, sich auf das Massezentrum zuzubewegen. Das Ausschneidegebiet, welches Teile des schwarzen Lochs bedeckt, ist jedoch fest an das Simulationsgitter gebunden. Wir konnten zeigen, dass ein zusätzlicher Korrekturterm zur Verschiebung der Koordinaten dazu benutzt werden kann, die Bewegung des schwarzen Lochs auf dem Gitter zu minimieren. Diese Eichbedingung erlaubte stabile Simulationen, sogar viel länger als bis zum Zusammenstoß.

Die mit diesen Korrekturen erhaltenen Resultate sind jedoch als vorläufig zu betrachten. Die Simulationen sind für eine Zeit von mindestens 1700M nach dem Zusammenstoß bei $t \approx 300$M stabil. Das ist wichtig für die zukünftigen Pläne, die Gravitationswellen des Zusammenstoßes in diesen Simulationen zu messen, weil die Wellen eine gewisse Zeit brauchen, um ins Fernfeld zu gelangen, wo sie dann gemessen werden können.

Ein Problem, welches höchstwahrscheinlich die Folge der schon genannten anderen Probleme ist, ist das Fehlen von Konvergenz nach einiger Evolutionszeit. Wir glauben, dass dies mit den Fehlern, die von den äußeren Rändern her das Simulationsgebiet verunreinigen, zusammenhängt. Ein größeres Simulationsgebiet würde diese Fehler vermindern und das Eintreffen im Zentrum verzögern, aber solche Simulationen sind sehr rechenintensiv und müssen deshalb Thema zukünftiger Arbeit bleiben.

Bibliography

[1] A. Burrows. Supernova explosions in the Universe. *Nature*, 403:727–733, February 2000.

[2] G. Baym, H. A. Bethe, and C. J. Pethick. Neutron star matter. *Nucl. Phys. A*, 175:225–271, 1971.

[3] D. G. Ravenhall, C. J. Pethick, and J. R. Wilson. Structure of Matter below Nuclear Saturation Density. *Physical Review Letters*, 50:2066–2069, 1983.

[4] P. Magierski, A. Bulgac, and P.-H. Heenen. Exotic nuclear phases in the inner crust of neutron stars in the light of Skyrme-Hartree-Fock theory. *Nuclear Physics A*, 719:217–220, 2003.

[5] P. W. Anderson and N. Itoh. Pulsar glitches and restlessness as a hard superfluidity phenomenon. *Nature*, 256:25–27, 1975.

[6] M. A. Alpar, D. Pines, P. W. Anderson, and J. Shaham. Vortex creep and the internal temperature of neutron stars. I - General theory. *Astrophys. J.*, 276:325–334, 1984.

[7] M. Ruderman. Crust-breaking by neutron superfluids and the VELA pulsar glitches. *Astrophys. J.*, 203:213–222, 1976.

[8] J. R. Oppenheimer and H. Snyder. On continued gravitational contraction. *Phys. Rev. D*, 56:455–459, 1939.

[9] R. Crowley, D. Macdonald, R. Price, I. Redmount, Suen, K. Thorne, and X.-H. Zhang. *Black Holes: The Membrane Paradigm*. Yale University Press, 1986.

[10] R. Penrose. Gravitational collapse: The role of general relativity. *Riv. Nuovo Cimento*, 1:252, 1969.

[11] B. J. Carr and James E. Lidsey. Primordial black holes and generalized constraints on chaotic inflation. *Phys. Rev. D*, 48:543–553, 1993.

[12] Ilia Musco, John C. Miller, and Luciano Rezzola. Computations of primordial black-hole formation. *Class. Quantum Grav.*, 22:1405–1424, 2005.

[13] M. Burgay *et al.* The highly relativistic binary pulsar PSR J0737-3039A: Discovery and implications. 2004. astro-ph/0405194.

[14] Krzysztof Belczynski, Vassiliki Kalogera, and Tomasz Bulik. A comprehensive study of binary compact objects as gravitational wave sources: Evolutionary channels, rates, and physical properties. *Astroph. J.*, 572: 407, 2002.

[15] M. Burgay, N. D'Amico, A. Possenti, R.N. Manchester, A.G. Lyne, B.C. Joshi, M.A. McLaughlin, M. Kramer, J.M. Sarkissian, F. Camilo, V. Kalogera, C.Kim, and D.R. Lorimer. An increased estimate of the merger rate of double neutron stars from observations of a highly relativistic system. *Nature*, 426:531–533, 2003.

[16] V. Kalogera, C. Kim, D. R. Lorimer, M. Burgay, N. D'Amico, A. Possenti, R. N. Manchester, A. G. Lyne, B. C. Joshi, M. A. McLaughlin, M. Kramer, J. M. Sarkissian, and F. Camilo. In-spiral rates of double neutron stars. *Astrophys. J.L.*, 601:L179–L182, 2004.

[17] H. Bethe and G. Brown. Evolution of binary compact objects that merge. *Astroph. J.*, 506:780, 1998.

[18] I.H. Stairs, Z. Arzoumanian, F. Camilo, A.G. Lyne, D.J. Nice, J.H. Taylor, S.E. Thorsett, and A. Wolszczan. Measurement of relativistic orbital decay in the PSR B1534+12 binary system. *Astrophys. J.*, 505: 352, 1998.

[19] M. Vallisneri. What can we learn about neutron stars from gravity-wave observations? In *Proceedings of the 25th J. Hopkins Workshop on Current Problems in Particle Theory, 2001*, 2002.

[20] R. Narayan, Tsvi Piran, and A. Shemi. Neutron star and black hole binaries in the galaxy. *Astrophys. J.*, 379:L17–L20, 1991.

[21] M. Bejger, D. Gondek-Rosinska, E. Gourgoulhon, K. Taniguchi, and J.L. Zdunik. Impact of the nuclear equation of state on the last orbits of binary neutron stars. *Astron. Astroph.*, 431:297–306, 2005.

[22] R. Narayan, B. Paczynski, and Tsvi Piran. Gamma-ray bursts as the death throes of massive binary stars. *Astrophys. J.*, 395:L83, 1992.

[23] C.L. Fryer, S.E. Woosley, and D.H. Hartmann. Formation rates of black hole accretion disk gamma-ray bursts. *Astrophys. J.*, 526:152, 1999. astro-ph/9904122.

[24] Tsvi Piran. Gamma-ray bursts and the fireball model. *Phys.Rept.*, 314: 575–667, 1999.

[25] D. B. Fox, D. A. Frail, P. A. Price, S. R. Kulkarni, E. Berger, T. Piran, A. M. Soderberg, S. B. Cenko, P. B. Cameron, A. Gal-Yam, M. M. Kasliwal, D.-S. Moon, F. A. Harrison, E. Nakar, B. P. Schmidt, B. Penprase, R. A. Chevalier, P. Kumar, K. Roth, D. Watson, B. L. Lee, S. Shectman, M. M. Phillips, M. Roth, P. J. McCarthy, M. Rauch, L. Cowie, B. A. Peterson, J. Rich, N. Kawai, K. Aoki, G. Kosugi, T. Totani, H.-S. Park, A. MacFadyen, and K. C. Hurley. The afterglow of GRB050709 and the nature of the short-hard gamma-ray bursts. *Nature, in press (Oct 6 issue)*, 2005. astro-ph/0510110.

[26] C. Kouveliotou, C. A. Meegan, G. J. Fishman, N. P. Bhat, M. S. Briggs, T. M. Koshut, W. S. Paciesas, and G. N. Pendleton. Identification of two classes of gamma-ray bursts. *Astrophys. J.*, 413:L101–L104, 1993.

[27] S.F. Portegies Zwart. Gamma-ray binaries: Stable mass transfer from a neutron star to a black hole. *Astrophys. J. Lett.*, 503:L53, 1998.

[28] M. Coleman Miller. Prompt mergers of neutron stars with black holes. *Astrophys. J.*, 626:L41, 2005.

[29] M. Alcubierre, W. Benger, B. Brügmann, G. Lanfermann, L. Nerger, E. Seidel, and R. Takahashi. 3D Grazing Collision of Two Black Holes. *Phys. Rev. Lett.*, 87:271103, 2001.

[30] P. Anninos, D. Hobill, E. Seidel, L. Smarr, and W.-M. Suen. Collision of two black holes. *Phys. Rev. Lett.*, 71(18):2851–2854, 1993.

[31] P. Anninos, D. Hobill, E. Seidel, L. Smarr, and W.-M. Suen. The head-on collision of two equal mass black holes: Numerical methods. Technical Report 24, National Center for Supercomputing Applications, 6 1994.

[32] P. Anninos, D. Hobill, E. Seidel, L. Smarr, and W.-M. Suen. Head-on collision of two equal mass black holes. *Phys. Rev. D*, 52(4):2044–2058, 1995.

[33] P. Anninos, K. Camarda, J. Massó, E. Seidel, W.-M. Suen, and J. Towns. Three-dimensional numerical relativity: The evolution of black holes. *Phys. Rev. D*, 52(4):2059–2082, 1995.

[34] T. W. Baumgarte. Innermost stable circular orbit of binary black holes. *Phys. Rev. D*, 62:024018, 2000.

[35] S. Brandt, R. Correll, Roberto Gómez, Mijan F. Huq, P. Laguna, Luis Lehner, P. Marronetti, R. A. Matzner, D. Neilsen, J. Pullin, E. Schnetter, D. Shoemaker, and Jeffrey Winicour. Grazing collisions of black holes via the excision of singularities. *Phys. Rev. Lett.*, 85:5496–5499, 2000.

[36] B. Brügmann. Binary black hole mergers in 3D numerical relativity. *Int. J. Mod. Phys. D*, 8:85, 1999.

[37] Bernd Brügmann, Wolfgang Tichy, and Nina Jansen. Numerical simulation of orbiting black holes. *Phys. Rev. Lett.*, 92:211101, 2004.

[38] A. Čadež. *Colliding Black Holes*. PhD thesis, University of North Carolina at Chapel Hill, Chapel Hill, North Carolina, 1971.

[39] G. B. Cook. Three-dimensional initial data for the collision of two black holes II: Quasi-circular orbits for equal-mass black holes. *Phys. Rev. D*, 50(8):5025–5032, 1994.

[40] K. Eppley. *The Numerical Evolution of the Collision of Two Black Holes*. PhD thesis, Princeton University, Princeton, New Jersey, 1975.

[41] Eric Gourgoulhon, Philippe Grandclément, and Silvano Bonazzola. Binary black holes in circular orbits. I. A global spacetime approach. *Phys. Rev. D*, 65:044020, 2002.

[42] L. Smarr. *The Structure of General Relativity with a Numerical Illustration: The Collision of Two Black Holes*. PhD thesis, University of Texas, Austin, Austin, Texas, 1975.

[43] L. Smarr. Gauge conditions, radiation formulae and the two black hole collision. In L. Smarr, editor, *Sources of Gravitational Radiation*, page 245. Cambridge University Press, Cambridge, England, 1979.

[44] J. R. Wilson and G. J. Mathews. Instabilities in close neutron star binaries. *Phys. Rev. Lett.*, 75:4161, 1995.

[45] T. W. Baumgarte, G. B. Cook, M. A. Scheel, S. L. Shapiro, and S. A. Teukolsky. General relativistic models of binary neutron stars in quasiequilibrium. *Phys. Rev. D*, 57(12):7299–7311, 1998.

[46] Eric Gourgoulhon, Philippe Grandclément, Keisuke Taniguchi, Jean-Alain Marck, and Silvano Bonazzola. Quasiequilibrium sequences of synchronized and irrotational binary neutron stars in general relativity. I. method and tests. *Phys. Rev. D*, 63:064029, 2001.

[47] Gregory B. Cook. Initial data for numerical relativity. *Living Rev. Rel.*, 3:5, 2000. http://relativity.livingreviews.org/Articles/lrr-2000-5/index.html.

[48] W. H. Lee and W. Kluzniak. Newtonian hydrodynamics of the coalescence of black holes with neutron stars II: Tidally locked binaries with a soft equation of state. *MNRAS*, 308:780, 1999.

[49] W. H. Lee and W. Kluzniak. Newtonian hydrodynamics of the coalescence of black holes with neutron stars. I. tidally locked binaries with a stiff equation of state. *Astrophys. J.*, 526:178, 1999.

[50] C. W. Misner, K. S. Thorne, and J. A. Wheeler. *Gravitation*. W. H. Freeman, San Francisco, 1973.

[51] B. Paczynsky and P. J. Wiita. Thick accretion disks and supercritical luminosities. *Astron. Astrophys.*, 88:23–31, 1980.

[52] Stephan Rosswog. Mergers of neutron star black hole binaries with small mass ratios: nucleosynthesis, gamma-ray bursts and electromagnetic transients. *accepted for publication in Astrophys. J.*, 2005. astro-ph/0508138.

[53] Thomas W. Baumgarte, Monica L. Skoge, and Stuart L. Shapiro. Black hole-neutron star binaries in general relativity: Quasiequilibrium formulation. *Phys. Rev. D*, 70:064040, 2004.

[54] J. W. York. Conformal 'thin-sandwich' data for the initial-value problem of general relativity. *Phys. Rev. Lett.*, 82:1350–1353, 1999.

[55] Miguel Alcubierre, Bernd Brügmann, Peter Diener, Francisco Siddhartha Guzmán, Ian Hawke, Scott Hawley, Frank Herrmann, Michael Koppitz, Denis Pollney, Edward Seidel, and Jonathan Thornburg. Dynamical evolution of quasi-circular binary black hole data. *Physical Review D*, 72:044004 (14 pages), 5 August 2005. URL `http://link.aps.org/abstract/PRD/v72/e044004`.

[56] Mark Miller. On the circular orbit approximation for initial data in numerical relativity. *Phys. Rev. D*, 69:124013, 2004. gr-qc/0305024.

[57] Mark Miller, Philip Gressman, and Wai-Mo Suen. Towards a realistic neutron star binary inspiral: Initial data and multiple orbit evolution in full general relativity. *Phys. Rev. D*, 69:064026, 2004.

[58] Keisuke Taniguchi, Thomas W. Baumgarte, Joshua A. Faber, and Stuart L. Shapiro. Black hole-neutron star binaries in general relativity: effects of neutron star spin. *submitted to Phys. Rev.*, D, 2005. astro-ph/0505450.

[59] Nigel T. Bishop, Roberto Gómez, Luis Lehner, Manoj Maharaj, and Jeffrey Winicour. Characteristic initial data for a star orbiting a black hole. *Phys. Rev. D*, 72:024002, 2005.

[60] H. Friedrich and J. Stewart. *Proc. R. Soc.*, A385:345–371, 1983.

[61] R. Isaacson, J. Welling, and Jeffrey Winicour. Null cone computation of gravitational radiation. *J. Math. Phys.*, 24:1824, 1983.

[62] J. Winicour. Newtonian gravity on the null cone. *Journal of Mathematical Physics*, 24:1193–1198, 1983.

[63] Nigel T. Bishop, Roberto Gómez, Luis Lehner, Manoj Maharaj, and Jeffrey Winicour. High-powered gravitational news. *Phys. Rev. D*, 56 (10):6298–6309, 15 November 1997.

[64] I. Hawke, F. Löffler, and A. Nerozzi. Excision methods for high resolution shock capturing schemes applied to general relativistic hydrodynamics. *Phys. Rev. D*, 71:104006, 2005.

[65] Luca Baiotti, Ian Hawke, Pedro J. Montero, Frank Löffler, Luciano Rezzolla, Nikolaos Stergioulas, José A. Font, and Ed Seidel. Three-dimensional relativistic simulations of rotating neutron star collapse to a kerr black hole. *Phys. Rev. D*, 71:024035, 2005.

[66] Neil Ashby. Relativity in the global positioning system. *Living Rev. Rel.*, 6:1, 2003. http://www.livingreviews.org/lrr-2003-1.

[67] Terry Pratchett, Ian Stewart, and Jack Cohen. *The Science of Discworld*. Ebury press, revised 2002 edition, 1999. ISBN 0091886570.

[68] Terry Pratchett, Ian Stewart, and Jack Cohen. *The Science of Discworld II, The Globe*. Ebury press, 2003 edition, 2002. ISBN 0091888050.

[69] E. Poisson. Gravitational radiation from a particle in circular orbit around a black hole. VI. Accuracy of the post-Newtonian expansion. *Phys. Rev. D*, 52:5719–5723, 1995.

[70] E. Poisson. Erratum and Addendum: Gravitational radiation from a particle in circular orbit around a black hole. VI. Accuracy of the post-Newtonian expansion. *Phys. Ref. D*, 55:7980–7981, 1997.

[71] K. Schwarzschild. Über das Gravitationsfeld eines Massenpunktes nach der Einsteinchen Theorie. *Sitzunsber. Dtsch. Akad. Wiss Berlin, Kl. Math. Phys. Tech.*, pages 189–196, 1916.

[72] K. Schwarzschild. Über das Gravitationsfeld einer Kugel aus inkompressibler Flüssigkeit nach der Einsteinschen Theorie. *Sitzunsber. Dtsch. Akad. Wiss Berlin, Kl. Math. Phys. Tech.*, pages 424–434, 1916.

[73] H. Stephani. *General Relativity*. Press Syndicate of the University of Cambridge, The Pitt Building, Trumpington Street, Cambridge CB2 1RP, reprint of second edition, 2000 (original 1977). ISBN 0-521-37941-5.

[74] H. Reissner. Über die Eigengravitationn des elektrischen Felds nach der Einsteinshen Theorie. *Ann. Phys.*, 50:106–120, 1916.

[75] S. W. Hawking and G. F. R. Ellis. *The Large Scale Structure of Space-time*. Cambridge University Press, Cambridge, England, 1973.

[76] R.M. Wald and Vivek Iyer. Trapped surfaces in the Schwarzschild geometry and cosmic censorship. *Phys. Rev. D*, 44:R3719–R3722, 1992.

[77] Roger Penrose. Gravitational collapse and space-time singularities. *Phys. Rev. Lett.*, 14:57, 1965.

[78] R. P. Kerr. Gravitational field of a spinning mass as an example of algebraically special metrics. *Phys. Rev. Lett.*, 11:237–238, 1963.

[79] T. E. Newman, E. Couch, K. Chinnapared, A. Exton, A. Prakash, and R. Torrence. Metric of a rotating charged mass. *J. Math. Phys.*, 6: 918–919, 1965.

[80] I. Fukuda. A statistical study of rotational velocities of the stars. *Astronomical Society of the Pacific*, 94:271–284, 1982.

[81] W. Baade and F. Zwicky. On Super-novae. *Proceedings of the National Academy of Science*, 20:254, 1934.

[82] W. Baade and F. Zwicky. Remarks on Super-Novae and Cosmic Rays. *Physical Review*, 46:76–77, 1934.

[83] N. Itoh. Hydrostatic Equilibrium of Hypothetical Quark Stars. *Progress of Theoretical Physics*, 44:291–292, 1970.

[84] E. Witten. Cosmic separation of phases. *Phys. Rev. D*, 30:272–285, 1984.

[85] R. X. Xu. Strange quark stars - a review. 1996. astro-ph/0211348.

[86] P. Haensel. Equation of state of dense matter and maximum mass of neutron stars. In C. Motch and J.-M. Hameury, editors, *Final Stages of Stellar Evolution*, 7. EDP Sciences, 2003. astro-ph/0301073.

[87] I.H. Stairs, S.E. Thorsett, J.H. Taylor, and A. Wolszczan. Studies of the relativistic binary pulsar PSR B1534+12. *Astrophys. J.*, 581: 501–508, 2001.

[88] H. Dimmelmeier, J. A. Font, and E. Müller. Relativistic simulations of rotational core collapse. II. Collapse dynamics and gravitational radiation. *Astron. Astrophys.*, 393:523–542, 2002.

[89] M. Shibata and K. Uryu. Gravitational waves from the merger of binary neutron stars in a fully general relativistic simulation. *Prog. Theor. Phys.*, 107:265, 2002.

[90] S. L. Shapiro. Differential Rotation in Neutron Stars: Magnetic Braking and Viscous Damping. *Astrophys. J.*, 544:397–408, November 2000.

[91] J. N. Cook, S. L. Shapiro, and B. C. Stephens. Magnetic Braking and Viscous Damping of Differential Rotation in Cylindrical Stars. *Astrophys. J.*, 599:1272–1292, December 2003.

[92] Y. T. Liu and S. L. Shapiro. Magnetic Braking in Differentially Rotating, Relativistic Stars. *ArXiv Astrophysics e-prints*, December 2003.

[93] J. M. Lattimer and M. Prakash. Neutron star structure and the equation of state. *Astrophys. J.*, 550:426–442, 2000.

[94] Masaru Shibata, Keisuke Taniguchi, and Takashi Nakamura. Location of the innermost stable circular orbit of binary neutron stars in the post Newtonian approximations of general relativity. *Prog. Theor. Phys. Suppl.*, 128:295–333, 1997. gr-qc/9801004.

[95] B. Mukhopadhyay and R. Misra. Pseudo-Newtonian Potentials to Describe the Temporal Effects on Relativistic Accretion Disks around Rotating Black Holes and Neutron Stars. *Astrophys. J.*, 582:347–351, 2003.

[96] J. Fukue. General Relativity and the Pseudo-Newtonian Potential. *Publications of the Astronomical Society of Japan*, 56:681–683, 2004.

[97] J. Fukue. Easy relativity 1: Introduction to the pseudo-Newtonian potential. *Astronomical Herald*, 98:75–82, 2005.

[98] J. Fukue. Easy relativity 2: Correction to the pseudo-Newtonian potential. *Astronomical Herald*, 98:169–175, 2005.

[99] James M. Lattimer and F. Douglas Swesty. A generalized equation of state for hot, dense matter. *Nucl. Phys. A*, 535:331–376, 1991.

[100] H. Shen, H. Toki, K. Oyamatsu, and K. Sumiyoshi. Relativistic equation of state of nuclear matter for supernova and neutron star. *Nucl. Phys. A*, 637:435–450, 1998. nucl-th/9805035.

[101] P. Haensel and A. Y. Potekhin. Analytical representations of unified equations of state of neutron-star matter. *Astronomy and Astrophysics*, 428:191–197, 2004.

[102] S. L. Shapiro and S. A. Teukolsky. *Black Holes, White Dwarfs, and Neutron Stars*. John Wiley & Sons, New York, 1983.

[103] M. Ruffert and H.-T. Janka. Coalescing neutron stars - A step towards physical models. III. Improved numerics and different neutron star masses and spins. *Astronomy and Astrophysics*, 380:544–577, 2001.

[104] R. C. Tolman. Static solutions of Einstein's field equations for spheres of fluids. *Phys. Rev.*, 55:364, 1939.

[105] J. R. Oppenheimer and G. Volkoff. On massive neutron cores. *Phys. Rev.*, 55:374, 1939.

[106] F. C. Michel. Accretion of matter by condensed objects. *Astrophys. Spa. Sci.*, 15:153, 1972.

[107] Philippos Papadopoulos and J. A. Font. Relativistic hydrodynamics around black holes and horizon adapted coordinate systems. *Phys. Rev. D*, 58:24005, 1998.

[108] J. A. Font and J. M. Ibánez. A numerical study of relativistic Bondi-Hoyle accretion onto a moving black hole: Axisymmetric computations in a Schwarzschild background. *Astrophys. J.*, 494:297, 1998.

[109] A. Lichnerowicz. L'intégration des équations de la gravitation relativiste et la problème des n corps. *J. Math Pures et Appl.*, 23:37, 1944.

[110] James W. York Jr. Gravitational degrees of freedom and the initial-value problem. *Phys. Rev. Lett.*, 26:1656, 1971.

[111] James W. York Jr. Role of conformal three-geometry in the dynamics of gravitation. *Phys. Rev. Lett.*, 28:1082–1085, 1972.

[112] Harald P. Pfeiffer and Jr. York, James W. Extrinsic curvature and the Einstein constraints. *Phys. Rev.*, D67:044022, 2003.

[113] Jeffrey M. Bowen and James W. York, Jr. Time-asymmetric initial data for black holes and black hole collisions. *Phys. Rev. D*, 21(8): 2047–2056, 1980.

[114] Anil D. Kulkarni, L.C. Shepley, and James York. Initial data for n black holes. *Physics Lett.*, 96A(5):228, 1983.

[115] R. Arnowitt, S. Deser, and C. W. Misner. The dynamics of general relativity. In L. Witten, editor, *Gravitation: An Introduction to Current Research*, pages 227–265. John Wiley, New York, 1962.

[116] G. B. Cook, M. F. Huq, S. A. Klasky, M. A. Scheel, A. M. Abrahams, A. Anderson, P. Anninos, T. W. Baumgarte, N.T. Bishop, S. R. Brandt, J. C. Browne, K. Camarda, M. W. Choptuik, R. R. Correll, C. R. Evans, L. S. Finn, G. C. Fox, Roberto Gómez, T. Haupt, L. E. Kidder, P. Laguna, W. Landry, Luis Lehner, J. Lenaghan, R. L. Marsa, J. Masso, R. A. Matzner, S. Mitra, Philippos Papadopoulos, M. Parashar, L. Rezzolla, M. E. Rupright, F. Saied, P. E. Saylor, E. Seidel, S. L. Shapiro, D. Shoemaker, L. Smarr, W. M. Suen, B. Szilagyi, S. A. Teukolsky, M. H. P. M. van Putten, P. Walker, Jeffrey Winicour, and J. W. York Jr. Boosted three-dimensional black-hole evolutions with singularity excision. *Phys. Rev. Lett*, 80:2512–2516, 1998.

[117] A. M. Abrahams, L. Rezzolla, M. E. Rupright, A. Anderson, P. Anninos, T. W. Baumgarte, N. T. Bishop, S. R. Brandt, J. C. Browne, K. Camarda, M. W. Choptuik, G. B. Cook, R. R. Correll, C. R. Evans, L. S. Finn, G. C. Fox, R. Gómez, T. Haupt, M. F. Huq, L. E. Kidder, S. A. Klasky, P. Laguna, W. Landry, L. Lehner, J. Lenaghan,

R. L. Marsa, J. Massó, R. A. Matzner, S. Mitra, P. Papadopoulos, M. Parashar, F. Saied, P. E. Saylor, M. A. Scheel, E. Seidel, S. L. Shapiro, D. Shoemaker, L. Smarr, B. Szilagyi, S. A. Teukolsky, M. H. P. M. van Putten, P. Walker, J. Winicour, and Jr J. W. York. Gravitational wave extraction and outer boundary conditions by perturbative matching. *Phys. Rev. Lett.*, 80:1812–1815, 1998.

[118] Roberto Gómez, Luis Lehner, R.L. Marsa, Jeffrey Winicour, A. M. Abrahams, A. Anderson, P. Anninos, T. W. Baumgarte, N. T. Bishop, S. R. Brandt, J. C. Browne, K. Camarda, M. W. Choptuik, G. B. Cook, R. Correll, C. R. Evans, L. S. Finn, G. C. Fox, T. Haupt, M. F. Huq, L. E. Kidder, S. A. Klasky, P. Laguna, W. Landry, J. Lenaghan, J. Masso, R. A. Matzner, S. Mitra, Philippos Papadopoulos, M. Parashar, L. Rezzolla, M. E. Rupright, F. Saied, P. E. Saylor, M. A. Scheel, E. Seidel, S. L. Shapiro, D. Shoemaker, L. Smarr, B. Szilagyi, S. A. Teukolsky, M. H. P. M. van Putten, P. Walker, and J. W. York Jr. Stable characteristic evolution of generic three-dimensional single-black-hole spacetimes. *Phys. Rev. Lett.*, 80:3915–3918, 1998.

[119] Erik Schnetter. *Gauge fixing for the simulation of black hole spacetimes.* PhD thesis, Universität Tübingen, Tübingen, Germany, 2003. URN: urn:nbn:de:bsz:21-opus-8191.

[120] Silvano Bonazzola, Eric Gourgoulhon, Philippe Grandclement, and Jerome Novak. A constrained scheme for Einstein equations based on Dirac gauge and spherical coordinates. *Phys. Rev.*, D70:104007, 2004.

[121] Luis Lehner. Numerical relativity: A review. *Class. Quantum Grav.*, 18:R25–R86, 2001.

[122] Takashi Nakamura, Ken-ichi Oohara, and Y. Kojima. General relativistic collapse to black holes and gravitational waves from black holes. *Prog. Theor. Phys. Suppl.*, 90:1–218, 1987.

[123] M. Shibata and Takashi Nakamura. Evolution of three-dimensional gravitational waves: Harmonic slicing case. *Phys. Rev. D*, 52:5428, 1995.

[124] T. W. Baumgarte and S. L. Shapiro. Numerical integration of Einstein's field equations. *Phys. Rev. D*, 59:024007, 1999.

[125] M. Shibata, T. W. Baumgarte, and S. L. Shapiro. Stability and collapse of rapidly rotating, supramassive neutron stars: 3D simulations in general relativity. *Phys. Rev. D*, 61:044012, 2000. gr-qc/9911308.

[126] Masaru Shibata. Axisymmetric general relativistic hydrodynamics: Long-term evolution of neutron stars and stellar collapse to neutron stars and black holes. *Phys. Rev. D*, 67:024033, 2003.

[127] M. Alcubierre, B. Brügmann, T. Dramlitsch, J. A. Font, Philippos Papadopoulos, E. Seidel, N. Stergioulas, and R. Takahashi. Towards a stable numerical evolution of strongly gravitating systems in general relativity: The conformal treatments. *Phys. Rev. D*, 62:044034, 2000.

[128] J. A. Font, T. Goodale, S. Iyer, M. Miller, L. Rezzolla, E. Seidel, N. Stergioulas, W. M. Suen, and M. Tobias. Three-dimensional general relativistic hydrodynamics. II. Long-term dynamics of single relativistic stars. *Phys. Rev. D*, 65:084024, 2002.

[129] G. Yoneda and H. Shinkai. Advantages of modified ADM formulation: Constraint propagation analysis of the Baumgarte-Shapiro-Shibata-Nakamura system. *Phys. Rev. D*, 66:124003, 2002.

[130] M. Kawamura, K. Oohara, and T. Nakamura. General relativistic numerical simulation on coalescing binary neutron stars and gauge-invariant gravitational wave extraction. 2003. astro-ph/0306481.

[131] M. Kawamura and K. Oohara. Gauge-invariant gravitational wave extraction from coalescing binary neutron stars. *Prog. Theor. Phys.*, 111:589–594, 2004.

[132] M. Alcubierre, G. Allen, B. Brügmann, G. Lanfermann, E. Seidel, W.-M. Suen, and M. Tobias. Gravitational collapse of gravitational waves in 3D numerical relativity. *Phys. Rev. D*, 61:041501 (R), 2000.

[133] M. Alcubierre and B. Brügmann. Simple excision of a black hole in 3+1 numerical relativity. *Phys. Rev. D*, 63:104006, 2001.

[134] Miguel Alcubierre, Bernd Brügmann, Peter Diener, Michael Koppitz, Denis Pollney, Edward Seidel, and Ryoji Takahashi. Gauge conditions for long-term numerical black hole evolutions without excision. *Phys. Rev. D*, 67:084023, 2003.

[135] Luca Baiotti, Ian Hawke, Luciano Rezzolla, and Erik Schnetter. Gravitational-wave emission from rotating gravitational collapse in three dimensions. *Phys. Rev. Lett.*, 94:131101, 2005.

[136] R. D. Richtmyer and K.W. Morton. *Difference Methods for Initial Value Problems*. Interscience Publishers, New York, 1967.

[137] M. Alcubierre, G. Allen, B. Brügmann, E. Seidel, and W.-M. Suen. Towards an understanding of the stability properties of the 3+1 evolution equations in general relativity. *Phys. Rev. D*, 62:124011, 2000.

[138] O. Sarbach, G. Calabrese, J. Pullin, and M. Tiglio. Hyperbolicity of the BSSN system of Einstein evolution equations. *Phys. Rev. D*, 66: 064002, 2002.

[139] C. Bona, T. Ledvinka, C. Palenzuela, and M. Zacek. A symmetry-breaking mechanism for the Z4 general-covariant evolution system. *Phys. Rev. D*, 69:064036, 2004.

[140] G. Nagy, O. E. Ortiz, and O. A. Reula. Strongly hyperbolic second order Einstein's evolution equations. *Phys. Rev. D*, 70:044012, 2004.

[141] J. A. Font, M. Miller, W. M. Suen, and M. Tobias. Three-dimensional numerical general relativistic hydrodynamics: Formulations, methods, and code tests. *Phys. Rev. D*, 61:044011, 2000. gr-qc/9811015.

[142] J. Balakrishna, G. Daues, E. Seidel, W.-M. Suen, M. Tobias, and E. Wang. Coordinate conditions in three-dimensional numerical relativity. *Class. Quantum Grav.*, 13:L135–L142, 1996.

[143] G. D. Smith. *Numerical Solution of Partial Differential Equations.* Oxfort University Press, third edition, 1985. ISBN 0198596502.

[144] E. F. Toro. *Riemann Solvers and Numerical Methods for Fluid Dynamics.* Springer-Verlag, 1999.

[145] T. Y. Hou and P. G. LeFloch. Why Nonconservative Schemes Converge to Wrong Solutions: Error Analysis. *Math. of Comp.*, 62:497–530, 1994.

[146] J. A. Font. Numerical hydrodynamics in general relativity. *Liv. Rev. Relativ.*, 6:4, 2003. http://relativity.livingreviews.org/Articles/lrr-2003-4.

[147] J. M. Martí, J. M. Ibánez, and J. M. Miralles. Numerical relativistic hydrodynamics: Local characteristic approach. *Phys. Rev. D*, 43:3794, 1991.

[148] F. Banyuls, J. A. Font, J. M. Ibánez, J. M. Martí, and J. A. Miralles. Numerical 3+1 general-relativistic hydrodynamics: A local characteristic approach. *Astrophys. J.*, 476:221, 1997.

[149] J.M. Ibánez, M.A. Aloy, J.A. Font, J.M. Martí, J.A. Miralles, and J.A. Pons. In E.F. Toro, editor, *Godunov methods: theory and applications*, New York, 2001. Kluwer Academic/Plenum Publishers.

[150] P. D. Lax and B. Wendroff. Systems of conservation laws. *Comm. Pure Appl. Math.*, 13:217–237, 1960.

[151] C. B. Laney. *Computational Gasdynamics*. Cambridge University Press, 1998.

[152] R. J. Leveque. yhg. In Steiner O. and Gautschy A., editors, *Computational Methods for Astrophysical Fluid Flow*. Springer-Verlag, 1998.

[153] Miguel Alcubierre, Bernd Brügmann, Denis Pollney, Edward Seidel, and Ryoji Takahashi. Black hole excision for dynamic black holes. *Phys. Rev. D*, 64:061501(R), 2001.

[154] C. Bona, J. Massó, E. Seidel, and J. Stela. New Formalism for Numerical Relativity. *Phys. Rev. Lett.*, 75:600–603, 1995.

[155] D. Bernstein. *A Numerical Study of the Black Hole Plus Brill Wave Spacetime*. PhD thesis, University of Illinois Urbana-Champaign, 1993.

[156] D. Eardley and L. Smarr. Time functions in numerical relativity: Marginally bound dust collapse. *Phys. Rev. D*, 19:2239, 1979.

[157] M. Alcubierre. The appearance of coordinate shocks in hyperbolic formulations of general relativity. *Phys. Rev. D*, 55:5981–5991, 1997.

[158] M. Alcubierre and J. Massó. Pathologies of hyperbolic gauges in general relativity and other field theories. *Phys. Rev. D*, 57(8):4511–4515, 1998.

[159] Miguel Alcubierre. Hyperbolic slicings of spacetime: singularity avoidance and gauge shocks. *Class. Quantum Grav.*, 20(4):607–624, 2003.

[160] Larry Smarr and James W. York, Jr. Kinematical conditions in the construction of spacetime. *Phys. Rev. D*, 17(10):2529–2552, 15 May 1978.

[161] Mark Miller. Accuracy requirements for the calculation of gravitational waveforms from coalescing compact binaries in numerical relativity. *Phys. Rev. D*, 71:104016, 2005.

[162] Cactus Computational Toolkit. `http://www.cactuscode.org`.

[163] Marsha J. Berger. *Adaptive Mesh Refinement for Hyperbolic Partial Differential Equations*. PhD thesis, Stanford University, 1982. University Microfilms #DA 83-01196.

[164] Marsha J. Berger and Joseph Oliger. Adaptive mesh refinement for hyperbolic partial differential equations. *J. Comput. Phys.*, 53:484–512, 1984.

[165] Marsha J. Berger. Data structures for adaptive grid generation. *SIAM Journal of Scientific and Statistical Computing*, 7(3):904–916, July 1986.

[166] Marsha J. Berger and P. Colella. Local adaptive mesh refinement for shock hydrodynamics. *J. Comp. Phys.*, 82:64–84, 1989.

[167] M. Berger and I. Rigoutsos. Adaptive mesh refinement for hyperbolic partial differential equations. *IEEE Transactions on Systems, Man and Cybernetics*, 21(5), 1991.

[168] M. W. Choptuik. 1995. URL: `http://wwwrel.ph.utexas.edu/Members/matt/Doc/texas95.amr.ps`.

[169] J. Willard Gibbs. Fourier series. *Nature*, 59:200, 1898.

[170] J. Willard Gibbs. Fourier series. *Nature*, 59:606, 1899.

[171] James M. Hyman. The method of lines solution of partial differential equations. Technical Report COO-3077-139, ERDA Mathematics and Computing Laboratory, Courant Institute of Mathematical Sciences, New York University, October 1976.

[172] C. Runge. *Math. Ann.*, 46:167, 1895.

[173] M. Kutta. *Z. für Math. u. Phys.*, 46:435, 1901.

[174] C. W. Shu and S. J. Osher. *Journal of Computational Physics*, 77:439, 1988.

[175] S. Gottlieb and C. Shu. Total Variation Diminishing Runge-Kutta schemes. *Math. Comp.*, 67:73–85, 1998.

[176] Jonathan Thornburg. *Numerical Relativity in Black Hole Spacetimes*. PhD thesis, University of British Columbia, Vancouver, British Columbia, 1993.

[177] Jonathan Thornburg. A 3+1 computational scheme for dynamic spherically symmetric black hole spacetimes – II: Time evolution. 1999. gr-qc/9906022.

[178] S. K. Godunov. *Mat. Sb.*, 47:271, 1959. in Russian.

[179] R. J. Leveque. *Numerical Methods for Conservation Laws*. Birkhauser Verlag, Basel, 1992.

[180] Bertil Gustafsson, Heinz-Otto Kreiss, and Joseph Oliger. *Time dependent problems and difference methods*. Wiley, New York, 1995.

[181] B. J. van Leer. Towards the ultimative conservative difference scheme I. the quest for monotonicity. *Lecture Notes in Physics*, 18:163–168, 1973.

[182] A. Harten, B. Engquist, S. Osher, and S. R. Chakrabarty. Uniformly high order accurate essentially non-oscillatory schemes III. *J. Comput. Phys.*, 71:2311, 1987.

[183] P. Colella and P. R. Woodward. *J. Comput. Phys.*, 54:174, 1984.

[184] A. Harten, P. D. Lax, and B. van Leer. *SIAM Rev.*, 25:35, 1983.

[185] P. D. Lax. *Hyperbolic Systems of Conservation Laws and the Mathematical Theory of Shock Waves*. Society for Industrial and Applied Mathematics, Philadelphia, 1990.

[186] B. J. van Leer. *Journal of Computational Physics*, 32:101, 1979.

[187] P. K. Sweby. High resolution schemes using flux limiters for hyperbolic conservation laws. *SIAM J. Numer. Anal.*, 21:995–1011, 1984.

[188] C. W. Shu. High Order ENO and WENO Schemes for Computational Fluid Dynamics. In T. J. Barth and H. Deconinck, editors, *High-Order Methods for Computational Physics*. Springer, 1999.

[189] J. M. Martí and E. Müller. *J. Comput. Phys.*, 123:1, 1996.

[190] J. A. Pons, J. M. Martí, and E. Müller. The exact solution of the Riemann problem with non-zero tangential velocities in relativistic hydrodynamics. *J. Fluid Mech.*, 422:125–139, 2000.

[191] L. Rezzolla and O. Zanotti. An improved exact riemann solver for relativistic hydrodynamics. *Journ. of Fluid Mech.*, 449:395, 2001.

[192] L. Rezzolla, O. Zanotti, and J. A. Pons. An improved exact riemann solver for relativistic hydrodynamics with non-zero tangential velocities. *Journ. of Fluid Mech.*, 479:199, 2003.

[193] P. L. Roe. Approximate riemann solvers, parameter vectors and difference schemes. *J. Comput. Phy.*, 43:357, 1981.

[194] R. Donat and A. Marquina. Capturing shock reflections: an improved flux formula. *Journal of Computational Physics*, 125:42, 1996.

[195] R. Donat, J. A. Font, J. M. Ibánez, and A. Marquina. A flux-split algorithm applied to relativistic flows. *Journal of Computational Physics*, 146:58–81, 1998.

[196] M. A. Aloy, J. M$^{\underline{a}}$. Ibánez, J. M$^{\underline{a}}$. Martí, and E. Müller. *Astroph. J. Supp.*, 122:151, 1999.

[197] M. A. Aloy, J. A. Pons, and J. M. Ibánez. *Comput. Phys. Commun.*, 120:115, 1999.

[198] Matthew D. Duez, Pedro Marronetti, Stuart L. Shapiro, and Thomas W. Baumgarte. Hydrodynamic simulations in 3+1 general relativity. *Phys. Rev. D*, 67:024004, 2003.

[199] J. Centrella and J.R. Wilson. Planar numerical cosmology. II - The difference equations and numerical tests. *Astrophys. J. SS*, 54:229–245, 1984.

[200] EU Astrophysics Network Home Page http://www.eu-network.org.

[201] L. Baiotti, I. Hawke, P. Montero, and L. Rezzolla. A new three-dimensional general-relativistic hydrodynamics code. In R. Capuzzo-Dolcetta, editor, *Computational Astrophysics in Italy: Methods and Tools*, volume 1, page 327, Trieste, 2003. Mem. Soc. Astron. It. Suppl.

[202] S. L. Shapiro and S. A. Teukolsky. Relativistic stellar dynamics on the computer. In J. M. Centrella, editor, *Dynamical Spacetimes and Numerical Relativity*, pages 74–100. Cambridge University Press, Cambridge, England, 1986.

[203] L. Smarr and J. York. Radiation gauge in general relativity. *Phys. Rev.D*, 17:1945, 1978.

[204] S. Brandt and B. Brügmann. A simple construction of initial data for multiple black holes. *Phys. Rev. Lett.*, 78(19):3606–3609, 1997.

[205] L. E. Kidder, M. A. Scheel, S. A. Teukolsky, E. D. Carlson, and G. B. Cook. Black hole evolution by spectral methods. *Phys. Rev. D*, 62: 084032, 2000.

[206] L. E. Kidder, M. A. Scheel, and S. A. Teukolsky. Extending the lifetime of 3D black hole computations with a new hyperbolic system of evolution equations. *Phys. Rev. D*, 64:064017, 2001.

[207] H.-J. Yo, T. W. Baumgarte, and S. L. Shapiro. Improved numerical stability of stationary black hole evolution calculations. *Phys. Rev. D*, 66:084026, 2002.

[208] P. Laguna and D. Shoemaker. Numerical stability of a new conformal-traceless 3+1 formulation of the Einstein equation. *Class. Quantum Grav.*, 19:3679–3686, 2002. gr-qc/0202105.

[209] Matthew W. Choptuik, Eric W. Hirschmann, Steven L. Liebling, and Frans Pretorius. Critical collapse of the massless scalar field in axisymmetry. *Phys. Rev. D*, 68:044007, 2003.

[210] Ulrich Sperhake, Kenneth L. Smith, Bernard Kelly, Pablo Laguna, and Deirdre Shoemaker. Impact of densitized lapse slicings on evolutions of a wobbling black hole. *Phys. Rev.*, D69:024012, 2004.

[211] William G. Unruh. personal communication to Jonathan Thornburg. August 1984.

[212] Jonathan Thornburg. Coordinates and boundary conditions for the general relativistic initial data problem. *Class. Quantum Grav.*, 4(5):1119–1131, September 1987. URL `http://stacks.iop.org/0264-9381/4/1119`.

[213] Gioel Calabrese, Luis Lehner, David Neilsen, Jorge Pullin, Oscar Reula, Olivier Sarbach, and Manuel Tiglio. Novel finite-differencing techniques for numerical relativity: application to black hole excision. *Class. Quantum Grav.*, 20:L245–L252, 2003.

[214] Gioel Calabrese, Luis Lehner, Oscar Reula, Olivier Sarbach, and Manuel Tiglio. Summation by parts and dissipation for domains with excised regions. *Class. Quantum Grav.*, 21:5735–5758, 2004.

[215] J. M. Bardeen and Tsvi Piran. General relativistic axisymmetric rotating systems: Coordinates and equations. *Phys. Reports*, 196:205, 1983.

[216] Deirdre Shoemaker, Kenneth L. Smith, Ulrich Sperhake, Pablo Laguna, Erik Schnetter, and David Fiske. Moving black holes via singularity excision. *Class. Quantum Grav.*, 20:3729–3744, 2003. gr-qc/0301111.

[217] E. Seidel and W.-M. Suen. Towards a singularity-proof scheme in numerical relativity. *Phys. Rev. Lett.*, 69(13):1845–1848, 1992.

[218] J. York. Initial data for collisions of black holes and other gravitational miscellany. In C. Evans, L. Finn, and D. Hobill, editors, *Frontiers in Numerical Relativity*, pages 89–109. Cambridge University Press, Cambridge, England, 1989.

[219] Jonathan Thornburg. 1991. A talk given at CITA, Toronto, May, 1991.

[220] M. M. May and R. H. White. Stellar dynamics and gravitational collapse. In B. Alder, editor, *Methods in Computational Physics*, volume 7, page 129, 1967.

[221] M. Alcubierre and B. Schutz. Time–symmetric adi and causal reconnection: Stable numerical techniques for hyperbolic systems on moving grids. *J. Comp. Phys.*, 112:44, 1994.

[222] Miguel Alcubierre, Bernd Brügmann, Peter Diener, Frank Herrmann, Denis Pollney, Edward Seidel, and Ryoji Takahashi. Testing excision techniques for dynamical 3D black hole evolutions. *submitted to Phys. Rev. D*, 2004.

[223] J. A. Font, N. Stergioulas, and K. D. Kokkotas. Nonlinear hydrodynamical evolution of rotating relativistic stars: Numerical methods and code tests. *Mon. Not. R. Astron. Soc.*, 313:678, 2000.

[224] Masaru Shibata. Collapse of rotating supramassive neutron stars to black holes: Fully general relativistic simulations. *Astrophys. J.*, 595: 992, 2003.

[225] S. Brandt, J. A. Font, J. M. Ibáñez, J. Massó, and E. Seidel. Numerical evolution of matter in dynamical axisymmetric black hole spacetimes. I. method and tests. *Comp. Phys. Comm.*, 124:169–196, 2000.

[226] Matthew D. Duez, Stuart L. Shapiro, and Hwei-Jang Yo. Relativistic hydrodynamic evolutions with black hole excision. *Phys. Rev. D*, 69: 104016, 2004.

[227] Matthew D. Duez, Yuk Tung Liu, Stuart L. Shapiro, and Branson C. Stephens. General relativistic hydrodynamics with viscosity: Contraction, catastrophic collapse, and disk formation in hypermassive neutron stars. *Phys. Rev. D*, 69:104030, 2004.

[228] Jonathan Thornburg. A fast apparent-horizon finder for 3-dimensional Cartesian grids in numerical relativity. *Class. Quantum Grav.*, 21(2): 743–766, 2004. gr-qc/0306056.

[229] P. Diener. A new general purpose event horizon finder for 3D numerical spacetimes. *Class. Quantum Grav.*, 20(22):4901–4917, 2003.

[230] N. O'Murchadha and J. York. Gravitational energy. *Phys. Rev. D*, 10 (8):2345–2357, 1974.

[231] J. Bardeen and L. Buchman. Numerical tests of evolution systems, gauge conditions, and boundary conditions of 1D colliding gravitational plane waves. *Phys. Rev. D*, 65:064037, 2002.

[232] C. Bona, T. Ledvinka, C. Palenzuela-Luque, J. A. Pons, and M. Žáček. Gauge pathologies in singularity-avoidant spacetime foliations. 2004.

[233] Gioel Calabrese and David Neilsen. Spherical excision for moving black holes and summation by parts for axisymmetric systems. *Phys. Rev. D*, 69:044020, 2004.

[234] Jonathan Thornburg. Black hole excision with multiple grid patches. *Class. Quantum Grav.*, 21(15):3665–3691, 2004. gr-qc/0404059.

[235] Takashi Nakamura and M. Sasaki. *Phys. Lett.*, 106 B:69, 1981.

[236] Takashi Nakamura. *Prog. Theor. Phys.*, 70:1144, 1983.

[237] R. F. Stark and Tsvi Piran. Gravitational-wave emission from rotating gravitational collapse. *Phys. Rev. Lett.*, 55:891, 1985.

[238] R. F. Stark and Tsvi Piran. A numerical computation of the gravitational radiation from rotating gravitational collapse. In Remo Ruffini, editor, *Proceedings of the Fourth Marcell Grossman Meeting on General Relativity*, page 327. Elsevier Science Publisher, 1986.

[239] R. F. Stark and Tsvi Piran. A general relativistic code for rotating axisymmetric configurations and gravitational radiation: numerical methods and tests. *Comp. Phys. Rep.*, 5:221, 1987.

[240] M. Alcubierre, S. Brandt, B. Brügmann, D. Holz, E. Seidel, R. Takahashi, and J. Thornburg. Symmetry without symmetry: Numerical simulation of axisymmetric systems using Cartesian grids. *Int. J. Mod. Phys. D*, 10(3):273–289, 2001. gr-qc/9908012.

[241] J. Frauendiener. Discretizations of axisymmetric systems. *Phys. Rev. D*, 66:104027, 2002. gr-qc/0207092.

[242] M. Shibata. Axisymmetric Simulations of Rotating Stellar Collapse in Full General Relativity. *Prog. Theor. Phys.*, 104:325–358, 2000.

[243] M. Shibata and Y. Sekiguchi. Three-dimensional simulations of stellar core collapse in full general relativity: Nonaxisymmetric dynamical instabilities. *Phys. Rev. D in print*, 2005.

[244] S. L. Shapiro. Collapse of uniformly rotating stars to black holes and the formation of disks. *astro-ph/0404338*, 2004.

[245] M. E. Rupright, A. M. Abrahams, and L. Rezzolla. Cauchy-perturbative matching and outer boundary conditions I: Methods and tests. *Phys. Rev. D*, 58:044005, 1998.

[246] L. Rezzolla, A. M. Abrahams, Richard A. Matzner, M. Rupright, and S. L. Shapiro. Cauchy-perturbative matching and outer boundary conditions: computational studies. *Phys. Rev. D*, 59:064001, 1999.

[247] Erik Schnetter, Scott H. Hawley, and Ian Hawke. Evolutions in 3D numerical relativity using fixed mesh refinement. *Class. Quantum Grav.*, 21(6):1465–1488, 21 March 2004.

[248] Lawrence Kidder, Mark Scheel, Saul Teukolsky, and Greg Cook. Spectral evolution of Einstein's equations. In *Miniprogram on Colliding Black Holes: Mathematical Issues in Numerical Relativity*, Santa Barbara, CA, 2000. Institute for Theoretical Physics, UCSB.

[249] J. L. Friedman, J. R. Ipser, and R. D. Sorkin. Turning-point method for axisymmetric stability of rotating relativistic stars. *Astrophys. J.*, 325:722–724, 1988.

[250] N. Stergioulas and J. L. Friedman. Comparing models of rapidly rotating relativistic stars constructed by two numerical methods. *Astrophys. J.*, 444:306, 1995.

[251] N. Stergioulas and J.A. Font. Nonlinear r-modes in Rapidly Rotating Relativistic Stars. *Phys. Rev. Lett.*, 86:1148–1151, 2001.

[252] N. Stergioulas. Rotating stars in relativity. *Living Rev. Relativity*, 6:3, 2003.

[253] N. Stergioulas and I. Hawke. Equilibrium and pulsations of rotating stars in numerical relativity. In K. D. Kokkotas and N. Stergioulas, editors, *Recent Developments in Gravity, Proceedings of the 10th Hellenic Relativity Conference*, page 185, Singapore, 2003. World Scientific.

[254] S. E. Woosley. Gamma-ray bursts in the afterglow era. In E. Costa, F. Frontera, and J. Hjorth, editors, *Proceedings of the International Workshop held in Rome, CNR headquarters, October, 2000*, page 257, Berlin Heidelberg, 2000. Springer.

[255] Olindo Zanotti, Luciano Rezzolla, and Jose A. Font. Quasi-periodic accretion and gravitational waves from oscillating "toroidal neutron stars" around a Schwarzschild black hole. 2002. gr-qc/0210018.

[256] M. Shibata. Fully general relativistic simulation of coalescing binary neutron stars: Preparatory tests. *Phys. Rev. D*, 60:104052, 1999. gr-qc/9908027.

[257] J.M. Bardeen. A variational principle for rotating stars in general relativity. *Astrophys. J.*, 162:171, 1970.

[258] A. Cumming, S. M. Morsink, L. Bildsten, J. L. Friedman, and D. E. Holz. Hydrostatic expansion and spin changes during type I X-Ray bursts. *Astrophys. J.*, 564:343–352, 2000.

[259] L. Rezzolla, F. K. Lamb, and S. L. Shapiro. r-mode oscillations in rotating magnetic neutron stars. *Astrophys. J.*, 531:L139, 2000.

[260] H. C. Spruit. *Astron. and Astrophys.*, 341:L1, 1999.

[261] P. Anninos, D. Bernstein, S. R. Brandt, D. Hobill, E. Seidel, and L. Smarr. Dynamics of black hole apparent horizons. *Phys. Rev. D*, 50:3801–3815, 1994.

[262] P. Anninos, D. Bernstein, S. Brandt, J. Libson, J. Massó, E. Seidel, L. Smarr, W.-M. Suen, and P. Walker. Dynamics of apparent and event horizons. *Phys. Rev. Lett.*, 74(5):630–633, 30 January 1995. URL `http://link.aps.org/abstract/PRL/v74/p630`.

[263] P. Anninos, D. Bernstein, S. Brandt, D. Hobill, E. Seidel, and L. Smarr. Oscillating apparent horizons in numerically generated spacetimes. *Australian Journal of Physics*, 48:1027, 1995.

[264] S. R. Brandt and E. Seidel. Evolution of distorted rotating black holes II: Dynamics and analysis. *Phys. Rev. D*, 52(2):870–886, 1995.

[265] S. Brandt and E. Seidel. Evolution of distorted rotating black holes I: Methods and tests. *Phys. Rev. D*, 52(2):856–869, 1995. PHY94-07882,ASC93-18152.

[266] Abhay Ashtekar, Christopher Beetle, and Stephen Fairhurst. Mechanics of isolated horizons. *Class. Quantum Grav.*, 17:253–298, 2000.

[267] Abhay Ashtekar, Christopher Beetle, Olaf Dreyer, Stephen Fairhurst, Badri Krishnan, Jerzy Lewandowski, and Jacek Wisniewski. Generic isolated horizons and their applications. *Phys. Rev. Lett.*, 85:3564–3567, 2000.

[268] Abhay Ashtekar, Christopher Beetle, and Jerzy Lewandowski. Mechanics of rotating isolated horizons. *Phys. Rev. D*, 64:044016, 2001.

[269] Abhay Ashtekar and Badri Krishnan. Dynamical Horizons: Energy, angular momentum, fluxes, and balance laws. *Phys. Rev. Lett.*, 89: 261101, 2002.

[270] Olaf Dreyer, Badri Krishnan, Deirdre Shoemaker, and Erik Schnetter. Introduction to Isolated Horizons in Numerical Relativity. *Phys. Rev. D*, 67:024018, 2003.

[271] Abhay Ashtekar and Badri Krishnan. Dynamical horizons and their properties. *Phys. Rev. D*, 68:104030, 2003.

[272] D. Christodoulou. Reversible and irreversible transformations in black-hole physics. *Phys. Rev. Lett.*, 25(22):1596–1597, 1970.

[273] B. Brügmann. Bifunctional adaptive mesh (bam) for 3d numerical relativity. In A. Olinto, J. Frieman, and D. Schramm, editors, *Proceedings of The 18th Texas Symposium on Relativistic Astrophysics*, Singapore, 1998. World Scientific.

[274] James W. York. Kinematics and dynamics of general relativity. In Larry L. Smarr, editor, *Sources of Gravitational Radiation*, pages 83–126. Cambridge University Press, Cambridge, UK, 1979. ISBN 0-521-22778-X.

[275] Marcus Ansorg, Bernd Brügmann, and Wolfgang Tichy. A single-domain spectral method for black hole puncture data. *Phys. Rev. D*, 70:064011, 2004.

[276] C. Misner. Wormhole initial conditions. *Phys. Rev.*, 118(4):1110–1111, 1960.

[277] Heinz-Otto Kreiss and Joseph Oliger. Methods for the approximate solution of time dependent problems. *Global atmospheric research programme publications series*, 10, 1973.

[278] Frans Pretorius. Numerical relativity using a generalized harmonic decomposition. *Class.Quant.Grav.*, 22:425, 2005.

[279] P. Anninos, G. Daues, J. Massó, E. Seidel, and W.-M. Suen. Horizon boundary conditions for black hole spacetimes. *Phys. Rev. D*, 51(10): 5562–5578, 1995.

[280] K. D. Kokkotas and B. G. Schmidt. Quasi-normal modes of stars and black holes. *Living Rev. Rel.*, 2:1999–2, 1999. `http://www.livingreviews.org/lrr-1999-2`.

[281] E.W. Leaver. An analytic representation for the quasi-normal modes of Kerr black holes. *Proc. R. Soc. London, Ser. A*, 402:285–298, 1985.

[282] G. Calabrese, Luis Lehner, and M. Tiglio. Constraint-preserving boundary conditions in numerical relativity. *Phys. Rev. D*, 65:104031, 2002.

[283] G. Calabrese, J. Pullin, O. Reula, O. Sarbach, and M. Tiglio. Well posed constraint-preserving boundary conditions for the linearized Einstein equations. *Communications in Mathematical Physics*, 240:377–395, 2003.

[284] G. Calabrese, J. Pullin, O. Reula, O. Sarbach, and M. Tiglio. Well posed constraint-preserving boundary conditions for the linearized Einstein equations. *Communications in Mathematical Physics*, 240:377–395, 2003.

[285] Simonetta Frittelli and Roberto Gomez. Einstein boundary conditions for the 3+1 Einstein equations. 2003.

[286] Carsten Gundlach and Jose M. Martin-Garcia. Symmetric hyperbolicity and consistent boundary conditions for second-order Einstein equations. *Phys. Rev.*, D70:044032, 2004.

[287] B. Szilagyi and Jeffrey Winicour. Well-posed initial-boundary evolution in general relativity. *Phys. Rev. D*, 68:041501, 2002.

[288] Matthew D. Duez, Yuk Tung Liu, Stuart L. Shapiro, and Branson C. Stephens. Relativistic magnetohydrodynamics in dynamical spacetimes: Numerical methods and tests. 2005. astro-ph/0503420.

[289] Matthew D. Duez, Yuk Tung Liu, Stuart L. Shapiro, and Branson C. Stephens. Excitation of MHD modes with gravitational waves: A testbed for numerical codes. 2005. astro-ph/0503421.

[290] Lamport L. *LaTeX User's Guide & Reference Manual*. Addison-Wesley Publishing Company, 1994. LaTeX Handbuch.

[291] John P. Boyd. *Chebyshev and Fourier Spectral Methods (Second Edition, Revised)*. Dover Publications, New York, 2000.

[292] R. M. Wald. *General Relativity*. The University of Chicago Press, Chicago, 1984. ISBN 0-226-87032-4 (hardcover), 0-226-87033-2 (paperback).

[293] Beverly K. Berger. Numerical approaches to spacetime singularities. *Living Rev. Rel.*, 5:1, 2002. http://www.livingreviews.org/lrr-2002-1.

[294] Luca Baiotti. *Numerical relativity simulations of non-vaccum spacetimes in three dimensions*. PhD thesis, Scuola Internazionale Superioure di Studi Avanzati, 2004.

[295] Frank Herrmann. *Evolution and Analysis of Binary Black Hole Spacetimes*. PhD thesis, University of Potsdam (Germany), AEI, 2005.

[296] Andrea Nerozzi. *Towards BH-NS Merger Simulations: Initial Data, Evolution and Wave Extraction*. PhD thesis, University of Portsmouth, 2004.